FRICTION MODELING FOR INTERNAL COMBUSTION ENGINES

FRICTION MODELLING FOR INTERNAL COMBUSTION ENGINES

By

Li Sheng Yang

BSc(Eng), MSc(Eng)

A thesis submitted in accordance with the requirements for the degree of

Doctor of Philosophy

DEPARTMENT OF MECHANICAL ENGINEERING

THE UNIVERSITY OF LEEDS

LEEDS LS2 9JT

U.K.

October 1992

ABSTRACT

In recent times, engine designers and manufacturers have devoted considerable attention to the overall improvement in efficiency of internal combustion engines due to economic and environmental considerations. Although mechanical losses in an engine are just a small proportion of the total energy losses, they are nevertheless significant in relation to the output of useful work. The majority of frictional losses can be attributed to the tribological components of an engine, particularly, the bearings, the valve train and the piston assembly. To save time and cost during the pre-development and design stages it is very helpful to optimize the engine by means of analytical computer modelling.

A model has been established for the prediction of film thickness and friction for engine bearings. The computer programs developed include the study of a single dynamically loaded journal bearing and the analyses of all big-end and main bearings in an engine. Bearing loadings, journal orbits and frictional power losses have been evaluated. A case study and parametric studies have been taken for the well documented big-end bearing of a Ruston & Hornsby 6VEB-X MK III diesel engine. The bearings in the Ford 1.8L (Litre) H.O. (High Output) Zeta engine have been analysed with the dynamic load analysis, Petroff method and a steady load approximation and good results have been achieved.

A similar model has been developed for the engine valve train. The software can analyse the tribological conditions existing at the cam/follower interfaces for a cam and flat-faced follower system and a tapered cam and domed follower system. The model can evaluate the loadings, minimum film thicknesses, Hertzian stresses, frictional torques and power losses around the cam cycle. Analysis of camshaft bearing performance was carried out using the same techniques as for the crankshaft main bearings. Friction between follower/guide and valve/guide interfaces was also estimated. Parametric studies of the tapered cam and domed follower system have been presented. The whole valve train system in the Ford Zeta engine mentioned above has been studied throughout the development of the model.

A model for the prediction of film thickness, lubricant transport and friction has been established for the engine piston assembly. Computer programs were developed for the determination of gas pressures acting on each ring, for the analysis of the hydrodynamic lubrication of a single piston ring of fixed geometry and for the lubrication analysis of all rings within a ring pack taking account of the interaction between the rings. Studies of minimum film thicknesses, friction, power losses and oil flow passing each ring face were undertaken. Friction in the oil control ring and the piston skirt were also investigated. The piston assembly in the Ford Zeta engine has been analysed as a case study.

An overall friction and lubrication analysis model for engines has been established. This model is an integration of all the component models stated above and it can analyse lubrication and predict friction for any type of internal combustion engine. The Ford Zeta engine as a whole was analysed by this model and the results calculated were compared with experimental findings of some engines tested by other researchers. Good agreement was found for the relative friction contributions from major engine components.

ACKNOWLEDGEMENTS

Thanks are due to many people who have provided assistance and useful discussion during the course of this study.

I would like to express my sincerest thanks to the supervisors of the present work, Professor D.Dowson and Professor C.M.Taylor, for their constant help, guidance and encouragement. It is really a great pleasure to work under the supervision of two such distinguished scholars.

The assistance of my fellow students and members of staff have also been greatly valued. Special thanks are due to Dr.R.Chittenden and Mr.M.Priest of the Industrial Unit of Tribology, Dr.G.Zhu formerly of the Institute of Tribology at this Department and Mr.S.Edward of Leyland-DAF, for their valuable discussion and advice on some aspects of the work. The provision of engine bearing data from the Glacier Metal Company Ltd and Ruston Diesels Ltd is also appreciated. Thanks are also due to Mr.N.W.E.Weaver and Mr.S.Dadgostar of the Ford Motor Company Ltd (Limited) for their help in finding the technical data and procuring parts of the Ford Zeta engine.

The generous financial support from the State Education Commission of China, from the Committee of Vice-Chancellors and Principals of the Universities of the United Kingdom through an Overseas Research Student Award and from the Ford Motor Company Ltd are gratefully acknowledged.

Finally, I wish to thank my parents, my sisters and my wife for their love, support and encouragement. I hope that the completion of this work will in some way help to repay them for the many sacrifices they have made.

CONTENTS

List of Figures

List of Tables

NOTATION

Part I Friction Modelling for Engine Bearings

a	Piston acceleration	(m/s^2)
A	Area	(m^2)
b	Bearing length	(m)
c	Bearing radial clearance	(m)
C	Out of balance force	(N)
D	Cylinder bore	(m)
d	Bearing diameter	(m)
e	Eccentricity	(m)
F	Bearing Load	(N)
F_B	Big-end bearing load	(N)
F_G	Gas force	(N)
F_{rec}	Reciprocating inertia force	(N)
F_{rot}	Rotating inertia force	(N)
F_T	Side-thrust force	(N)
F_m	Main bearing load	(N)
g	Acceleration due to gravity	(9.81 m/s^2)
H	Bearing frictional power loss	(W)
L	Connecting rod length	(m)
m_p	Piston assembly mass	(kg)
m_c	Connecting rod mass	(kg)

M_o	Out of balance moment	(N.m)
M^ϵ, M^ϕ	Mobility components	
M^ξ, M^μ	Mobility components	
P	Gas pressure in cylinders	(Pa)
p	Oil film pressure	(Pa)
R	Crank radius	(m)
r	Bearing journal radius	(m)
V, V^ξ	Journal centre velocity & its component	(m/s)
x,y	Cartesian-coordinates	
α	Angular coordinate measured from	(^{0})
	h_{max} in the direction of rotation	
α_1, α_2	Oil film boundary	(^{0})
β	Angle measured from $\vec{F}$ to $\vec{V}$	(^{0})
ϵ	Eccentricity ratio	
θ	Crank angle	(^{0})
ξ, μ	Rectangular coordinates (of $\vec{\epsilon}$ relative to $\vec{F}$)	
ψ	Angle between connecting rod	(^{0})
	axes and cylinder axes	
ϕ	Attitude angle (of $\vec{\epsilon}$ relative to $\vec{F}$)	(^{0})
η	Lubricant dynamic viscosity	(Pa.s)
ω_{es}	Engine angular velocity	(rad/s)
ω_l	Bearing load angular velocity	(rad/s)
ω_b	Bearing bush angular velocity	(rad/s)
ω_j	Bearing journal angular velocity	(rad/s)

Part II Friction Modelling for an Engine Valve Train

a	Semi-major axis of contact ellipse	(m)
a_c	Follower acceleration	(m/s^2)
b	Semi-minor axis of contact ellipse (b≤a)	(m)
c	Radial clearance	(m)
d	Follower or valve stem diameter	(m)
e	Eccentricity	(m)
E_A, E_B	Young's modulus of elasticity of solids in contact	(N/m^2)
E'	Equivalent elastic modulus	(N/m^2)
F	Frictional force	(N)
F_c	Horizontal force causing follower to tilt	(N)
F_d	Force due to follower domed surface	(N)
F_{f1}, F_{f2}	Friction forces between follower and its guide	(N)
F_t	Force due to cam tapered shape	(N)
F_v	Vertical force	(N)
F_{xb}, F_{yb}	Camshaft bearing loads	(N)
F_{xp}, F_{yp}	Pulley loads on camshaft	(N)
F_z	Cam load	(N)
G	Dimensionless material parameter	
h_{cen}	Central lubricant film thickness	(m)
h_{min}	Minimum film thickness	(m)
H_f	Follower height	(m)
H_v	Average cam/follower frictional power loss	(W)
I_1, I_2	First and second complete elliptic integrals	

I_c	Inertia force	(N)
k	Ellipticity ratio (k≥1)	
K_s	Valve spring stiffness	(N/m)
L	Reciprocating length	(m)
L_c	Cam lift	(m)
m	Spring mass	(kg)
M	Reciprocating mass	(kg)
N_1, N_2	Normal loads between follower and its guide	(N)
p	Pressure	(N/m^2)
P_{max}	Maximum Hertzian pressure	(N/m^2)
r_{ax}, r_{ay}	Principal radii of curvature of contacting ellipsoids	(m)
r_{bx}, r_{by}	Principal radii of curvature of contacting ellipsoids	(m)
R_b	Base circle radius	(m)
R_c	Radius of curvature of contact point on cam	(m)
R_e	Equivalent radius of curvature	(m)
R_E	Equivalent radius of curvature in the entraining direction	(m)
r_f	Perpendicular distance from the cam centre of rotation to the frictional force vector	(m)
R_f	Radius of curvature of spherical face of follower	(m)
R_s	Equivalent radius of curvature in direction normal to lubricant entrainment	(m)
R_x, R_y	Equivalent radius of curvature in X,Y direction	(m)
S	Valve spring force	(N)
U_e	Dimensionless speed parameter	

V	Follower or valve reciprocating speed	(m/s)
V_c	Velocity of point of contact along the cam surface	(m/s)
V_e	Mean entraining velocity	(m/s)
V_f	Velocity of point of contact along the follower surface	(m/s)
V_s	Sliding velocity	(m/s)
W	Total load	(N)
W_e	Dimensionless load parameter	
Z	Distance between centre of camshaft rotation and centre of curvature of follower face	(m)
α	Pressure-viscosity coefficient	(m^2/N)
θ_c	Cam rotating angle, measured from top lift position	(^{0})
ψ_c	Angle between common tangent at the point of contact and X axis	(^{0})
η	Dynamic viscosity of lubricant	(Pa.s)
η_0	Reference dynamic viscosity at inlet to the contact	(Pa.s)
γ	Cam taper angle	(^{0})
δ	Initial compression of valve spring	(m)
ν_A, ν_B	Poisson's ratio of solids in contact	
ω_c	Camshaft angular velocity	(rad/s)

Part III Friction Modelling for an Engine Piston Assembly

b	Ring axial height	(m)
$C_1 \sim C_5$	Constants	
C_s	Radial clearance between piston skirt and cylinder liner	(m)

D	Cylinder bore	(m)
F_r	Viscous traction per unit circumferential length on ring	(N/m)
F_s	Viscous traction per unit circumferential length on skirt	(N/m)
F_x	Axial component of hydrodynamic force on ring face	(N/m)
F_z	Radial component of hydrodynamic force on ring face	(N/m)
h	Lubricant film thickness	(m)
h_i	Inlet film thickness	(m)
h_l	Film thickness on the liner between two adjacent rings	(m)
h_m	Film thickness at location where $\frac{dp}{dx} = 0$	(m)
h_{min}	Minimum film thickness	(m)
h_o	Outlet film thickness	(m)
L	Connecting rod length	(m)
L_s	Piston skirt height	(m)
O	Offset of parabolic profile of ring face	(m)
p	Pressure	(Pa)
p_a	Oil film pressure in inlet region of piston ring	(Pa)
p_b	Oil film pressure in outlet region of piston ring	(Pa)
p_{n-1}	Gas pressure above the nth ring	(Pa)
p_n	Gas pressure below the nth ring	(Pa)
Q	Volume rate of oil flow per unit circumferential length	(m^2/s)
R	Crank radius	(m)
R_r	Effective radius of curvature of ring face	(m)
T	Ring elastic tension	(Pa)
U_l	Equivalent axial velocity of cylinder liner	(m/s)

U_r	Axial velocity of piston ring	(m/s)
x	Axial coordinate relative to the entraining flank of ring	
x_1	Axial coordinate corresponding to inlet film h_i	(m)
x_2	Axial coordinate at which cavitation occurs	(m)
x_3	Axial coordinate at which reformation occurs	(m)
x_4	Axial coordinate corresponding to outlet film h_o	(m)
x_{min}	Axial coordinate at minimum film thickness point	(m)
θ	Crank angle	
η	Mean oil viscosity through film at a specified crank angle	(Pa.s)
τ	Viscous shear stress	(N/m^2)
ω_{es}	Engine crankshaft angular velocity	(rad/s)

INTRODUCTION

Since the discovery of crude oil and the development of technology, petroleum has been used as the source of motor fuel for the internal combustion engine for more than a century. Despite the successive discoveries of new oil fields around the world, oil consumption rose steadily up to 1973, bringing a dramatic decline in the oil reserves available. Low consumer oil prices throughout the 1960s encouraged relative wastage with the effect that the critical ratio of proven reserves to production, expressed in numbers of years to exhaustion, fell from nearly 100 in 1960 to less than 50 in 1973, according to the Ford Energy Report (Dorgham [1982]) published in 1982.

Following the Oil Crisis in the mid 1970s the western countries became increasingly aware of the fact that the earth's reserves of crude oil were a non-renewable resource. Political and environmental pressures caused many governments to campaign for more efficient usage of energy. To reduce oil demand and improve oil revenues, a steady program of price rises began and is still taking place. The engine and component manufacturers were put under increasing pressure from the government, and particular from the consumer, to design vehicles that not only had good reliability and durability but also returned better fuel consumption figures.

In recent years, environmental considerations arising from global warming and the so-called Greenhouse Effect have forced many countries to introduce tough regulations to limit the pollution caused by motor vehicles. From the economic point of view, the most effective way of lowering emissions is to reduce the level of fuel consumption. High engine efficiency and hence low fuel consumption means low overall gaseous emissions.

World political, economic and environmental pressures place significant emphasis once again upon the improvement of the efficiency of automobile engines.

It is widely recognized that the internal combustion engine is thermodynamically inefficient. Figure I.1(a) shows the results of one energy analysis for a typical urban drive cycle for a passenger car. It suggested that about 88% of the energy is uselessly dissipated in the form of heat to the environment either from the surfaces of the engine and its auxiliaries or down the exhaust pipe, leaving only 12% of the original energy being consumed for useful work. Another example (Figure I.1(b)) also shows that at the output of the engine the same small percentage from the total input energy is available at the wheels to drive the car. The distribution of energy may show substantial differences from results obtained by different sources. This depends on the type of engine, the load condition and specific operational situation in which the vehicle is being operated. However, the percentage figure of the so-called useful power from the total input energy will not differ significantly. There is no doubt that by tribological measures only the mechanical losses can be reduced. It can be seen from the first example (Figure I.1(a)) that about 13% of the total energy input is wasted due to the engine friction, while the energy loss due to engine mechanical friction caused about 7.5% of the total energy in the second example (Figure I.1(b)). Although the frictional losses are low relative to the total input of fuel energy, they form a significant loss considering that only about 25% of the energy gets converted to brake power and only around half of that is used at the wheels. Generally speaking, about 30% of the input energy in an internal combustion engine is dissipated via the exhaust gases, another 30% is lost through the cooling system, about 25% is available as brake power and about 15% is lost due to the mechanical friction (Taylor [1992]).

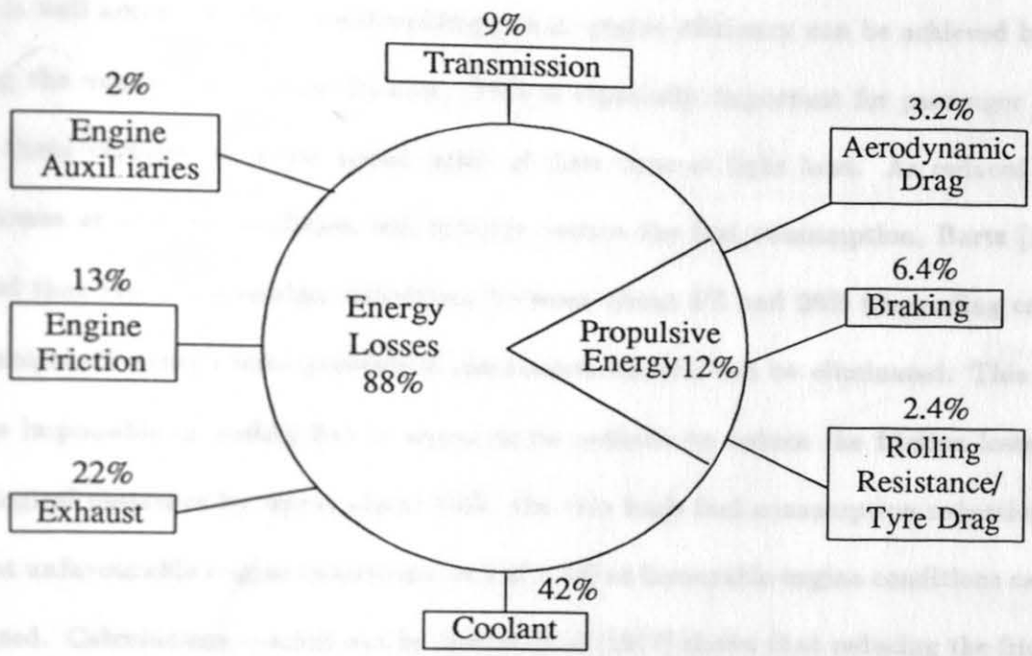

(a) Car Energy Usage in a Typical Metropolitan Cycle (Dorgham [1982])

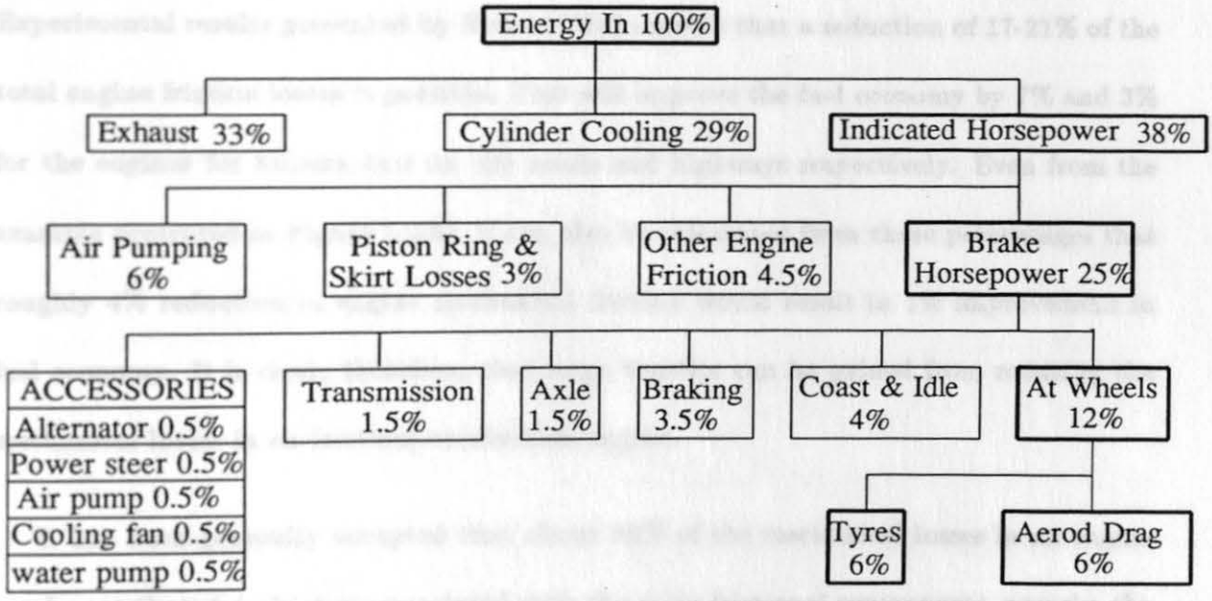

(b) Energy Distribution in a Passenger Car during a EPA City/Highway Cycle (Pinkus & Wilcock [1978])

Figure I.1 Energy Distributions in Passenger Cars for Specific Driving Cycles

It is well accepted that considerable gains in engine efficiency can be achieved by reducing the engine mechanical friction. This is especially important for passenger cars, since these vehicles normally spend most of their time at light load. As reduced friction losses at a given condition will directly reduce the fuel consumption, Bartz [1985] showed that fuel consumption reductions between about 5% and 28% (depending on the mechanical efficiency) were possible if mechanical friction can be eliminated. This is of course impossible in reality but it seems to be realistic to reduce the friction losses by tribological measures by up to about 30%. On this basis fuel consumption reductions of 11% at unfavourable engine conditions and of 1.5% at favourable engine conditions can be expected. Calculations carried out by Auiler et al [1977] shows that reducing the friction of the gasoline engine by 10% would yield a fuel economy improvement of some 5% and a similar proportional reduction of the diesel engine's friction would give as much as 7%. Experimental results presented by Hoshi [1984] suggest that a reduction of 17-21% of the total engine friction losses is possible. This will improve the fuel economy by 7% and 3% for the engines for Subaru cars on city roads and highways respectively. Even from the example presented in Figure I.1(b), it can also be calculated from those percentages that roughly 4% reduction in engine mechanical friction would result in 1% improvement in fuel economy. It is clear, therefore, that large benefits can be gained from reducing the mechanical losses in an internal combustion engine.

It has been generally accepted that about 80% of the mechanical losses in an engine can be attributed to friction associated with the main frictional components, namely, the engine bearings, the valve train and the piston assembly. A schematic diagram of these components in an engine is shown in Figure I.2. The bearings consist of the big-end bearings and the crankshaft main bearings; the valve train friction includes contributions

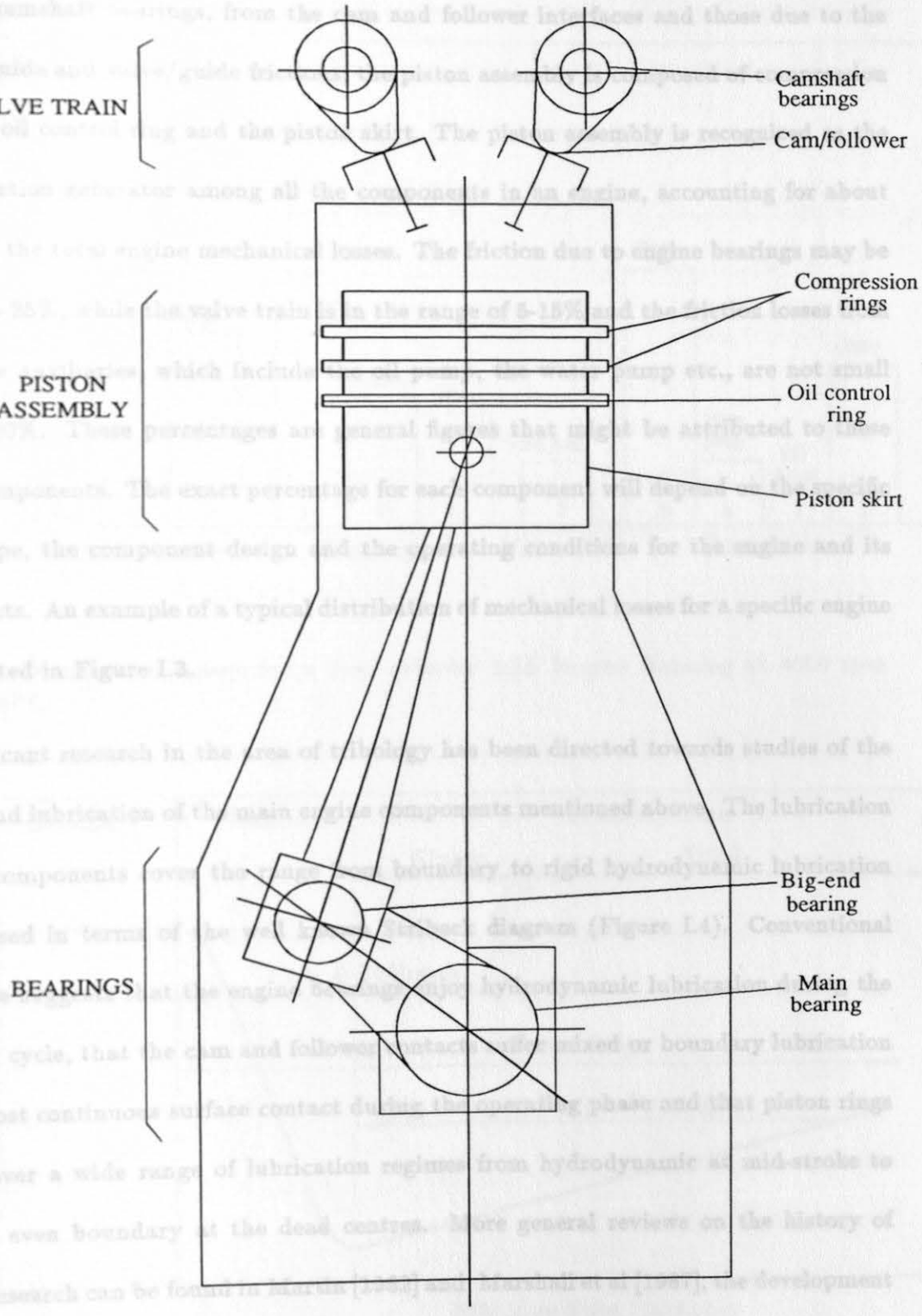

Figure I.2. Schematic Diagram for the Main Frictional Components in an Engine

from the camshaft bearings, from the cam and follower interfaces and those due to the follower/guide and valve/guide frictions; the piston assembly is composed of compression rings, the oil control ring and the piston skirt. The piston assembly is recognized as the largest friction generator among all the components in an engine, accounting for about 40-60% of the total engine mechanical losses. The friction due to engine bearings may be around 15-25%, while the valve train is in the range of 5-15% and the friction losses from the engine auxiliaries, which include the oil pump, the water pump etc., are not small at some 20%. These percentages are general figures that might be attributed to these engine components. The exact percentage for each component will depend on the specific engine type, the component design and the operating conditions for the engine and its components. An example of a typical distribution of mechanical losses for a specific engine is illustrated in Figure I.3.

Significant research in the area of tribology has been directed towards studies of the friction and lubrication of the main engine components mentioned above. The lubrication of these components cover the range from boundary to rigid hydrodynamic lubrication as expressed in terms of the well known Stribeck diagram (Figure I.4). Conventional experience suggests that the engine bearings enjoy hydrodynamic lubrication during the operating cycle, that the cam and follower contacts suffer mixed or boundary lubrication with almost continuous surface contact during the operating phase and that piston rings operate over a wide range of lubrication regimes from hydrodynamic at mid-stroke to mixed or even boundary at the dead centres. More general reviews on the history of bearing research can be found in Martin [1982] and Marshall et al [1987], the development of valve train research has been presented by Taylor [1991] and research in the lubrication and friction of piston rings was reviewed by McGeehan [1978], Ting [1985], Parker [1990]

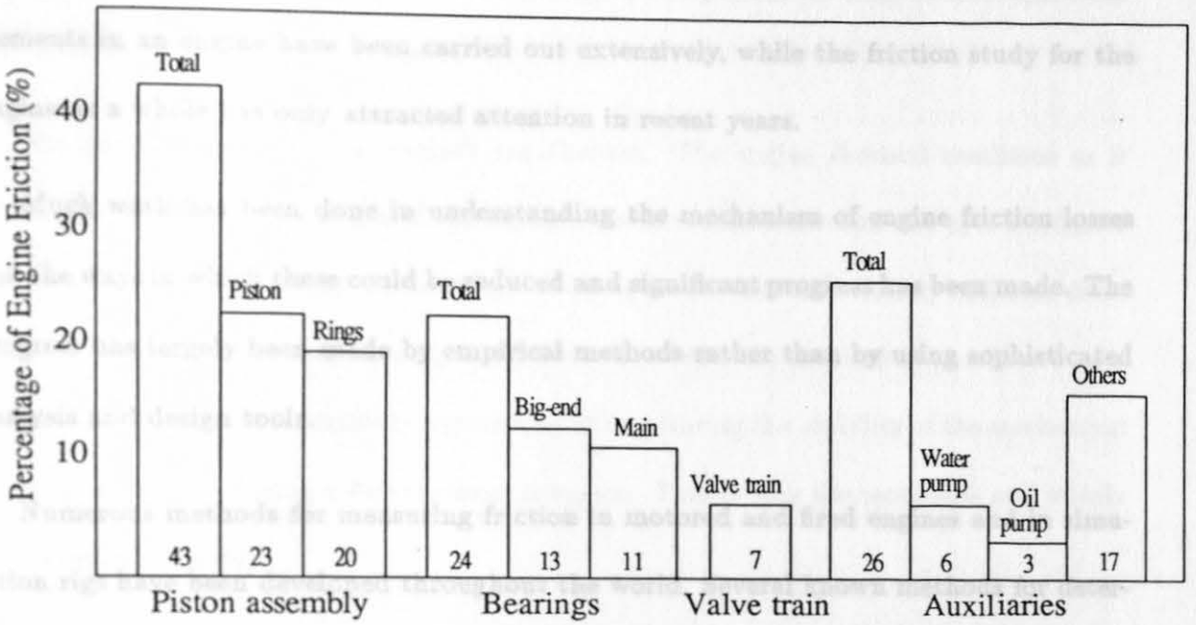

Figure I.3. Distribution Losses for a Four-cylinder 1.5L Engine Running at 4000 rpm (Groth [1977])

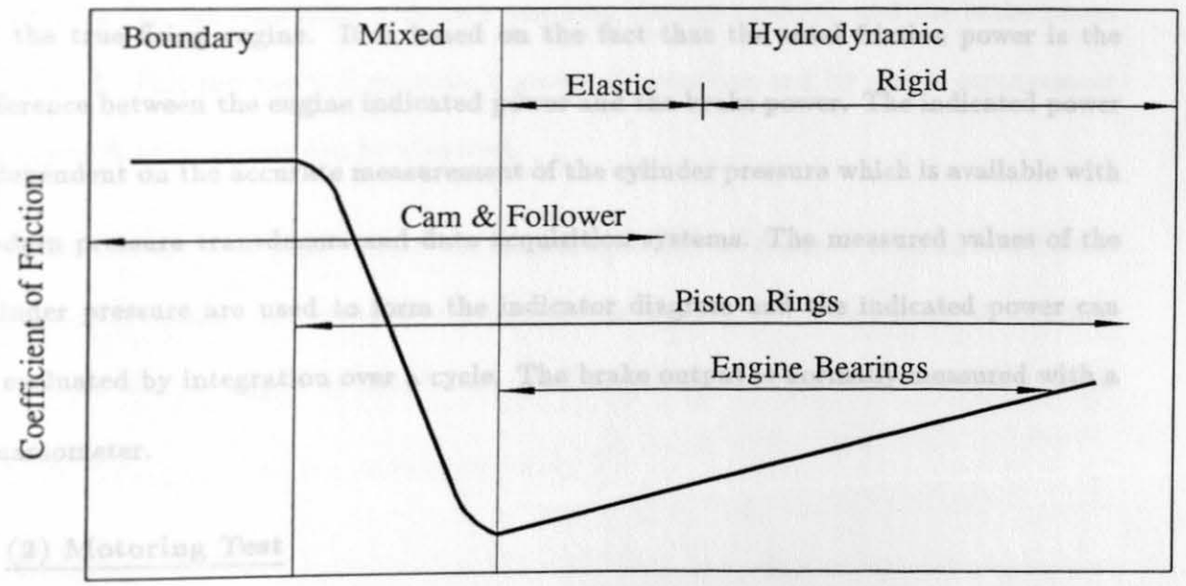

$$\text{Film Thickness Ratio} = \frac{\text{Effective Film Thickness}}{\text{Composite Surface Roughness}}$$

Figure I.4 Lubrication Regimes for the Main Engine Components

and Ruddy and Hildyard [1991]. The friction and lubrication studies of these individual elements in an engine have been carried out extensively, while the friction study for the engine as a whole has only attracted attention in recent years.

Much work has been done in understanding the mechanism of engine friction losses and the ways in which these could be reduced and significant progress has been made. The progress has largely been made by empirical methods rather than by using sophisticated analysis and design tools.

Numerous methods for measuring friction in motored and fired engines and in simulation rigs have been developed throughout the world. Several known methods for determining the total friction losses are listed below.

(1) Indicator Method

This is the method much preferred by many researchers as a measuring technique for the true firing engine. It is based on the fact that the total friction power is the difference between the engine indicated power and the brake power. The indicated power is dependent on the accurate measurement of the cylinder pressure which is available with modern pressure transducers and data acquisition systems. The measured values of the cylinder pressure are used to form the indicator diagram and the indicated power can be evaluated by integration over a cycle. The brake output is normally measured with a dynamometer.

(2) Motoring Test

In this test the engine is driven by an electric motor and the power required to drive the engine is measured and taken as the friction power. Progressive strip down of the

engine or selective addition of the removed engine components is used to investigate the contribution of different components.

The disadvantages of this method are obvious. The engine thermal condition as it affects the lubricant viscosity and the expansions of components and the cyclic cylinder gas pressure as it influences the loadings of components are unavoidably different from those in the engine normal running condition. However, the method is considered as a useful comparator and is certainly a good way of monitoring the stability of the mechanical losses in the engine during a development program. That is why the method is still widely used worldwide today.

(3) Morse Test

With a multi-cylinder engine at a given speed, the brake power produced by the engine is measured. Under the same operating condition each of the cylinders is cut out in turn, leaving the remaining cylinders motoring the one misfired, and the brake power is recorded. This process will generate a group of equations and by simple arrangement the engine friction power can be obtained.

Again this method suffers from the inaccuracies due to changed thermal conditions. The action of cutting one cylinder will disturb the fuel supply to the others. A modified Morse Test was developed by Smith and Griffiths [1985] and more accurate results have been claimed.

(4) P-ω Method

This method is based on the fact that the instantaneous cylinder gas forces and the instantaneous frictional, inertia and load forces cause an instantaneous variation in the

flywheel angular velocity. It requires the measurement of the cylinder gas pressure, P, during a cycle and the measurement of the instantaneous angular velocity, ω, at the flywheel. A more detailed description of this method can be found in Rezeka and Henein [1984].

(5) Run-out Test

The test starts with the engine operating under certain specified conditions at a state of thermal equilibrium. Then the fuel injection is suddenly stopped at a selected time by an automatic control mechanism, and maintained at that setting for one or more revolutions after which it is restored to its previous value. There is thus little change in the thermal conditions of the engine. The drop in speed during zero fuel injection is measured and recorded and the friction torque can then be calculated.

(6) Millans Line Method

Here the gross fuel consumption is measured at a number of brake outputs for a fixed engine speed. Then a line of the gross fuel consumption against the BMEP (Brake Mean Effective Pressure) is plotted and it is extrapolated back to zero fuel consumption to enable the FMEP (Friction Mean Effective Pressure) to be read off from the BMEP axis.

This method relies on very accurate test procedures and close control of the engine at very light loads. Generally the line has a slight curve, making accurate extrapolation difficult. Therefore, it is not perfectly rigorous.

It is popular in industry to develop analytical models to simulate the real engine performance. In the course of developing a new engine, there are several stages such as concept formation, setting performance requirement, trial production, engine test, mod-

ification and mass production. After trial production, testing is usually undertaken to confirm reliability and durability targets. When the test results indicate that a certain performance criteria has not been met, the specifications may have to be modified repeatedly until the targets are attained. That work can be very time-consuming and lead to unacceptable delays or cost increase. It is thus essential to make every effort to reduce the extent of testing and the expense involved. The normal way to deal with this problem is to establish a computer simulation model to make very accurate performance predictions at the predevelopment stage. Since engine friction is a very important performance factor, engine friction modelling seems inevitable.

Theoretical studies of friction for individual engine components have been carried out extensively in the past, while the analysis of the whole engine friction is less well advanced. Nearly all the engine friction models found in the published literature are based on a combination of empirical results and a simple mathematical method such as curve-fitting. They normally involve many constants and strongly depend on the engine type, operating conditions and the mathematical approach adopted. Examples include models presented by Pohlmann and Kuck [1984], Rezeka and Henein [1984], Hoshi [1984], Pohlmann and Kuck [1985] and Patton et al [1989]. The wider application of these semi-empirical approaches is unfortunately very limited. The model presented by Goto et al [1990] and Hamai et al [1991] assumed rigid engine components, sufficient lubricant on all sliding surfaces and constant oil viscosity for each single component. The fundamental equations for each component in this model are from published papers dealing with these components separately. This engine friction model, although still simple, is more sophisticated than those mentioned above.

The aims of the present work are;

1. To develop a lubrication and friction prediction model for engine bearings. It will include

   (a) the evaluation of bearing loadings for the big-end and main bearings;

   (b) the prediction of bearing journal locus and the minimum film thickness;

   (c) the estimation of bearing frictional power loss;

   (d) the influence of bearing design variables on the bearing tribological performance by carrying out parametric studies.

2. To create a lubrication and friction prediction model for an engine valve train. It will include

   (a) the analysis of the kinematics of a tapered cam acting against a non-rotating follower and a cam acting against a flat-faced follower;

   (b) the evaluation of the loadings at the cam/follower interfaces;

   (c) the studies of Hertzian stress at the cam/follower contact and the lubricant film thickness between the cams and followers;

   (d) the estimation of frictional torque and power loss at the cam/follower conjunction;

   (e) the analysis of camshaft bearing performance;

   (f) the modelling of friction predictions for the follower/guide and the valve/guide interfaces;

   (g) parametric studies of the tribological characteristics of the cams and followers.

3. To establish a lubrication and friction prediction model for an engine piston assembly. It will include

(a) the determination of inter-ring gas pressures;

(b) the lubrication analysis for a single ring and a complete ring pack;

(c) the calculations of oil film thickness, friction, power loss and oil transport for each ring;

(d) the investigation of frictional losses for the oil control ring and the piston skirt.

4. To form a lubrication and friction prediction model for the internal combustion engine by combining all the component models mentioned above into one integrated model.

The development of the model will involve simplifications in the design procedures established for the individual components. Such simplifications will be based on judgements made possible by the more detailed research studies of the past, particularly those undertaken in the University of Leeds. It is anticipated that the current study will be of benefit to engineers within industry in designing low-friction engine components and high-efficiency engines.

Throughout the course of the project, the Ford 1.8L H.O. Zeta engine, which is a four-cylinder, sixteen-valve double-overhead-camshaft, fuel-injected engine, has been analysed as a study case.

Part I

FRICTION MODELLING FOR ENGINE BEARINGS

Chapter One

Theoretical Basis for Engine Bearings

1.1 Introduction

To meet the needs for energy conservation, a deeper understanding of the mechanisms of frictional losses within all components of an internal combustion engine is required. Engine bearings are one major component which contribute to the overall engine frictional losses. Reduction in the losses will obviously help with energy conservation.

The lubrication and friction analysis of engine bearings requires the loads on bearings to be determined. The first part of this chapter, therefore, will show a basic force balance analysis for the big-end bearing loading evaluations and a simplified approach for the main bearing loading calculations.

The second part of the chapter presents an analytical method involving a solution of Reynolds equation for dynamically loaded journal bearings. The method that is most widely used is the so-called Short Bearing Mobility Method. Its great attraction at the present time is due to its simplicity, rapid solution procedure and excellent agreement of results with those of numerical solutions. It will be outlined and used for the present work.

The final part of the chapter will show a general formula for the calculation of power losses for dynamically loaded journal bearings. Two more approaches are also illustrated.

One is the equations derived for steadily loaded journal bearings and the other is the Petroff equation.

1.2 Bearing Loadings

Big-end bearings in the connecting rods and main bearings in the cylinder block in reciprocating engines are dynamically loaded journal bearings. When studying the performance of such bearings, it is necessary to determine the bearing loads and their changes in both magnitude and direction with time (usually it is convenient to represent time by crank angle positions). These are conveniently presented in the form of polar load diagrams.

1.2.1 Big-end Bearing Loadings

The loads on the connecting rod big-end bearing can be attributed to three components: due to gas forces in the cylinders, reciprocating inertia forces generated by the reciprocating parts of the mechanism and rotating inertia forces by the rotating parts.

To obtain the inertia forces, the commonly-used method is to consider this mechanism as a two-mass system. The reciprocating mass, which undergoes pure translational motion, is situated at the small-end bearing and consists of the mass of piston assembly and part of the connecting rod mass (usually about one third). The rotating mass which rotates around the crankshaft centre line is fixed at the big-end bearing and takes the remaining two thirds of the connecting rod mass. Although a more accurate description of the loading analysis is possible, this would require knowledge of both the connecting rod moment of inertia and the position of its centre of gravity. This obviously will complicate the analysis but particularly the acquisition of the required data.

The gas force acting on a piston surface is

$$F_G = \frac{\pi}{4} P D^2 \tag{1.1}$$

The acceleration of the reciprocating part, which can be found in Shaw and Macks [1949], is shown to be

$$a = R\omega_{es}^2 \left(\cos\theta + \frac{\left[\left(\left(\frac{L}{R}\right)^2 - 1 \right) \cos 2\theta + \cos^4\theta \right]}{\left[\left(\frac{L}{R}\right)^2 - \sin^2\theta \right]^{\frac{3}{2}}} \right) \tag{1.2}$$

then the reciprocating inertia force F_{rec} is

$$F_{rec} = \left(m_p + \frac{1}{3} m_c \right) a \tag{1.3}$$

and the rotating inertia force F_{rot} is

$$F_{rot} = \frac{2}{3} m_c R \omega_{es}^2 \tag{1.4}$$

The final force, the so-called side-thrust force, is due to the obliquity of the connecting rod. It acts through the piston normal to the cylinder liner.

$$\vec{F_T} = \left(\vec{F_G} + \vec{F}_{rec} \right) \tan\psi \tag{1.5}$$

Thus the instantaneous load on the big-end bearing at any particular crank angle is given by the vector sum of these forces, as shown in Figure 1.1. By calculating the resultant force $\vec{F_B}$ at a large number of crank angles through the engine cycle and plotting them on polar coordinates, a polar load diagram can be constructed. This diagram may be drawn relative to any convenient set of axes. The most common one for the big-end bearing is a set of axes fixed to the connecting rod centre line, and it is the one used in this analysis.

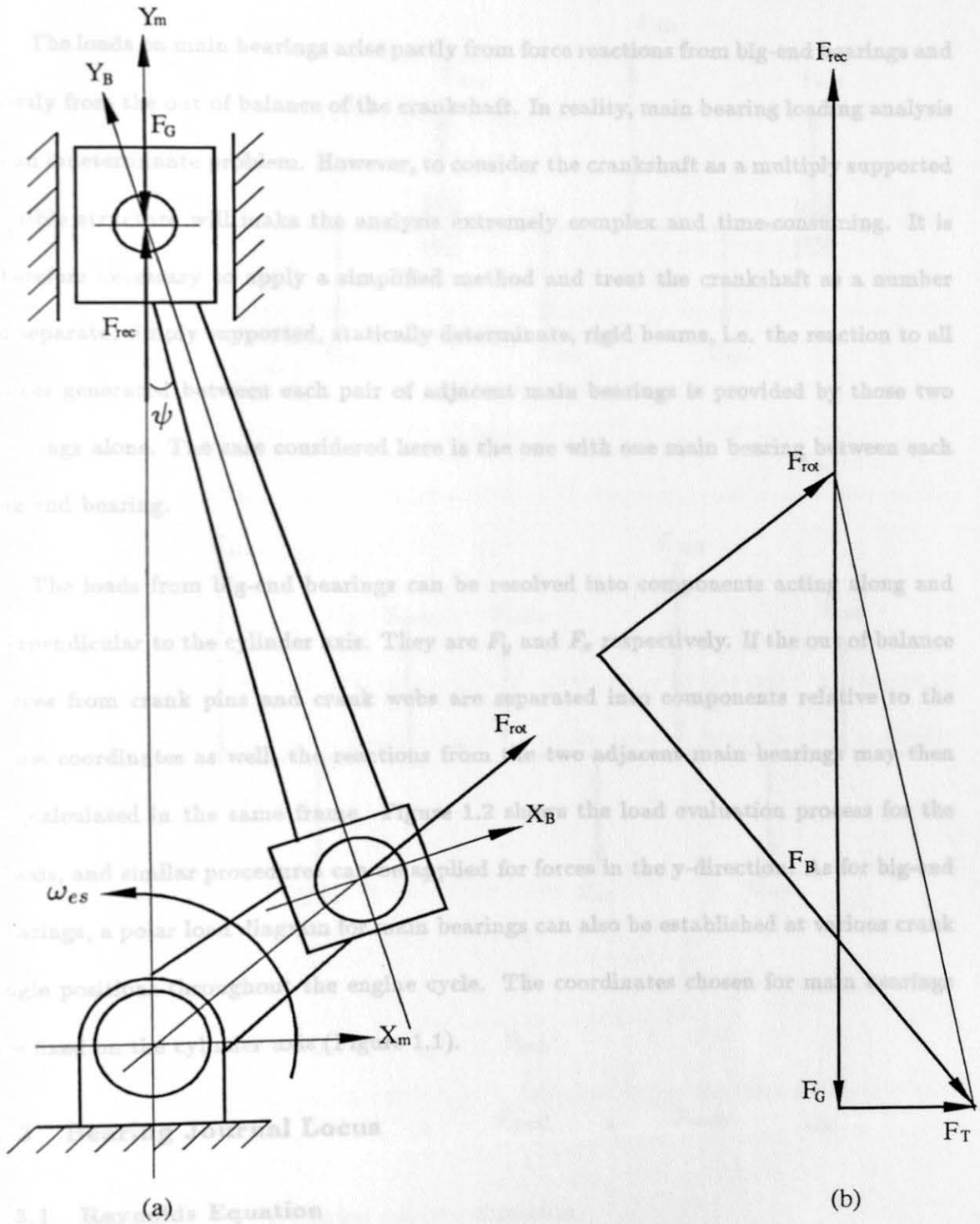

Figure 1.1. Slider-crank Mechanism and Vector Summation for Big-end Bearing Load Calculation

1.2.2 Main Bearing Loadings

The loads on main bearings arise partly from force reactions from big-end bearings and partly from the out of balance of the crankshaft. In reality, main bearing loading analysis is an indeterminate problem. However, to consider the crankshaft as a multiply supported flexible structure will make the analysis extremely complex and time-consuming. It is therefore necessary to apply a simplified method and treat the crankshaft as a number of separate, simply supported, statically determinate, rigid beams, i.e. the reaction to all forces generated between each pair of adjacent main bearings is provided by those two bearings alone. The case considered here is the one with one main bearing between each big-end bearing.

The loads from big-end bearings can be resolved into components acting along and perpendicular to the cylinder axis. They are F_y and F_x respectively. If the out of balance forces from crank pins and crank webs are separated into components relative to the same coordinates as well, the reactions from the two adjacent main bearings may then be calculated in the same frame. Figure 1.2 shows the load evaluation process for the x-axis, and similar procedures can be applied for forces in the y-direction. As for big-end bearings, a polar load diagram for main bearings can also be established at various crank angle positions throughout the engine cycle. The coordinates chosen for main bearings are fixed on the cylinder axis (Figure 1.1).

1.3 Bearing Journal Locus

1.3.1 Reynolds Equation

The equation governing pressure distribution in a fluid film bearing is well known as the Reynolds equation (Reynolds [1886]). It was derived on the basis of the following

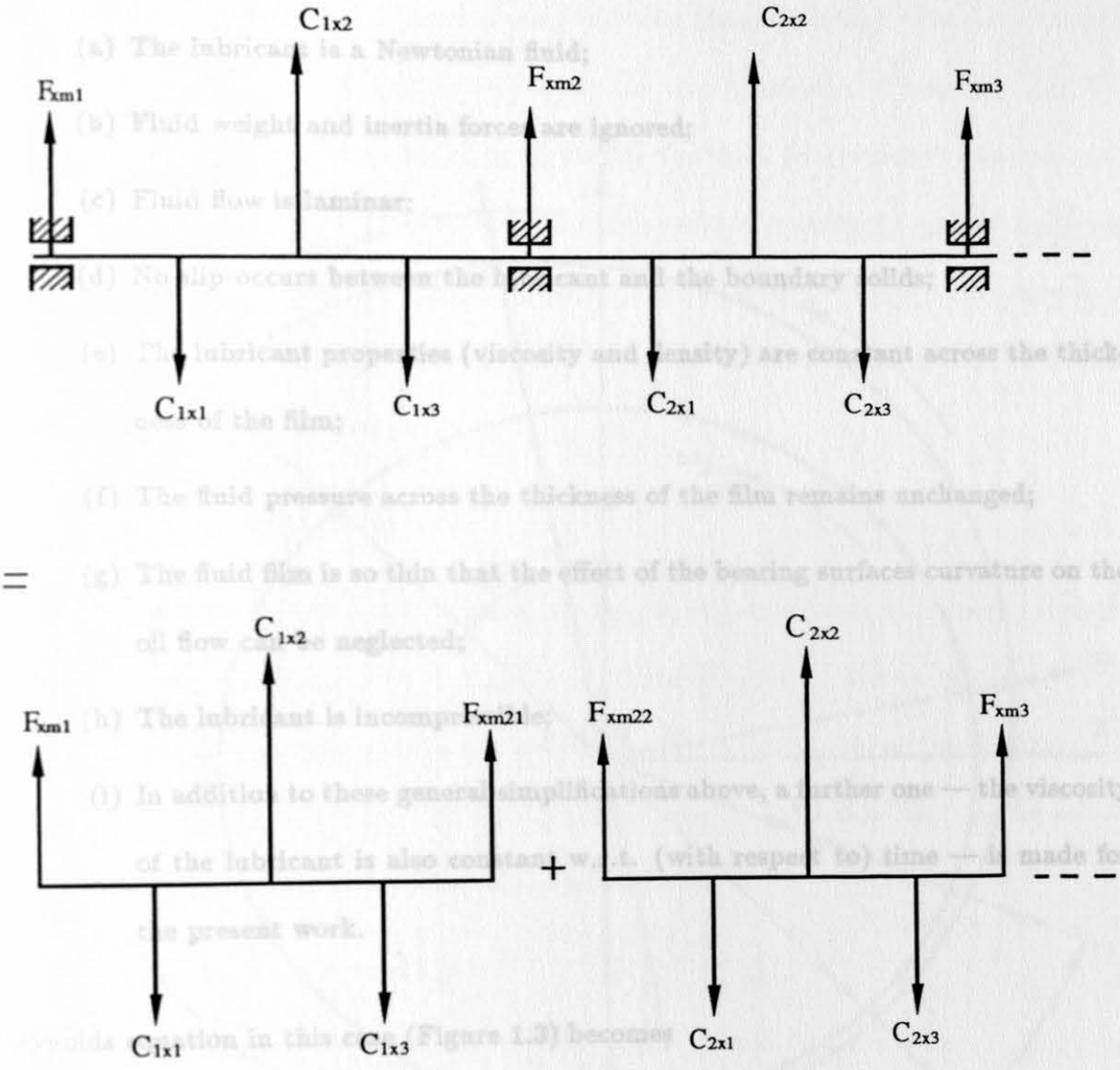

where

$$F_{xm1} = F_{xm1}$$

$$F_{xm2} = F_{xm21} + F_{xm22} \quad \text{etc.}$$

A similar process can be carried out in y-direction

Figure 1.2. Main Bearing Load Evaluation Process

assumptions:

(a) The lubricant is a Newtonian fluid;

(b) Fluid weight and inertia forces are ignored;

(c) Fluid flow is laminar;

(d) No slip occurs between the lubricant and the boundary solids;

(e) The lubricant properties (viscosity and density) are constant across the thickness of the film;

(f) The fluid pressure across the thickness of the film remains unchanged;

(g) The fluid film is so thin that the effect of the bearing surfaces curvature on the oil flow can be neglected;

(h) The lubricant is incompressible;

(i) In addition to these general simplifications above, a further one — the viscosity of the lubricant is also constant w.r.t. (with respect to) time — is made for the present work.

Reynolds equation in this case (Figure 1.3) becomes

$$\frac{\partial}{\partial\alpha}\left[(1+\epsilon\cos\alpha)^3\frac{\partial p}{\partial\alpha}\right]+r^2\frac{\partial}{\partial y}\left[(1+\epsilon\cos\alpha)^3\frac{\partial p}{\partial y}\right] = 12\eta\left(\frac{r}{c}\right)^2\left[\dot{\epsilon}\cos\alpha+\epsilon\sin\alpha\left(\dot{\phi}-\frac{\omega_b+\omega_j}{2}\right)\right] \tag{1.6}$$

and the bearing edge boundary condition for a complete film at ambient pressure would be simply

$$p\left(\alpha,\pm\frac{b}{2}\right)=0 \tag{1.7}$$

The complete solution of equations (1.6) and (1.7) requires considerable numerical effort and a useful approximate solution is then needed. Generally there are three ap-

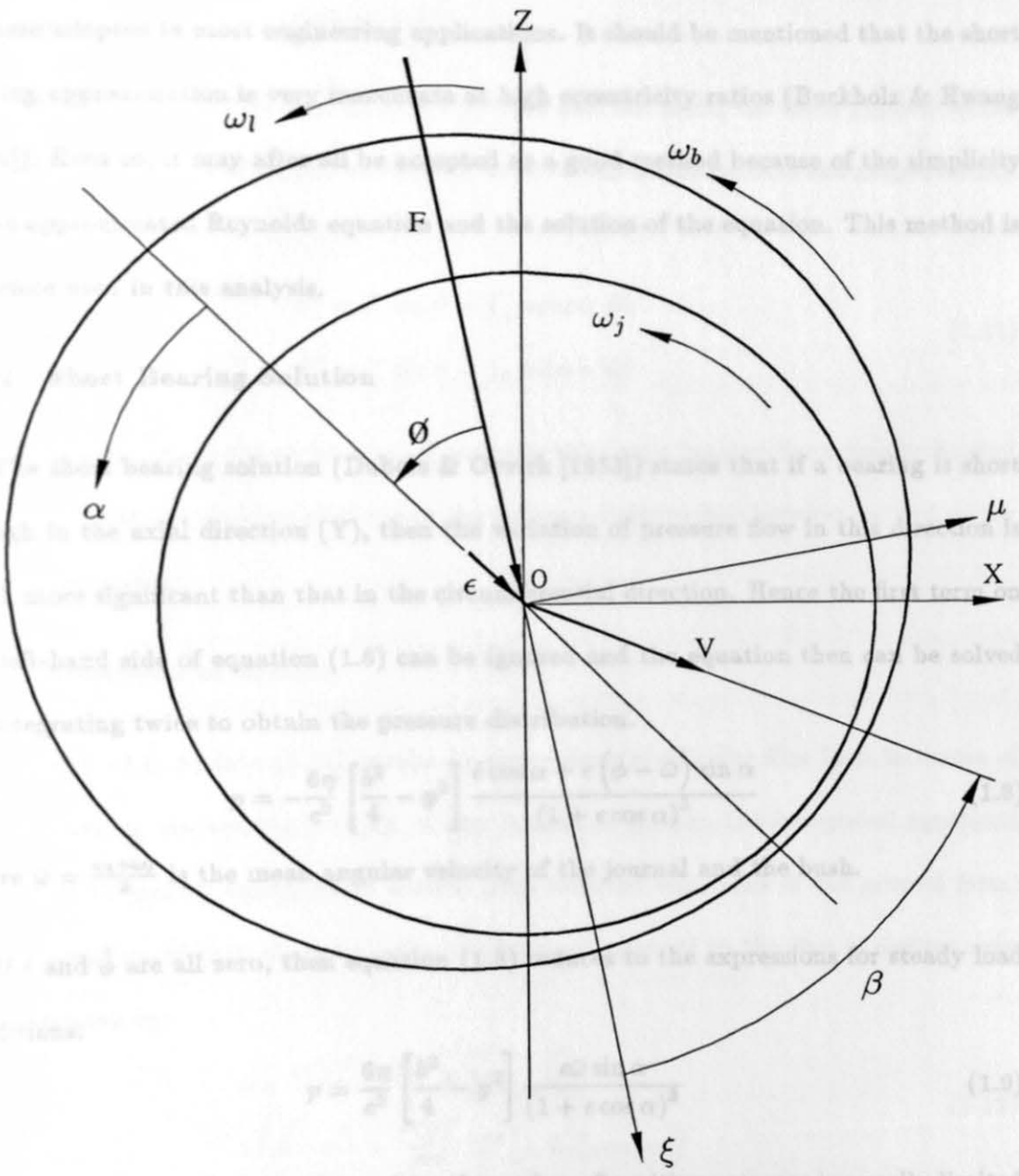

Figure 1.3. Journal Bearing Geometry and Coordinates Used

proximate analytical solutions (Booker [1965]): Ocvirk Solution (short bearing), Sommerfeld Solution (long bearing) and Warner Solution (finite bearing). The short bearing solution is fairly valid for $\frac{b}{d}$ ratios less than 0.7 in axially symmetric bearings, and it is the case adopted in most engineering applications. It should be mentioned that the short bearing approximation is very inaccurate at high eccentricity ratios (Buckholz & Hwang [1986]). Even so, it may after all be accepted as a good method because of the simplicity of the approximated Reynolds equation and the solution of the equation. This method is therefore used in this analysis.

1.3.2 Short Bearing Solution

The short bearing solution (Dubois & Ocvirk [1953]) states that if a bearing is short enough in the axial direction (Y), then the variation of pressure flow in this direction is much more significant than that in the circumferential direction. Hence the first term on the left-hand side of equation (1.6) can be ignored and the equation then can be solved by integrating twice to obtain the pressure distribution.

$$p = -\frac{6\eta}{c^2}\left[\frac{b^2}{4} - y^2\right]\frac{\dot{\epsilon}\cos\alpha + \epsilon\left(\dot{\phi} - \bar{\omega}\right)\sin\alpha}{(1+\epsilon\cos\alpha)^3} \tag{1.8}$$

where $\bar{\omega} = \frac{\omega_b + \omega_j}{2}$ is the mean angular velocity of the journal and the bush.

If $\dot{\epsilon}$ and $\dot{\phi}$ are all zero, then equation (1.8) reduces to the expressions for steady load conditions:

$$p = \frac{6\eta}{c^2}\left[\frac{b^2}{4} - y^2\right]\frac{\epsilon\bar{\omega}\sin\alpha}{(1+\epsilon\cos\alpha)^3} \tag{1.9}$$

As film rupture or cavitation exists, the region of positive pressure is usually limited in extent to roughly half the bearing. By using the half-Sommerfeld type of cavitation boundary condition, which sets all negative gauge pressures to zero, an oil film of π radians extent from α_1 to α_2 can be achieved:

$$\begin{aligned} &\dot{\epsilon}\cos\alpha_1 + \epsilon\left(\dot{\phi} - \bar{\omega}\right)\sin\alpha_1 = 0 \\ &\dot{\epsilon}\sin\alpha_1 - \epsilon\left(\dot{\phi} - \bar{\omega}\right)\cos\alpha_1 \geq 0 \\ &\alpha_2 = \alpha_1 + \pi \end{aligned} \tag{1.10}$$

Considering the line of centres of the journal and the bush, the force applied to the lubricant film by the journal can be resolved to two components parallel and perpendicular to it, they are

$$\begin{aligned} F^{\epsilon} &= F\cos\phi = \int_A p\cos\alpha \; dA \\ F^{\phi} &= F\sin\phi = \int_A p\sin\alpha \; dA \end{aligned} \tag{1.11}$$

These integrations are to be carried out over the entire bearing for a totally flooded bearing, or over the positive portions of the pressure distribution between α_1 and α_2 for a cavitated bearing.

1.3.3 Equations of Motion

Insertion of (1.8) into (1.11) results in expressions giving the film load in terms of journal motion. As bearing loading at any instant is known, the integrated equations (1.11) lead to journal equations of motion from inverted equations of the general form. The components of journal centre velocity along and normal to the line of centres may be represented by:

$$\begin{aligned} \dot{\epsilon} &= \frac{F\left(\frac{c}{r}\right)^2}{\eta b d} M^{\epsilon}\left(\epsilon, \phi, \frac{b}{d}, \alpha_1, \alpha_2\right) \\ \epsilon\left(\dot{\phi} - \bar{\omega}\right) &= \frac{F\left(\frac{c}{r}\right)^2}{\eta b d} M^{\phi}\left(\epsilon, \phi, \frac{b}{d}, \alpha_1, \alpha_2\right) \end{aligned} \tag{1.12}$$

where M^{ϵ} and M^{ϕ} are dimensionless ratios of velocity to force, called mobilities.

If equation (1.9) is inserted in (1.11), and integrations are from 0 to π, then the eccentricity ratio for steadily loaded bearings under cavitation conditions can be obtained

as:

$$\epsilon\bar{\omega} = \frac{4Fc^2}{\eta d b^3} \frac{(1-\epsilon^2)^2}{[16\epsilon^2 + \pi^2(1-\epsilon^2)]^{\frac{1}{2}}} \tag{1.13}$$

1.3.4 Mobility Method of Solution

In general, direct formal integration of the equations of motion (1.12) is impossible. Analytical solutions do exist, but they are only for a very few simple situations. Numerical solutions are rather complicated and time-consuming, even with the modern digital computers.

About 27 years ago, Booker [1965] presented the now established mobility method and accommodated this problem. He took M^{ϵ} and M^{ϕ} as components of a mobility vector $\vec{M}$, and eliminated the ruptured film boundary α_1, α_2 by iterating between equations (1.10) and (1.12), such that $\vec{M}$ is a function of the position vector $\vec{\epsilon}$ and the $\frac{b}{d}$ ratio only. It was also found that for a short bearing solution the $\frac{b}{d}$ ratio just affected the magnitude of $\vec{M}$ and not its direction. So the values of $\vec{M}$ need only be calculated once for a $\frac{b}{d}$ ratio of unity. Thus the $\vec{M}$ function could be plotted on an eccentricity ratio circle to give a mobility map. Such a map consists of lines of constant mobility number and squeeze paths relative to a fixed load line.

The velocity of the journal may be expressed in a vector form as

$$\vec{V} = \frac{d\vec{\epsilon}}{dt} = \overrightarrow{\dot{\epsilon} + \epsilon\dot{\phi}} \tag{1.14}$$

therefore the journal locus can be stepped out either graphically or numerically. This begins with an initial guess for the journal centre position on the mobility chart. With the mobility data, $\vec{V}$ can be found from the vectorial addition of its two components (equation (1.14)). It is then possible to march out the next position for a time increment.

By doing things in such a way, convergence of the journal orbit is readily attained in less than two cycles.

Booker has also derived approximate expressions for mobility components in a load frame of axes ξ and μ

$$M^{\xi} \approx \frac{(1-\xi)^{\frac{5}{2}}}{\pi \left(\frac{b}{d}\right)^2} \tag{1.15}$$

$$M^{\mu} \approx \frac{-4\mu\,(1-\xi)^{\frac{3}{2}}}{\pi^2 \left(\frac{b}{d}\right)^2} \tag{1.16}$$

It should be noted that the short bearing mobility method is subject to all the assumptions implied in its own derivation (for example, neither elastic nor thermal distortion is considered for either the shaft or the sleeve, the shaft is well-aligned with the bearing and its inertial effects are neglected etc.), and the deduction of Reynolds equation as well. However it is nevertheless felt that the information provided may best be used for qualitative interpretation.

1.4 Bearing Friction Power Loss

1.4.1 Steadily Loaded Journal Bearing

Bearing friction power loss analysis for steady load conditions has been presented by Martin [1985]. It may be simplified by assuming that the load carrying film extends throughout the converging part of the clearance space (i.e. π film extent). If only shear effects were taken (both in the converging area and the diverging region), then power loss for this "π film shear" is given by

$$H = \frac{\eta r^3 b}{c} \frac{\pi}{(1-\epsilon^2)^{\frac{1}{2}}} \left(\frac{2+\epsilon}{1+\epsilon}\right) (\omega_j - \omega_b)^2 \tag{1.17}$$

If a complete film is assumed to occur over the full eccentricity range, the losses given

by the "2π film shear" will be

$$H = \frac{\eta r^3 b}{c} \frac{2\pi}{(1-\epsilon^2)^{\frac{1}{2}}} (\omega_j - \omega_b)^2 \tag{1.18}$$

When the shaft is concentric with the bush (i.e. $\epsilon = 0$), the angular extent film will be 2π. Equation (1.18) for this case becomes

$$H = 2\pi \frac{\eta r^3 b}{c} (\omega_j - \omega_b)^2 \tag{1.19}$$

and it is known as Petroff equation (Cameron [1976]).

1.4.2 Dynamically Loaded Journal Bearing

For bearing friction losses of the dynamic load case, there is a wide range of prediction equations (Martin [1985]) in terms of frictional torque, power loss and FMEP, based on both theory and experiments. These different styles of equation from various sources differ in both format and result. It undoubtedly was confusing and rigorous derivation from first principles was required.

More recently, Booker [1989] presented a very general power dissipation formula which, if reformulated for limited property variations, reduces to the more conventional formula for journal bearings (Booker [1982]). The formula has been rearranged by Martin [1985] into algebraic form to make it more understandable (also see Figure 1.3).

$$H = \frac{\eta r^3 b}{c} J_1^{00} (\omega_j - \omega_b)^2 + \left(\frac{\omega_j + \omega_b}{2}\right) Fe \sin\phi + FV \cos\beta \tag{1.20}$$

where J_1^{00} is a journal bearing integral. For a π film extent

$$J_1^{00} = \int_{\alpha_1}^{\alpha_1 + \pi} \frac{d\alpha}{1 + \epsilon \cos\alpha} \tag{1.21}$$

and its value can be found in Booker's table of journal bearing integrals (Booker [1965]).

For a complete 2π film

$$J_1^{00} = \frac{2\pi}{(1-\epsilon^2)^{\frac{1}{2}}} \tag{1.22}$$

The first two terms of equation (1.20), which are the rate of work done on the film due to rotation of journal and bush, are called shear and pressure terms respectively. The last term, generated due to movement of the journal centre relative to bush centre, is the translatory term.

Equation (1.20) can be simplified by choosing an appropriate frame of reference for particular situations. A reference used by Booker [1971] in his numerical application of mobility method was the case where the observer is rotating at an average film velocity of $\frac{\omega_j+\omega_b}{2}$. The friction loss due to shear will remain unchanged no matter where the observer is placed, since the shear term involves the difference of two angular velocities. As the total loss is not affected by the choice of the reference frame, the sum of the other two terms, namely pressure and translation, will be constant as well. Therefore in this case, the second term of equation (1.20) disappeared and the last term becomes the product of bearing load and the apparent velocity of the journal parallel to the instantaneous load line.

$$H = \frac{\eta r^3 b}{c} J_1^{00} (\omega_j - \omega_b)^2 + F V^{\xi} \tag{1.23}$$

This form of equation is particularly useful for rapid solution as V^{ξ} is directly related to the mobility component M^{ξ}

$$V^{\xi} = \frac{F\left(\frac{c}{r}\right)^2 c}{\eta b d} M^{\xi} \tag{1.24}$$

and for short bearing theory, from equation (1.15)

$$M^{\xi} \approx \frac{(1-\epsilon\cos\phi)^{\frac{5}{2}}}{\pi\left(\frac{b}{d}\right)^2} \tag{1.25}$$

With these equations, bearing frictional power loss at any crank position or its average value through a complete cycle can be calculated.

1.5 Conclusions

A load evaluation analysis for engine big-end bearings has been detailed. The loadings on the main bearings were estimated assuming that the crankshaft was a statically determinate rigid beam.

Reynolds equation was applied for the lubrication analysis of a dynamically loaded journal bearing. The Short Bearing Mobility Method has been adopted for the solution of Reynolds equation. The derived equations will enable the bearing journal locus to be determined and the oil film thickness to be calculated.

Equations for the estimation of bearing frictional power losses have been given. They include a general equation for dynamically loaded journal bearings, an equation for steadily loaded journal bearings and the Petroff equation. Both cavitated bearings and totally flooded bearings were considered.

Chapter Two

Computer Programs and Results for Engine Bearings

2.1 Introduction

To achieve a high level of bearing reliability with minimum experimental testing, it is essential to predict the performance of bearings with great confidence. This is particularly necessary at the design stage when various options have to be studied. A rapid assessment of the effects of design changes upon bearing behaviour will obviously help to achieve such a goal.

Computer programs have been developed for the tribological analysis of a dynamically loaded journal bearing. The extension of the above programs, when applied to an engine, includes the loading evaluations for big-end bearing and main bearings. The software for the prediction of engine bearing performance is capable of evaluating bearing loads, predicting journal locus and estimating power losses. The well documented big-end bearing of a Ruston & Hornsby 6VEB-X MK III diesel engine has been studied for the purpose of validating the software. Parametric studies for the same bearing have been undertaken. The main bearings in the same engine were also analysed. The lubrication and friction analysis has been carried out for the Ford 1.8L H.O. Zeta engine bearings.

The steady load approach and the Petroff method were also applied for the power loss calculation. Martin [1985] showed that power loss calculation for dynamically loaded journal bearings with the Short Bearing Mobility Method gave excellent comparison with

that predicted by more accurate but complicated methods if the bearings were assumed to be totally flooded. This assumption has been adopted in the present work.

2.2 Description of Programs

Four programs have been developed to undertake bearing power loss analysis. The first two, which require the bearing loads and dimensions as input data, are for a single dynamically loaded journal bearing. They were then extended to include a subprogram for load calculations for both big-end and main bearings in any in-line engine. Therefore the last two programs can calculate bearing loads, predict journal centre orbit and estimate friction power loss, on condition that cylinder pressure, bearing geometry and other related data are known.

For either single bearing analysis or full engine bearing analysis, one program is based on the theory for dynamically loaded journal bearings; the other used equations derived for steadily loaded journal bearings, when for a short period of crank rotation, the load was assumed to be steady. This quasi-steady load approach (i.e. calculate eccentricity ratios based on steady operating conditions and then the average power loss over a cycle from this) is for comparison with the most technically advanced method.

Cylinder pressures are input at either 10^0 or 5^0 (V-engines for example) intervals of crankshaft rotation and then the loads on bearings are calculated and output at 10^0 intervals of crankshaft rotation for the full engine cycle. For main bearings, the calculation is from the front main bearing (at the engine belt system side) to the rear one (at the engine flywheel side). From the convenience point of view, the big-end bearing loads are output on a frame of axes attached to the connecting rod centre line and the main bearing loads relative to the cylinder centre line.

In bearing behaviour analysis, two frames of reference have been used in the computation. The computation frame has been fixed either to the connecting rod centre line for the big-end bearings or to the cylinder centre line for the main bearings. The load frame was attached to the resultant load vector and rotated with it. In order to draw the journal locus diagram more accurately, the time interval used is that taken for the crankshaft rotating one half degree; the loads on bearings then have to be interpolated from those previously computed.

The initial journal position chosen is at zero degree of crankshaft rotation; this corresponds to the TDC (top dead centre) position of cylinder number one (No.1). In a V-engine this is the front left hand cylinder and in other in-line engines this is the front cylinder. Mobility components in the load frame then are calculated and changed to give components in the computation frame.

In the calculation of journal centre velocities, the average angular velocity of journal and bush $\bar{\omega}$ differs between the big-end bearing analysis and the main bearing analysis in their individual computational frame. For a big-end bearing

$$\bar{\omega} = \frac{\omega_{es}}{2}\left(1 + \frac{R}{L}cos\theta\right) \tag{2.1}$$

but for a main bearing

$$\bar{\omega} = \frac{\omega_{es}}{2} \tag{2.2}$$

The initial value of the eccentricity ratio used is zero. The product of the journal centre velocity and the time interval will give the corresponding new eccentricity ratio for each step. If the journal orbit goes out of the clearance circle (i.e. the new eccentricity ratio is greater than unity), the programs will pull it back by halving the time interval. It was found that the journal locus formed a closed curve within 6π radians of crankshaft

rotation. The program has set 8π radians of crankshaft rotation to complete the curve.

For the bearing analysis section with equations for steady load conditions, the relation between bearing load and eccentricity ratio is non-linear (equation (1.13)); it can be solved by either the Newton-Raphson method or a bisection technique in the programs.

As the parameters needed are available from above, bearing friction power loss can be determined. The programs output the results at 10^0 interval of crankshaft rotation, and both π and 2π oil film extent, with all the three terms of shear, pressure and translation considered or the shear term considered only, are included. A simplified flow chart is shown in Figure 2.1.

It should be noted that the thermal effect was not considered in the analysis used. Instead, an effective operating viscosity for the lubricant has to be provided.

2.3 Program Validation

To validate the programs, the Ruston and Hornsby 6VEB-X Mk III diesel engine was used as a benchmark. This is a four-stroke six-cylinder in-line turbo-charged diesel engine delivering 450 kW at 600 rpm. The big-end bearing of the engine has been studied extensively and become a standard case for comparison purpose (Campbell et al [1967]). The input data for the main bearings of the engine were from the Glacier Metal Company Limited, kindly supplied by F.A. Martin and J.F. Warriner [1990]. All these technical data for such an engine are listed in Appendix A.

The results for the big-end bearing are very close to those documented in the literature. The polar load diagram (Figure 2.2) compares well with those published in learned society papers (Martin & Booker [1966], Campbell et al [1967], Booker [1971] and Goenka [1984]),

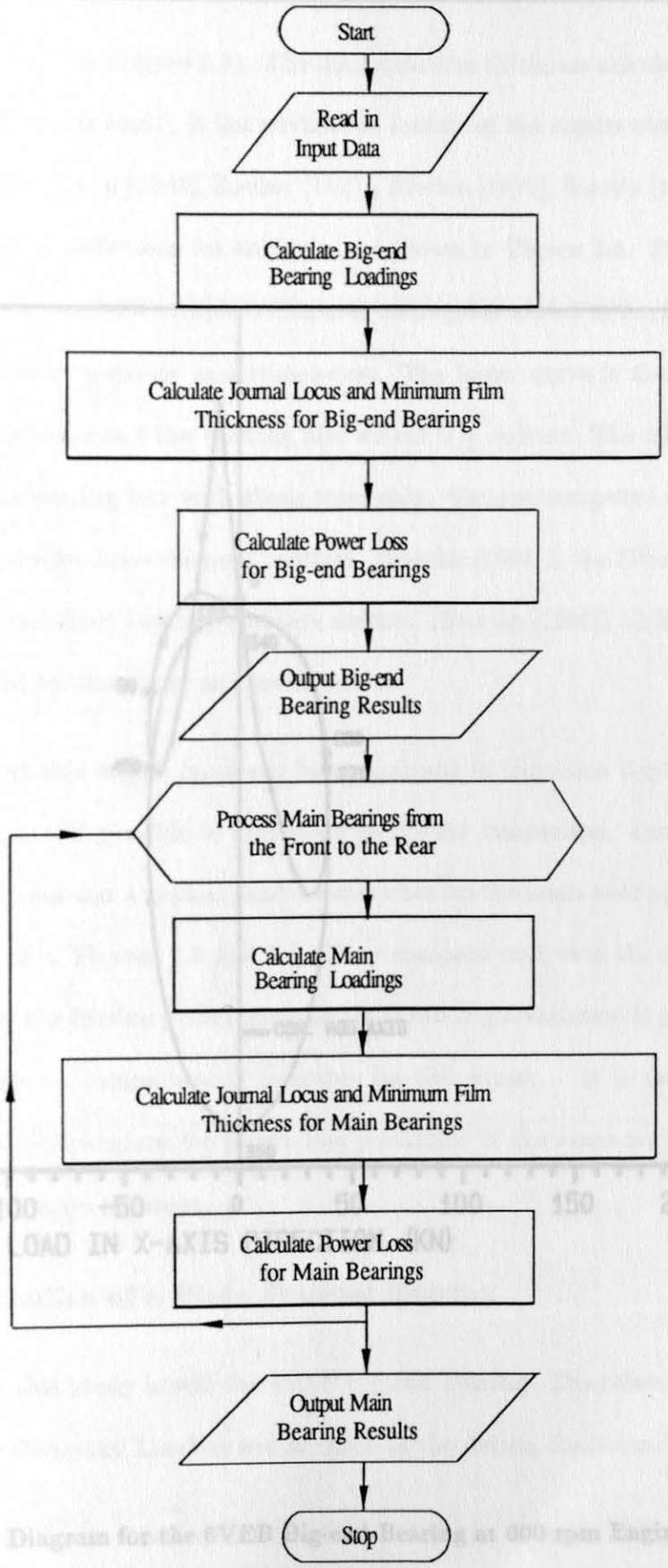

Figure 2.1. A Simplified Program Flow Chart for Bearing Lubrication Analysis

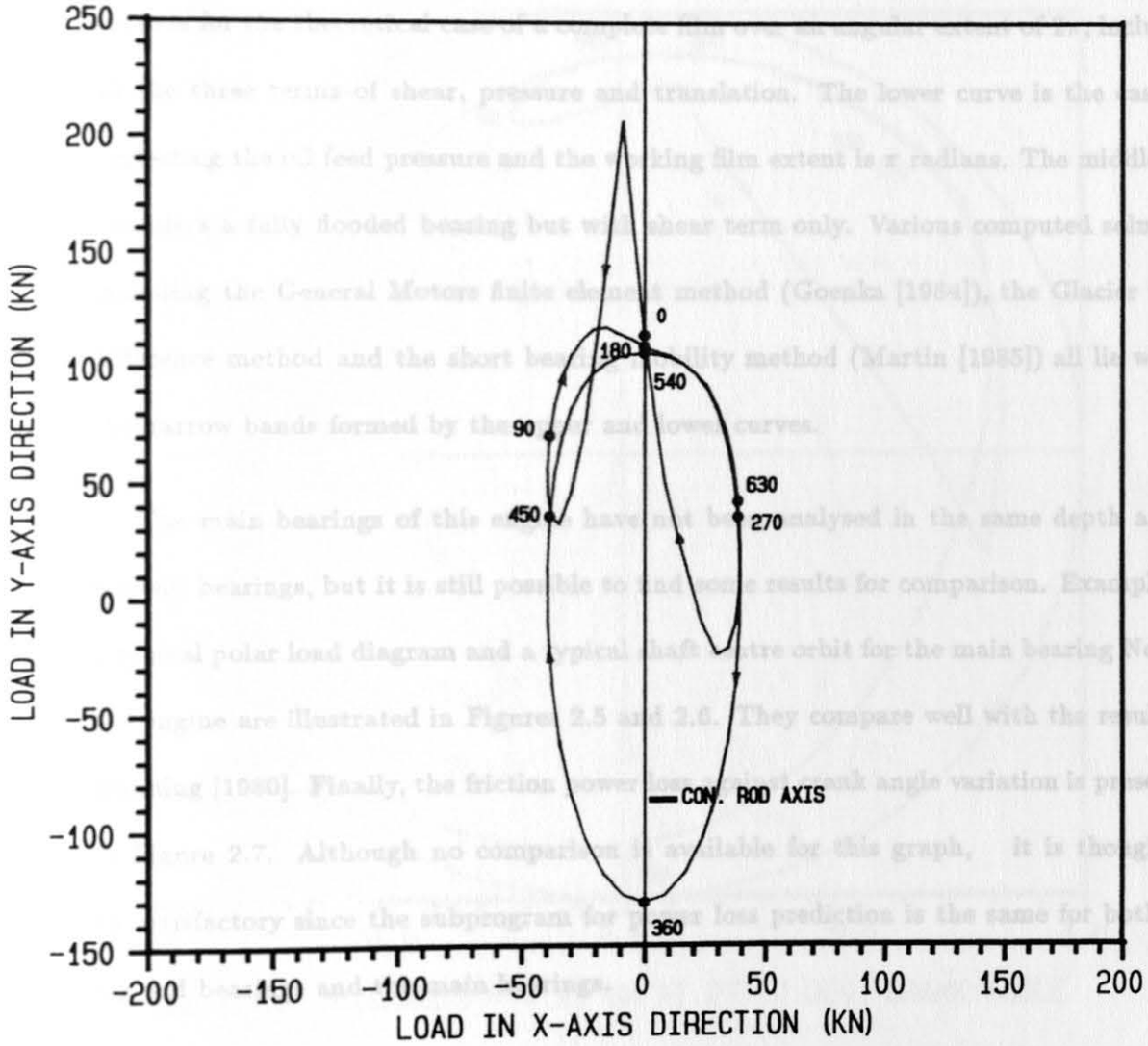

Figure 2.2. Polar Load Diagram for the 6VEB Big-end Bearing at 600 rpm Engine Speed

as does the journal centre locus (Figure 2.3). The minimum film thickness calculated here is about 4.91 μm at 277^0 crank angle. It lies within the scatter of the results obtained by various methods (Campbell et al [1967], Booker [1971], Ritchie [1975], Martin [1982] and White [1989]). Power loss predictions for this case are shown in Figure 2.4. The upper curve is for the theoretical case of a complete film over an angular extent of 2π, including all the three terms of shear, pressure and translation. The lower curve is the case for neglecting the oil feed pressure and the working film extent is π radians. The middle one considers a fully flooded bearing but with shear term only. Various computed solutions including the General Motors finite element method (Goenka [1984]), the Glacier finite difference method and the short bearing mobility method (Martin [1985]) all lie within the narrow bands formed by the upper and lower curves.

The main bearings of this engine have not been analysed in the same depth as the big-end bearings, but it is still possible to find some results for comparison. Examples of a typical polar load diagram and a typical shaft centre orbit for the main bearing No.3 of the engine are illustrated in Figures 2.5 and 2.6. They compare well with the results of Dunning [1980]. Finally, the friction power loss against crank angle variation is presented in Figure 2.7. Although no comparison is available for this graph, it is thought to be satisfactory since the subprogram for power loss prediction is the same for both the big-end bearings and the main bearings.

2.4 Parametric Studies of a Plain Journal Bearing

The bearing used in this study is still the 6VEB big-end bearing. The related data is from the Glacier Metal Company Limited and is taken as the datum condition.

Each parameter studied was changed from its datum, and the effect on the predicted

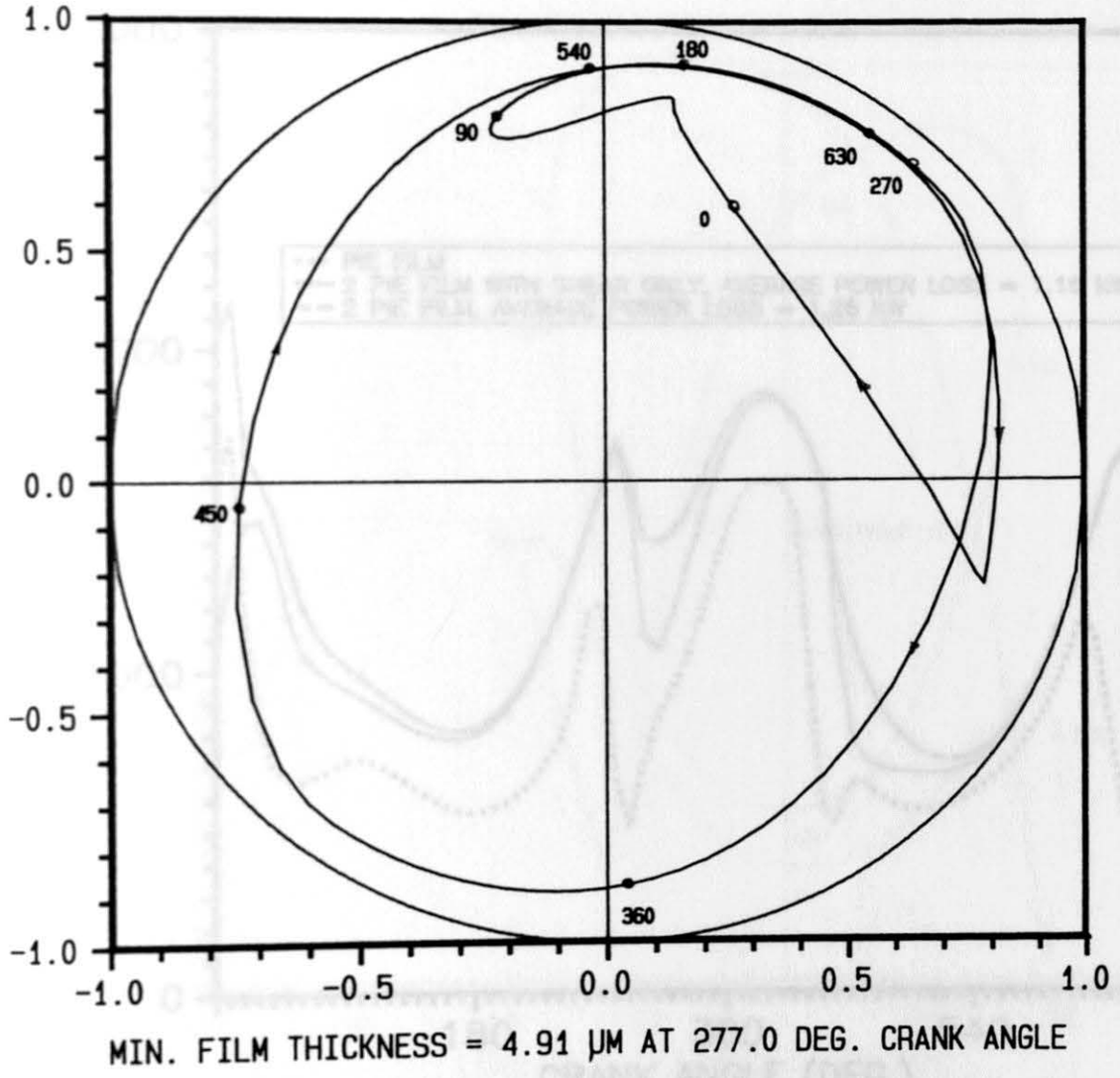

Figure 2.3. Journal Locus for the 6VEB Big-end Bearing at 600 rpm Engine Speed

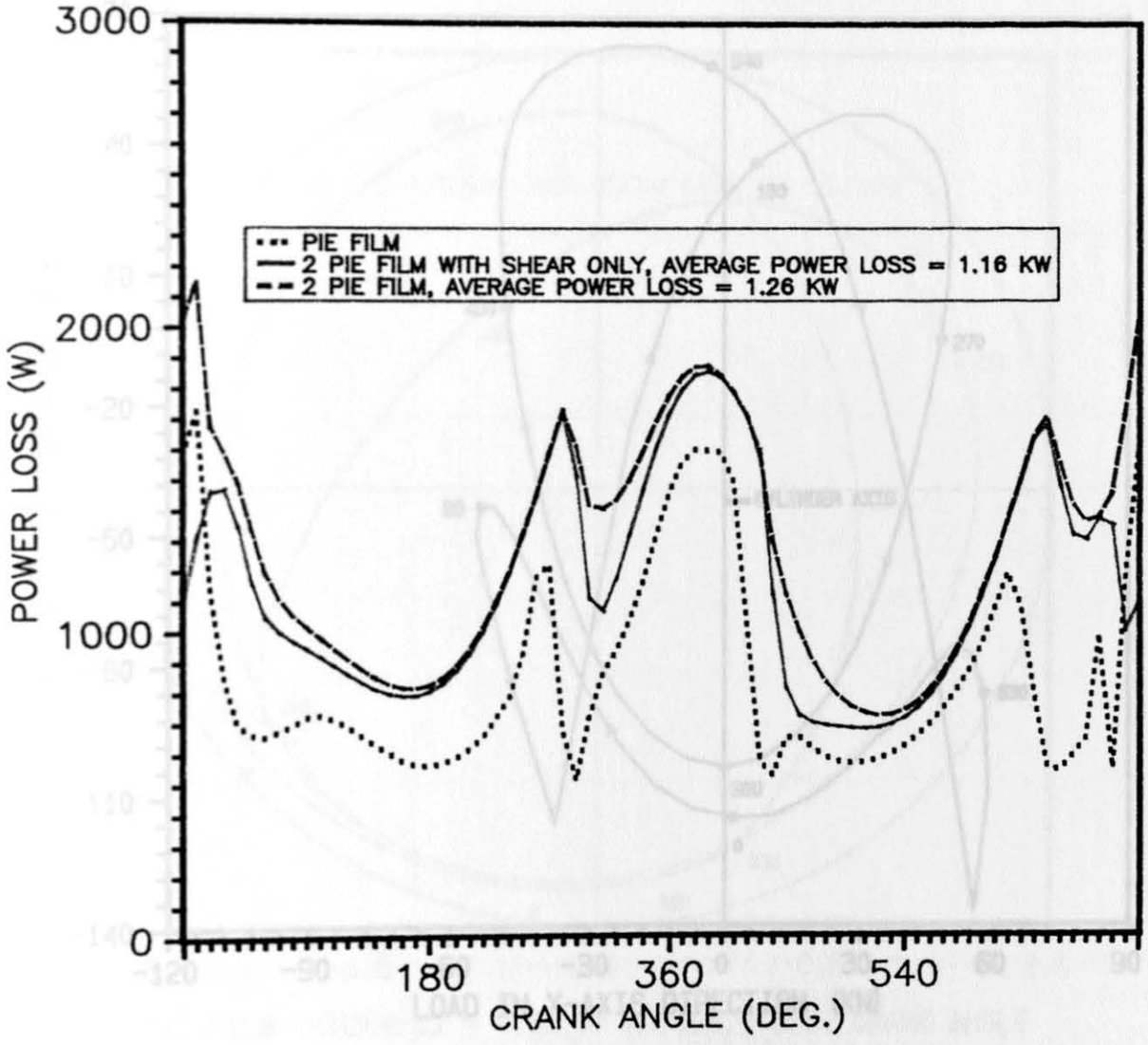

Figure 2.4. Power Loss for the 6VEB Big-end Bearing at 600 rpm Engine Speed

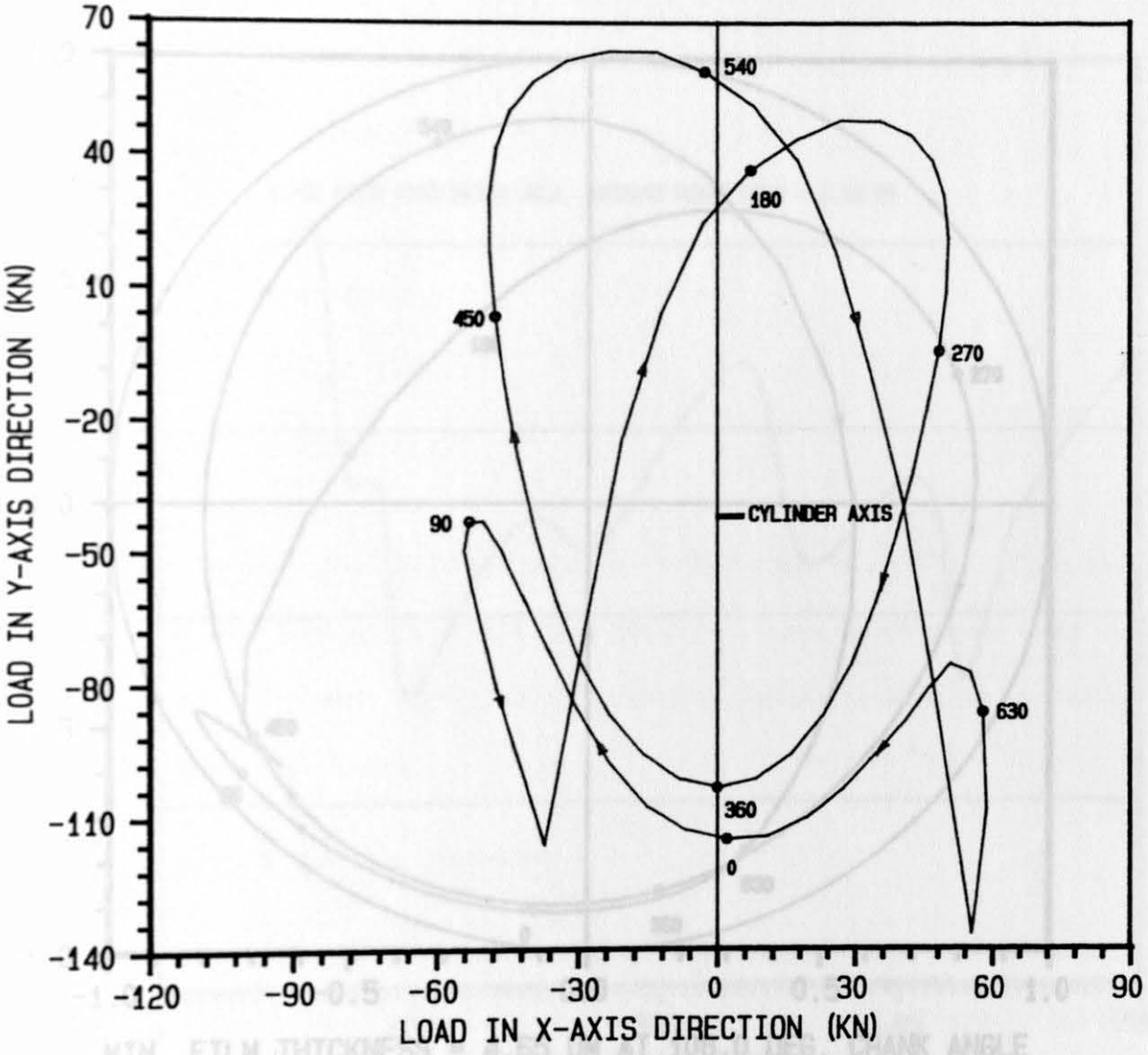

Figure 2.5. Polar Load Diagram for the 6VEB Main Bearing No.3 at 600 rpm Engine Speed

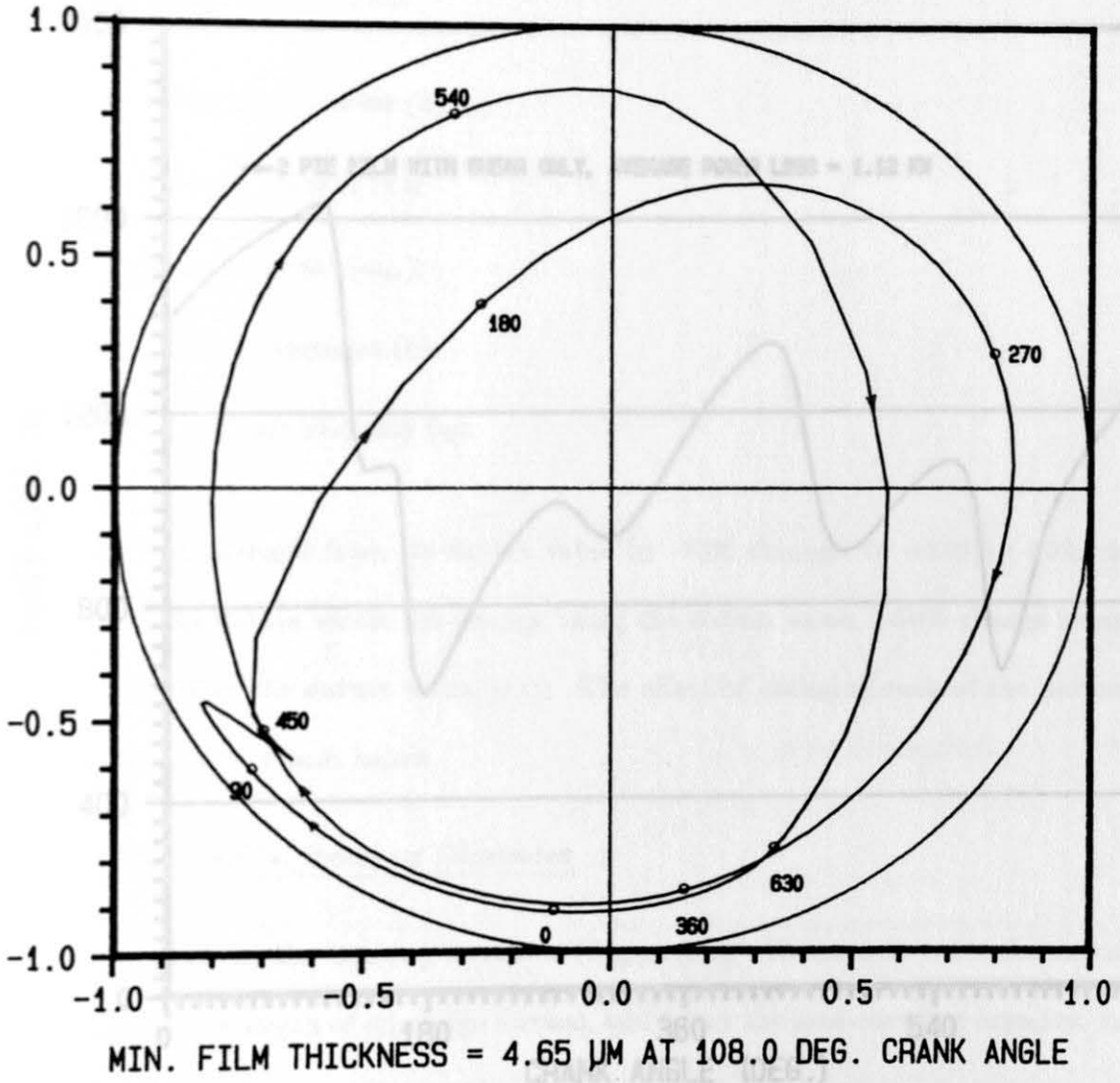

Figure 2.6. Journal Locus for the 6VEB Main Bearing No.3 at 600 rpm Engine Speed

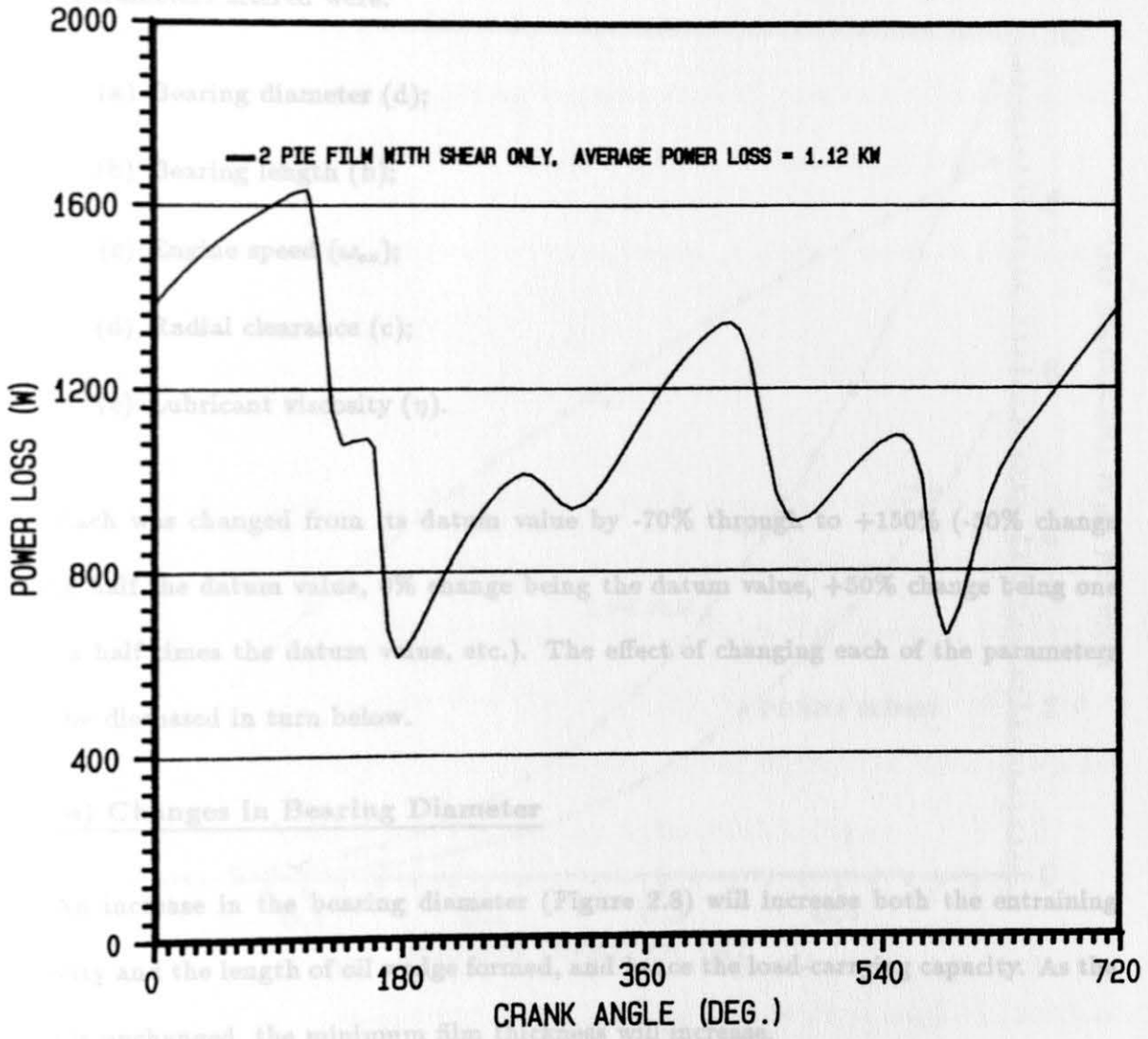

Figure 2.7. Power Loss for the 6VEB Main Bearing No.3 at 600 rpm Engine Speed

average power loss for the totally flooded bearing (2π film), on the friction loss estimated with Petroff method, and on the minimum film thickness computed was determined. This study was for the period of one complete cycle (4 strokes), and the change of each parameter has been carried out independently with no consideration of coupled effects. The parameters altered were:

(a) Bearing diameter (d);

(b) Bearing length (b);

(c) Engine speed (ω_{es});

(d) Radial clearance (c);

(e) Lubricant viscosity (η).

Each was changed from its datum value by -70% through to +150% (-50% change being half the datum value, 0% change being the datum value, +50% change being one and a half times the datum value, etc.). The effect of changing each of the parameters will be discussed in turn below.

(a) Changes in Bearing Diameter

An increase in the bearing diameter (Figure 2.8) will increase both the entraining velocity and the length of oil wedge formed, and hence the load-carrying capacity. As the load is unchanged, the minimum film thickness will increase.

Larger diameter journal bearings will result in much more friction power loss than with smaller ones due to the increase of shear area and the shear rate of the lubricant. A near cubic relationship between power loss and diameter was found, and the special case of zero eccentricity (Petroff conditions) reflects exactly the cubic relation.

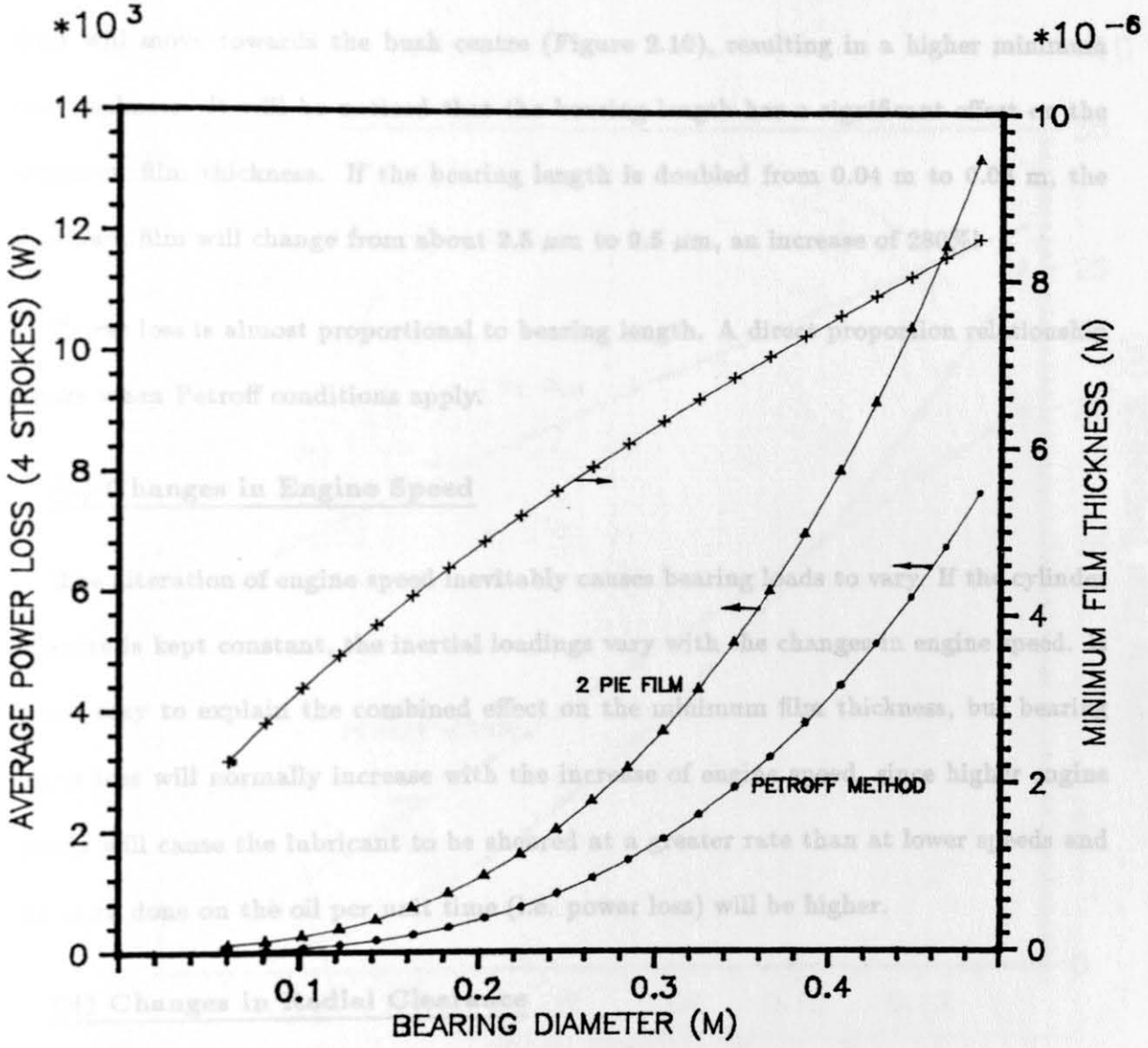

Figure 2.8. Bearing Diameter Effect on Power Loss and Minimum Film Thickness for the 6VEB Big-end Bearing

(b) Changes in Bearing Length

As the bearing length increases (Figure 2.9), the load supporting area increases, leading to an increase of load-bearing capacity. With the load remaining unchanged, the shaft will move towards the bush centre (Figure 2.10), resulting in a higher minimum film thickness. It will be noticed that the bearing length has a significant effect on the minimum film thickness. If the bearing length is doubled from 0.04 m to 0.08 m, the minimum film will change from about 2.5 μm to 9.5 μm, an increase of 280%!

Power loss is almost proportional to bearing length. A direct proportion relationship occurs when Petroff conditions apply.

(c) Changes in Engine Speed

The alteration of engine speed inevitably causes bearing loads to vary. If the cylinder pressure is kept constant, the inertial loadings vary with the changes in engine speed. It is not easy to explain the combined effect on the minimum film thickness, but bearing power loss will normally increase with the increase of engine speed, since higher engine speeds will cause the lubricant to be sheared at a greater rate than at lower speeds and the work done on the oil per unit time (i.e. power loss) will be higher.

(d) Changes in Radial Clearance

Radial clearance was changed from its datum value by -85% through to +150% in order to examine the changing influence clearly. As the clearance goes up (Figure 2.11), the minimum film thickness curve exhibits a local maximum when the radial clearance reaches about 20 μm. Very similar results were also reported by Rosenberg [1982] and Maspeyrot and Frene [1988]. Three points were marked out on the curve and the locus

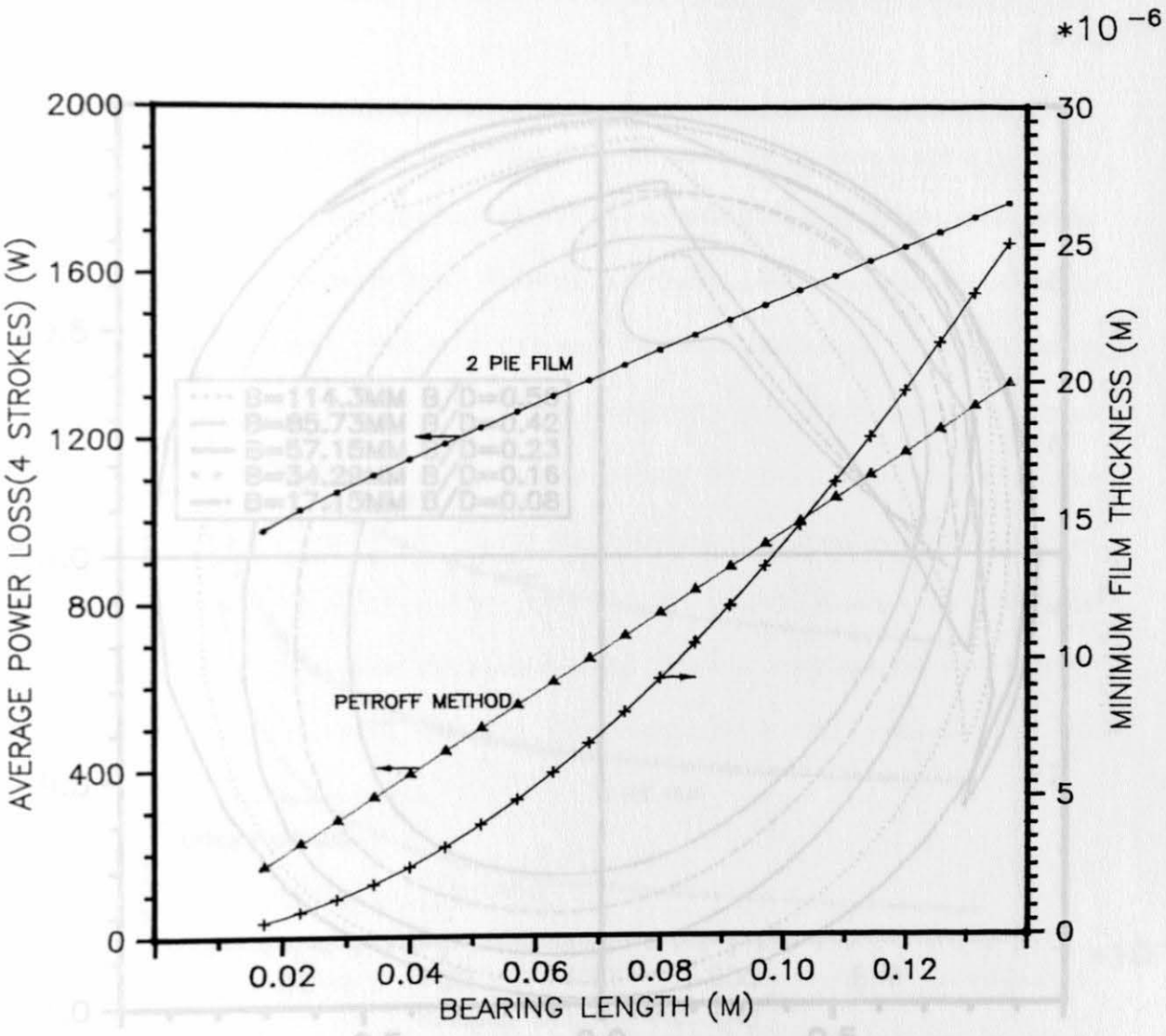

Figure 2.9. Bearing Length Effect on Power Loss and Minimum Film Thickness for the 6VEB Big-end Bearing

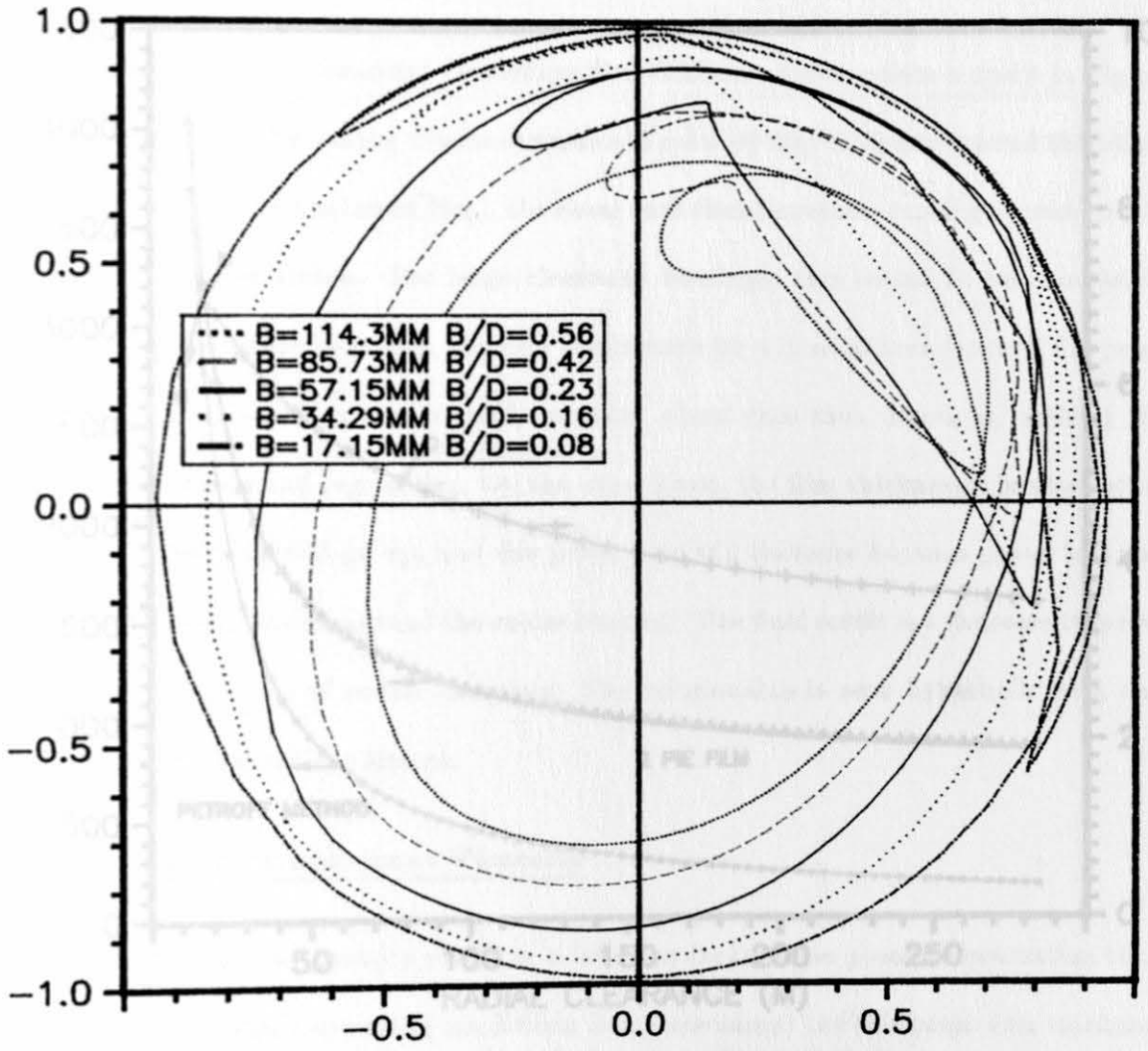

Figure 2.10. Bearing Length Effect on Journal Locus for the 6VEB Big-end Bearing

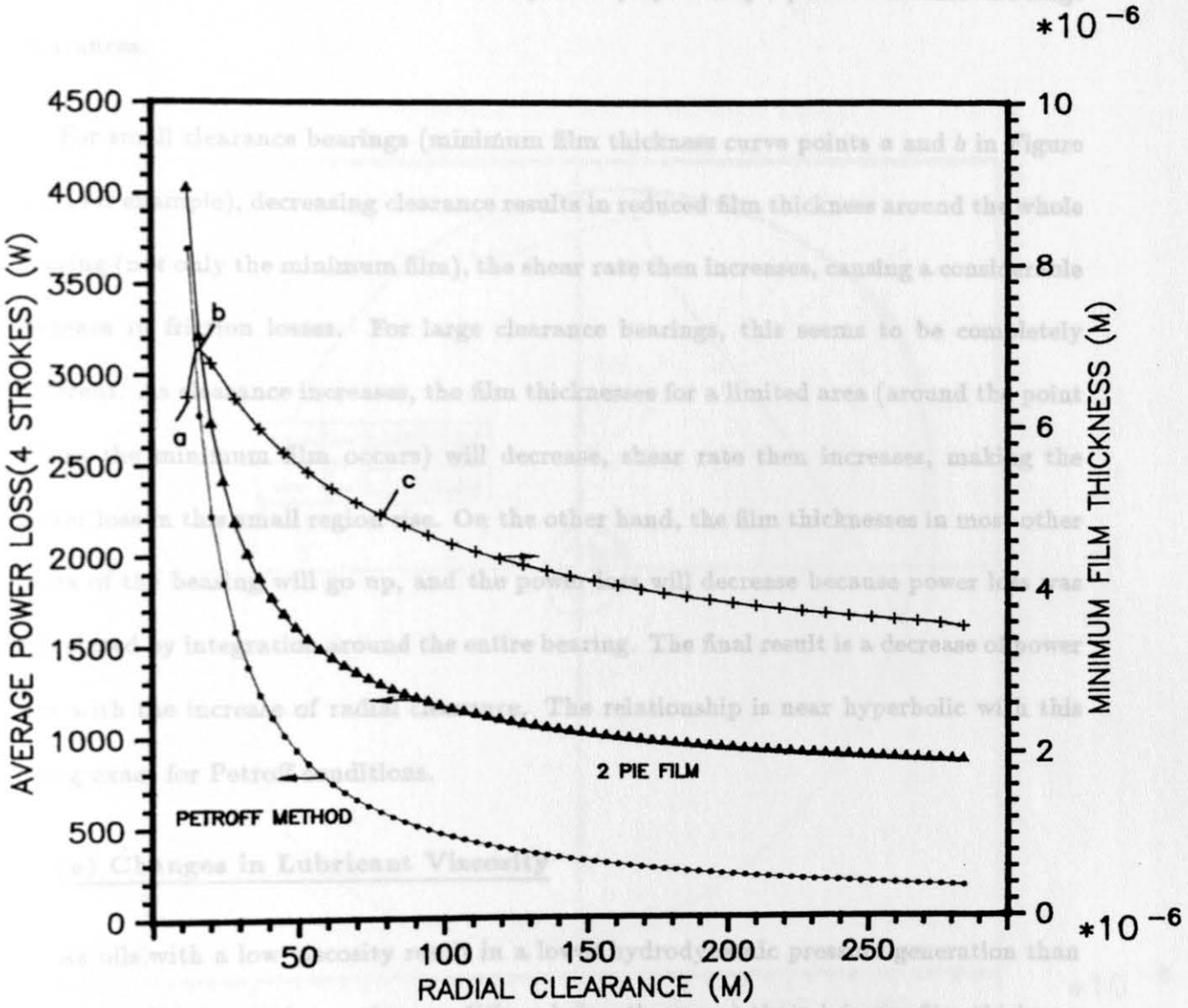

Figure 2.11. Bearing Radial Clearance Effect on Power Loss and Minimum Film Thickness for the 6VEB Big-end Bearing

curves at these specific clearances were plotted out in Figure 2.12. The minimum film thickness is determined by $(c(1-\epsilon))$. As clearance increases, it can be seen that the eccentricity ratio increases as well. It seems that clearance dominates the minimum film thickness at its low values, and eccentricity ratio plays a major part for normal and large clearances.

For small clearance bearings (minimum film thickness curve points *a* and *b* in Figure 2.11, for example), decreasing clearance results in reduced film thickness around the whole bearing (not only the minimum film), the shear rate then increases, causing a considerable increase in friction losses. For large clearance bearings, this seems to be completely different. As clearance increases, the film thicknesses for a limited area (around the point where the minimum film occurs) will decrease, shear rate then increases, making the power loss in this small region rise. On the other hand, the film thicknesses in most other parts of the bearing will go up, and the power loss will decrease because power loss was calculated by integration around the entire bearing. The final result is a decrease of power loss with the increase of radial clearance. The relationship is near hyperbolic with this being exact for Petroff conditions.

(e) Changes in Lubricant Viscosity

As oils with a low viscosity result in a lower hydrodynamic pressure generation than for thicker lubricants (operating conditions being the same) the minimum film thickness is reduced with a decrease of lubricant viscosity (Figure 2.13).

Increasing oil viscosity will increase the shear stress and hence the power loss. In other words, thicker oils will need more energy to be sheared at the same rate. The relationship is nearly directly proportional and exactly so for Petroff conditions.

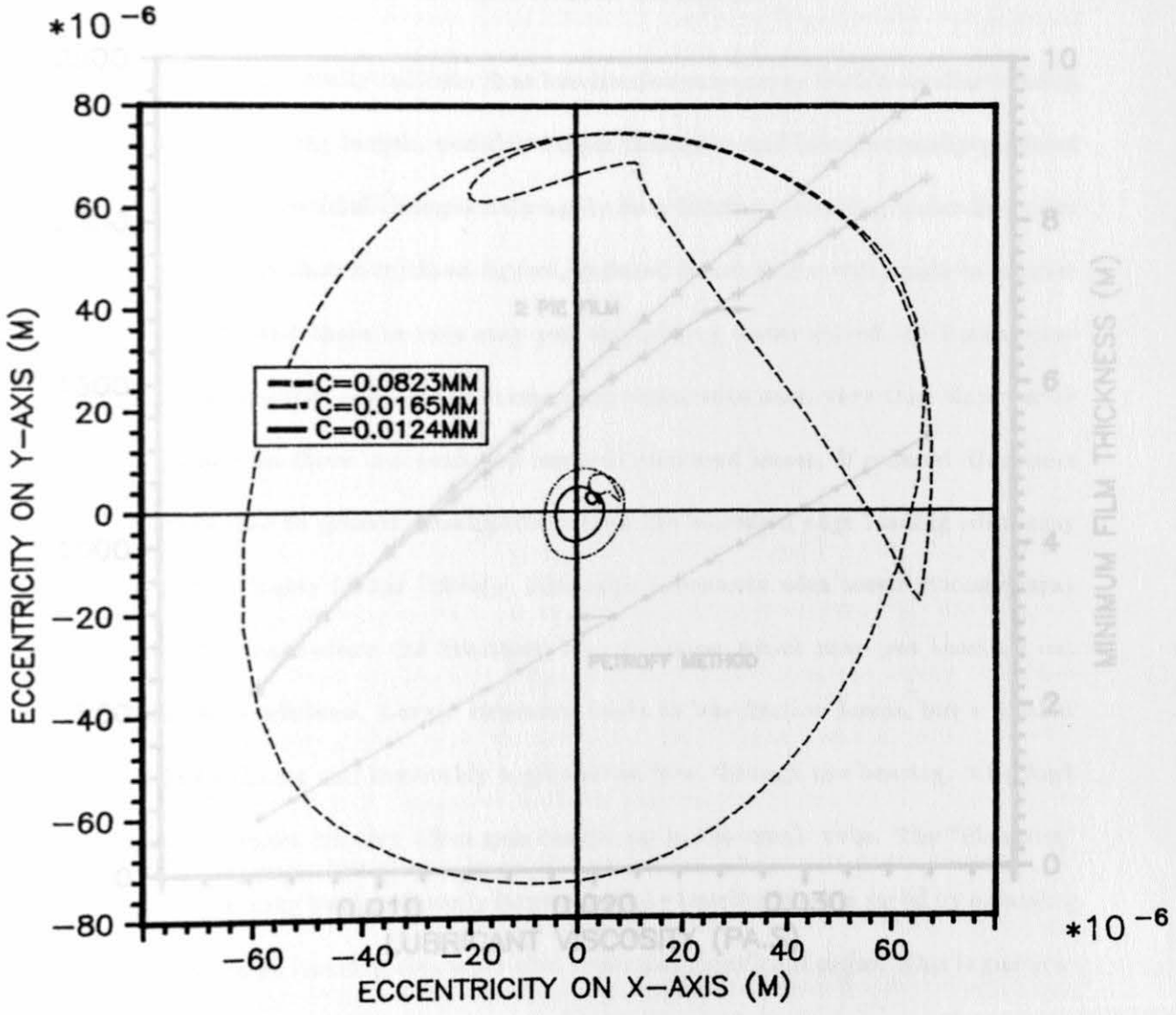

Figure 2.12. Bearing Radial Clearance Effect on Eccentricity for the 6VEB Big-end Bearing

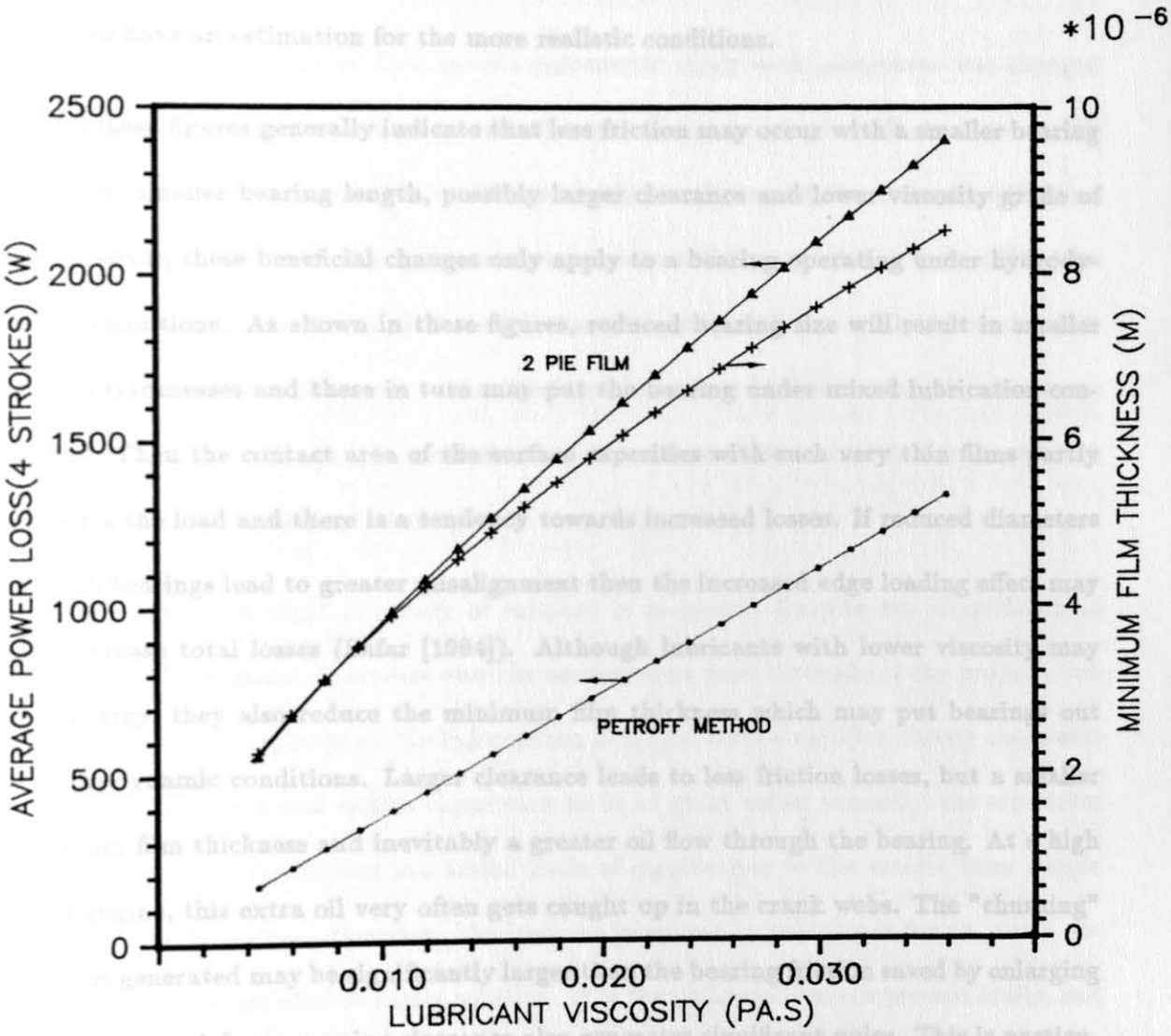

Figure 2.13. Lubricant Viscosity Effect on Power Loss and Minimum Film Thickness for the 6VEB Big-end Bearing

From the above parametric studies it can be seen (Figures 2.8, 2.9, 2.11 and 2.13) that the power loss predicted for the 2π film bearings are roughly about 1.5 to 2.0 times those computed with Petroff method. Therefore from the engineering point of view it may be reasonable to calculate bearing power loss by the Petroff equation and modify this by a factor to have an estimation for the more realistic conditions.

All these figures generally indicate that less friction may occur with a smaller bearing diameter, smaller bearing length, possibly larger clearance and lower viscosity grade of oil. However, these beneficial changes only apply to a bearing operating under hydrodynamic conditions. As shown in these figures, reduced bearing size will result in smaller oil film thicknesses and these in turn may put the bearing under mixed lubrication conditions. Then the contact area of the surface asperities with such very thin films partly supports the load and there is a tendency towards increased losses. If reduced diameters in main bearings lead to greater misalignment then the increased edge loading effect may also increase total losses (Safar [1984]). Although lubricants with lower viscosity may save energy, they also reduce the minimum film thickness which may put bearings out of hydrodynamic conditions. Larger clearance leads to less friction losses, but a smaller minimum film thickness and inevitably a greater oil flow through the bearing. At a high speed engine, this extra oil very often gets caught up in the crank webs. The "churning" loss thus generated may be significantly larger than the bearing friction saved by enlarging the clearance. A large running clearance also generates significant noise. This is particularly relevant in passenger car engines, since all motor manufacturers are concerned about noise from the engine. Minimizing clearance is a well known method of restricting the production of noise at the bottom of the engine. However, if carried too far a reduced minimum film thickness may result in overheating and reduced reliability. Generally all

these changes tend towards a more adverse situation and great care is necessary in producing a viable design to operate under the required range of conditions. Not only have the bearings to operate reliably, but any new design must meet the requirement of the whole engine system and the various interaction of other engine components.

It should be emphasized that in this parametric study each parameter was changed from its datum whilst the others remained constant, i.e. no coupled effects were considered. This may not be the case in reality. Increasing engine speed, for example, will cause the power loss to increase, the lubricant temperature will rise and this in turn will reduce the oil viscosity. This means that the lubricant viscosity will not really be unchanged. The same problems will appear when bearing dimensions (diameter, length, clearance) are altered. This indicates the need to carry out a heat balance calculation in order to obtain a realistic operating viscosity.

The question is what accuracy of solution is required. Despite the simplifications adopted in the parametric studies and the assumptions used throughout the project, two facts emerge. Firstly, most of the information achieved from simplified theory correlates sufficiently well with real engine experience to be of great value; secondly, the expensive calculation of real conditions has added little of significance to the results from simple assumptions. It is clear, therefore, the basic requirement in practice is for an easily obtained but still reasonably accurate solution. It is the philosophy of the present study, and as expected, the predicted results present very good correlations with other researchers (Vickery [1975], Rosenberg [1982], Hoshi [1984], Martin [1985] and Martin & Booker [1987]), some of these authors estimated the effective oil viscosity with a heat balance method.

2.5 Zeta Engine Bearing Analysis

The bearings used in this study are those in a Ford 1.8L Zeta engine. This is a four-cylinder in-line engine with four ungrooved big-end bearings and five partially grooved main bearings. Bearing conditions were investigated at seven engine speeds: 2000, 3000, 4000, 5000, 6000, 6400 and 7000 rpm. All the input data concerning these bearings are attached in Appendix B. The thermal influence on lubricant viscosity was not calculated in the software; an effective dynamic viscosity at each engine speed was calculated using a heat balance method. This was supplied by the Glacier Metal Company who was responsible for the design of the Zeta engine bearings.

The computer programs developed are not able to predict precisely the performance of partially circumferentially grooved bearings, but two extremes, ungrooved and fully circumferentially grooved cases, have been dealt with.

The power loss calculation capability includes both π oil film extent (considering oil film rupture) and 2π oil film extent (completely full film bearings). This will predict the lower and upper limit to power loss. In reality, the total power loss with a striated cavitation zone will probably lie between these two conditions. For simplicity and to be on the safe side (higher friction), a completely void-free film has been considered. The actual shear area may be only slightly less than this for both the VEB bearings and Zeta engine bearings, since the oil is supplied from circumferential grooves.

Figures 2.14 and 2.15 show the power loss of each bearing for the centrally grooved main bearing case and ungrooved case, respectively. It seems that the big-end bearing wastes less energy than any of the main bearings. The main bearing No.3 is the worst, with main bearing No.1 and No.5 following.

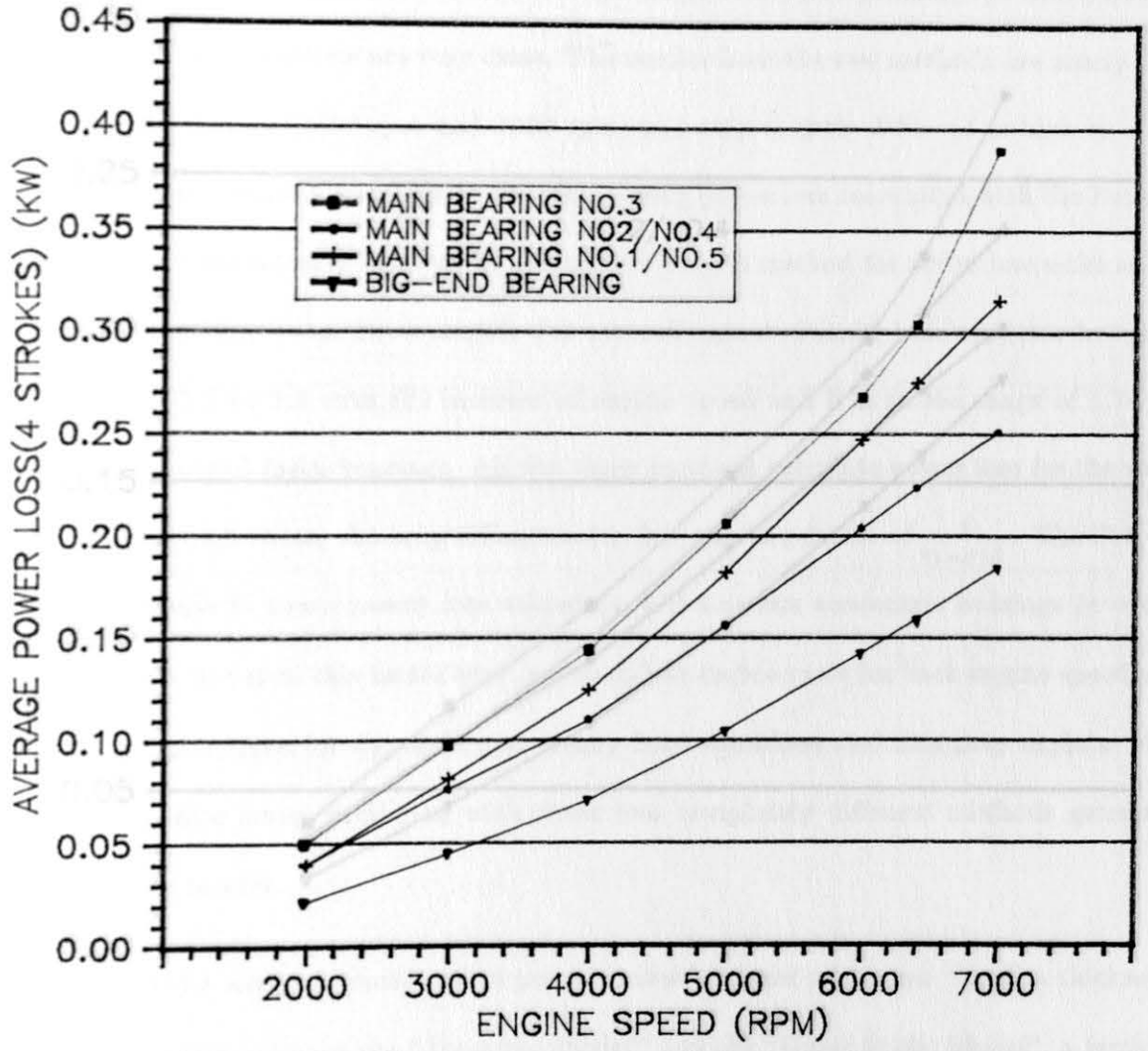

Figure 2.14. Power Losses for the Ford Zeta Engine Bearings (Centrally Grooved Main Bearings)

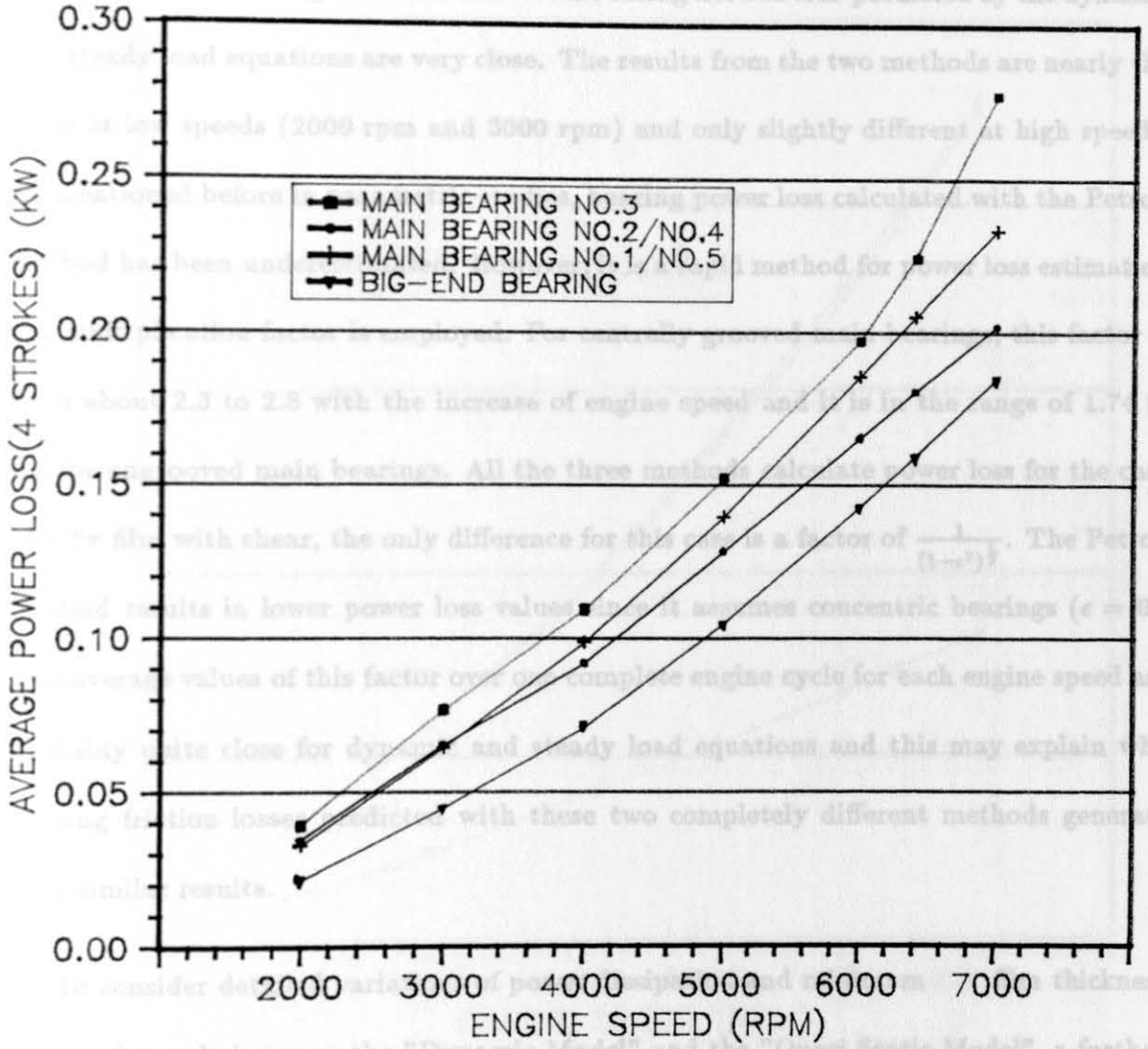

Figure 2.15. Power Losses for the Ford Zeta Engine Bearings (Ungrooved Main Bearings)

The total power loss of the big-end and main bearings for centrally grooved and ungrooved main bearing cases can be found in Figures 2.16 and 2.17. They are based on three methods: dynamically loaded bearing theory (the most precise method), the equations derived for steady load conditions and the Petroff equation (bearing eccentricity is zero). It is interesting to see that the total bearing friction loss predicted by the dynamic and steady load equations are very close. The results from the two methods are nearly the same at low speeds (2000 rpm and 3000 rpm) and only slightly different at high speeds. As mentioned before in parametric studies, bearing power loss calculated with the Petroff method has been underestimated. However, it is a rapid method for power loss estimation if a multiplication factor is employed. For centrally grooved main bearings, this factor is from about 2.3 to 2.8 with the increase of engine speed and it is in the range of 1.74 to 2.0 for ungrooved main bearings. All the three methods calculate power loss for the case of a 2π film with shear, the only difference for this case is a factor of $\frac{1}{(1-\epsilon^2)^{\frac{1}{2}}}$. The Petroff method results in lower power loss values since it assumes concentric bearings ($\epsilon = 0$). The average values of this factor over one complete engine cycle for each engine speed are probably quite close for dynamic and steady load equations and this may explain why bearing friction losses predicted with these two completely different methods generate such similar results.

To consider detailed variations of power dissipation and minimum film thickness during the cycle between the "Dynamic Model" and the "Quasi Static Model", a further study for a specific case (Zeta big-end bearing) was carried out. The minimum film thickness predicted by the dynamic load equations is bigger than those by steady load equations at low engine speeds (2000, 3000 and 4000 rpm) and smaller at high speeds (5000, 6000, 6400 and 7000 rpm). The power loss (at 3000 rpm) at specific crank angles

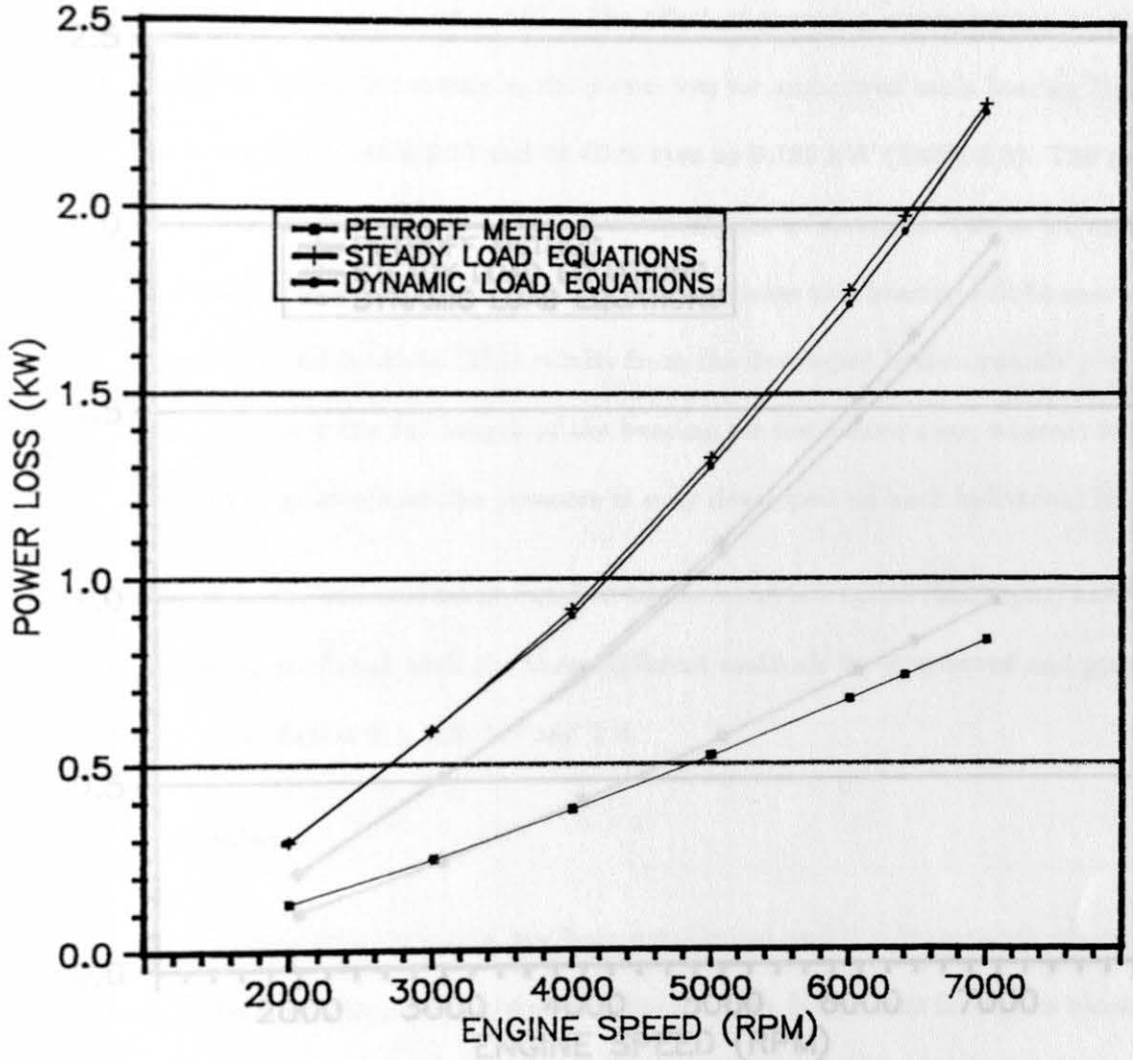

Figure 2.16. Power Losses for the Ford Zeta Engine Bearings with Three Different Methods (Centrally Grooved Main Bearings)

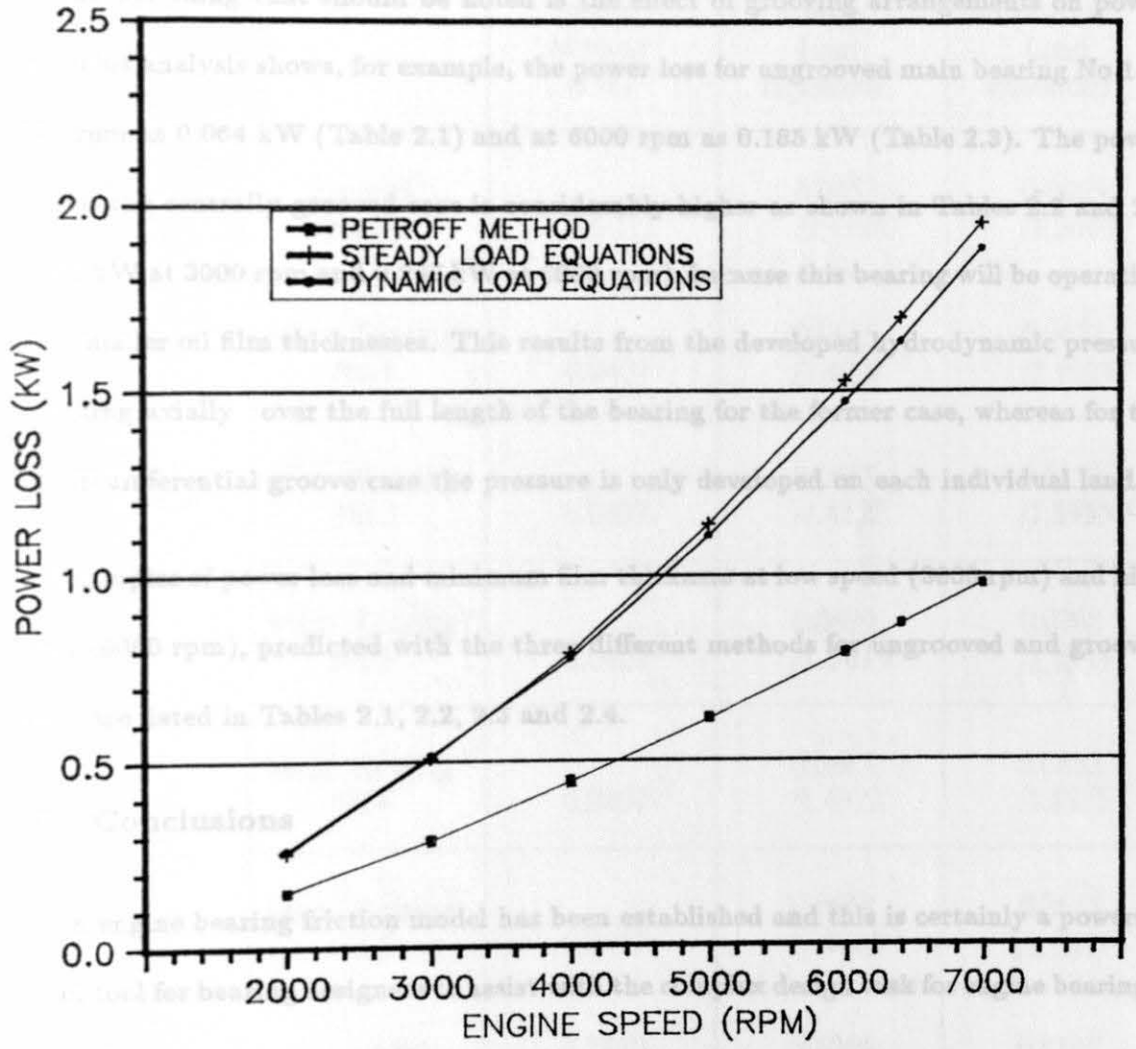

Figure 2.17. Power Losses for the Ford Zeta Engine Bearings with Three Different Methods (Ungrooved Main Bearings)

is quite different with the two methods, but the areas under the curves (power loss versus crank angle) for the cycle (i.e. average power loss) are very close. From this point of view the "Quasi Static Method" may be appropriate for bearing power loss estimation because of its simplicity and rapidness.

Another thing that should be noted is the effect of grooving arrangements on power loss. This analysis shows, for example, the power loss for ungrooved main bearing No.1 at 3000 rpm as 0.064 kW (Table 2.1) and at 6000 rpm as 0.185 kW (Table 2.3). The power loss for the centrally grooved case is considerably higher as shown in Tables 2.2 and 2.4 (0.081 kW at 3000 rpm and 0.247 kW at 6000 rpm), because this bearing will be operating with smaller oil film thicknesses. This results from the developed hydrodynamic pressure extending axially over the full length of the bearing for the former case, whereas for the full circumferential groove case the pressure is only developed on each individual land.

Examples of power loss and minimum film thickness at low speed (3000 rpm) and high speed (6000 rpm), predicted with the three different methods for ungrooved and grooved cases, are listed in Tables 2.1, 2.2, 2.3 and 2.4.

2.6 Conclusions

An engine bearing friction model has been established and this is certainly a powerful design tool for bearing designers to assist with the complex design task for engine bearings.

The hydrodynamic lubrication analysis for a single dynamically loaded journal bearing provides an essential element for the studies of engine bearings. The loading evaluations for big-end and main bearings have been reported. The prediction of bearing journal locus and frictional power losses have also been detailed. The widely studied 6VEB big-end bearing has been analysed and the results bear excellent comparison with those of others

		Petroff Method (kW)	Steady Load Equations	Dynamic Load Equations
Power Loss (kW) /Minimum Film Thickness (μm)	Big-end Bearings	0.0211	0.0453 /0.9398	0.0445 /1.5070
	Main Bearing No.1	0.0407	0.0615 /1.4908	0.0643 /2.1983
	Main Bearing No.2	0.0407	0.0665 /1.4322	0.0652 /1.8955
	Main Bearing No.3	0.0407	0.0699 /1.5619	0.0768 /2.1537
	Main Bearing No.4	0.0407	0.0665 /1.4322	0.0652 /1.8955
	Main Bearing No.5	0.0407	0.0618 /1.4866	0.0645 /2.1867
Total Power Loss (kW)		0.2879	0.5068	0.5140

Table 2.1. Comparison of Three Methods for the Calculation of Power Loss and Minimum Film Thickness for the Ford Zeta Engine Bearings (Engine Speed = 3000 rpm, Ungrooved Bearings, 2π Film with Shear Only)

		Petroff Method (kW)	Steady Load Equations	Dynamic Load Equations
Power Loss (kW) /Minimum Film Thickness (μm)	Big-end Bearings	0.0211	0.0451 /0.9398	0.0445 /1.5070
	Main Bearing No.1	0.0319	0.0764 /0.5236	0.0813 /0.6846
	Main Bearing No.2	0.0319	0.0832 /0.5026	0.0760 /0.6250
	Main Bearing No.3	0.0319	0.0886 /0.5487	0.0973 /0.6859
	Main Bearing No.4	0.0319	0.0832 /0.5026	0.0760 /0.6250
	Main Bearing No.5	0.0319	0.0769 /0.5215	0.0813 /0.6821
Total Power Loss (kW)		0.2439	0.5889	0.5900

Table 2.2. Comparison of Three Methods for the Calculation of Power Loss and Minimum Film Thickness for the Ford Zeta Engine Bearings (Engine Speed = 3000 rpm, Centrally Grooved Main Bearings, 2π Film with Shear Only)

		Petroff Method (kW)	Steady Load Equations	Dynamic Load Equations
Power Loss (kW) /Minimum Film Thickness (μm)	Big-end Bearings	0.0602	0.1447 /1.4096	0.1424 /0.9377
	Main Bearing No.1	0.1107	0.1860 /2.1795	0.1854 /1.9574
	Main Bearing No.2	0.1107	0.1860 /1.7985	0.1651 /2.0878
	Main Bearing No.3	0.1107	0.2025 /2.1000	0.1971 /1.3088
	Main Bearing No.4	0.1107	0.1860 /1.7985	0.1651 /2.0878
	Main Bearing No.5	0.1107	0.1862 /2.1712	0.1858 /1.9510
Total Power Loss (kW)		0.7943	1.5258	1.4681

Table 2.3. Comparison of Three Methods for the Calculation of Power Loss and Minimum Film Thickness for the Ford Zeta Engine Bearings (Engine Speed = 6000 rpm, Ungrooved Bearings, 2π Film with Shear Only)

		Petroff Method (kW)	Steady Load Equations	Dynamic Load Equations
Power Loss (kW) /Minimum Film Thickness (μm)	Big-end Bearings	0.0602	0.1447 /1.4096	0.1432 /0.9378
	Main Bearing No.1	0.0868	0.2353 /0.7706	0.2471 /0.5636
	Main Bearing No.2	0.0868	0.2355 /0.6324	0.2036 /0.6436
	Main Bearing No.3	0.0868	0.2585 /0.7413	0.2685 /0.3726
	Main Bearing No.4	0.0868	0.2355 /0.6324	0.2036 /0.6436
	Main Bearing No.5	0.0868	0.2357 /0.7664	0.2474 /0.5653
Total Power Loss (kW)		0.6748	1.7794	1.7397

Table 2.4. Comparison of Three Methods for the Calculation of Power Loss and Minimum Film Thickness for the Ford Zeta Engine Bearings (Engine Speed = 6000 rpm, Centrally Grooved Main Bearings, 2π Film with Shear Only)

obtained using various techniques. The performance of the Ford Zeta engine bearings have also been analysed.

Parametric studies has been undertaken of the tribological performance of the 6VEB big-end bearing. It has been shown that great benefits could be achieved by careful redesign.

The Short Bearing Mobility Method has been successfully applied for bearing lubrication analysis. Both the quasi-steady load approach and the Petroff method have shown good comparison for the calculation of bearing power loss.

Part II

FRICTION MODELLING FOR AN ENGINE VALVE TRAIN

Chapter Three

Theoretical Basis for an Engine Valve Train

3.1 Introduction

The analysis of cam/follower performance is an important feature of valve train design for internal combustion engines. Classically the cam mechanism has been designed with considerations of the choice of materials, suitable anti-wear additives for the lubricant and the calculation of Hertzian stresses. More recently designers have become more energy conscious and the frictional power loss associated with the cam mechanism has become important. The cam and follower friction study forms a part of the whole effort in dealing with the problem of engine friction reduction.

The first half of this chapter, therefore, provides a simple tool using the existing lubrication theories to estimate the friction and hence power loss concerned with the contact between a tapered cam and a non-rotating domed follower. It also covers the kinematics of this direct acting overhead cam mechanism, three-dimensional contact loading evaluations, elliptical contact Hertzian stress calculations and the full film EHL (elastohydrodynamic lubrication) analysis for the minimum and the central film thickness predictions.

Apart from the friction at the cam and follower interface, the camshaft bearings, the follower/guide and the valve/guide contacts also contribute to the friction losses associated with the valve train. Cam/follower friction studies have received much more attention in the past than the studies on any other interfaces in the system. The second half of

this chapter carries out such a study of the friction losses concerned with these associated parts of a typical modern automotive valve train.

The camshafts are carried in suitable bearings. Although in some cases ball or roller bearings are used, these are usually plain bearings and normally designed using similar methods to those used for the crankshaft bearings. The performance of the camshaft bearings has thus been studied in the same way as for the main bearings, i.e. the Short Bearing Mobility Method as described in Part I.

The friction between the follower and its guide was modelled using both a boundary lubrication approximation and a full film lubrication approach. The appropriate model largely depends on the lubrication system of the engine considered.

The valve/guide friction was calculated assuming it was generated by the shear of the lubricant between the concentric working surfaces.

The current analysis method has a general application. Any other valve train systems in common use in passenger car engines can be studied following a similar procedure.

3.2 Theoretical Basis for a Tapered Cam and Domed Follower System

3.2.1 Kinematic Analysis

The analysis of the kinematics of a cam and follower pair is a necessary preliminary for the associated studies of lubrication and friction. Such an analysis can be carried out once the cam and follower characteristics are known. It should be noted that the present study is for a tapered cam acting against a non-rotating domed hydraulic lash adjusted follower.

The geometrical specification of a cam acting against domed follower is shown in Figure 3.1. A detailed analysis of the kinematics of the system has been given by Dyson and Naylor [1960] and the important cam radius of curvature of the contact point and surface velocities of the system are reproduced below.

The radius of curvature of the cam profile at the contact, R_c, is given by

$$R_c = \frac{\left[Z^2 + \left(\frac{dZ}{d\theta_c}\right)^2\right]^{\frac{3}{2}}}{Z^2 + 2\left(\frac{dZ}{d\theta_c}\right)^2 - Z\frac{d^2Z}{d\theta_c^2}} - R_f \tag{3.1}$$

The velocity of the point of contact relative to the cam, V_c, is

$$V_c = \omega_c \left(\left[Z^2 + \left(\frac{dZ}{d\theta_c}\right)^2\right]^{\frac{1}{2}} - \frac{R_f\left[Z^2 + 2\left(\frac{dZ}{d\theta_c}\right)^2 - Z\frac{d^2Z}{d\theta_c^2}\right]}{Z^2 + \left(\frac{dZ}{d\theta_c}\right)^2} \right) \tag{3.2}$$

and the velocity of the point of contact relative to the follower, V_f, is

$$V_f = \omega_c \left(\frac{R_f\left[Z\frac{d^2Z}{d\theta_c^2} - \left(\frac{dZ}{d\theta_c}\right)^2\right]}{Z^2 + \left(\frac{dZ}{d\theta_c}\right)^2} \right) \tag{3.3}$$

where the distance, $Z = L_c + R_b + R_f$, can be found from Figure 3.1. The mean entraining velocity, V_e, is

$$V_e = \frac{1}{2}(V_c + V_f) \tag{3.4}$$

and the sliding velocity is

$$V_s = V_c - V_f \tag{3.5}$$

3.2.2 The Contact Loading at the Cam/Follower Interface

To carry out the lubrication and stress analysis for a cam and follower pair, the load at the contact needs to be ascertained. The precise determination of the load during a cycle is a complex matter. In general the forces associated with the operation of the mechanism are the inertia force, the spring force, the friction force arising as a result of

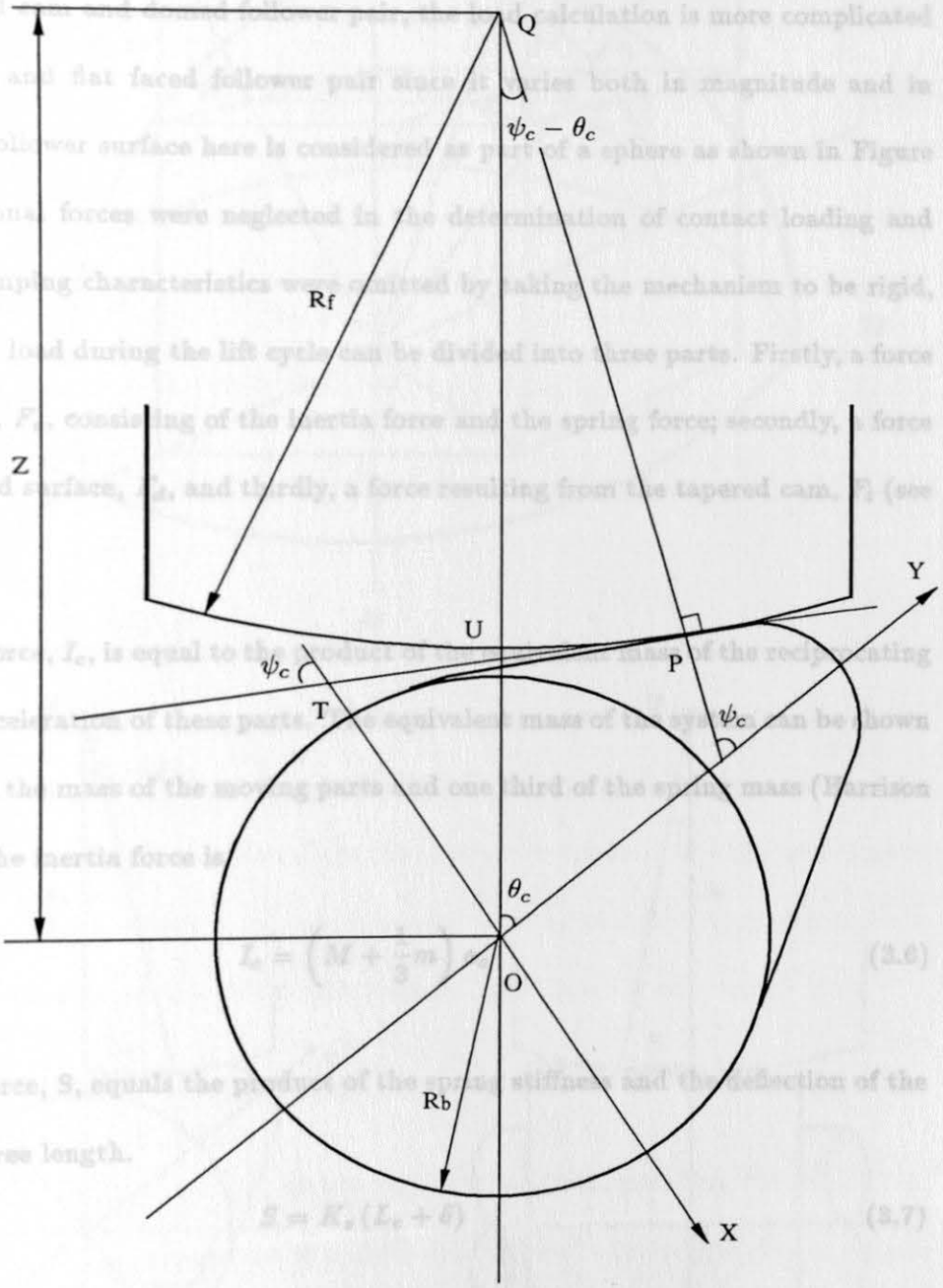

Figure 3.1. Geometry of the Cam and Follower System

relative motion between the contacting parts and the forces resulting from the stiffness and damping characteristics of the overall structure.

For a tapered cam and domed follower pair, the load calculation is more complicated than for a cam and flat faced follower pair since it varies both in magnitude and in direction. The follower surface here is considered as part of a sphere as shown in Figure 3.2(a). If frictional forces were neglected in the determination of contact loading and stiffness and damping characteristics were omitted by taking the mechanism to be rigid, then the contact load during the lift cycle can be divided into three parts. Firstly, a force acting vertically, F_v, consisting of the inertia force and the spring force; secondly, a force due to the domed surface, F_d, and thirdly, a force resulting from the tapered cam, F_t (see Figure 3.2).

The inertia force, I_c, is equal to the product of the equivalent mass of the reciprocating parts and the acceleration of these parts. The equivalent mass of the system can be shown to be the sum of the mass of the moving parts and one third of the spring mass (Harrison [1985]). Hence the inertia force is

$$I_c = \left(M + \frac{1}{3}m\right) a_c \tag{3.6}$$

The spring force, S, equals the product of the spring stiffness and the deflection of the spring from its free length.

$$S = K_s (L_c + \delta) \tag{3.7}$$

The vertical force is therefore

$$F_v = I_c + S \tag{3.8}$$

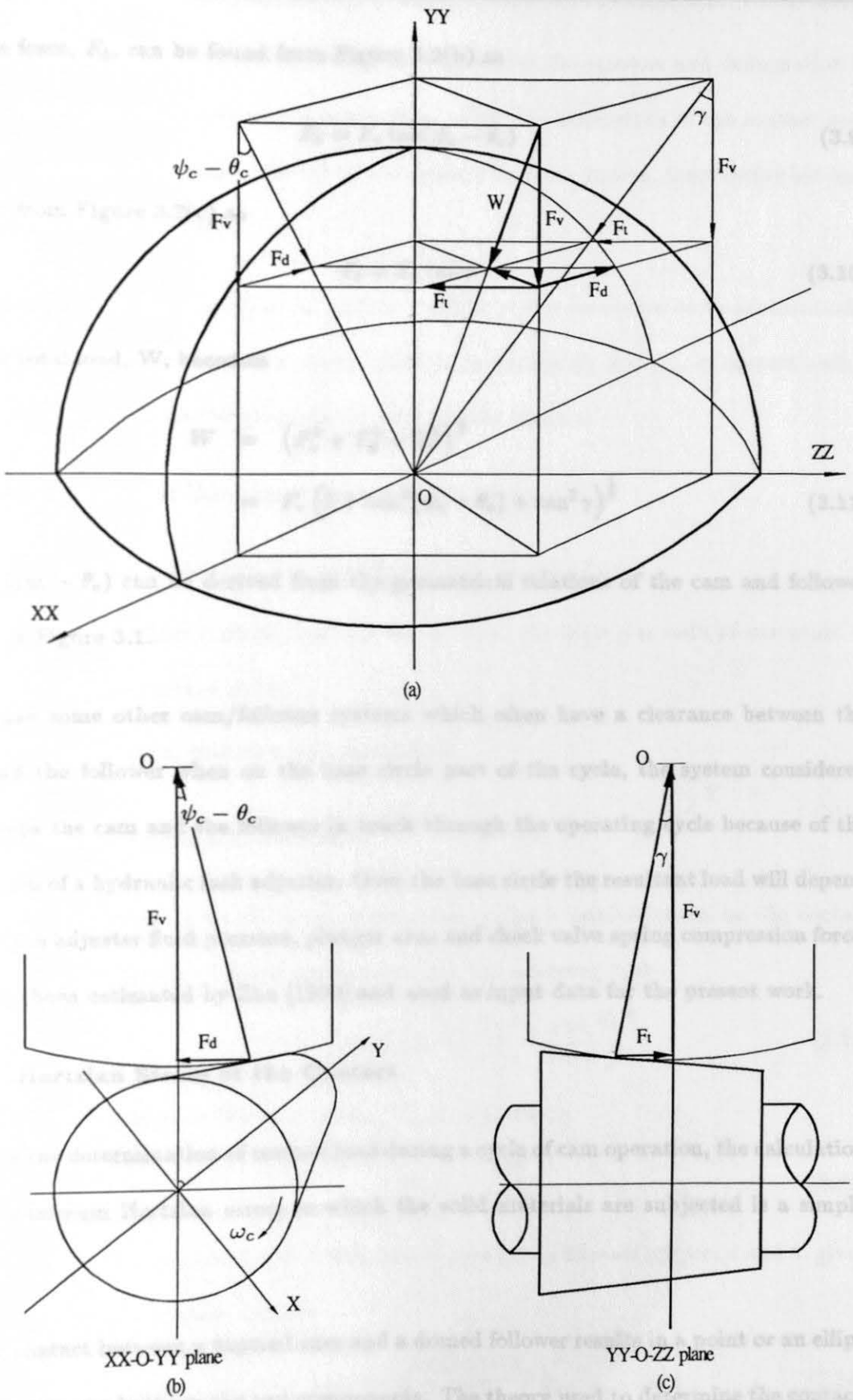

Figure 3.2. Load Analysis for a Tapered Cam and Domed Follower System

The force, F_d, can be found from Figure 3.2(b) as

$$F_d = F_v \tan(\psi_c - \theta_c) \tag{3.9}$$

and F_t, from Figure 3.2(c) as

$$F_t = F_v \tan\gamma \tag{3.10}$$

The total load, W, becomes

$$\begin{aligned} W &= \left(F_v^2 + F_d^2 + F_t^2\right)^{\frac{1}{2}} \\ &= F_v \left(1 + \tan^2(\psi_c - \theta_c) + \tan^2\gamma\right)^{\frac{1}{2}} \end{aligned} \tag{3.11}$$

and $\tan(\psi_c - \theta_c)$ can be derived from the geometrical relations of the cam and follower shown in Figure 3.1.

Unlike some other cam/follower systems which often have a clearance between the cam and the follower when on the base circle part of the cycle, the system considered here keeps the cam and the follower in touch through the operating cycle because of the utilization of a hydraulic lash adjuster. Over the base circle the resultant load will depend on the lash adjuster fluid pressure, plunger area and check valve spring compression force. This has been estimated by Zhu [1990] and used as input data for the present work.

3.2.3 Hertzian Stress at the Contact

. With the determination of contact load during a cycle of cam operation, the calculation of the maximum Hertzian stress to which the solid materials are subjected is a simple matter.

The contact between a tapered cam and a domed follower results in a point or an elliptical contact area between the two components. The theory used to determine the contact

stresses was established by Hertz [1882]. He considered the stresses and deformation in two perfectly smooth, contacting elastic solids. Once the dimensions of the contact zone and the pressure distribution normal to the applied load are known, the pressure between the two bodies can be found.

The contact in the cam/follower system considered can be shown to be geometrically equivalent to an ellipsoid, with principal radii of curvature R_x and R_y, in contact with a plane. Figure 3.3 shows the geometry of such a point contact.

In his derivation of the contact stresses, Hertz assumed that

(a) the bodies are elastic in accordance with Hooke's Law;

(b) the principal contact length is small w.r.t. the principal radii of curvature of the undeformed solids;

(c) only normal pressures are considered.

The following results were derived

(a) The pressure distribution between the bodies is semi-elliptical on the contact patch for an elliptical contact and has the following form

$$p = P_{max}\left(1 - \left(\frac{x}{a}\right)^2 - \left(\frac{y}{b}\right)^2\right)^{\frac{1}{2}} \tag{3.12}$$

(b) The maximum Hertzian stress, P_{max}, is given by

$$P_{max} = \frac{3W}{2\pi ab} \tag{3.13}$$

with the semi-major and semi-minor axes of the contact ellipse, a and b, given by the expressions below

$$a = \left(\frac{6k^2 I_1 W R_e}{\pi E'}\right)^{\frac{1}{3}} \tag{3.14}$$

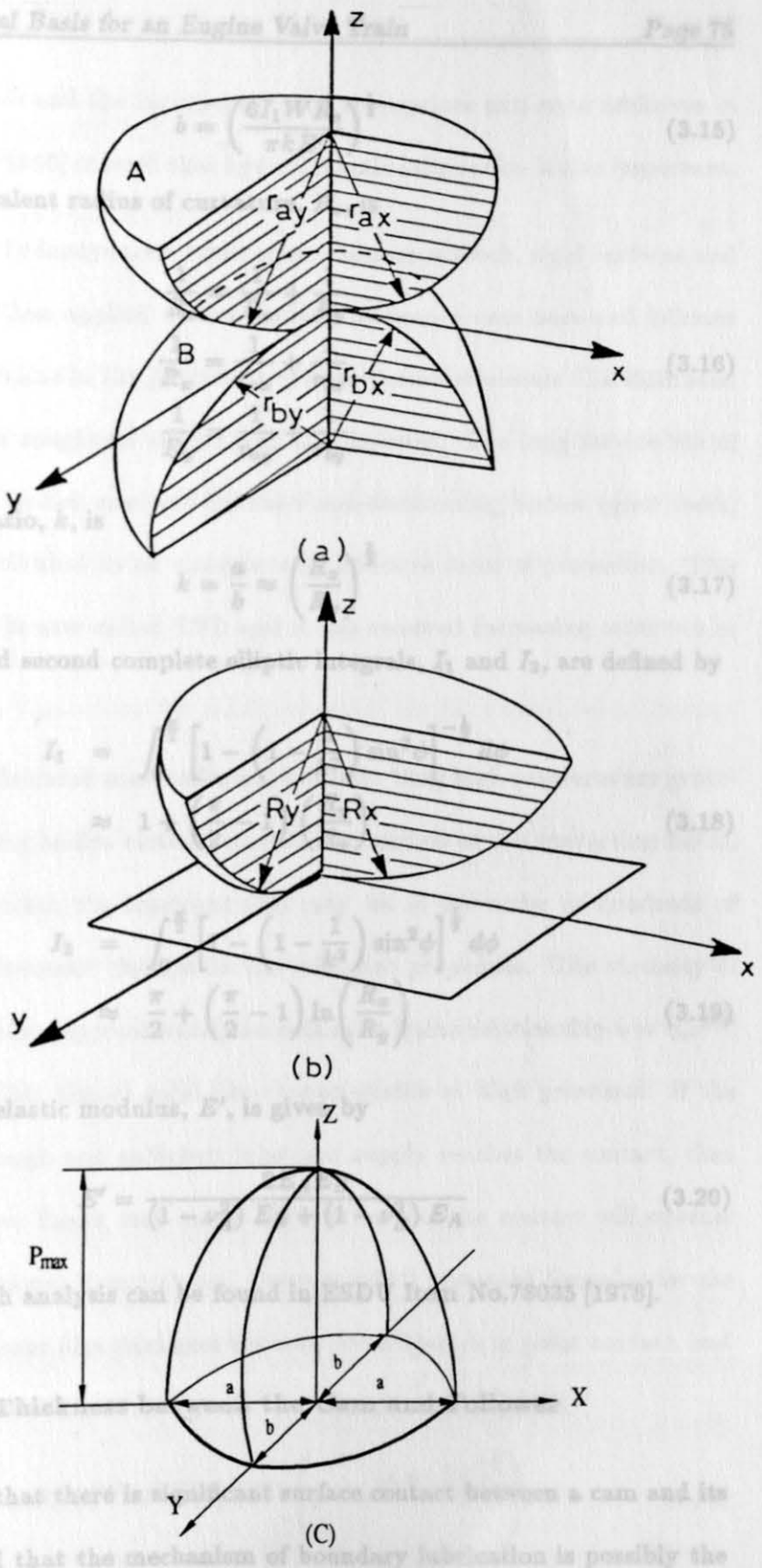

Figure 3.3. Geometry of Point or Elliptical Contacts

(a) Contact of two ellipsoidal solids

(b) Equivalent geometry

(c) Pressure distribution

$$b = \left(\frac{6I_1 W R_e}{\pi k E'}\right)^{\frac{1}{3}} \tag{3.15}$$

where the equivalent radius of curvature, R_e, is

$$\begin{aligned} \frac{1}{R_e} &= \frac{1}{R_x} + \frac{1}{R_y} \\ \frac{1}{R_x} &= \frac{1}{r_{ax}} + \frac{1}{r_{bx}} \\ \frac{1}{R_y} &= \frac{1}{r_{ay}} + \frac{1}{r_{by}} \end{aligned} \tag{3.16}$$

the ellipticity ratio, k, is

$$k = \frac{a}{b} \approx \left(\frac{R_x}{R_y}\right)^{\frac{2}{3}} \tag{3.17}$$

and the first and second complete elliptic integrals, I_1 and I_2, are defined by

$$\begin{aligned} I_1 &= \int_0^{\frac{\pi}{2}} \left[1 - \left(1 - \frac{1}{k^2}\right)\sin^2\phi\right]^{-\frac{1}{2}} d\phi \\ &\approx 1 + \left(\frac{\pi}{2} - 1\right)\left(\frac{R_y}{R_x}\right) \end{aligned} \tag{3.18}$$

$$\begin{aligned} I_2 &= \int_0^{\frac{\pi}{2}} \left[1 - \left(1 - \frac{1}{k^2}\right)\sin^2\phi\right]^{\frac{1}{2}} d\phi \\ &\approx \frac{\pi}{2} + \left(\frac{\pi}{2} - 1\right)\ln\left(\frac{R_x}{R_y}\right) \end{aligned} \tag{3.19}$$

The equivalent elastic modulus, E', is given by

$$E' = \frac{2E_A E_B}{(1-\nu_A^2)\,E_B + (1-\nu_B^2)\,E_A} \tag{3.20}$$

A more thorough analysis can be found in ESDU Item No.78035 [1978].

3.2.4 Lubricant Film Thickness between the Cam and Follower

It is widely recognized that there is significant surface contact between a cam and its follower during a cycle and that the mechanism of boundary lubrication is possibly the most important action in ensuring an acceptable life for this component. Apart from the

proper selection of materials and the incorporation of appropriate anti-wear additives in the lubricating oil, Muller [1966] showed that hydrodynamic lubrication is also important.

The classical theory of hydrodynamic lubrication assumes smooth, rigid surfaces and an isoviscous lubricant. When applied to the contact between a cam nose and follower application of the theory results in the prediction of a very small minimum film thickness, compared with the surface roughness of the cam and follower. The long service life of these and similar heavily loaded contacts between non-conforming bodies (gear teeth, for example) has been attributed to an unexpectedly effective form of protection. This hydrodynamic mechanism is now called EHL and it has received increasing attention in recent years.

EHL occurs between lubricated non-conformal surfaces. Very high pressures are generated between the interacting bodies causing elastic deformation of the contacting solids. The pressure generated within the lubricant film may be of the order of hundreds of mega-pascals, leading to dramatic changes in the lubricant properties. The viscosity of the lubricant increases rapidly (approximately according to Barus relationship $\eta = \eta_0 e^{\alpha p}$) and the lubricant can exhibit almost solid like characteristics at high pressures. If the camshaft speed is high enough and sufficient lubricant supply reaches the contact, then the contact around the cam flanks may enjoy EHL, otherwise the contact will operate in mixed lubrication conditions. Hamrock and Dowson [1981] presented formulae for the minimum and central lubricant film thickness between two ellipsoids in point contact, and modified forms of the formulae have been given by Chittenden et al [1985].

$$h_{min} = 3.68 R_E U_e^{0.68} G^{0.49} W_e^{-0.073} \left(1 - e^{-0.67 \left(\frac{R_S}{R_E} \right)^{\frac{2}{3}}} \right) \qquad (3.21)$$

$$h_{cen} = 4.31 R_E U_e^{0.68} G^{0.49} W_e^{-0.073} \left(1 - e^{-1.23 \left(\frac{R_S}{R_E} \right)^{\frac{2}{3}}} \right) \tag{3.22}$$

where the three dimensionless parameters U_e, G and W_e are equal to $\frac{\eta_0 V_e}{E' R_E}$, $\alpha E'$ and $\frac{W}{E' R_E^2}$, respectively.

Over the base circle part of the cycle the lubrication regime chart (Chittenden et al [1987]) has been used to ensure the appropriate use of the film thickness prediction formulae for the given situation. It has been found that for the given conditions the cam and follower operate in the piezoviscous-elastic regime over the base circle, hence the equations above can be used.

Around the nose of the cam where the lubricant entrainment is small, some element of boundary lubrication can almost always be anticipated. Boundary lubrication occurs when surface contact of the solids takes place over an area comparable to that which develops in dry contact. The frictional characteristics are determined in this case by the physical and chemical properties of the solids and the lubricant at their common interfaces. In such conditions the laws of dry friction are often taken to apply since the coefficient of friction is independent of load, viscosity, speed and apparent area of contact to a first approximation.

It should be mentioned that the formulas listed above are for steady state EHL conditions. Although squeeze film action has been recognized as being very important, especially around the areas where entrainment of the lubricant is quite small, the approach is felt to be adequate for steady state analysis to be used in the qualitative analysis of valve train design.

3.2.5 Friction and Power Loss

The elastic deformation between the cam and follower is large compared with the lubricant film thickness and the contact can be approximated by a lubricated Hertzian contact. The friction is almost entirely due to the rolling of the components in the inlet region to the contact, but it is dominated by the sliding of the surfaces in the lubricated contact zone. As shear stress, and hence frictional force, is proportional to the velocity gradient across the thickness of the film, by approximating the lubricated contact region between the cam and follower as a region of constant film thickness h_{cen} and neglecting the contribution of any rolling friction either in the contact or in the inlet zone, the friction force F may be estimated as

$$F = \iint \eta \frac{V_S}{h_{cen}} \, dx \, dy \tag{3.23}$$

Substituting the Barus relationship for pressure dependent viscosity ($\eta = \eta_0 e^{\alpha p}$) and noting that pressure distribution for a Hertzian elliptical contact is given by equation (3.12), F becomes

$$F = 4\eta_0 \frac{V_S}{h_{cen}} \int_0^a \int_0^b e^{\alpha P_{max}\left(1-\frac{x^2}{a^2}\right)^{\frac{1}{2}}} e^{\alpha P_{max}\left(1-\frac{x^2}{a^2}-\frac{y^2}{b^2}\right)^{\frac{1}{2}}} \, dx \, dy \tag{3.24}$$

where the semi-major and semi-minor axes of the contact ellipse, a and b, and the maximum Hertzian stress P_{max} can be found in equations (3.14), (3.15) and (3.13), respectively.

It has been recognized that the Barus relationship is unrealistic at higher pressures, and the friction forces predicted using equation (3.24) become very large under such circumstances. Rheological studies of the behaviour of lubricants in highly-loaded non-conformal contacts have indicated the existence of a limiting traction coefficient. The value of the coefficient of friction here was taken to be 0.08. Empirical evidence (Zhu

[1988]) and work at the University of Leeds has shown that this value is quite reasonable. If the prediction of equation (3.24) for friction according to classical thin fluid film analysis resulted in a local value of coefficient of friction greater than the limiting value, then this limiting value was taken to apply and a boundary friction calculation ($F = \mu W$) was carried out.

The average frictional power loss over a cam cycle becomes

$$H_v = \frac{1}{2\pi} \int_0^{2\pi} F\, r_f\, \omega_c\, d\theta_c \tag{3.25}$$

where r_f is the perpendicular distance from the cam rotational centre to the friction force vector.

3.3 Theoretical Study of Camshaft Bearing Performance, Follower/Guide and Valve/Guide Friction Estimation for the Zeta Engine

3.3.1 Camshaft Bearing Performance

The Ford 1.8L H.O. Zeta engine has two camshafts: one intake, one exhaust. The intake camshaft is shown schematically in Figure 3.4(a), and the angular relations of all cams is presented in Figure 3.4(b). It has eight cams, directly controlling eight intake valves. The camshaft is supported by five plain bearings and driven by a toothed belt via a pulley located at one end of the camshaft. The exhaust camshaft has the same arrangement as for the intake camshaft.

3.3.1.1 Bearing Loadings

The camshaft bearing loads arise from the reaction forces from the followers to the cams, the friction forces at the cam/follower interfaces and the pulley loads from the driving belt. The calculation of these loads is a statically indeterminate problem and can

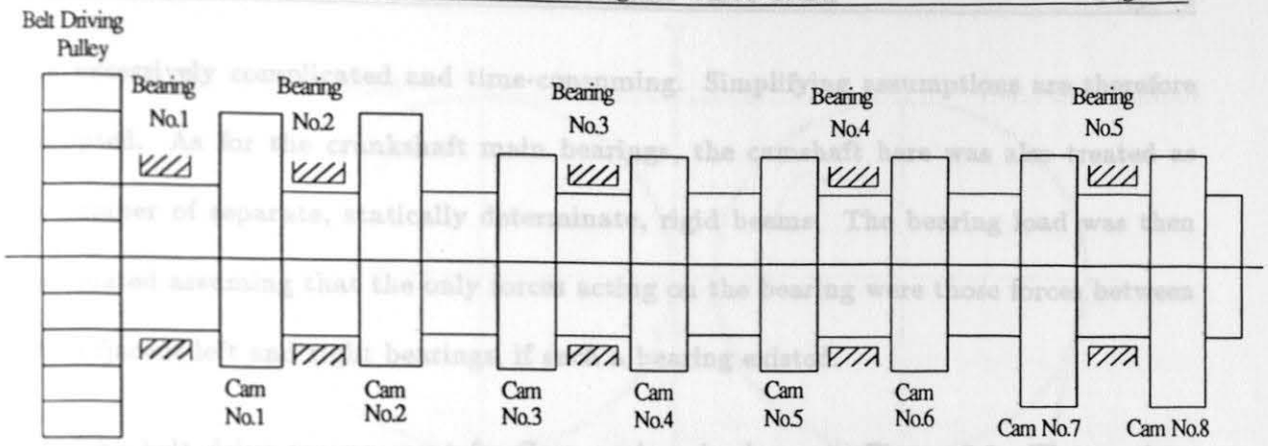

(a) Intake Camshaft Bearing Arrangement

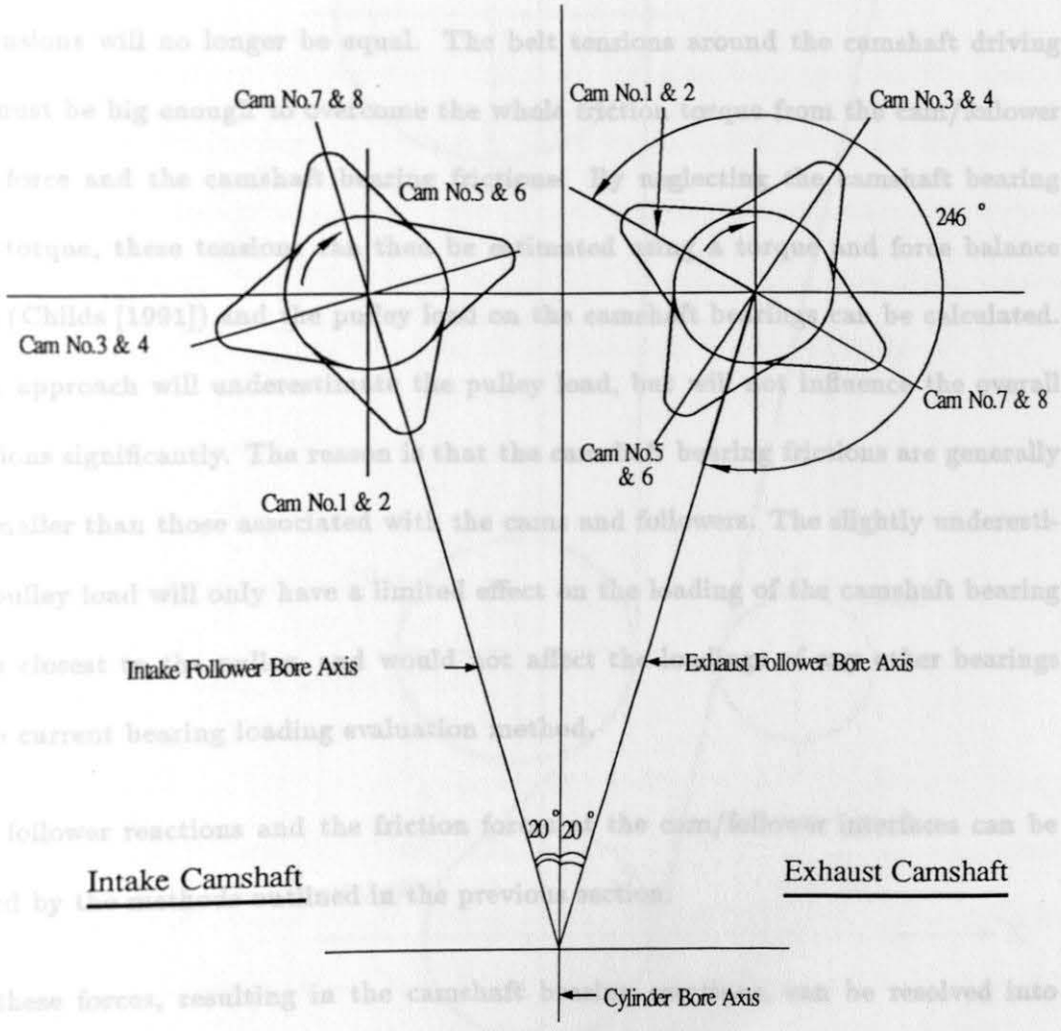

(b) Angular Relations of Cams

Figure 3.4. Schematic Camshaft Arrangement of the Ford Zeta Engine

be excessively complicated and time-consuming. Simplifying assumptions are therefore adopted. As for the crankshaft main bearings, the camshaft here was also treated as a number of separate, statically determinate, rigid beams. The bearing load was then estimated assuming that the only forces acting on the bearing were those forces between its adjacent left and right bearings, if such a bearing existed.

The belt drive arrangement for Zeta engines is shown in Figure 3.5. The tensions within each portion of the belt, due to the pre-load applied through the tensioner, are the same when the system is at rest. When a driving torque is applied through the crankshaft these tensions will no longer be equal. The belt tensions around the camshaft driving pulley must be big enough to overcome the whole friction torque from the cam/follower friction force and the camshaft bearing frictions. By neglecting the camshaft bearing friction torque, these tensions can then be estimated using a torque and force balance method (Childs [1991]) and the pulley load on the camshaft bearings can be calculated. Such an approach will underestimate the pulley load, but will not influence the overall calculations significantly. The reason is that the camshaft bearing frictions are generally much smaller than those associated with the cams and followers. The slightly underestimated pulley load will only have a limited effect on the loading of the camshaft bearing which is closest to the pulley, and would not affect the loadings of any other bearings with the current bearing loading evaluation method.

The follower reactions and the friction forces at the cam/follower interfaces can be evaluated by the methods outlined in the previous section.

All these forces, resulting in the camshaft bearing reactions, can be resolved into components acting along, and perpendicular to, the cylinder bore axis. Knowing the angular relations of all the cams and the distances between cam lobes and bearings, a

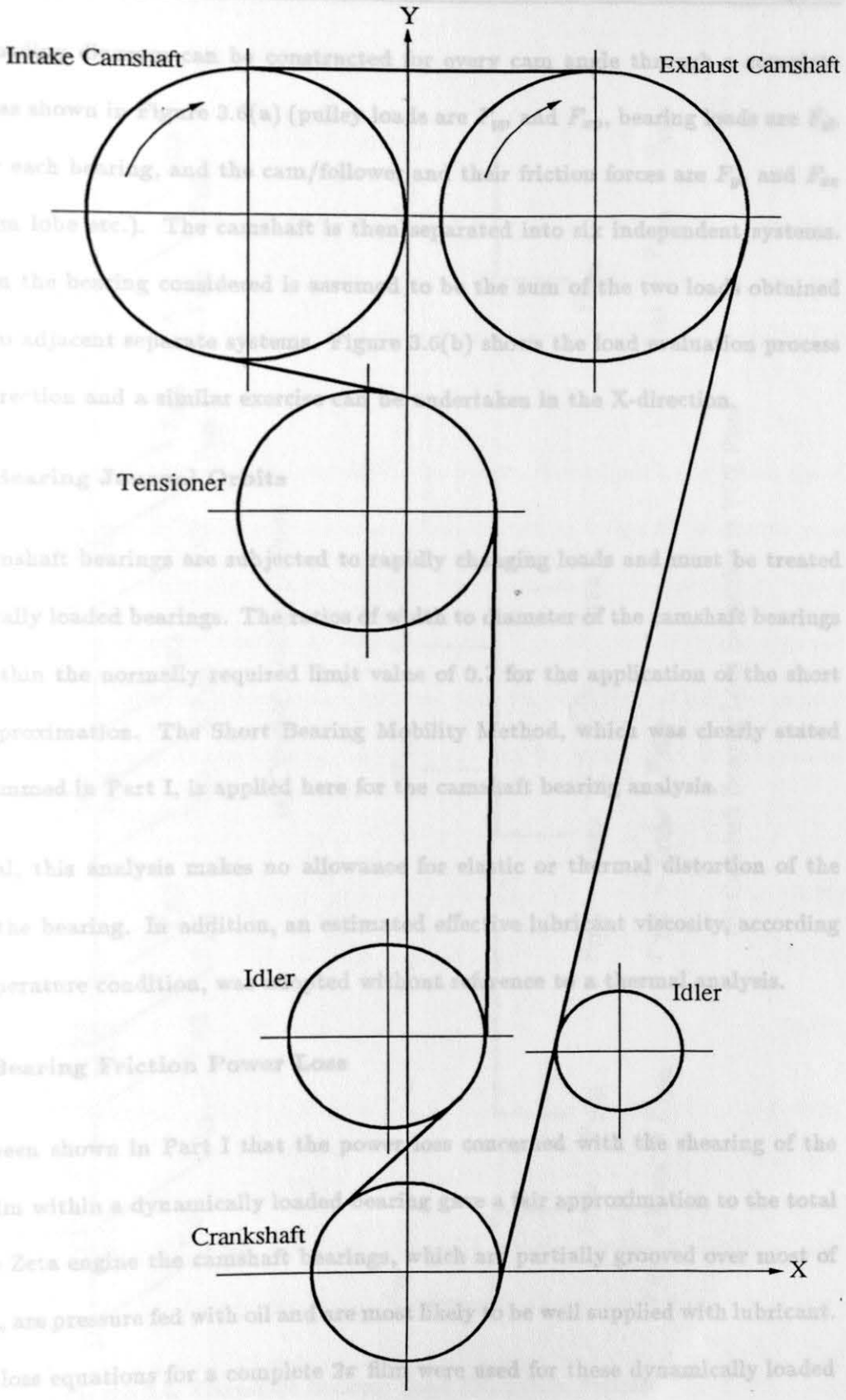

Figure 3.5. Ford Zeta Engine Belt Arrangement

camshaft loading diagram can be constructed for every cam angle through a complete cam cycle, as shown in Figure 3.6(a) (pulley loads are F_{yp} and F_{xp}, bearing loads are F_{yb} and F_{xb} for each bearing, and the cam/follower and their friction forces are F_{yc} and F_{xc} for each cam lobe etc.). The camshaft is then separated into six independent systems. The load on the bearing considered is assumed to be the sum of the two loads obtained from its two adjacent separate systems. Figure 3.6(b) shows the load evaluation process in the Y-direction and a similar exercise can be undertaken in the X-direction.

3.3.1.2 Bearing Journal Orbits

The camshaft bearings are subjected to rapidly changing loads and must be treated as dynamically loaded bearings. The ratios of width to diameter of the camshaft bearings are well within the normally required limit value of 0.7 for the application of the short bearing approximation. The Short Bearing Mobility Method, which was clearly stated and programmed in Part I, is applied here for the camshaft bearing analysis.

As usual, this analysis makes no allowance for elastic or thermal distortion of the journal or the bearing. In addition, an estimated effective lubricant viscosity, according to the temperature condition, was adopted without reference to a thermal analysis.

3.3.1.3 Bearing Friction Power Loss

It has been shown in Part I that the power loss concerned with the shearing of the complete film within a dynamically loaded bearing gave a fair approximation to the total loss. In the Zeta engine the camshaft bearings, which are partially grooved over most of the bearing, are pressure fed with oil and are most likely to be well supplied with lubricant. The power loss equations for a complete 2π film were used for these dynamically loaded camshaft bearings.

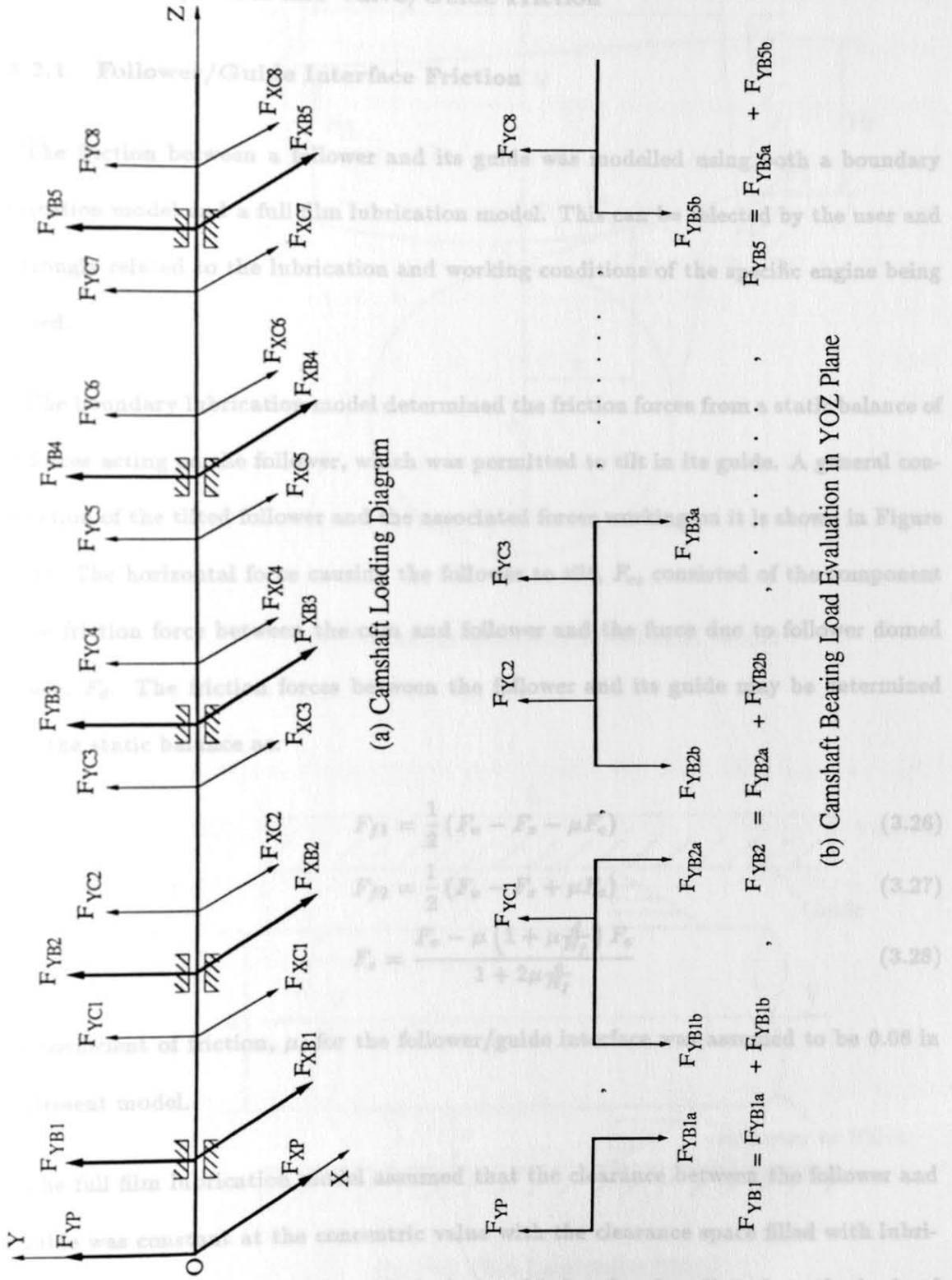

Figure 3.6. Camshaft Bearing Load Evaluation Process

3.3.2 Follower/Guide and Valve/Guide Friction

3.3.2.1 Follower/Guide Interface Friction

The friction between a follower and its guide was modelled using both a boundary lubrication model and a full film lubrication model. This can be selected by the user and is strongly related to the lubrication and working conditions of the specific engine being studied.

The boundary lubrication model determined the friction forces from a static balance of the forces acting on the follower, which was permitted to tilt in its guide. A general configuration of the tilted follower and the associated forces working on it is shown in Figure 3.7(a). The horizontal force causing the follower to tilt, F_c, consisted of the component of the friction force between the cam and follower and the force due to follower domed surface, F_d. The friction forces between the follower and its guide may be determined from the static balance as:

$$F_{f1} = \frac{1}{2}(F_v - F_z - \mu F_c) \tag{3.26}$$

$$F_{f2} = \frac{1}{2}(F_v - F_z + \mu F_c) \tag{3.27}$$

$$F_z = \frac{F_v - \mu\left(1 + \mu\frac{d}{H_f}\right)F_c}{1 + 2\mu\frac{e}{H_f}} \tag{3.28}$$

The coefficient of friction, μ, for the follower/guide interface was assumed to be 0.08 in the present model.

The full film lubrication model assumed that the clearance between the follower and its guide was constant at the concentric value with the clearance space filled with lubricant. The hydrodynamic friction calculation could therefore be effected on the basis of consideration of Couette flow between the components with a knowledge of the operating

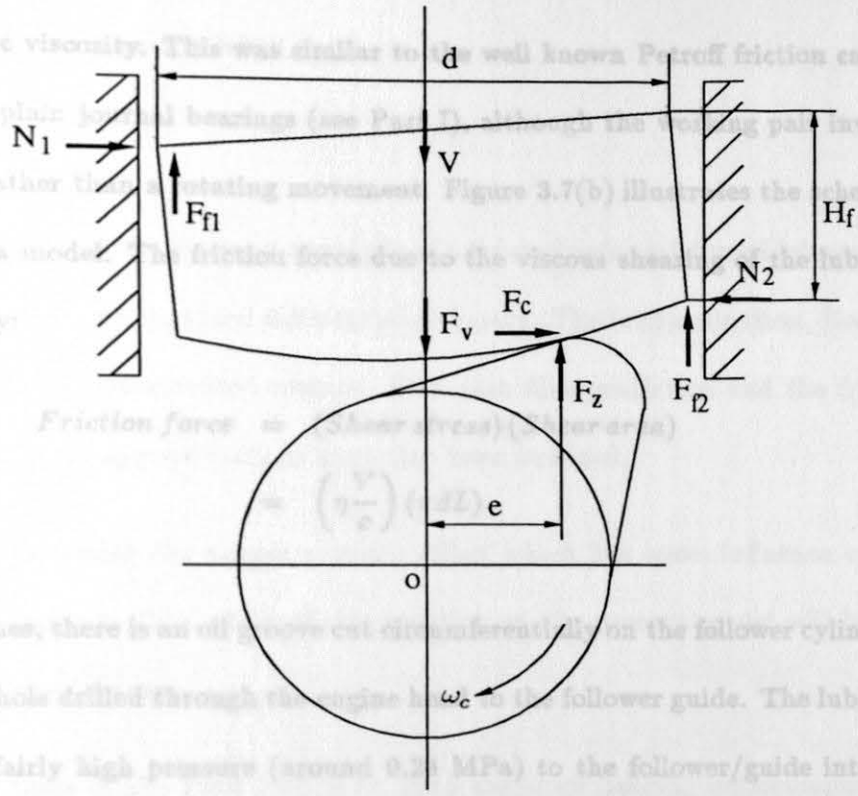

(a) Forces for Boundary Lubrication Model

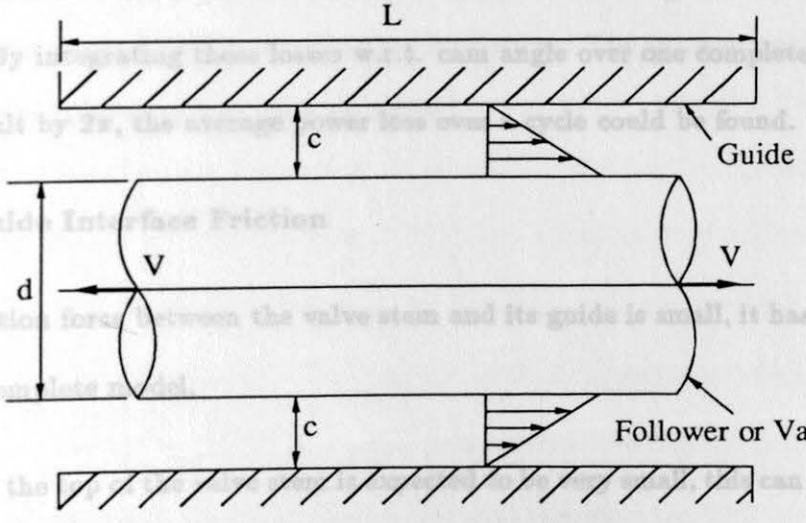

(b) Full Film Lubrication Model

Figure 3.7. Friction Modelling for Follower/Guide and Valve/Guide Contacts

lubricant dynamic viscosity. This was similar to the well known Petroff friction calculation for rotating plain journal bearings (see Part I), although the working pair involved a reciprocating rather than a rotating movement. Figure 3.7(b) illustrates the schematic diagram of such a model. The friction force due to the viscous shearing of the lubricant is simply given by:

$$\begin{aligned} Friction\ force &= (Shear\ stress)\,(Shear\ area) \\ &= \left(\eta \frac{V}{c}\right)(\pi d L) \end{aligned} \tag{3.29}$$

For Zeta engines, there is an oil groove cut circumferentially on the follower cylindrical surface and a oil hole drilled through the engine head to the follower guide. The lubricant is pumped at a fairly high pressure (around 0.24 MPa) to the follower/guide interface through the hole. It is therefore expected that a plentiful supply of oil would be available and full film lubrication is the most likely lubrication condition.

Once the instantaneous friction forces were known, the frictional power loss could easily be obtained. By integrating these losses w.r.t. cam angle over one complete cycle and dividing the result by 2π, the average power loss over a cycle could be found.

3.3.2.2 Valve/Guide Interface Friction

Although the friction force between the valve stem and its guide is small, it has been included to form a complete model.

As the friction on the top of the valve stem is expected to be very small, this can cause little tilting of the stem. The valve stem was thus considered to be concentric within its guide. The valve/guide friction, due to the viscous shear of the lubricant between the moving part and its guide, can be estimated in a similar way to that for the follower/guide

friction calculation (see Figure 3.7(b)).

3.4 Conclusions

It has been shown that the kinematic analysis of a tapered cam and domed follower system can be evaluated using standard differential geometry. The load evaluation, Hertzian stress calculation for a concentrated contact, EHL thin film prediction and the friction force and the power loss approximations have also been outlined.

The derivation excludes the tappet rotation effect which has some influence on the cam/follower performance. The effect of this rotation on the present model will be discussed in the following chapter.

An analytical basis of the Ford 1.8L H.O. Zeta camshaft bearing performance, follower/guide and valve/guide interface frictions has been described. The evaluation of bearing loads for each of the five bearings has been detailed and a dynamically loaded journal bearing lubrication analysis can then be undertaken. Bearing frictional power loss was predicted using a complete film shearing approximation. The follower/guide and valve/guide interface frictions have also been modelled.

Chapter Four

Computer Programs and Results for an Engine Valve Train

4.1 Introduction

The complicated interactions of design parameters upon each other and upon the tribological behaviour of the valve train often make the designer feel the necessity for a design aid which would reveal the overall performance of the mechanism. Computer-aided analysis is commonly accepted as an effective and efficient tool in optimizing many design features of engineering components (the engine valve train, for example) in the modern world.

Based on the theories stated in the previous chapter, a computer program has been developed and coded in a structured manner on an Amdahl mainframe computer. The software, which is an extension of the work of Ball [1988], is capable of analysing the kinematics and tribological performance of a cam and flat faced follower mechanism and a tapered cam and domed follower system. The Ford 1.8L H.O. Zeta engine valve train has been analysed as a study case. The camshaft bearing performance (loading, film thickness, friction and power loss), the follower/guide friction and the valve/guide friction have also been determined. Parametric studies for the Zeta cam and follower behaviour have been carried out

4.2 A Description of the Program

A simplified flow chart for the computer program developed is shown in Figure 4.1. It comprises four main parts: the cam and follower lubrication analysis, camshaft bearing performance study, follower/guide and valve/guide friction modelling and a parametric study of a given design of the cam/follower.

All input data is read via an input file which is edited as a standard data file. The file is designed to be as simple as possible with the user being led through the file being asked to respond to prompts for data. The data is then processed into a form suitable for later use. All of the data is introduced to the program in SI units unless requested otherwise. The valve lift and its first and second derivatives w.r.t. time (it is convenient to represent time by cam angle) are required for the kinematic analysis. The lift data may be input as discrete data points, as a four-power polynomial or as multi-polynomials. Lift data given by discrete data points is numerically differentiated w.r.t. cam angle to obtain the derivatives. This was done using a central difference formula. Lift data described in polynomial forms is evaluated at a requested number of points. Their derivatives w.r.t. cam angle were given by polynomials obtained by differentiating the original polynomials.

The program can deal with both a cam and flat faced follower system and a tapered cam and domed follower system, depending on the appropriate valve train type selected when running the software.

The tribological performance study requires the surface velocities of the cam and follower w.r.t. the point of contact and the equivalent radius of curvature to be evaluated. These kinematic parameters, along with the load at the cam/follower contact, are calculated using the theory which has been detailed. The program enables calculations to be

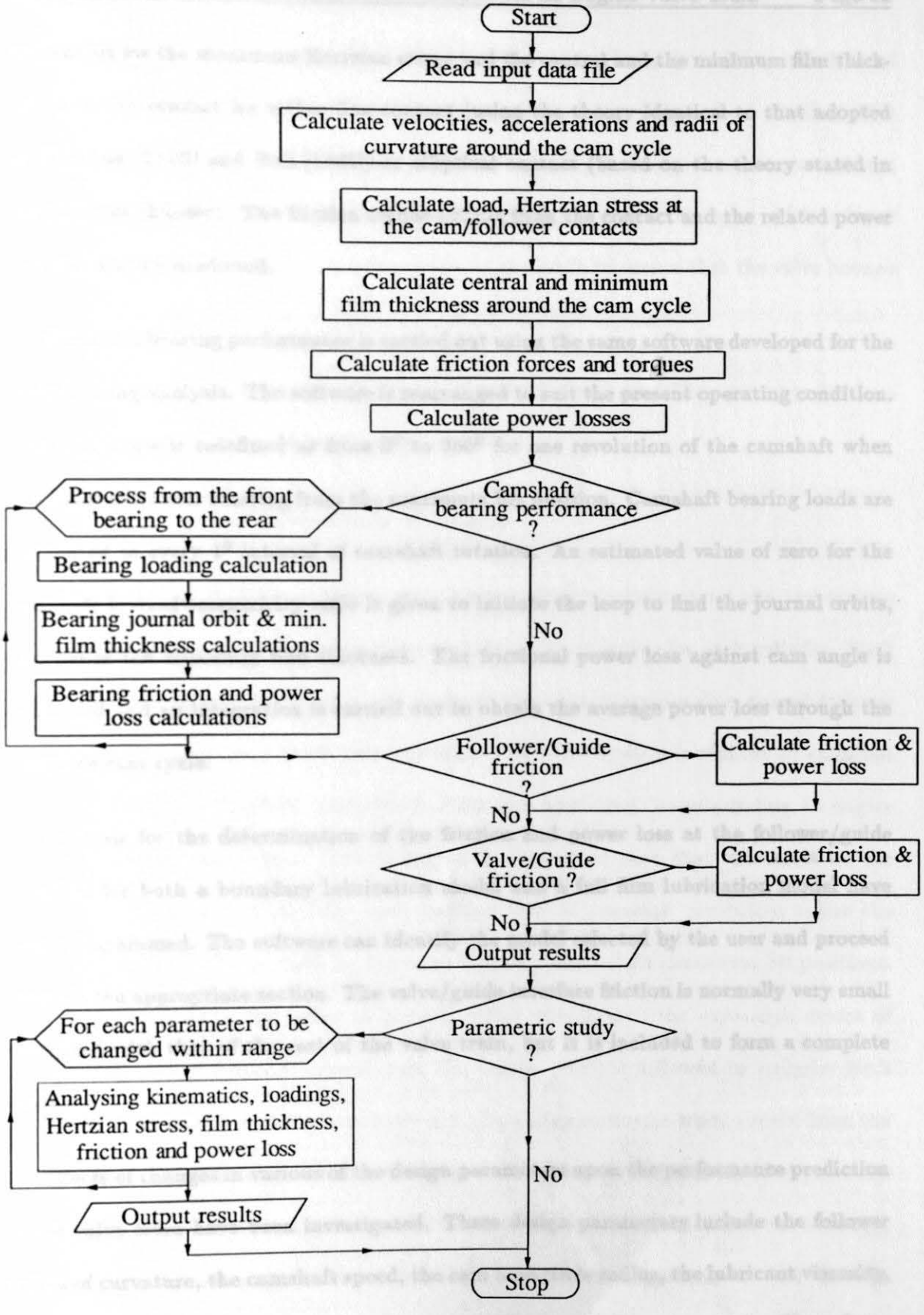

Figure 4.1. A Simplified Program Flow Chart for Valve Train Lubrication Analysis

carried out for the maximum Hertzian stress and the central and the minimum film thicknesses at the contact for either line contact (using the theory identical to that adopted by Harrison [1985] and Ball [1988]) or elliptical contact (based on the theory stated in the previous chapter). The friction torque arising from the contact and the related power loss can also be predicted.

Camshaft bearing performance is carried out using the same software developed for the main bearing analysis. The software is rearranged to suit the present operating condition. The cam angle is redefined as from 0^0 to 360^0 for one revolution of the camshaft when it rotates clockwise starting from the maximum lift position. Camshaft bearing loads are calculated at every 1^0 interval of camshaft rotation. An estimated value of zero for the camshaft journal eccentricity ratio is given to initiate the loop to find the journal orbits, and hence the minimum film thickness. The frictional power loss against cam angle is estimated and an integration is carried out to obtain the average power loss through the complete cam cycle.

Analysis for the determination of the friction and power loss at the follower/guide interface for both a boundary lubrication model and a full film lubrication model have been programmed. The software can identify the model selected by the user and proceed through the appropriate section. The valve/guide interface friction is normally very small compared with that of the rest of the valve train, but it is included to form a complete model.

Effects of changes in various of the design parameters upon the performance prediction of the valve train have been investigated. These design parameters include the follower radius of curvature, the camshaft speed, the cam base circle radius, the lubricant viscosity, the equivalent mass at the valve, the spring stiffness and the cam width. The effects

of changes in these parameters upon the frictional power loss, the minimum lubricant film thickness and the maximum Hertzian stress at the contact have been studied. The software stores the original values of the parameters to be changed and the associated results, then processes the parameter selected within the range of changes which is input before the study. During the calculations checks are made to ensure that the valve bounce and the minimum radius of curvature limitations are not violated.

The output is available in both graphical and tabular form. They are arranged in a concise and clear manner to be easily understood.

4.3 Zeta Engine Valve Train Analysis

The Ford 1.8L H.O. Zeta engine valve train system has twin camshafts and sixteen controlling valves with two intake valves and two exhaust valves for each cylinder. Each cam has been tapered to a very small angle to meet the corresponding domed follower which also incorporates a valve lash adjuster. The valve train was studied at camshaft speeds of 1000, 1500, 2000, 2500, 3000, 3200 and 3500 rpm, corresponding to engine speeds of twice these values. The timing of the system is such that the valves on the intake camshaft are at their fully open position 246^0 of camshaft revolution before the valves on the exhaust camshaft for the same cylinder reach their maximum lift positions. The engine is fired in the order of 1-3-4-2, which means that the expansion stroke of cylinder No.1 (first cylinder viewed from the engine front) is followed by cylinder No.3 and so on. The engine and the camshafts are all rotating clockwise when viewed from the front. All the input data concerning the valve train system, which includes the geometry of the cams, followers, valves, guides and the partially grooved camshaft journal bearings, the operating conditions and the related data are listed in Appendix C. The thermal

analysis of the system is beyond the scope of the present work. Instead, an effective dynamic viscosity for the lubricant used was determined with a knowledge of the oil operating temperature provided by the Ford Motor Company Ltd.

4.3.1 Cam/Follower Performance

The results in this section are for a cam operating against a non-rotating follower. The influence of this limitation on cam/follower performance will be mentioned at the end of this section.

Figure 4.2 shows the cam operating characteristics at a camshaft speed of 1500 rpm for the intake cams; the exhaust cams which have a different profile can be studied in a very similar way. On the first sheet of Figure 4.2 is detailed the operating conditions under consideration together with the cyclic average frictional power loss. Five graphs detail the variation of specific data of interest to a designer as a function of the cam rotational angle. The second of the output sheets of Figure 4.2 was developed to give data to assist in the interpretation of the characteristics shown on the first sheet.

Figure 4.2(a) shows the instantaneous frictional power loss against cam angle. On the cam base circle (-180^0 to -75^0 and $+80^0$ to $+180^0$) the friction force and the radius at which the friction traction applied (equals to the sum of base circle radius and cam lift) are small and constant, hence the friction torque and power loss remain unchanged; Over the cam ramps (about -75^0 to -60^0 and $+60^0$ to $+80^0$) the increased friction is caused by the increase of load. The small crescent on this part of the curve is the effect of slightly increased film thickness due to the modest increases of both the entraining velocity and the equivalent radius of curvature. The cam flanks (-60^0 to -55^0 and $+55^0$ to $+60^0$) enjoy a high thickness of lubricant film and hence very low shear stress and low

Cam Base Radius (mm)	=	18.00
Maximum Valve Lift (mm)	=	9.30
Cam Width (mm)	=	11.00
Rotational Speed (rpm)	=	1500.0
Spring Stiffness (kN/m)	=	37.634
Initial Spring Disp. (mm)	=	5.6
Equiv. Mass At Valve (kg)	=	.118
Lubricant Viscosity (Ns/m^2)	=	.010
Press. Visc. Coeff. (/Pa)	=	22.0E-9
Youngs Mod. (Cam) (GPa)	=	170.0
Youngs Mod. (Foll.) (GPa)	=	204.0
Poissons Ratio (Cam)	=	.28
Poissons Ratio (Foll.)	=	.29
Frictional Power Loss (W)	=	39.68

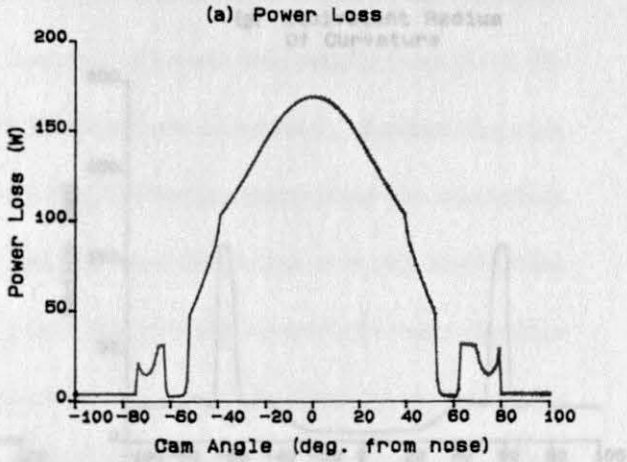

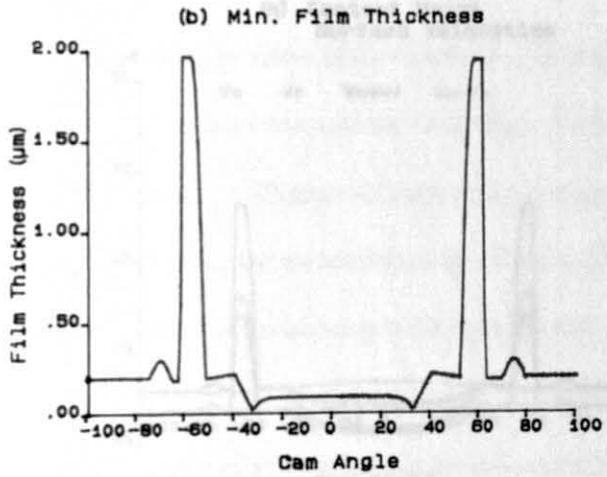

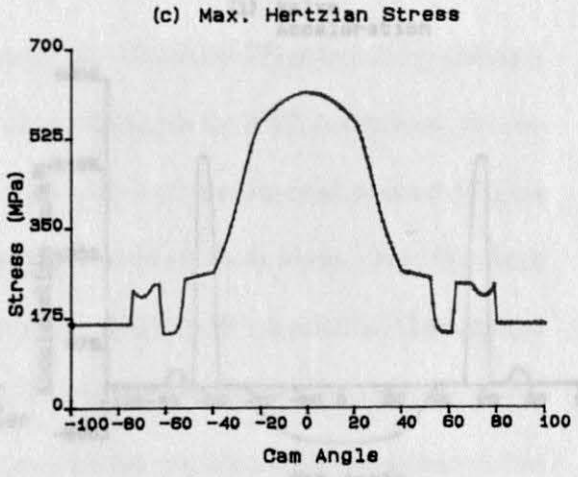

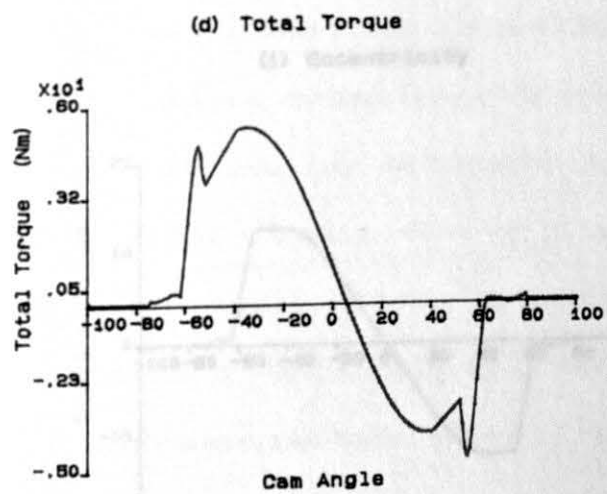

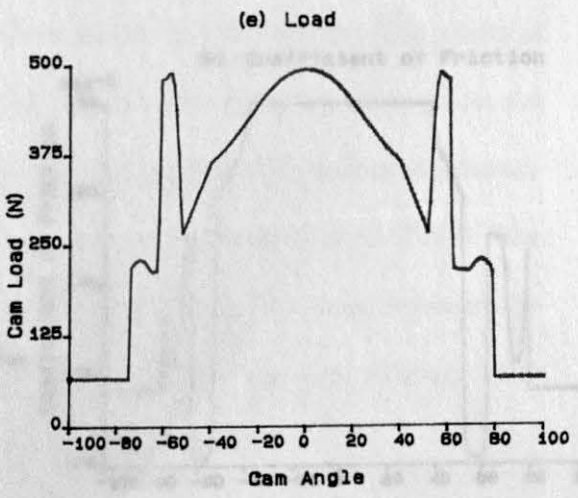

Figure 4.2. Ford Zeta Engine Intake Cam Operating Characteristics at 1500 rpm Camshaft Speed

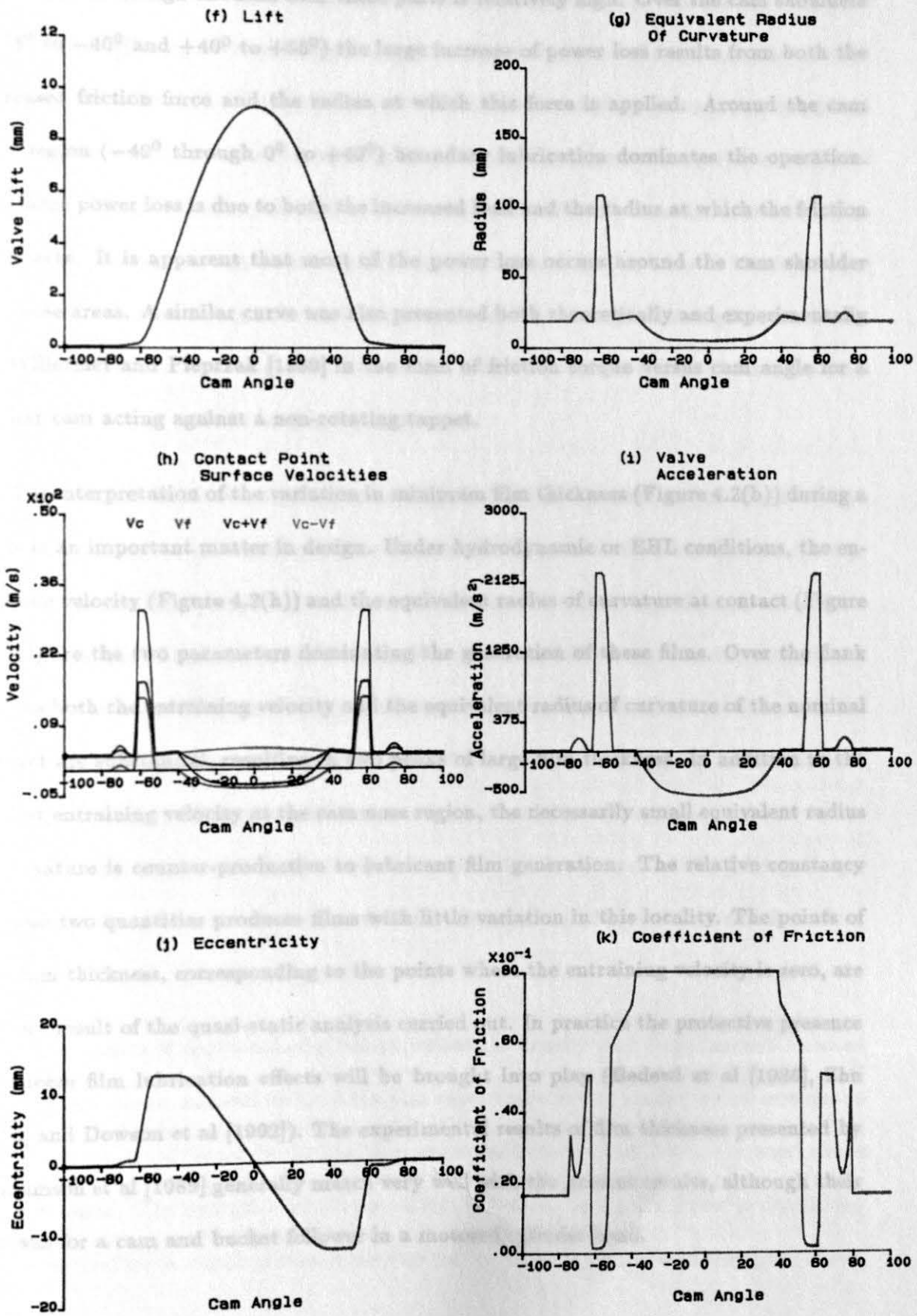

Figure 4.2 (Continued)

friction, even though the load over these parts is relatively high. Over the cam shoulders (-55^0 to -40^0 and $+40^0$ to $+55^0$) the large increase of power loss results from both the increased friction force and the radius at which this force is applied. Around the cam nose region (-40^0 through 0^0 to $+40^0$) boundary lubrication dominates the operation. The large power loss is due to both the increased load and the radius at which the friction force acts. It is apparent that most of the power loss occurs around the cam shoulder and nose areas. A similar curve was also presented both theoretically and experimentally by Willermet and Pieprzak [1989] in the form of friction torque versus cam angle for a similar cam acting against a non-rotating tappet.

The interpretation of the variation in minimum film thickness (Figure 4.2(b)) during a cycle is an important matter in design. Under hydrodynamic or EHL conditions, the entraining velocity (Figure 4.2(h)) and the equivalent radius of curvature at contact (Figure 4.2(g)) are the two parameters dominating the generation of these films. Over the flank regions both the entraining velocity and the equivalent radius of curvature of the nominal contact are substantial, resulting in two peaks of large film thickness. In addition to the modest entraining velocity at the cam nose region, the necessarily small equivalent radius of curvature is counter-productive to lubricant film generation. The relative constancy of these two quantities produces films with little variation in this locality. The points of zero film thickness, corresponding to the points where the entraining velocity is zero, are a direct result of the quasi-static analysis carried out. In practice the protective presence of squeeze film lubrication effects will be brought into play (Bedewi et al [1986], Zhu [1988] and Dowson et al [1992]). The experimental results of film thickness presented by Williamson et al [1989] generally match very well with the present results, although their test was for a cam and bucket follower in a motored cylinder head.

The maximum Hertzian stress (Figure 4.2(c)) is proportional to the load to the power of one third ($\frac{1}{3}$) and inversely proportional to the equivalent radius of curvature to the power of two thirds ($\frac{2}{3}$). The slight increase of the stress around the ramp region compared with that over the base circle is caused by the increase of load since the equivalent radius of curvature changes little in this region. The equivalent radius of curvature over cam flanks rises significantly, causing an increase in the contact area and a drop in the maximum Hertzian stress even though the load at this moment is quite high. The highest maximum Hertzian stress over cam nose area, due to the lowest equivalent radius of curvature, the small contact area and the large load, is evident.

The positive total torque (Figure 4.2(d)) during the upward side of the lift curve (negative values of cam angle) indicates that effort is required to rotate the cam. At approximately five degrees past the maximum lift point, the torque sign changes to negative (positive values of cam angle) indicating that the cam/follower system is putting work back into the drive. The two blips on the curve in the cam flank regions are caused by the sharp increase of load with the eccentricity (Figure 4.2(j)) reaching the maximum level at the same period. The shape of the curve is not strictly anti-symmetrical due to the presence of friction at the cam/follower interface. Similar shapes of the driving torque from empirical measurements can be found in Bair et al [1986] and Sun and Rosenberg [1987].

As the radius of curvature of a domed follower is usually very large (several hundred to several thousand millimetres) and the cam taper angle is very small (several minutes to several degrees), the forces due to the follower crowned surface and the cam tapered shape are very small. The contact load (Figure 4.2(e)) between cam and follower is dominated by the vertical force, which in turn is determined by the inertia force and the spring force.

The sharp rises of the load over cam flanks result from the large increase of the inertia force (due to the large acceleration in Figure 4.2(i)). The load around cam nose area is the combined action of the inertia and spring forces with the latter playing a main role at this camshaft speed. The general rule that the load is generated mainly from the spring rate at low speeds and mainly from the inertia at high speeds was demonstrated by Dyson and Naylor [1960] and Bair et al [1986] with experiments.

Figure 4.2(h) shows the contact point surface velocity variations against cam angle. As the cam always rotates in the same direction, the velocity of the point of contact w.r.t. cam surface, V_c, is always directed in the same sense, which is defined as positive here. Since the nominal contact point traverses across the follower surface the velocity of this point w.r.t. the face of the follower, V_f, is sometimes positive and sometimes negative. The entraining velocity, $V_c + V_f$, which is very important to the lubrication of the contact is certainly of interest to designers. The sliding velocity, $V_c - V_f$, which is directly related to friction generation, remains approximately constant through the cycle.

Figure 4.2(k) shows the cyclic variations of the coefficient of friction. The general similarity of the shape of the curve, compared with the calculated and experimental friction coefficient curves for a similar cam and non-rotating tappet system presented by Willermet and Pieprzak [1989], is encouraging.

An alternative presentation of cyclic film thickness and Hertzian stress variations around the cam periphery is shown in Figure 4.3. These graphs give clearer pictures of film thickness and Hertzian stress at specific locations on the cam surface. Although the film thickness peaks and the Hertzian stress valleys are brief in time span, an extensive portion of the rising and falling flanks of the cam enjoy the relatively enhanced oil film and reduced Hertzian stress. Correspondingly the lengthy time period over the nose

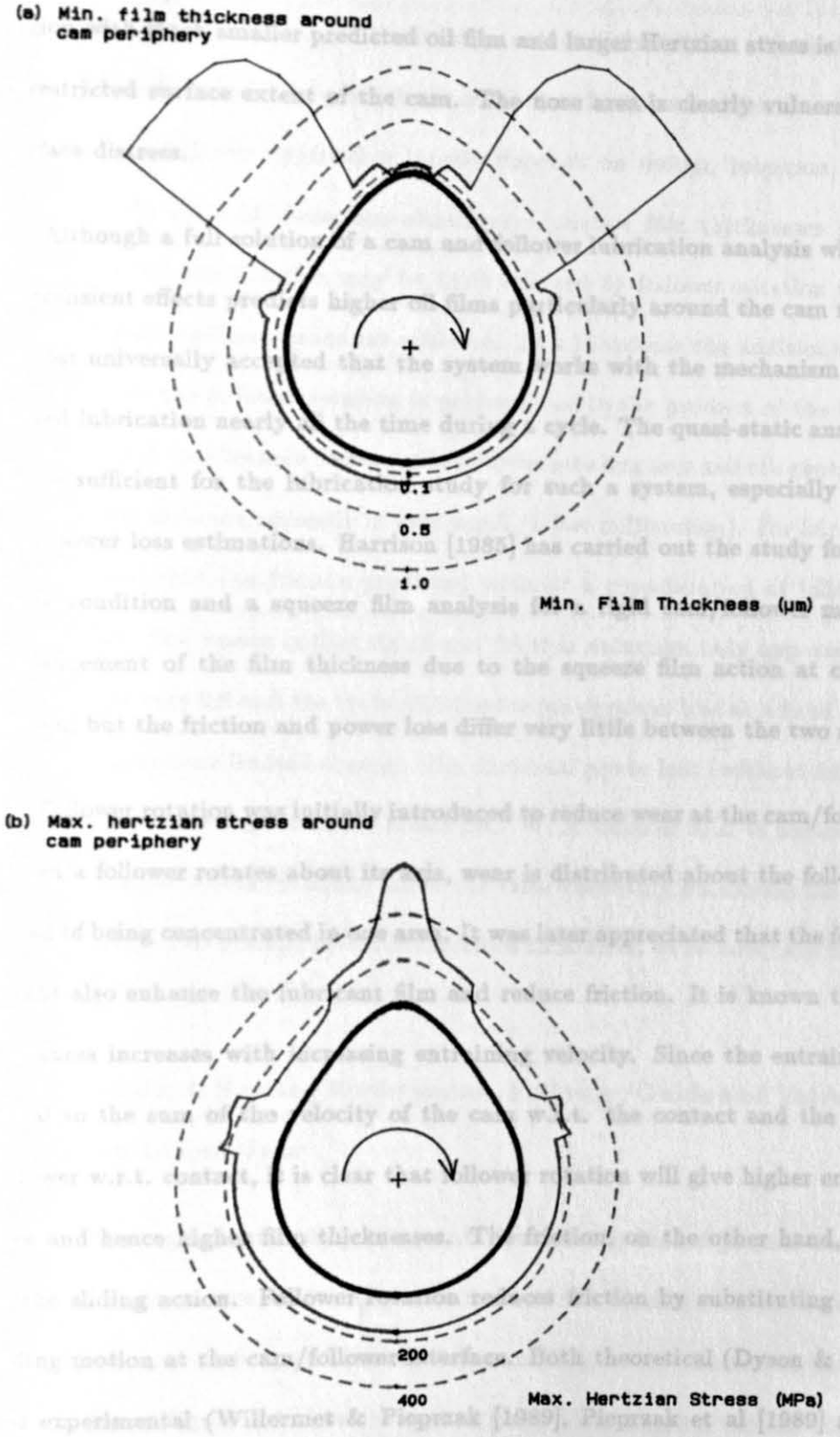

Figure 4.3. An Alternative Presentation of Film Thickness and Hertzian Stress Variation

region with much smaller predicted oil film and larger Hertzian stress is linked with only a restricted surface extent of the cam. The nose area is clearly vulnerable to potential surface distress.

Although a full solution of a cam and follower lubrication analysis with the inclusion of transient effects predicts higher oil films particularly around the cam nose region, it is almost universally accepted that the system works with the mechanism of boundary or mixed lubrication nearly all the time during a cycle. The quasi-static analysis is thought to be sufficient for the lubrication study for such a system, especially for the friction and power loss estimations. Harrison [1985] has carried out the study for both a steady state condition and a squeeze film analysis for a rigid cam/follower mechanism. The enhancement of the film thickness due to the squeeze film action at critical points is shown, but the friction and power loss differ very little between the two approaches.

Follower rotation was initially introduced to reduce wear at the cam/follower contacts. When a follower rotates about its axis, wear is distributed about the follower surface instead of being concentrated in one area. It was later appreciated that the follower rotation might also enhance the lubricant film and reduce friction. It is known that the oil film thickness increases with increasing entraining velocity. Since the entraining velocity is equal to the sum of the velocity of the cam w.r.t. the contact and the velocity of the follower w.r.t. contact, it is clear that follower rotation will give higher entraining velocities and hence higher film thicknesses. The friction, on the other hand, is mainly due to the sliding action. Follower rotation reduces friction by substituting a rolling for a sliding motion at the cam/follower interface. Both theoretical (Dyson & Naylor [1960]) and experimental (Willermet & Pieprzak [1989], Pieprzak et al [1989] and Willermet et al [1990]) work has suggested that the greatest follower rotation is in the region of

maximum cam lift, with a relatively large reduction in friction observed around this region. The difference in the predictions of oil film thickness and friction with rotating and non-rotating follower approaches largely depends on design, lubricant and operational variables. In spite of these, the elastohydrodynamic film thicknesses predicted in the absence of follower rotation may be little affected by follower rotation unless very high angular rotational frequencies are achieved. This is because the additional velocity, introduced due to the follower rotation is proportional to the product of the follower angular frequency and the distance between the follower rotating axis and the centre of the contact ellipse. This distance normally is very small (a few millimetres). For friction estimation, it is believed that the friction predicted without a consideration of follower rotation is satisfactory. The reason is that significant friction reduction only appeared in the region of maximum cam lift and the cyclic friction torque or power loss at a fixed camshaft speed will only experience limited change. The frictional power loss (without follower rotation) predicted here (see Figure 4.2) is about 39.7 W. A value of 37.6 W for exactly the same cam and follower (with rotation) under the same operating conditions has been obtained by Zhu [1991]. The present model is therefore considered to be adequate based on the above discussion.

4.3.2 Camshaft Bearing Performance, Follower/Guide and Valve/Guide Friction Estimations

The Zeta engine camshaft bearings are dynamically loaded journal bearings with oil grooves extending circumferentially over most of the bearing surface. The five bearings on the intake camshaft have been studied according to the theoretical basis detailed in Chapter One. Figure 4.4 shows a typical polar load diagram for the intake camshaft bearing No.3 at 1500 rpm camshaft speed. It can be seen that the load is directed along

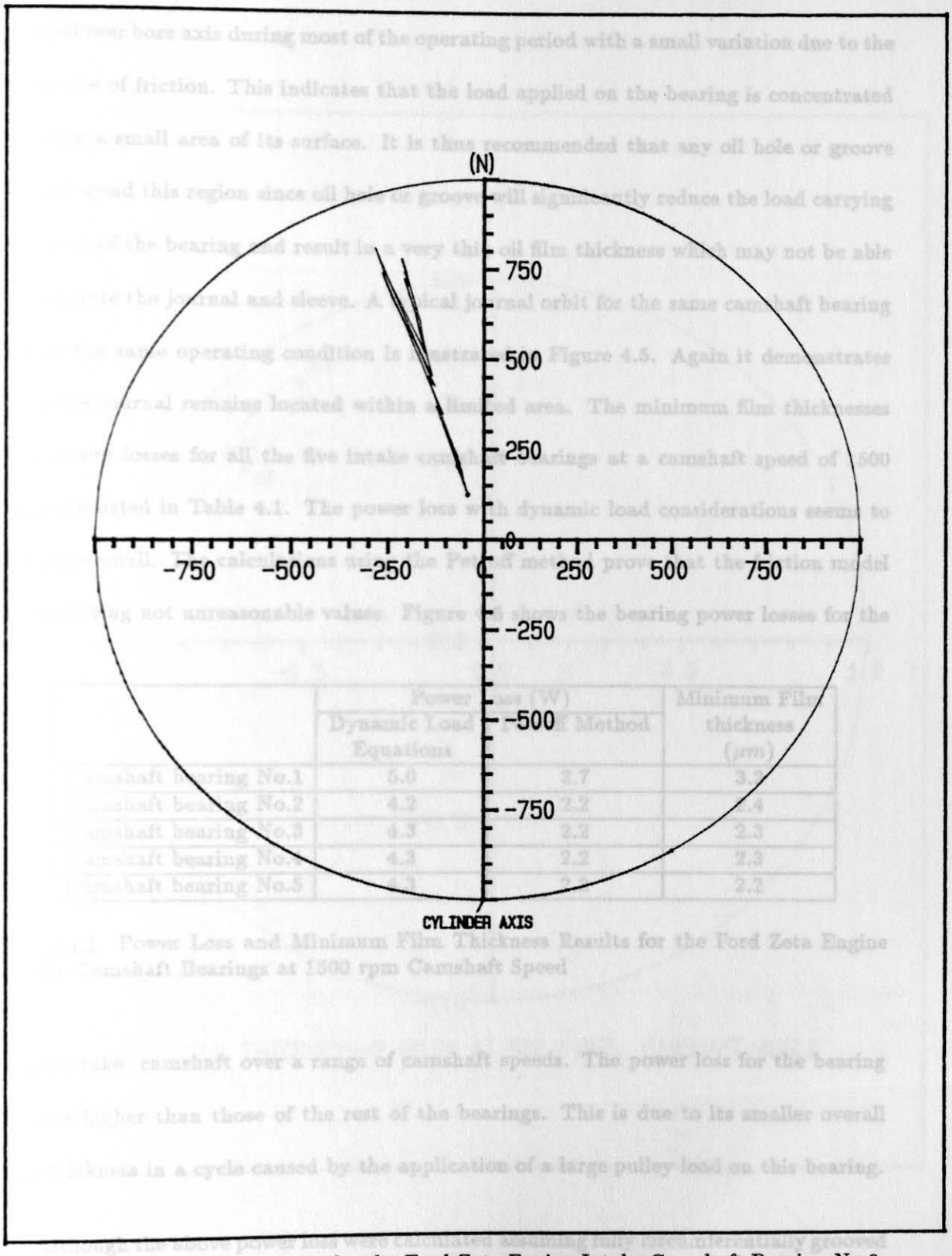

Figure 4.4. Polar Load Diagram for the Ford Zeta Engine Intake Camshaft Bearing No.3 at 1500 rpm Camshaft Speed

the follower bore axis during most of the operating period with a small variation due to the existence of friction. This indicates that the load applied on the bearing is concentrated on only a small area of its surface. It is thus recommended that any oil hole or groove should avoid this region since oil hole or groove will significantly reduce the load carrying capacity of the bearing and result in a very thin oil film thickness which may not be able to separate the journal and sleeve. A typical journal orbit for the same camshaft bearing under the same operating condition is illustrated in Figure 4.5. Again it demonstrates that the journal remains located within a limited area. The minimum film thicknesses and power losses for all the five intake camshaft bearings at a camshaft speed of 1500 rpm are listed in Table 4.1. The power loss with dynamic load considerations seems to be quite small. The calculations using the Petroff method prove that the friction model is predicting not unreasonable values. Figure 4.6 shows the bearing power losses for the

	Power Loss (W)		Minimum Film thickness (μm)
	Dynamic Load Equations	Petroff Method	
Camshaft bearing No.1	5.0	2.7	3.2
Camshaft bearing No.2	4.2	2.2	2.4
Camshaft bearing No.3	4.3	2.2	2.3
Camshaft bearing No.4	4.3	2.2	2.3
Camshaft bearing No.5	4.3	2.2	2.2

Table 4.1. Power Loss and Minimum Film Thickness Results for the Ford Zeta Engine Intake Camshaft Bearings at 1500 rpm Camshaft Speed

same intake camshaft over a range of camshaft speeds. The power loss for the bearing No.1 is higher than those of the rest of the bearings. This is due to its smaller overall film thickness in a cycle caused by the application of a large pulley load on this bearing.

Although the above power loss were calculated assuming fully circumferentially grooved bearings with 2π oil film, it may still look quite low, compared with the cam/follower fric-

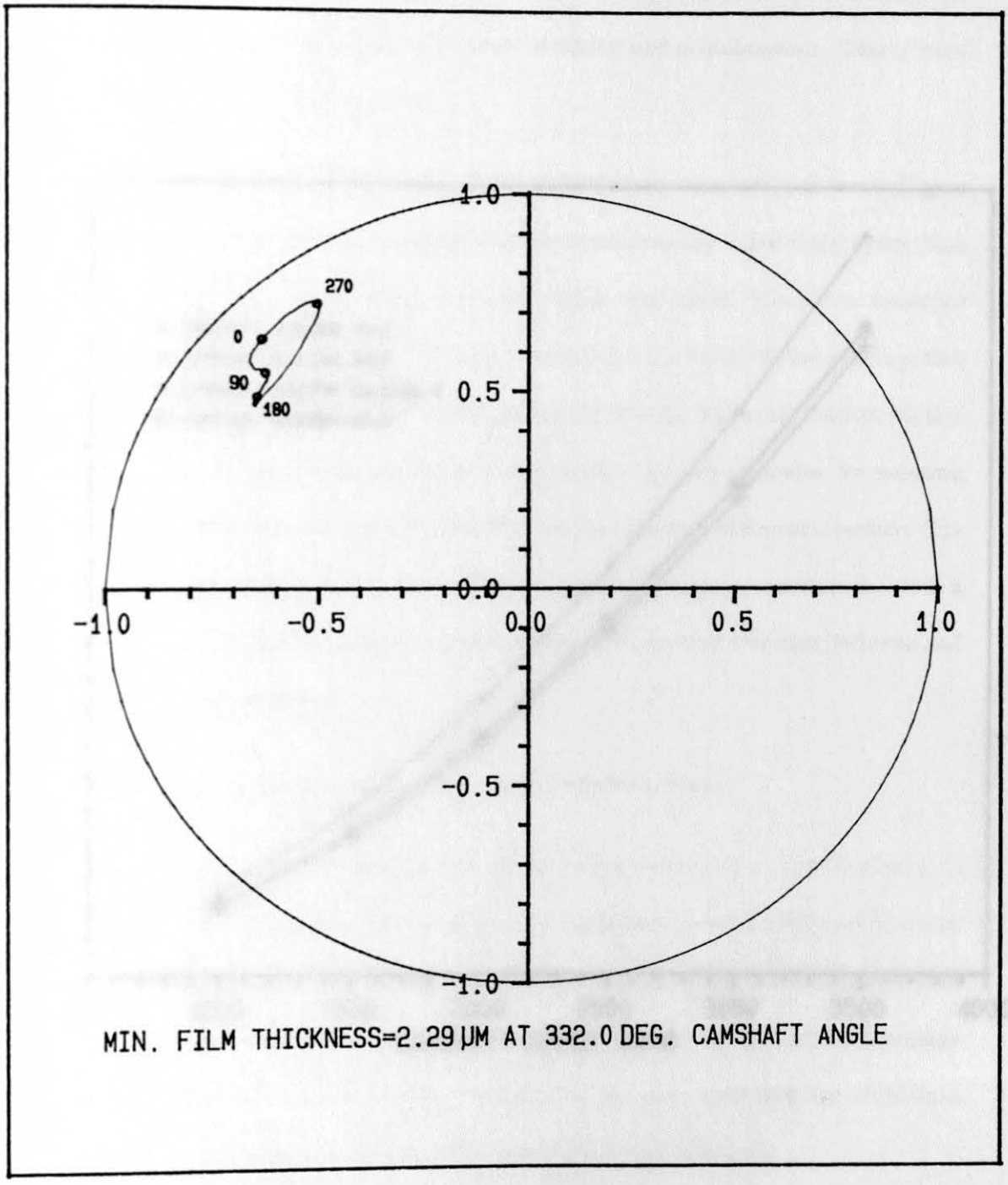

Figure 4.5. Bearing Journal Locus for the Ford Zeta Engine Intake Camshaft Bearing No.3 at 1500 rpm Camshaft Speed

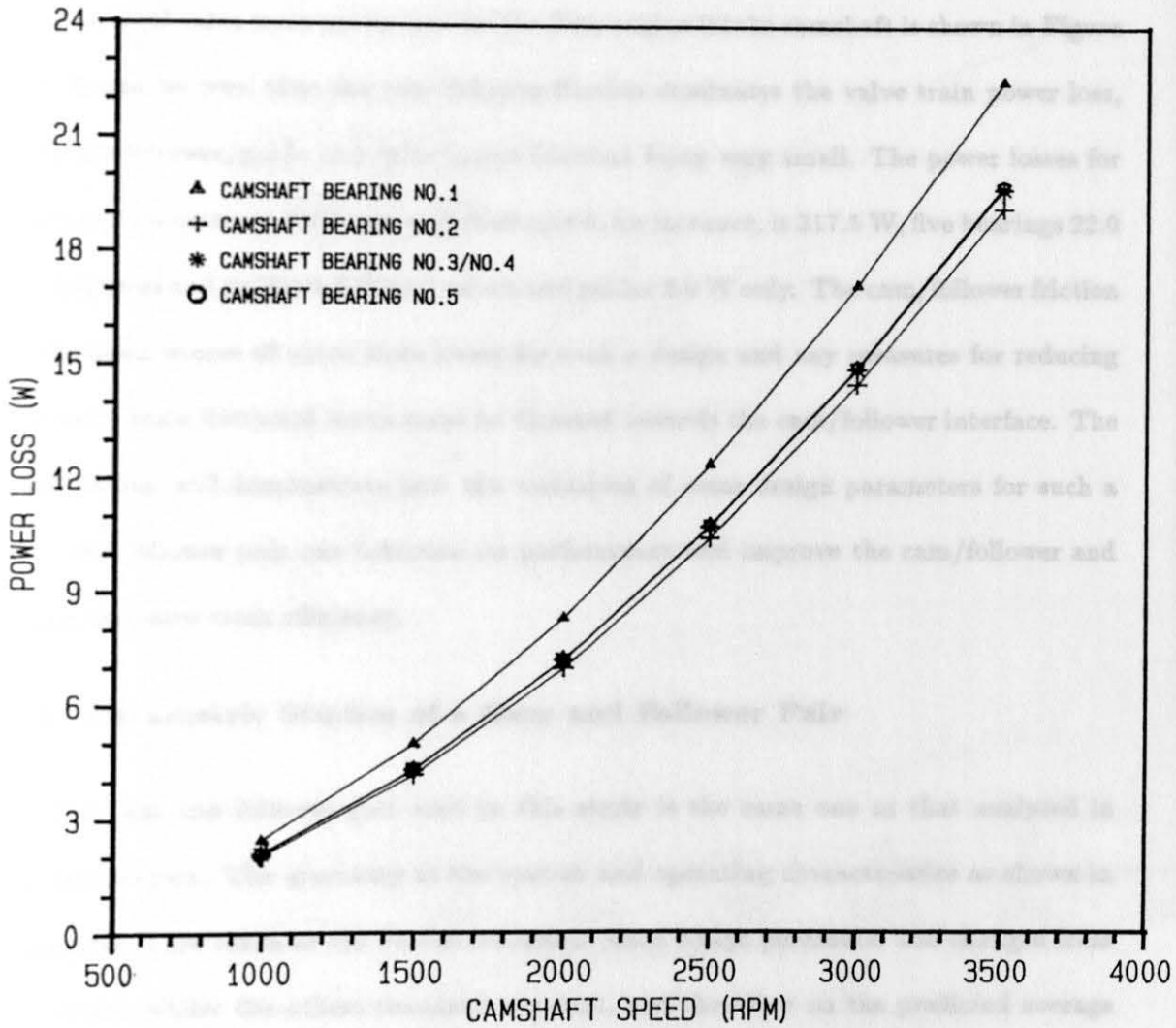

Figure 4.6. Intake Camshaft Bearing Power Losses for the Ford Zeta Engine

tional loss. As mentioned before, the present analysis excluded only thermal or elastic distortion effects which could influence the bearing behaviour significantly. In reality, the camshaft elastic distortion will definitely result in tilting and misalignment. This in turn will increase the bearing frictional loss.

The total valve train power loss for the Zeta engine intake camshaft is shown in Figure 4.7. It can be seen that the cam/follower friction dominates the valve train power loss, with the follower/guide and valve/guide frictions being very small. The power losses for cams and followers at 1500 rpm camshaft speed, for instance, is 317.5 W, five bearings 22.0 W, followers and guides 4.9 W and valves and guides 2.0 W only. The cam/follower friction is the main source of valve train losses for such a design and any measures for reducing the valve train frictional losses must be directed towards the cam/follower interface. The next section will demonstrate how the variations of some design parameters for such a cam and follower pair can influence its performance and improve the cam/follower and hence the valve train efficiency.

4.4 Parametric Studies of a Cam and Follower Pair

The cam and follower pair used in this study is the same one as that analysed in the last section. The geometry of the system and operating characteristics as shown in Appendix C are taken as the datum condition. Each design parameter was changed from its datum, whilst the others remained constant, and the effect on the predicted average frictional power loss, the minimum film thickness at the cam nose and the maximum Hertzian stress at the nose was studied. The parameters changed were:

(a) Radius of curvature of domed follower (R_f);

(b) Camshaft speed (ω_c);

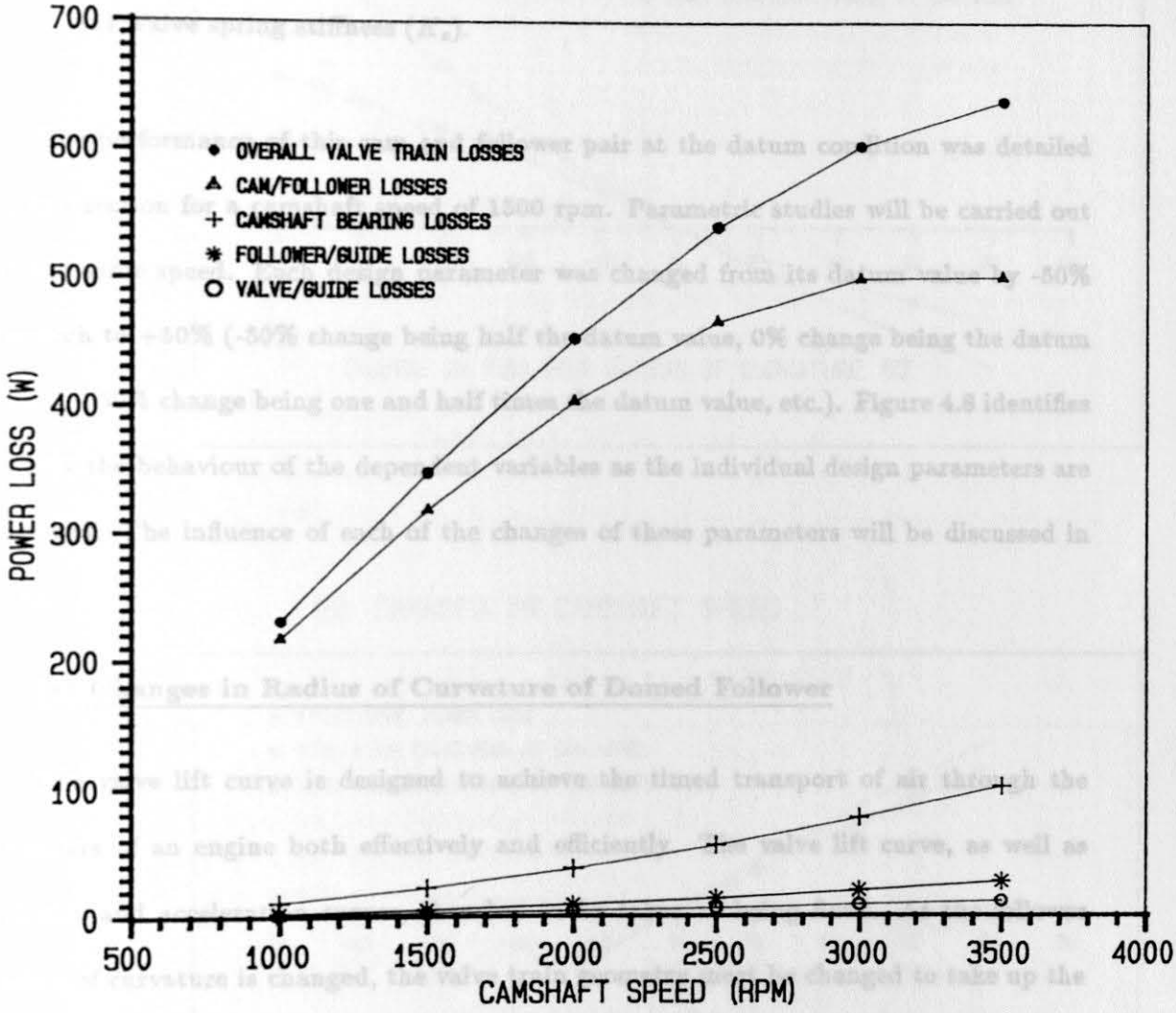

Figure 4.7. Power Losses in Intake Valve Train for the Ford Zeta Engine

(c) Cam base circle radius (R_b);

(d) Lubricant viscosity (η_0);

(e) Equivalent or reciprocating mass (M);

(f) Valve spring stiffness (K_s).

The performance of this cam and follower pair at the datum condition was detailed in last section for a camshaft speed of 1500 rpm. Parametric studies will be carried out at the same speed. Each design parameter was changed from its datum value by -50% through to +50% (-50% change being half the datum value, 0% change being the datum value, +50% change being one and half times the datum value, etc.). Figure 4.8 identifies clearly the behaviour of the dependent variables as the individual design parameters are changed. The influence of each of the changes of these parameters will be discussed in turn.

(a) Changes in Radius of Curvature of Domed Follower

The valve lift curve is designed to achieve the timed transport of air through the cylinders of an engine both effectively and efficiently. The valve lift curve, as well as velocity and acceleration curves, thus has to be taken as being fixed. As the follower radius of curvature is changed, the valve train geometry must be changed to take up the clearance between the cam and follower. This inevitably changes the cam profile and cam radius of curvature in order to maintain those fixed curves. When the follower radius of curvature is increased the cam nose will become narrower. When the follower radius of curvature is decreased the cam nose will become broader and the positions of the cam minimum radius of curvature tend to be displaced from the cam nose towards the flanks.

(A) CHANGES IN RADIUS OF CURVATURE OF DOMED FOLLOWER

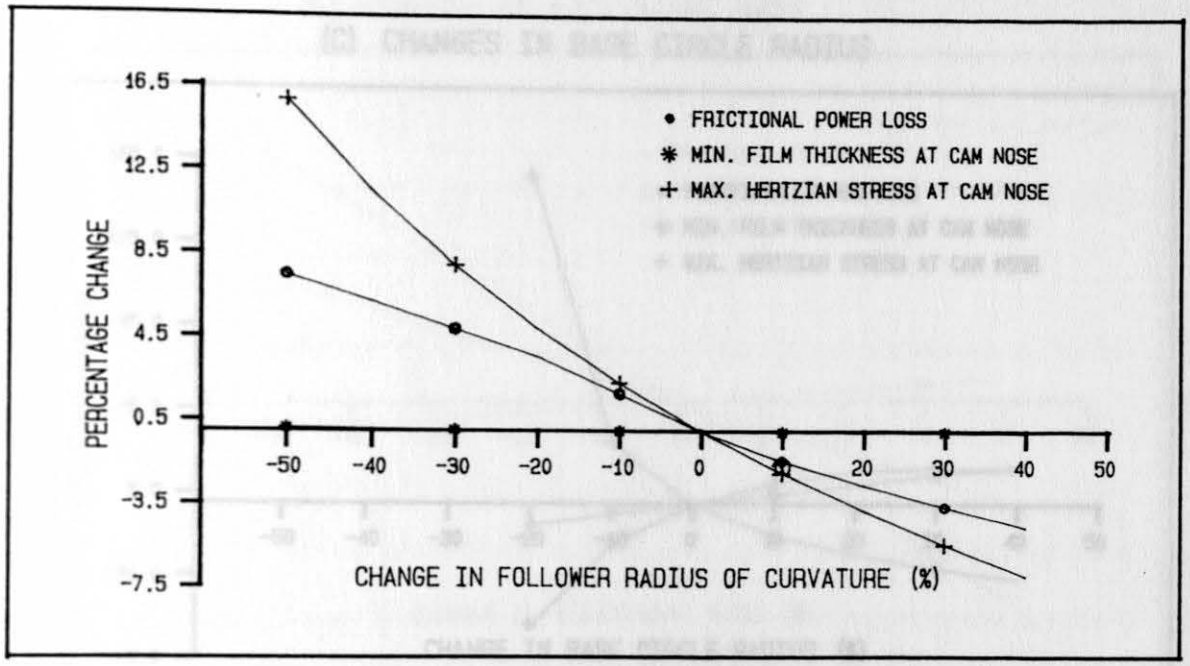

(B) CHANGES IN CAMSHAFT SPEED

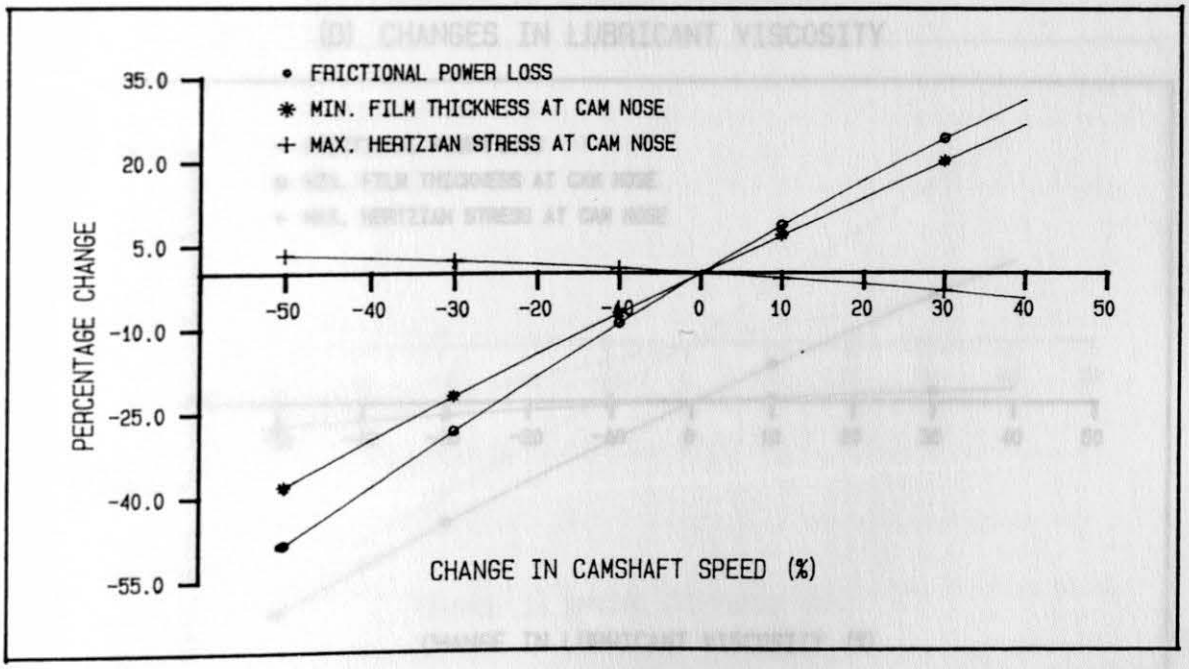

Figure 4.8. Parametric Study of the Cam/Follower Contact for the Ford Zeta Engine

(C) CHANGES IN BASE CIRCLE RADIUS

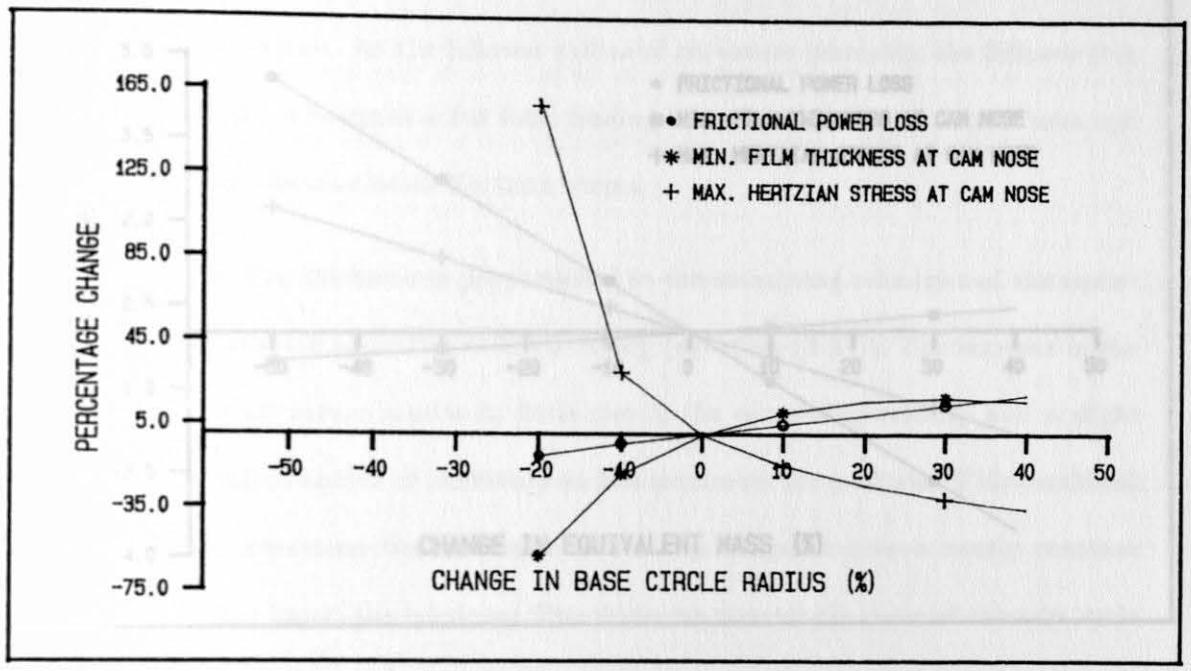

(D) CHANGES IN LUBRICANT VISCOSITY

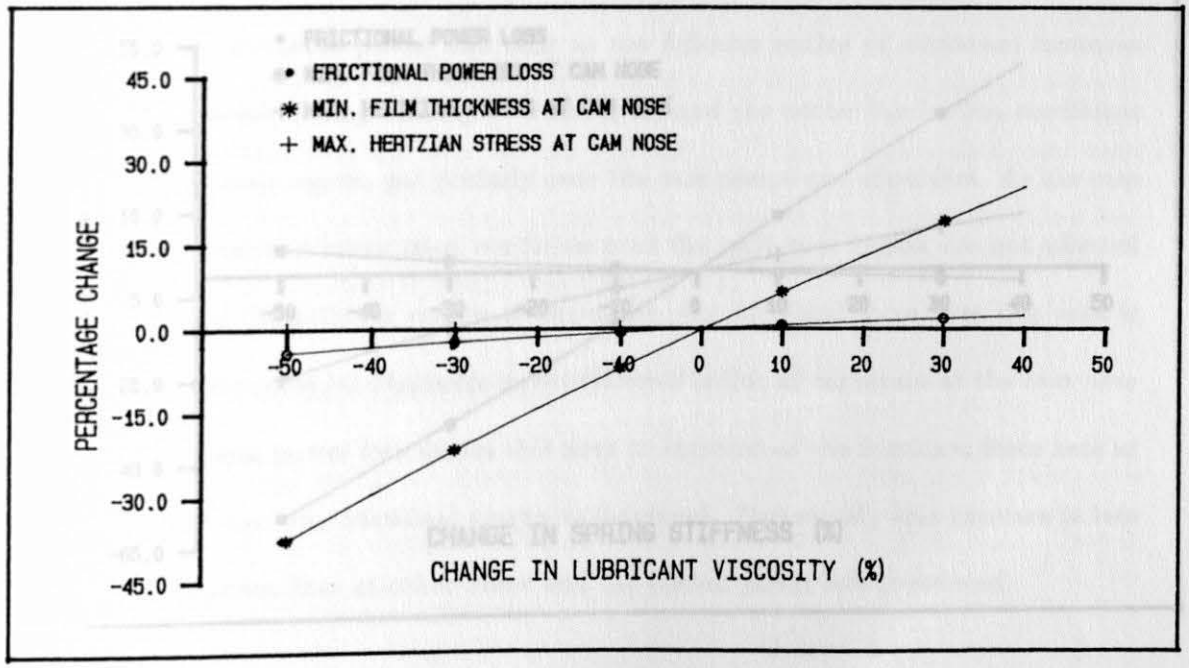

Figure 4.8 (Continued)

(E) CHANGES IN EQUIVALENT MASS

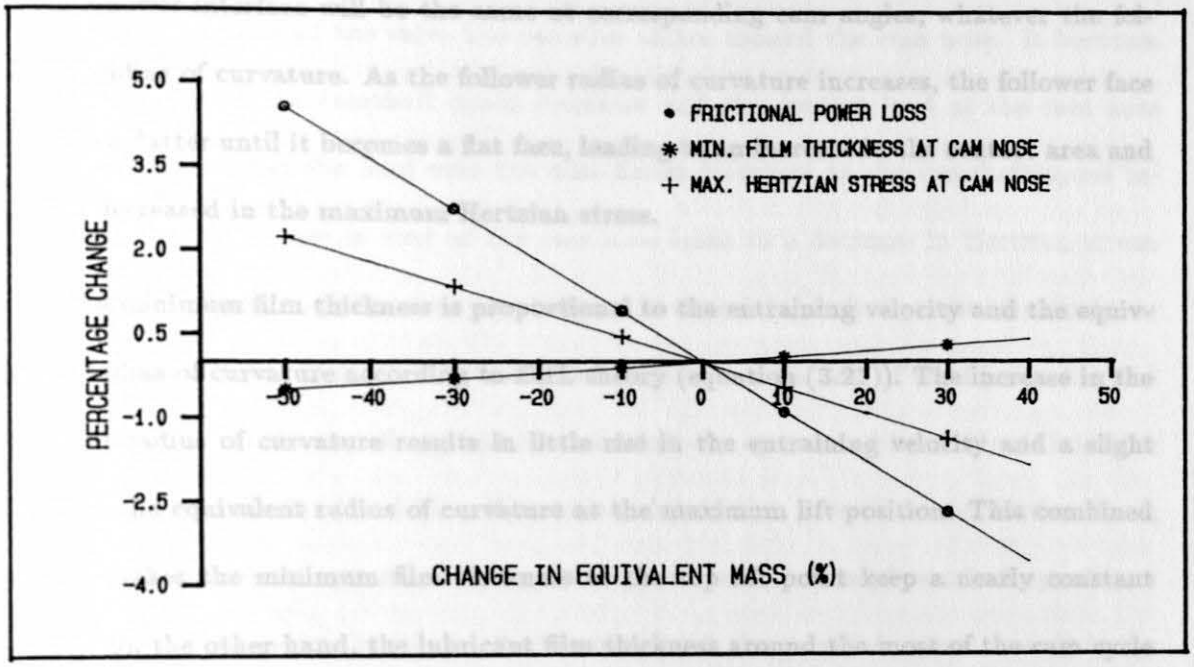

(F) CHANGES IN SPRING STIFFNESS

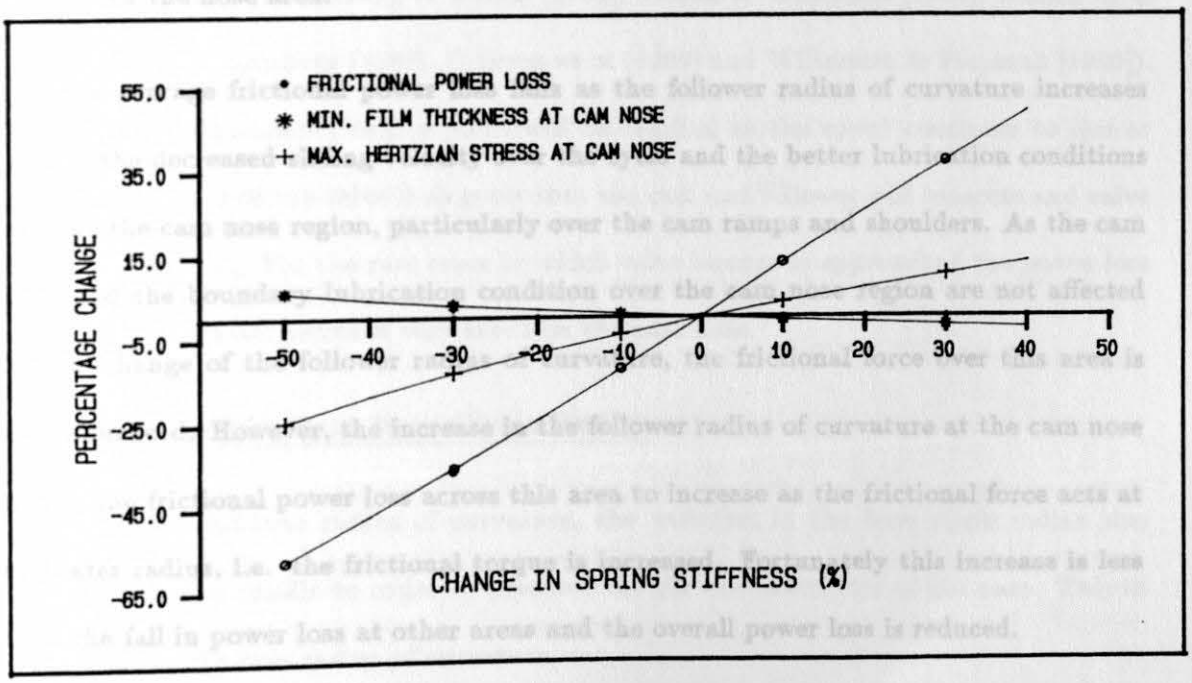

Figure 4.8 (Continued)

Since the lift, velocity and acceleration curves are fixed, the contact loading at the cam/follower interface will be the same at corresponding cam angles, whatever the follower radius of curvature. As the follower radius of curvature increases, the follower face becomes flatter until it becomes a flat face, leading to an increase in the contact area and hence decreased in the maximum Hertzian stress.

The minimum film thickness is proportional to the entraining velocity and the equivalent radius of curvature according to EHL theory (equation (3.21)). The increase in the follower radius of curvature results in little rise in the entraining velocity and a slight drop in the equivalent radius of curvature at the maximum lift position. This combined action makes the minimum film thickness at the top lift point keep a nearly constant value. On the other hand, the lubricant film thickness around the most of the cam cycle is improved as the follower radius of curvature increases. This is due to the enhanced entraining velocity and the equivalent radius of curvature over most parts of the cam, except for the nose area.

The average frictional power loss falls as the follower radius of curvature increases due to the decreased sliding velocity over the cycle and the better lubrication conditions outside the cam nose region, particularly over the cam ramps and shoulders. As the cam load and the boundary lubrication condition over the cam nose region are not affected by the change of the follower radius of curvature, the frictional force over this area is not influenced. However, the increase in the follower radius of curvature at the cam nose causes the frictional power loss across this area to increase as the frictional force acts at a greater radius, i.e. the frictional torque is increased. Fortunately this increase is less than the fall in power loss at other areas and the overall power loss is reduced.

(b) Changes in Camshaft Speed

The acceleration of the valve has negative values around the cam nose. It becomes more negative as the camshaft speed increases and the contact load at the cam nose decreases (note that the load over the cam flanks increases as the camshaft speed increases). This decrease in load at the cam nose leads to a decrease in Hertzian stress. This reduced load, together with an increase in entraining velocity, also results in an increase in lubricant film thickness and consequently a reduction of the friction force at the cam nose. On the cam flanks the cam and follower operate with full film lubrication and the increase in load had less effect on the lubrication as well as the friction force; the average friction torque usually drops slowly with an increase of camshaft speed over a cam cycle. The power loss generally increases with the camshaft speed since it is the work done per unit time. Both the useful work and the frictional work are rising per unit time as the camshaft speed increases. This general conclusion is widely observed by many researchers (Armstrong & Buuck [1981], Staron & Willermet [1983], Helden et al [1985], Sun & Rosenberg [1987], Dowson et al [1989] and Willermet & Pieprzak [1989]). It should be emphasized that a point will be reached as the speed continues to rise at which the inertia of the valve is so great that the cam and follower will separate and valve bounce will occur. For the rare cases in which valve bounce is approached the power loss may fall as the load becomes very small on the cam nose.

(c) Changes in Cam Base Circle Radius

As for the follower radius of curvature, the variation in the base circle radius also changes the cam profile in order to preserve the lift characteristics of the cam. This in turn changes the cam radius of curvature.

When the base circle radius is increased from its reference value, the cam radius of curvature increases and so the velocity of the point of contact w.r.t. the cam surface, V_c, increases, which means the V_c curve 'moves upward' and so does the entraining velocity curve $V_c + V_f$ (see Figure 4.2(h)). This indicates that the magnitude of the entraining velocity around the cam nose falls at first, passes through a zero value and may rise later as the cam base circle radius increases through a wider range. Because the minimum film thickness is proportional to both the cam radius of curvature and the mean entraining velocity, a corresponding change in this film with the variation of the entraining velocity can be predicted. As the base circle radius is increased from its datum value, the film thickness at the cam nose increases first, and then falls down to zero, reflecting the base circle radius which gives zero entraining velocity at the nose, and may rise again since the entraining velocity begins to pick up. Figure 4.8(c) clearly shows the rising and falling trend of the film thickness at the cam nose region but the final rise is not shown due to the limited range of variation of the cam base circle radius.

The increase in the base circle radius causes an increase in the cam radius of curvature, the contact area between the cam and follower interface becomes larger and the maximum Hertzian stress at the cam nose decreases.

At the current operating condition boundary lubrication and hence the limiting coefficient of friction apply around the majority of the cam cycle. The loading at the contact does not change and so the friction force remains unchanged over most part of the cycle, but the radius at which the friction force is applied increases as the base circle radius increases, i.e. the friction torque is increased. In addition, the sliding velocity increases as the base circle radius increases. The frictional power loss is thus increased. If there is no restriction on the variation of the base circle radius, at some very large base circle

radius the enhanced entraining velocity may generate a sufficient film which may separate the cam and follower from asperity contact. Then a downward trend in power loss may appear due to the limiting coefficient of friction no longer being applied.

To attain the required lift and acceleration characteristics of the cam, the program used for the parametric studies searches for the minimum allowable value of the base circle radius which has been found at a decrease of just over 20% from the reference value. As the base circle radius is increased a point is reached at which the cam must be concave to maintain the lift characteristics. This is not permitted in the software which has been developed.

(d) Changes in Lubricant Viscosity

As would be expected the influence of lubricant viscosity on film thickness is substantial, particularly at the cam nose. The increase in viscosity has no effect on the Hertzian stress and only limited effect on the power loss. As can be seen in equation (3.22), the central film thickness, h_{cen}, is proportional to the lubricant viscosity to the power of 0.68. The friction force (equation (3.24)) is proportional to the viscosity to the power of 1.0 and inversely proportional to h_{cen}. The overall result is the friction force (hence the power loss) is proportional to the oil viscosity to the power of 0.32, which can only affect the power loss slightly.

(e) Changes in Equivalent Mass

Increasing the equivalent mass at the valve decreases the load at the cam nose but causes higher loads on the cam flank. As the load at the cam nose decreases with increasing equivalent mass, the lubricant film thickness will increase and the Hertzian stress will decrease (the opposite results over the cam flank). An increase in equivalent mass causes

a fall in the frictional power loss due to the reduced load around the cam nose which governs the cyclic power loss and the reduced proportion of boundary lubrication in which the limiting coefficient of friction is applied. With the rise of equivalent mass at higher camshaft speeds, the separation of the cam and follower and hence valve bounce may tend to occur and this must be avoided.

(f) Changes in Spring Stiffness

As the spring stiffness is increased the loading at the cam/follower interface increases and so the Hertzian stress at the cam nose increases. The increase in load also moderately reduces the lubricant film thickness. As shown in equation (3.21), h_{min} is only proportional to load to the power of -0.073. Thus the changes in h_{min} with the variation of load would not be expected to be large. The frictional power loss increases since h_{cen} (equation (3.22)) decreases and P_{max} (equation (3.24)) increases. With the increase in the spring stiffness the limiting coefficient of friction is applied throughout the majority of the cam cycle. The increase in power loss is therefore significant.

It thus seems that reducing valve spring stiffness is especially valuable as a means of increasing the oil film thickness and reducing both the Hertzian stress and the power loss. Again care must be taken that the spring is strong enough to overcome the inertia and prevent the separation of the cam and follower and valve bounce at the higher camshaft speeds.

The diagrams of Figure 4.8 illustrate clearly the performance of the cam and follower pair with variations of each individual design parameter. It should be emphasized that the observations on the variations of the minimum film thickness and the maximum Hertzian stress reflect the situation at the cam nose region, which is the critical area of the system.

The same conclusions may not be true at the less critical flank portions of the cam. Indeed, a contrary result has been observed when the equivalent mass was altered. The alteration of the camshaft speed on the cam/follower behaviour, for example, will also be different on the flanks.

The limitations of the present parametric study should be noted. It was carried out for EHL conditions, and each design parameter has been varied independently from its reference condition assuming the others remained constant (the exceptions are the follower radius of curvature and the cam base circle radius as neither of them can be investigated separately. The cam profile has to be changed whichever of them is altered). This may not be the case in practice. Increasing the valve spring stiffness, for instance, will result in an increased power loss, the temperature will rise and this in turn may cause the lubricant viscosity to fall. This means that the oil viscosity will no longer be constant. The other design parameters may also have similar or other interactions.

Finally, any design improvement in the cam and follower pair should not only meet the requirement of the valve train system but also the engine system as a whole. Apart from the lubrication aspect many other requirements must be considered at the same time, and normally a compromise has to be made. An increase in the cam base circle radius, for example, decreases the maximum Hertzian stress dramatically and increases the minimum film thickness at the cam nose for a selected range of the base circle radius variations (though the power loss is increased as well). However, space limitations may restrict the extent of such changes. The beneficial alterations of the equivalent mass and the valve spring stiffness may well generate valve bounce problems as mentioned before. The positive effects of parameter changes discussed above may cause wear problems (scuffing, pitting or polishing) which would definitely be the concern of a new design. Also from the

combustion point of view some of the parameter changes may not be desirable. All these requirements (and others, noise control for example), sometimes demand contradictory changes of the design parameters and have to be considered carefully. The ideal cam and follower pair normally should achieve the required lift characteristics with a minimum physical size whilst keeping friction and detrimental wear to a minimum.

4.5 Conclusions

A valve train friction model has been developed and this will be useful as a guide in efforts to reduce friction.

A study of the lubrication of a tapered cam acting against a non-rotating domed follower has been reported. The study includes the determination of kinematics, loading and tribological conditions at the cam/follower interface. A cam and flat faced follower system is also included in the model. The results compare well with both the experimental and theoretical works published in the literature.

The performance of the Ford Zeta valve train camshaft bearings has been studied. The dynamic loadings of the bearings, journal loci and the friction have been analysed. Simple modelling of the follower/guide and the valve/guide friction has also been presented.

Parametric studies of the predicted behaviour of the tapered cam and the non-rotating follower pair have been carried out using the program developed. It has been found that improved performance and efficiency of the cam/follower pair are possible with modifications from the original design.

Part III

FRICTION MODELLING FOR AN ENGINE PISTON ASSEMBLY

Chapter Five

Theoretical Basis for an Engine Piston Assembly

5.1 Introduction

The piston assembly is widely recognized as the single largest contributor to engine friction and hence is an indispensable consideration in engine friction modelling. Piston assembly friction generally arises from three different sources: compression rings, oil control rings and piston skirts. Each of them plays a different role in the assembly.

The lubrication analysis of compression rings requires a knowledge of the loads acting on them, gas pressure loading being the principal source of the loading for these rings. Except for the measurement of the cyclic variation of combustion chamber pressure, the measurement of inter-ring gas pressures is not an easy task. A means by which the inter-ring gas pressures can be calculated is necessary. The first part of this chapter, therefore, presents the so-called orifice and volume theory to predict gas pressures between compression rings. This theory models the gas flow through a ring pack as that through a labyrinth seal and is now the accepted way of predicting inter-ring gas pressures.

The second part of this chapter is concerned with the hydrodynamic lubrication of a single ring, which is the essential element for the more realistic problem of the lubrication analysis of a complete ring pack. Assumptions are made concerning ring geometry, kinematics, loading and oil viscosity and the predictions of cyclic variation of film thickness, frictional force, power loss and lubricant transport are presented.

The procedures developed for a single ring are then extended and applied to the more complex problem of a complete ring pack in the third part of this chapter. The analysis of film thickness, friction and power loss and oil transport for each ring in the pack is essentially the same as that for a single ring. However, attention is focussed on the important role of flow continuity and lubricant starvation within a ring pack.

Finally, the oil control ring/cylinder liner friction and the piston skirt/cylinder liner friction are modelled using a simple boundary friction calculation and a viscous traction approximation, respectively.

The prediction of inter-ring gas pressures is based upon the work of Ruddy [1979], while the lubrication analysis of a single ring is dependent upon the study by Strachan [1973] and for the lubrication analysis of a complete ring pack on the analyses of both Economou [1976] and Ruddy [1979].

5.2 Prediction of Inter-ring Gas Pressures

The main function of a piston ring is to act as a seal to prevent leakage of the combustion chamber gases. It is difficult for a single ring to form a perfect seal and in most cases a pack of rings is used to share the pressure drop from the combustion chamber to the crankcase. In spite of this, some gas leakage may still be expected to occur. Practical considerations of a piston ring in its groove indicate that the gas may leak through the ring gap, between the ring face and the cylinder liner and between the ring flank and the ring groove. If a ring is working properly the existence of an oil film between it and the liner will prevent gas passing the ring face. Practical and experimental experience suggest that in most cases the gas pressure loading on the top flank of a ring is greater than that on the lower flank of the ring. This means that the ring is pushed onto the

lower flank of the ring groove during most of its working time and that little gas leakage will occur between the ring and its groove. The ring gap is then the primary opening for gas leakage. Although in reality this ideal condition does not always exist (axial movement of a ring, due to the unbalanced forces acting axially on it, may cause excessive gas leakage for example), it is universally accepted that ring gaps are of the most importance in determining the inter-ring gas pressures in most well-running engines.

The so-called orifice and volume model, which was first proposed by Eweis [1935] and widely utilized later (Ting & Mayer [1974], Ruddy [1979] and Kuo et al [1989]), is now the popular way of predicting inter-ring gas pressures. The model is based on the similarity of the gas flow through a ring pack to that through a labyrinth type of seal. Assuming that ring gaps are the only gas leakage paths, the ring pack may be represented by a system consisting of a series of volumes connected by square-edged orifices (Figure 5.1). The volumes represent the inter-ring spaces which are formed by two adjacent rings, the intervening piston land and the cylinder liner. The orifices are defined as equal in area to the effective leakage path formed by the ring gaps and the piston radial clearance. A ring pack consisting of any number of rings can be represented in this way. This orifice and volume method will be used as the basis for the present analysis and the two necessary equations of the flow rate through an orifice and the rate of change of pressure within a volume will be derived as follows.

The assumptions in the derivation of these equations are

(a) The gas satisfies the ideal gas law;

(b) The gas flow is unsteady and adiabatic;

(c) The flow is isentropic;

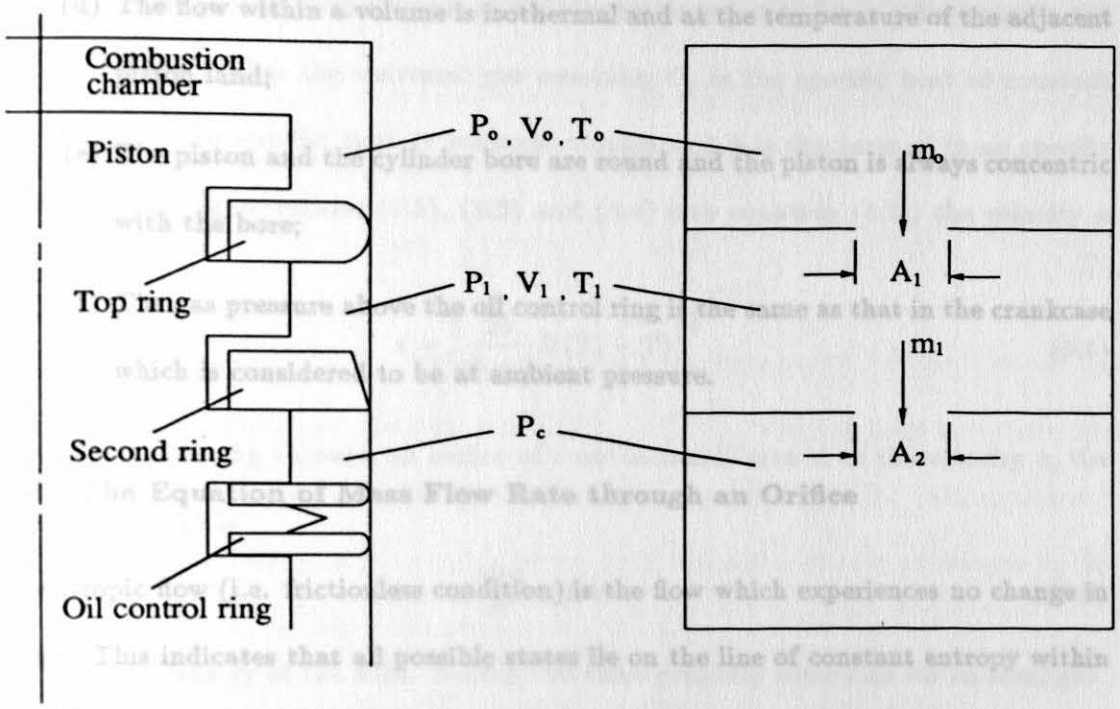

(a) Schematic Diagram of a Ring Pack and Corresponding Model

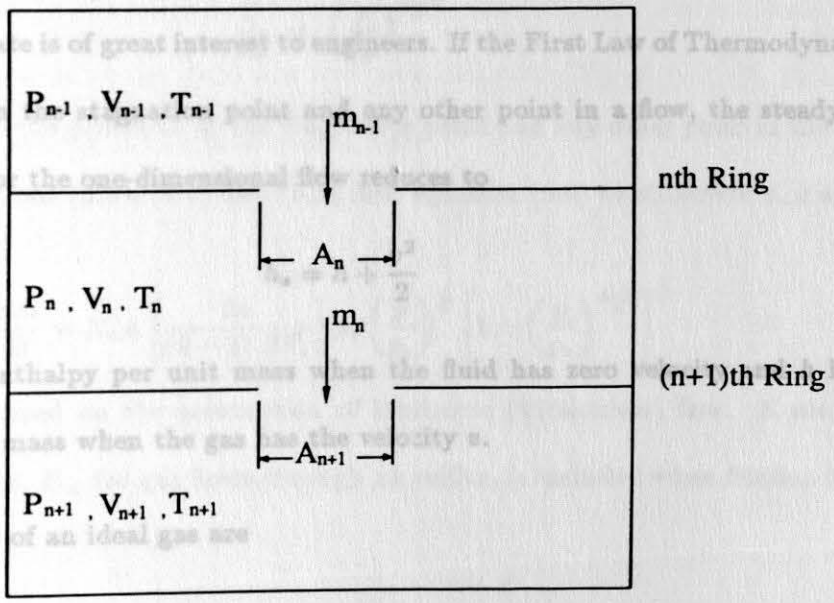

(b) Ring Pack Gas Flow Represented by Labyrinth Passage

Figure 5.1. Orifice and Volume Model for Inter-ring Gas Pressure Prediction

(d) The flow within a volume is isothermal and at the temperature of the adjacent piston land;

(e) The piston and the cylinder bore are round and the piston is always concentric with the bore;

(f) The gas pressure above the oil control ring is the same as that in the crankcase which is considered to be at ambient pressure.

5.2.1 The Equation of Mass Flow Rate through an Orifice

Isentropic flow (i.e. frictionless condition) is the flow which experiences no change in entropy. This indicates that all possible states lie on the line of constant entropy within which there is a special state called stagnation. Stagnation is defined as the state when a moving stream of fluid is brought to rest (i.e. velocity is zero) in an adiabatic process. The stagnation state is of great interest to engineers. If the First Law of Thermodynamics is applied between the stagnation point and any other point in a flow, the steady-flow energy equation for the one-dimensional flow reduces to

$$h_s = h + \frac{v^2}{2} \tag{5.1}$$

where h_s is the enthalpy per unit mass when the fluid has zero velocity and h is the enthalpy per unit mass when the gas has the velocity v.

The properties of an ideal gas are

$$h_s - h = C_p (T_s - T) \tag{5.2}$$

$$C_p - C_v = R \tag{5.3}$$

$$k = \frac{C_p}{C_v} \tag{5.4}$$

where T_s and T are the temperatures at the stagnation point and any other point in the flow, respectively. R is the universal gas constant, C_p is the specific heat at constant pressure, C_v is the specific heat at constant volume and k is the ratio of these specific heats. Introducing equations (5.2), (5.3) and (5.4) into equation (5.1), the velocity v becomes

$$v = \left[\frac{2k}{k-1}R(T_s - T)\right]^{\frac{1}{2}} \tag{5.5}$$

For a fluid passing through an orifice of cross-sectional area A at the velocity v, the mass flow rate $\frac{dm}{dt}$ is

$$\frac{dm}{dt} = \rho A v \tag{5.6}$$

where ρ is the density of the fluid. Noting two more property equations for an ideal gas

$$p = \rho RT \tag{5.7}$$

$$\frac{T}{T_s} = \left(\frac{p}{p_s}\right)^{\frac{k-1}{k}} \tag{5.8}$$

where p_s and p are the pressures at the stagnation point and any other point in the flow. Substituting equations (5.5), (5.7) and (5.8) into equation (5.6) to eliminate v, ρ and T yields

$$\frac{dm}{dt} = K_c A \left[\frac{2k}{(k-1)RT_s}\right] p_s \left(\frac{p}{p_s}\right)^{\frac{1}{k}} \left[1 - \left(\frac{p}{p_s}\right)^{\frac{k-1}{k}}\right]^{\frac{1}{2}} \tag{5.9}$$

This equation is based on the assumption of isentropic (frictionless) flow. A constant discharge coefficient, K_c, for gas flows through an orifice, is included when friction losses are considered.

5.2.2 Equation of the Rate of Change of Pressure within a Volume

Considering a volume V with some openings, the continuity equation can be written as (Namazian & Heywood [1982]):

$$\frac{m_i}{p_i}\frac{dp}{dt} = \left(\frac{dm}{dt}\right)_{in} - \left(\frac{dm}{dt}\right)_{out} \tag{5.10}$$

where m_i and p_i are the initial mass and pressure of the fluid in the volume respectively, $\frac{dp}{dt}$ is the rate of change of pressure and $\left(\frac{dm}{dt}\right)_{in}, \left(\frac{dm}{dt}\right)_{out}$ are the mass flow rate into and out of the volume respectively. For an ideal incompressible gas, the related property equations are $m_i = \rho_i V$ and $p_i = \rho_i RT$, where ρ_i is the initial density of the gas in the volume. Equation (5.10) can be rearranged as

$$\frac{dp}{dt} = \frac{RT}{V}\left[\left(\frac{dm}{dt}\right)_{in} - \left(\frac{dm}{dt}\right)_{out}\right] \tag{5.11}$$

Equations (5.9) and (5.11) are principal equations for inter-ring gas pressure predictions. For the general case of a ring pack gas flow determination (Figure 5.1(b)), these two equations may be written in non-dimensional form:

$$\frac{dM_{n-1}}{d\theta} = K\left(\frac{A_n}{A_1}\right)\left(\frac{P_{n-1}}{T_{n-1}^{\frac{1}{2}}}\right)\left(\frac{P_n}{P_{n-1}}\right)^{\frac{1}{k}}\left[1-\left(\frac{P_n}{P_{n-1}}\right)^{\frac{k-1}{k}}\right]^{\frac{1}{2}} \tag{5.12}$$

$$\frac{dP}{d\theta} = \overline{T}_n\left(\frac{V_1}{V_n}\right)\left(\frac{dM_{n-1}}{d\theta} - \frac{dM_n}{d\theta}\right) \tag{5.13}$$

where the non-dimensional parameters $P_n, \overline{T}_n$ and M_n are

$$P_n = \frac{p_n}{p_a}, \qquad \overline{T}_n = \frac{T_n}{T_0}, \qquad M_n = \frac{m_n}{M_0}$$

and the other variables are defined as

$$\theta = \omega t, \qquad m_0 = \frac{p_a V_1}{RT_0}, \qquad K = \frac{K_c A_1}{\omega V_1}\left(\frac{2kRT_0}{k-1}\right)^{\frac{1}{2}}$$

where p_a is the atmospheric pressure, θ is the crank angle, ω is the engine angular velocity and n refers to the ring number ($n = 0$ represents the combustion chamber).

If the flow velocity increases continually until it reaches the local speed of sound in the gas, the flow rate of the gas reaches its maximum value, since the cross-sectional area of the orifice is constant. The pressure ratio under this condition is called the critical pressure ratio. If k is assumed to be 1.3 throughout the present work and the K_c is taken to be 0.65 for a square-edged orifice, then the critical pressure ratio $\frac{p}{p_t} = 0.546$ (Ting & Mayer [1974]). If the pressure ratio across an orifice is less than this ratio, equation (5.12) can be simplified to

$$\frac{dM_{n-1}}{d\theta} = 0.227K\left(\frac{A_n}{A_1}\right)\left(\frac{P_{n-1}}{\overline{T}_{n-1}^{\frac{1}{2}}}\right) \tag{5.14}$$

Based on equations (5.12), (5.13) and (5.14), a computer program can be developed and the detailed procedures can be found in the next chapter.

5.3 Lubrication Analysis for a Single Ring

5.3.1 General Assumptions

It is assumed that a lubricating film separates the smooth surfaces of the ring and the cylinder liner at all times, so that the Reynolds equation is applicable throughout the the engine operational cycle. Both entraining and squeeze motions are considered as contributing factors to the hydrodynamic process. To solve the Reynolds equation for various crank angles by means of a direct iteration process, it is necessary to specify the shape of the ring face, the sliding speed, the cyclic variation of load and the lubricant viscosity to establish realistic cavitation boundary conditions.

5.3.1.1 Geometry

The general geometry for the lubrication analysis of a single ring is shown in cross-section in Figure 5.2. Surface roughness effects are not considered, i.e. the surfaces of the ring and the liner are assumed to be perfectly smooth for the present work. Circumferential curvature is neglected, this enables the problem to be reduced to two dimensions.

Practical measurements of the face profile of the ring after service exhibit a variety of worn rubbing profiles and some rings are even provided with a curved face during manufacture. On the other hand, the lubricating film between the ring and the liner behaves like a dynamically loaded slider bearing of axial length b and width equal to the circumference of the cylinder bore. It is well known from lubrication theory that the hydrodynamic performance of such a bearing relies more on the crown height and the effective bearing length than on the detailed shape of the profile. Finally, it can be seen that the effective radius of curvature of the ring face, R_r, is much larger than the axial ring height b. For these reasons, the ring face profile can be represented adequately by a parabola. The line of minimum film thickness, however, may be offset from the mid-plane of the ring by a distance which is called the ring face offset O. The offset is defined as positive if the line of minimum film thickness is displaced towards the combustion chamber. If the coordinates are selected as shown in Figure 5.2, then the shape of the ring can be defined as

$$h(x) = h_{min} + \frac{(x - x_{min})^2}{2R_r} \tag{5.15}$$

where $x_{min} = \frac{b}{2} - O$, is the x coordinate at the minimum film thickness point.

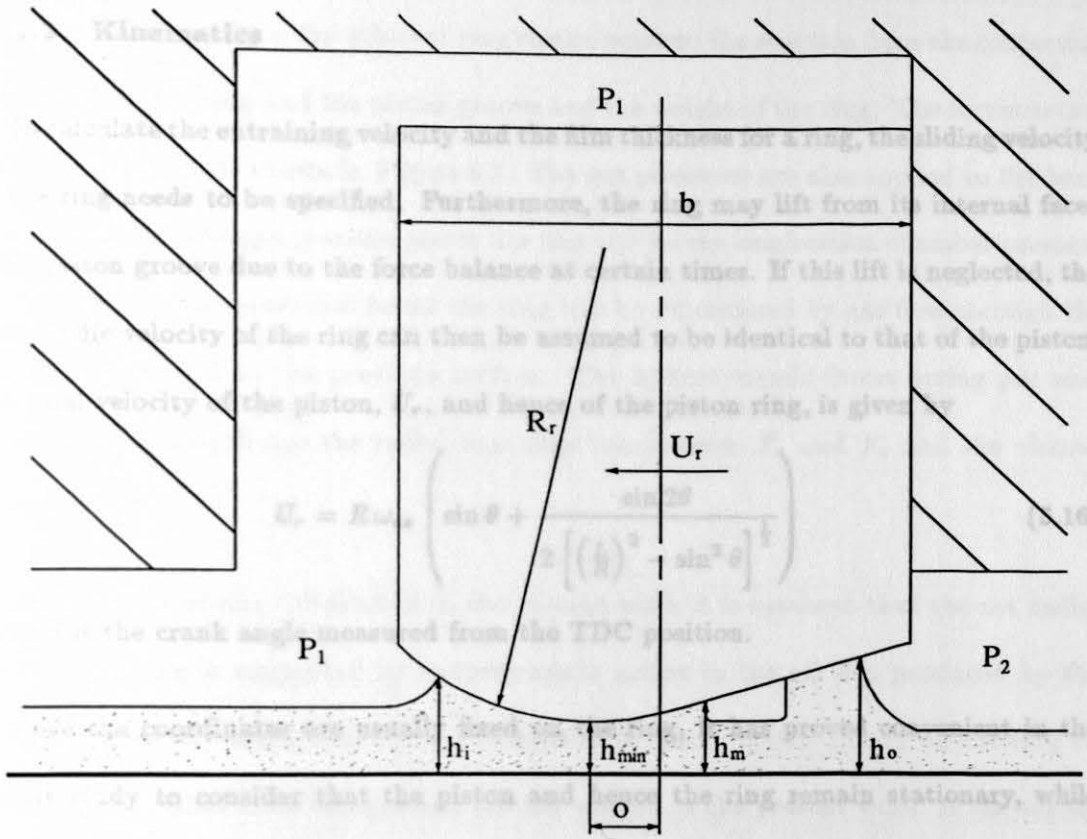

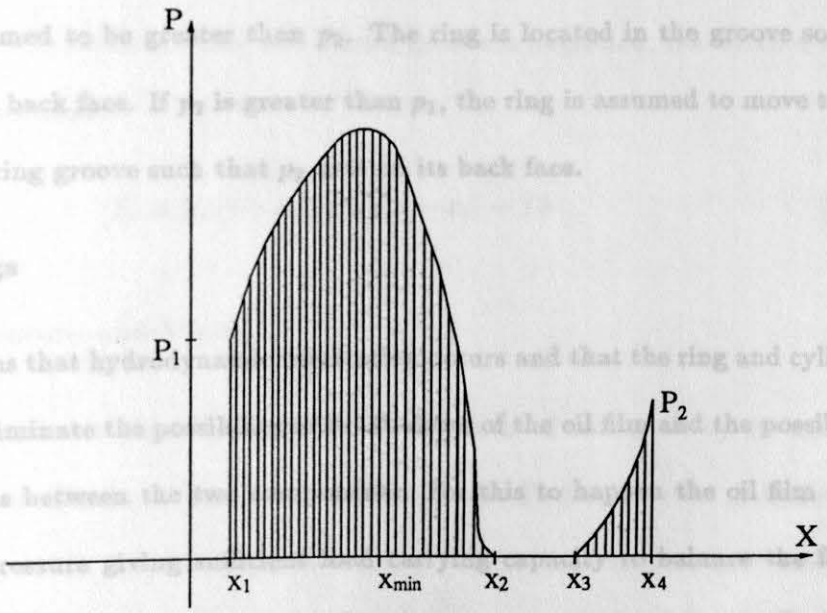

Figure 5.2. General Geometry for the Lubrication Analysis of a Piston Ring

5.3.1.2 Kinematics

To calculate the entraining velocity and the film thickness for a ring, the sliding velocity for the ring needs to be specified. Furthermore, the ring may lift from its internal faces of the piston groove due to the force balance at certain times. If this lift is neglected, the axial, cyclic velocity of the ring can then be assumed to be identical to that of the piston. The axial velocity of the piston, U_r, and hence of the piston ring, is given by

$$U_r = R\omega_{es}\left(\sin\theta + \frac{\sin 2\theta}{2\left[\left(\frac{L}{R}\right)^2 - \sin^2\theta\right]^{\frac{1}{2}}}\right) \tag{5.16}$$

where θ is the crank angle measured from the TDC position.

Since the coordinates are usually fixed on the ring, it has proved convenient in the present study to consider that the piston and hence the ring remain stationary, while the cylinder liner moves past the ring. The equivalent liner velocity, U_l, is then equal in magnitude, but opposite in direction, to the sliding velocity of the ring U_r. In Figure 5.2, pressure p_1 is assumed to be greater than p_2. The ring is located in the groove so that p_1 is applied on its back face. If p_2 is greater than p_1, the ring is assumed to move to the other flank of the ring groove such that p_2 acts on its back face.

5.3.1.3 Loadings

The assumptions that hydrodynamic lubrication occurs and that the ring and cylinder liner are smooth eliminate the possibility of break-down of the oil film and the possibility of asperity contacts between the two components. For this to happen the oil film must generate enough pressure giving sufficient load carrying capacity to balance the forces acting on the ring both axially and radially. The forces acting on the ring arise from gas pressures above (p_1), and below (p_2) the ring; the pressure (p) and the viscous traction

within the lubricant film; the inherent ring elastic tension; the reaction from the contacting flank between the ring and the piston groove and the weight of the ring. The forces acting radially on a ring are shown in Figure 5.3. The gas pressures are also applied to the back face of the ring. The gas pressure above the ring will be the combustion chamber pressure for the top ring and pressures below the ring will be determined by gas flow through the ring pack as stated in the previous section. The hydrodynamic forces acting per unit circumferential length are the radial and axial components F_z and F_x and the viscous traction force F_r.

In the study of ring lubrication in the present work it is assumed that the net radial force on the ring is supported by hydrodynamic action in the oil film produced by the combination of entraining and squeeze actions. The forces acting axially on the ring do not affect the radial force balance and are not needed in the present work. If the supply of lubricant is insufficient to fill the clearance space between the ring face and the liner, exposed lengths of the ring face will be subjected to gas pressures p_1 and p_2 respectively. If the radial friction between the ring and piston groove is neglected, the balance of the radial forces requires that

$$F_z = p_1 (b - x_1) - p_2 (b - x_4) + Tb \tag{5.17}$$

5.3.1.4 Temperature and Viscosity

The effective lubricant viscosity at each axial location of a ring along the cylinder liner is another essential item for ring lubrication analysis. To facilitate the analysis with adequate accuracy, some simplifications are made. Cross-film temperature variations within the lubricant film are neglected. Variation of viscosity across the ring face at each axial location is ignored and it is further assumed that the viscosity is not influenced by

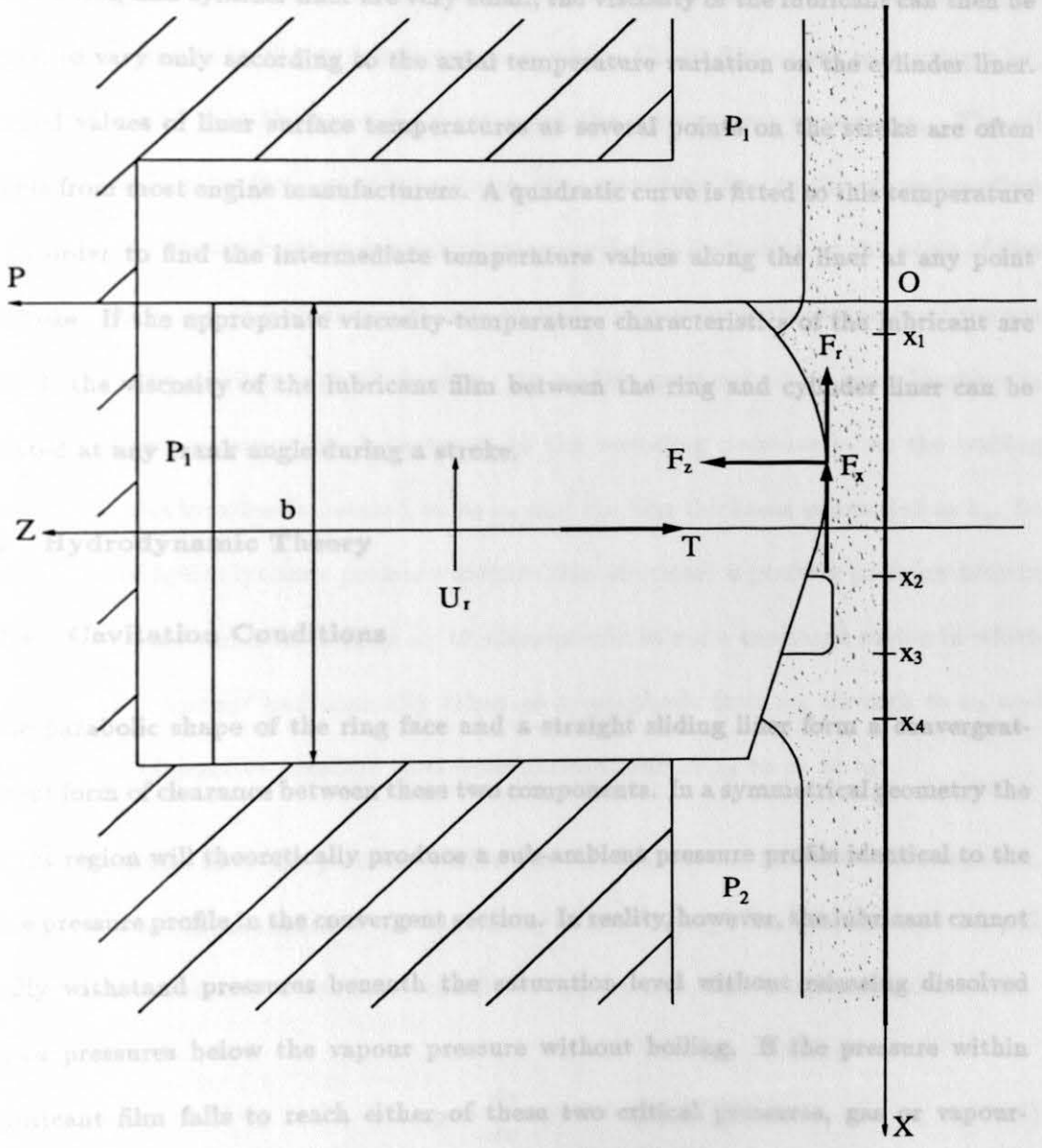

Figure 5.3. Hydrodynamic and Radial Forces Acting on a Piston Ring

pressure.

It is recognized that recording temperatures on a stationary liner is much easier than it is on the moving piston. It is also expected that since the values of film thicknesses between a ring and cylinder liner are very small, the viscosity of the lubricant can then be assumed to vary only according to the axial temperature variation on the cylinder liner. Measured values of liner surface temperatures at several points on the stroke are often available from most engine manufacturers. A quadratic curve is fitted to this temperature data in order to find the intermediate temperature values along the liner at any point in a stroke. If the appropriate viscosity-temperature characteristics of the lubricant are provided, the viscosity of the lubricant film between the ring and cylinder liner can be calculated at any crank angle during a stroke.

5.3.2 Hydrodynamic Theory

5.3.2.1 Cavitation Conditions

The parabolic shape of the ring face and a straight sliding liner form a convergent-divergent form of clearance between these two components. In a symmetrical geometry the divergent region will theoretically produce a sub-ambient pressure profile identical to the positive pressure profile in the convergent section. In reality, however, the lubricant cannot normally withstand pressures beneath the saturation level without releasing dissolved gases, or pressures below the vapour pressure without boiling. If the pressure within the lubricant film falls to reach either of these two critical pressures, gas or vapour-filled bubbles will be formed and cause the film to rupture in the phenomenon called cavitation. Experimental evidence of substantial sub-ambient pressures in the divergent region in the film lubricating a piston ring has been reported in the past (Brown &

Hamilton [1978]). The results in the present work, however, will refer to the conventional picture of cavitation in lubricating films.

Since the gas pressures above and below the ring are often above atmospheric, the hydrodynamic pressure within the oil film has to conform to the boundary conditions on pressure. So referring to Figure 5.2 the pressure within the oil film at the entraining inlet, at location x_1 and film thickness h_i, must equal the ambient gas pressure p_1. The oil pressure normally rises from p_1 at location x_1 to a maximum due to the oil wedge effect and then falls to atmospheric or saturation pressure due to cavitation at the point of film rupture x_2 where the film thickness is defined as h_m. Because of the presence of the gas pressure p_2 at the trailing edge of the ring, the oil film must reform at some location x_3 so that a positive pressure can be reached to the bounding pressure p_2 at the trailing outlet, where this location is deemed to be x_4 and the film thickness is denoted as h_o. So three regions of hydrodynamic pressure distribution are clear: a positive pressure zone in which the pressure varies from p_1 at x_1 to atmospheric at x_2; a cavitated region in which the pressure is constant and normally taken as atmospheric from x_2 through to x_3 and finally an area of positive pressure rises from atmospheric at x_3 to p_2 at x_4.

If it is assumed that the pressure within the oil film cannot fall below atmospheric, together with the consideration of the continuity of flow through the conjunction, the well known Reynolds cavitation boundary condition applies and can be expressed mathematically as

$$p = \frac{dp}{dx} = 0 \tag{5.18}$$

5.3.2.2 Reynolds Equation and Film Thickness

Reynolds equation is the governing equation for the pressure distribution in a fluid film bearing. It was derived under several assumptions, which are listed in Part I, for bearing lubrication analysis. If all the assumptions stated in this chapter are also considered, the Reynolds equation for the present application depicted in Figure 5.2 becomes

$$\frac{\partial}{\partial x}\left(h^3\frac{\partial p}{\partial x}\right) = 6\eta U_l\frac{\partial h}{\partial x} + 12\eta\omega_{es}\frac{\partial h}{\partial \theta} \tag{5.19}$$

If elastic deflections of the ring and the liner are neglected (i.e. $\frac{\partial h}{\partial \theta}$ is not a function of x at a given instant), the integration of the above equation gives an expression for the axial pressure gradient for the inlet region

$$\frac{dP_a}{dx} = \frac{1}{h^3}\left(C_1 h + C_2\frac{dh}{d\theta}x + C_3\right) \tag{5.20}$$

where $C_1 = 6\eta U_l$, $C_2 = 12\eta\omega_{es}$ and C_3 is an integration constant. Integrating equation (5.20) yields the expression for the hydrodynamic pressure within the lubricating film in the inlet region as follows

$$p_a = C_1 I_1 + C_2\frac{dh}{d\theta}I_2 + C_3 I_3 + C_4 \tag{5.21}$$

where

$$I_1 = \int\frac{1}{h^2}dx, \quad I_2 = \int\frac{x}{h^3}dx, \quad I_3 = \int\frac{1}{h^3}dx$$

and C_4 is another integration constant.

A solution of equation (5.21) requires that the integration constants C_3 and C_4 and the cavitation and reformation locations x_2 and x_3 should be evaluated. C_3, C_4 and x_2 can be found by applying the following boundary conditions on pressure to equations

(5.20) and (5.21)

$$\begin{aligned} p_a &= p_1 \qquad (x = x_1) \\ p_a &= \frac{dp_a}{dx} = 0 \qquad (x = x_2) \end{aligned} \tag{5.22}$$

and the reformation boundary x_3 can be determined by considering the continuity of flow and the boundary pressure condition at the trailing edge of the ring. Detailed procedures are as follows.

The expression for the volume rate of flow per unit circumferential length (Reynolds [1886]) for the present case, Q, can be presented as

$$Q = -\frac{h^3}{12\eta}\frac{dp}{dx} + \frac{U_l h}{2} \tag{5.23}$$

and the flow rate per unit length at the cavitation boundary x_2 then equals $\frac{U_l h_m}{2}$ since $\frac{dp}{dx} = 0$. This flow rate must be equal to that past the outlet region of the ring expressed by equation (5.23). Rearranging this relation produces a simplified expression for pressure gradient in the outlet zone as

$$\frac{dp_b}{dx} = C_1\left(\frac{h - h_m}{h^3}\right) \tag{5.24}$$

Integrating this equation provides an expression for the pressure distribution within the oil film in the outlet area

$$p_b = C_1\left(I_1 - h_m I_3\right) + C_5 \tag{5.25}$$

where C_5 is an integration constant. This constant, together with the reformation coordinate x_3, can then be found by introducing the following boundary conditions into equation (5.25)

$$\begin{aligned} p_b &= p_2 \qquad (x = x_4) \\ p_b &= 0 \qquad (x = x_3) \end{aligned} \tag{5.26}$$

Once integration constants C_3, C_4 and C_5 and the cavitation and reformation boundary locations x_2 and x_3 have been determined, the oil pressure in the region $[x_1, x_2]$ in front of the cavitation region, p_a, and the oil pressure in the area $[x_3, x_4]$ behind the cavitation zone, p_b, are all clear. The hydrodynamic radial force component per unit length, F_z, can be found directly by integration.

$$F_z = \int_{x_1}^{x_2} p_a dx + \int_{x_3}^{x_4} p_b dx \tag{5.27}$$

This force must be in equilibrium with the load applied radially on the ring as expressed by equation (5.17). Combining these two equations and rearranging yields an expression for $\frac{dh}{d\theta}$ of the form

$$\frac{dh}{d\theta} = f(F_z, \eta, U_l, \omega_{es}, h_{min}, x_2, x_3) \tag{5.28}$$

For a specified ring face profile and known operating conditions, the hydrodynamic force components are functions of the minimum film thickness h_{min} and the squeeze velocity $\frac{dh}{d\theta}$ only. Initially, neither of these quantities is known, but if an initial estimate is made of h_{min} at some crank angle where the film thickness is expected to change only slightly, $\frac{dh}{d\theta}$ can then be calculated from equation (5.28). Subsequent values of h_{min} can be marched out for a complete cycle by means of the Trapezoidal Rule

$$h_{\theta+d\theta} \approx h_\theta + \frac{d\theta}{2}\left[\left(\frac{dh}{d\theta}\right)_\theta + \left(\frac{dh}{d\theta}\right)_{\theta+d\theta}\right] \tag{5.29}$$

where h_θ is the minimum film thickness at crank angle θ and $d\theta$ is the crank angle increment. The iteration process for the calculation of minimum film thickness and squeeze velocity is detailed in the following chapter.

5.3.2.3 Friction and Power Loss

Since the surfaces of the ring and the liner are assumed to be separated by a lubricating film, the frictional force acting on the ring can be calculated by integrating the viscous

shear stress along the ring face. If the viscous shear stress on the ring face is τ_r, which is the product of the dynamic viscosity and the velocity gradient, then the frictional force per unit circumferential length of the liner can be expressed as

$$F_r = \int_{x_1}^{x_4} \tau_r dx \tag{5.30}$$

This equation can be further developed (Reynolds [1886]) across the ring face as

$$F_r = \int_{x_1}^{x_2} \left(-\frac{h}{2}\frac{dp_a}{dx} + \eta\frac{U_l}{h} \right) dx + \int_{x_2}^{x_3} \tau_r dx + \int_{x_3}^{x_4} \left(-\frac{h}{2}\frac{dp_b}{dx} + \eta\frac{U_l}{h} \right) dx \tag{5.31}$$

Assuming the oil film breaks and creates a finger pattern of air cavities in the cavitated region $[x_2, x_3]$ and considering the flow continuity condition, the shear stress and hence the friction over this area can be estimated (Dowson & Higginson [1977] and Richez et al [1983]). If the predicted minimum film thickness is not greater than the combined surface roughness of the ring and the liner, boundary lubrication is assumed to occur and a constant coefficient of friction of 0.08 is used throughout the present work.

The average frictional power loss over a complete cycle, H_r, is

$$H_r = \frac{1}{2\pi}\int_0^{2\pi} F_r \pi D U_l \, d\theta \tag{5.32}$$

where D is the engine cylinder bore.

5.3.2.4 Lubricant Flow Rate

The volume rate of flow of the lubricant is the same past each of the three pressure regions of a ring (Figure 5.2), and thus a knowledge of the variation of film thickness over an engine cycle enables the lubricant flow rate to be calculated. At points within the oil film where $\frac{dp}{dx} = 0$, i.e. there is only Couette flow. Thus

$$Q = \frac{1}{2} U_l h_m \tag{5.33}$$

Integration of this quantity w.r.t. crank angle allows the net quantity of lubricant flowing past the ring to be evaluated for the upstroke, the downstroke and over the complete engine cycle. The sign of the net oil flow indicates whether the oil flows towards the combustion chamber or towards the crankcase.

Although the oil flow across the ring face is not the only path concerning engine oil transport, it is an important element in determining the actual mechanism of oil consumption. The prediction of net oil flow here can give a rough picture as to how the lubricant is carried past the ring face and the potential oil loss by this path. Other paths for oil consumption are the ring gap and the leakage between the ring and groove.

5.4 Lubrication Analysis for a Complete Ring Pack

Generally it is difficult for a single ring to seal the combustion chamber perfectly and thus a pack of rings is used in nearly all applications. If the ring is plentifully filled with lubricant from its inlet edge, the ring is said to be fully flooded. If the inlet region is not completely full of lubricant, then the ring is said to be starved of lubricant. A fully flooded condition is normally assumed for the lubrication study of a single ring, but the ring pack situation is different. It is easy to imagine that any ring in a pack will obstruct the flow of lubricant to, and have the flow to itself obstructed by, the adjacent rings. Most of the rings may therefore be operating under starved conditions.

The interaction between rings in a pack has revealed that the problem is essentially one of continuity of oil flow. The situation for two adjacent rings working in a pack is shown in Figure 5.4. The general procedure is to calculate the oil film thickness left by the passage of any given ring (ring 1) and to calculate its effect on the position of the inlet boundary of the subsequent ring (ring 2). Using this information, the oil film thickness in

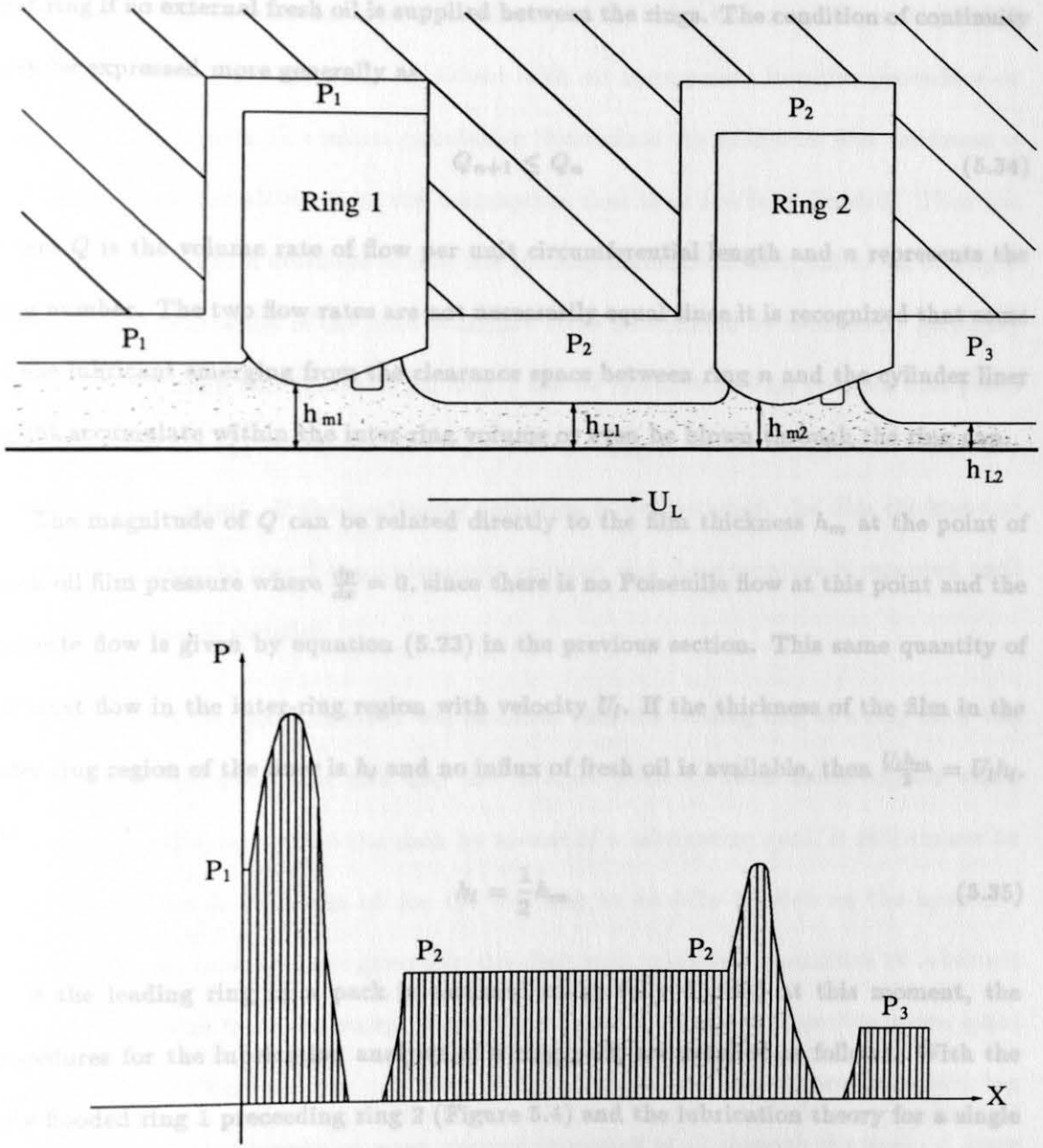

Figure 5.4. Lubricant Flow in a Ring Pack

the latter is calculated. This in turn leads to a knowledge of the oil flow past the second ring and allows it to be compared with that past the first ring. The principle of continuity demands that the volume rate of flow past the second ring cannot exceed that past the first ring if no external fresh oil is supplied between the rings. The condition of continuity may be expressed more generally as

$$Q_{n+1} \leq Q_n \tag{5.34}$$

where Q is the volume rate of flow per unit circumferential length and n represents the ring number. The two flow rates are not necessarily equal since it is recognized that some of the lubricant emerging from the clearance space between ring n and the cylinder liner might accumulate within the inter-ring volume or even be blown through the ring gap.

The magnitude of Q can be related directly to the film thickness h_m at the point of peak oil film pressure where $\frac{dp}{dx} = 0$, since there is no Poiseuille flow at this point and the Couette flow is given by equation (5.23) in the previous section. This same quantity of oil must flow in the inter-ring region with velocity U_l. If the thickness of the film in the inter-ring region of the liner is h_l and no influx of fresh oil is available, then $\frac{U_l h_m}{2} = U_l h_l$. Or

$$h_l = \frac{1}{2} h_m \tag{5.35}$$

If the leading ring in a pack is assumed to be fully flooded at this moment, the procedures for the lubrication analysis of a ring pack are detailed as follows. With the fully flooded ring 1 preceeding ring 2 (Figure 5.4) and the lubrication theory for a single ring presented in the last section, the minimum film thickness h_{min} and the film thickness h_m can be calculated. The uniform layer of lubricant h_l, which is left by the passage of ring 1 and available to ring 2, will then be $0.5h_m$ as indicated by equation (5.35). This

thickness of oil, however, may not be sufficient to fill the inlet region of ring 2 which is normally relatively lightly loaded compared with ring 1. The lubricant starvation for ring 2 reduces the load carrying capacity of the oil film and the film thickness for a given gas loading. This in turn disturbs the location of the inlet boundary for any specified value of h_l. Such a problem can be solved with an appropriate iterative procedure on a high speed computer.The initial calculation determines the minimum film thickness at each crank angle for all rings on the assumption that they are fully flooded. Then the thickness of the oil film available to ring 2 is initially assumed to be equal to h_m of ring 1. This enables the location of the inlet boundary to be determined by elementary geometry and a new minimum film thickness for ring 2 can be calculated. This solution also yields new prediction for h_m and hence new flow rate for ring 2, so the equation of continuity (5.34) can be checked. If the continuity condition is not satisfied, the film thickness at the inlet boundary to ring 2 is progressively reduced and the procedure is repeated until continuity of flow is satisfied.

In the theory presented above it was assumed that the leading ring of a ring pack was fully flooded at all times, but this may not be true. Even for some diesel engines which have oil supplied directly into the pack by means of a lubricating quill, it still cannot be certain that there is sufficient oil for the top ring to be fully flooded on the upstroke. Modern engines, however, are generally supplied with adequate quantities of lubricant by a splash system from the sump. The fully flooded assumption therefore seems quite reasonable for the bottom ring in a pack on the downstroke. The lubrication of the top ring in this case relies purely on a net upward transport of oil through the pack. A more reasonable assumption for the oil available to the top ring on the upstroke may be that the ring will have only the oil it left on the liner on the downstroke available to it on

the upstroke. Even this assumption may still be optimistic since some of the lubricant may be lost when it is exposed to the high temperature gases, but it is nevertheless more realistic than the original fully flooded assumption. The modified form of the continuity equation to be applied to the top ring on the upstroke can thus be written as

$$Q_{upstroke} \leq Q_{downstroke} \tag{5.36}$$

where Q is the volume rate of oil flow per unit circumferential length at any crank angle and it can be estimated from the theory presented above. The development of a computer program for the prediction of hydrodynamic performance of the rings in a ring pack based upon the above theory will be detailed in the next chapter.

5.5 Oil Control Ring/Cylinder Liner and Piston Skirt/Cylinder Liner Friction Estimations

The piston rings so far described are fitted for the purpose of preventing the escape of gas through the clearance between cylinder and piston and are usually called compression rings. Besides these rings one more ring is usually fitted in the groove nearest the crankcase and this is known as the oil control ring. The function of this ring is to restrict the amount of oil made available to the compression rings and distribute oil circumferentially around the cylinder liner to lubricate the compression rings and piston skirt. Normally the working-face width of this ring is narrower than the axial height of the compression rings, typically around 0.5 mm, and the tangential load of the ring is higher than that of the compression rings. These inevitably result in a large pressure between the ring and the cylinder liner. Conventional hydrodynamic analysis of oil control rings invariably predicts very thin oil films comparable to, or less than, the typical surface roughnesses of the ring and the liner (Pacherngg [1971]). It is, therefore, quite reasonable to assume

that the oil control rings are working in the mixed or boundary lubrication regime. For the present work boundary lubrication will be assumed for the friction calculation, which means that the friction force equals the product of the coefficient of boundary friction and the normal load. A constant value of the coefficient of friction is taken to be 0.08, as adopted in Part II in the valve train lubrication analysis. The normal or radial loading on the ring is assumed to be due only to the inherent elastic tension of the ring. The cyclic average power loss can be achieved by integrating the instantaneous frictional power loss w.r.t. crank angle over one complete cycle and dividing the result by 2π.

The piston skirt is that portion of the piston which continues below the zone in which the rings and lands are grouped together. Its function is to form a cross-head guide capable of carrying the side thrust force created by the oblique angle made by the connecting rod relative to the cylinder axis. The geometry of the piston and skirt is seldom made in the shape of a perfect cylinder. Circumferentially, piston skirts are often ground to an elliptical or oval shape, having the smallest diameter across the gudgeon-pin bosses to compensate for the expansion associated with the majority of heat flow. At working temperatures the oval shape will take a circular form and hence match the section of the cylinder bore. Axially, the piston and hence the skirt is tapered or barrelled along its axis to compensate for the unequal expansion due to the variation of temperature along the piston. This means that the clearance between the piston and the cylinder liner varies along the piston with the maximum clearance being evident at the top. Due to the relatively light loadings and large contact areas, piston skirts normally operate in the hydrodynamic lubrication regime. This observation has been proved by both direct measurements of film pressures and calculated coefficients of friction and indirect evidence in the form of skirt wear (Thring [1989]). It is assumed for the present work that the

clearance between the piston skirt and the cylinder liner is plentifully filled with lubricant at all times and that hydrodynamic lubrication takes place. It is further assumed that the piston skirt is rigid (i.e. thermal distortion and elastic deflection are not considered) and that the piston is concentric within the cylinder throughout the engine cycle. By taking into account the axial variations of the clearance and lubricant viscosity along the piston skirt, the frictional traction per unit circumferential length $F_s(\theta)$ due to the viscous shear of lubricant at crank angle θ is

$$\begin{aligned} F_s(\theta) &= \int_0^{L_s} \tau(\theta, x)\, dx \\ &= \int_0^{L_s} \eta(\theta, x) \frac{U_l(\theta)}{C_s(x)} dx \end{aligned} \tag{5.37}$$

where the x coordinate is fixed axially along the piston skirt, L_s is skirt height and $C_s(x)$ is the radial clearance between the skirt and the liner. Once the frictional traction at each crank angle is calculated, the instantaneous frictional power loss and the cyclic average power loss can be easily obtained as for the case of the oil control ring. The approach above is simple but reasonable. The full hydrodynamic and EHL analyses may be found in Knoll and Peeken [1982] and Oh et al [1987].

5.6 Conclusions

The established orifice and volume theory for predicting the gas pressures between compression rings has been outlined.

Hydrodynamic lubrication theory has been adopted for the lubrication analysis of a single piston ring with a parabolic profile. The kinematics, load evaluation, temperature and viscosity variations for the ring have been detailed. The minimum film thickness calculation, frictional force estimation, power loss prediction and lubricant transport study have been described.

The extension of the single ring lubrication approach gives a better understanding of the operating mechanism of the rings in a pack. The ring pack lubrication analysis demonstrated the important role of oil flow continuity and lubricant starvation in understanding the performance of a complete ring pack.

The friction between an oil control ring and cylinder wall has been modelled assuming a boundary lubrication condition. A full film approximation has been made for the estimation of friction between piston skirt and cylinder liner.

Chapter Six

Computer Programs and Results for an Engine Piston Assembly

6.1 Introduction

To design and manufacture high efficiency engines, engineers have to understand the various factors which affect the performance of engines. The performance of engine piston assembly is a major concern and the lubrication analysis of the assembly is currently an active research area.

The lubrication analysis of the piston assembly requires both the inter-ring gas pressures to be determined and the single ring lubrication analysis to be studied. Based on the theory expressed in the previous chapter, three computer programs have been developed and these are detailed in this chapter. One is for the prediction of inter-ring gas pressures, one for the lubrication analysis of a single ring and the last for the lubrication analysis of a complete ring pack. The software can analyse both two-stroke and four-stroke petrol or diesel engines and the ring pack lubrication analysis can be carried out under both fully flooded and starved lubrication conditions. The Ford 1.8L H.O. Zeta engine has been analysed. For the compression rings, the results for the cyclic variations of film thicknesses, friction forces, power losses and oil transports have been presented and discussed in detail. Finally, a friction model for the piston assembly has been established and the corresponding results are outlined.

6.2 Computer Programs

6.2.1 Inter-ring Gas Pressure Program

A computer program for the determination of inter-ring gas pressures has been coded based on the theory stated in section 5.1 in the previous Chapter. Both two-stroke and four-stroke engines can be analysed and the program flow chart is shown in Figure 6.1.

Input data are edited in a data file. They may be in SI units or British units as desired. The early theory assumed that the combustion chamber temperature was constant. The software was modified to enable this temperature to vary from one crank angle to the next. The measured gas pressure and the temperature in the combustion chamber are usually available for every 10^0 of crank angle and they can be interpolated to every 1^0 crank angle interval.

If an initial guess is made of the pressures within each volume, then the instantaneous flow rate through each orifice can be calculated using equation (5.12) or (5.14). The rate of change of pressure within each volume is given by equation (5.13). The inter-ring gas pressures were found using Trapezoidal Rule

$$(P_n)_{\theta+d\theta} = (P_n)_\theta + \frac{d\theta}{2}\left[\left(\frac{dP_n}{d\theta}\right)_\theta + \left(\frac{dP_n}{d\theta}\right)_{\theta+d\theta}\right] \tag{6.1}$$

where $(P_n)_\theta$ is P_n at crank angle θ and $d\theta$ is the crank angle increment which was assumed to be 1^0 at the present work. The new pressures generated from equation (6.1) were used to calculate new flow rates and the procedures were repeated until the pressures P_n had converged to within 0.5%.

The calculation was normally started from a crank angle, around which the pressure change is likely to be small, to the end of a cycle. Then the calculation was started again

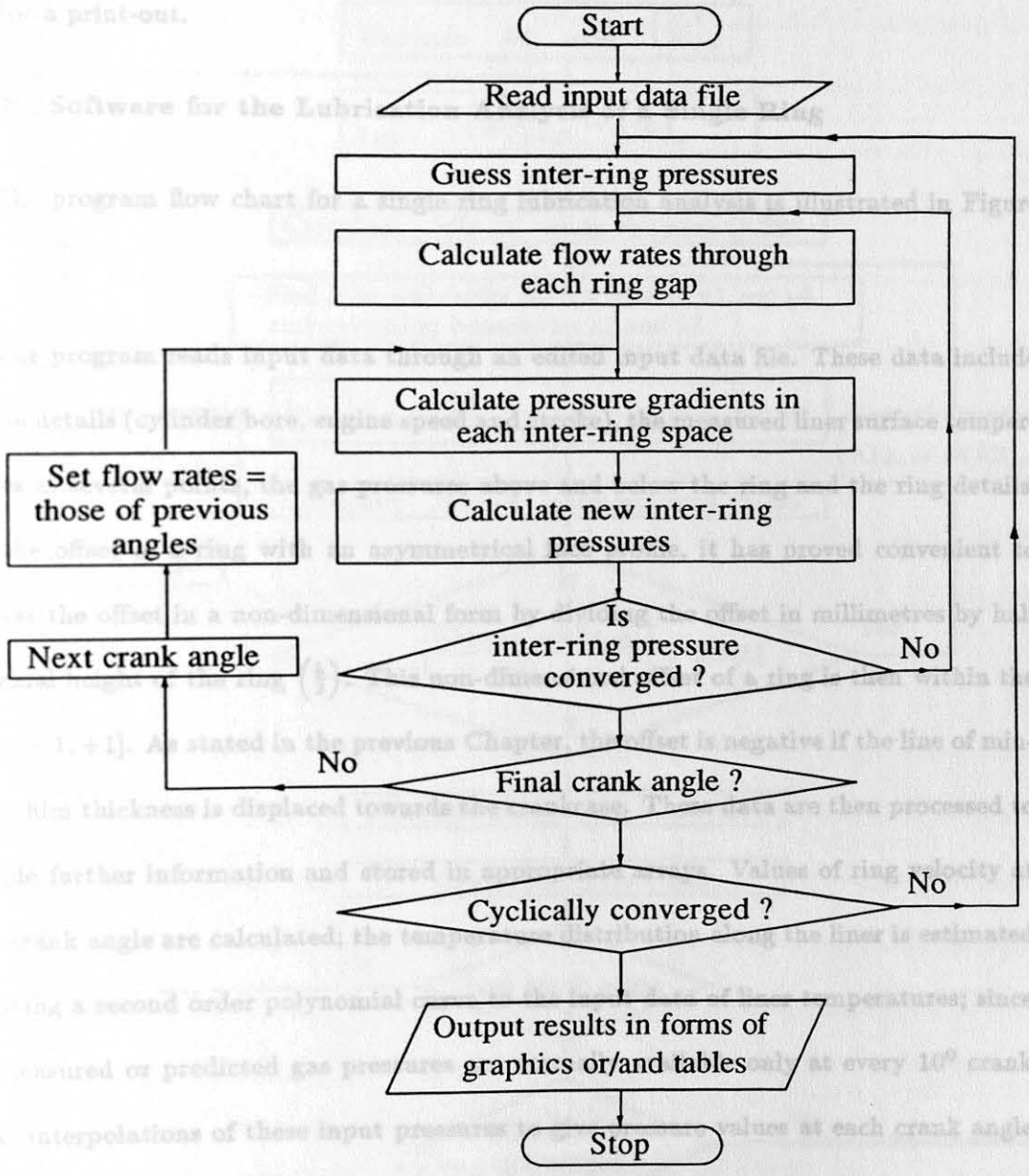

Figure 6.1. Flow Chart for the Inter-ring Gas Pressure Prediction Program

from the beginning of a cycle (i.e. 0^0 crank angle) to the end and cyclic convergence was checked during this round of computation. If the results were cyclically converged then the computation was stopped and the final results were displayed in the form of graphics and/or a print-out.

6.2.2 Software for the Lubrication Analysis of a Single Ring

The program flow chart for a single ring lubrication analysis is illustrated in Figure 6.2.

The program reads input data through an edited input data file. These data include engine details (cylinder bore, engine speed and stroke), the measured liner surface temperatures at several points, the gas pressures above and below the ring and the ring details. For the offset of a ring with an asymmetrical face profile, it has proved convenient to express the offset in a non-dimensional form by dividing the offset in millimetres by half the axial height of the ring $\left(\frac{b}{2}\right)$. This non-dimensional offset of a ring is then within the range $[-1, +1]$. As stated in the previous Chapter, the offset is negative if the line of minimum film thickness is displaced towards the crankcase. These data are then processed to provide further information and stored in appropriate arrays. Values of ring velocity at each crank angle are calculated; the temperature distribution along the liner is estimated by fitting a second order polynomial curve to the input data of liner temperatures; since the measured or predicted gas pressures are normally available only at every 10^0 crank angle, interpolations of these input pressures to give pressure values at each crank angle is essential.

The minimum film thickness calculation is started by estimating the minimum film thickness h_θ and the squeeze velocity $\left(\frac{dh}{d\theta}\right)_\theta$ at a starting crank angle θ. This starting

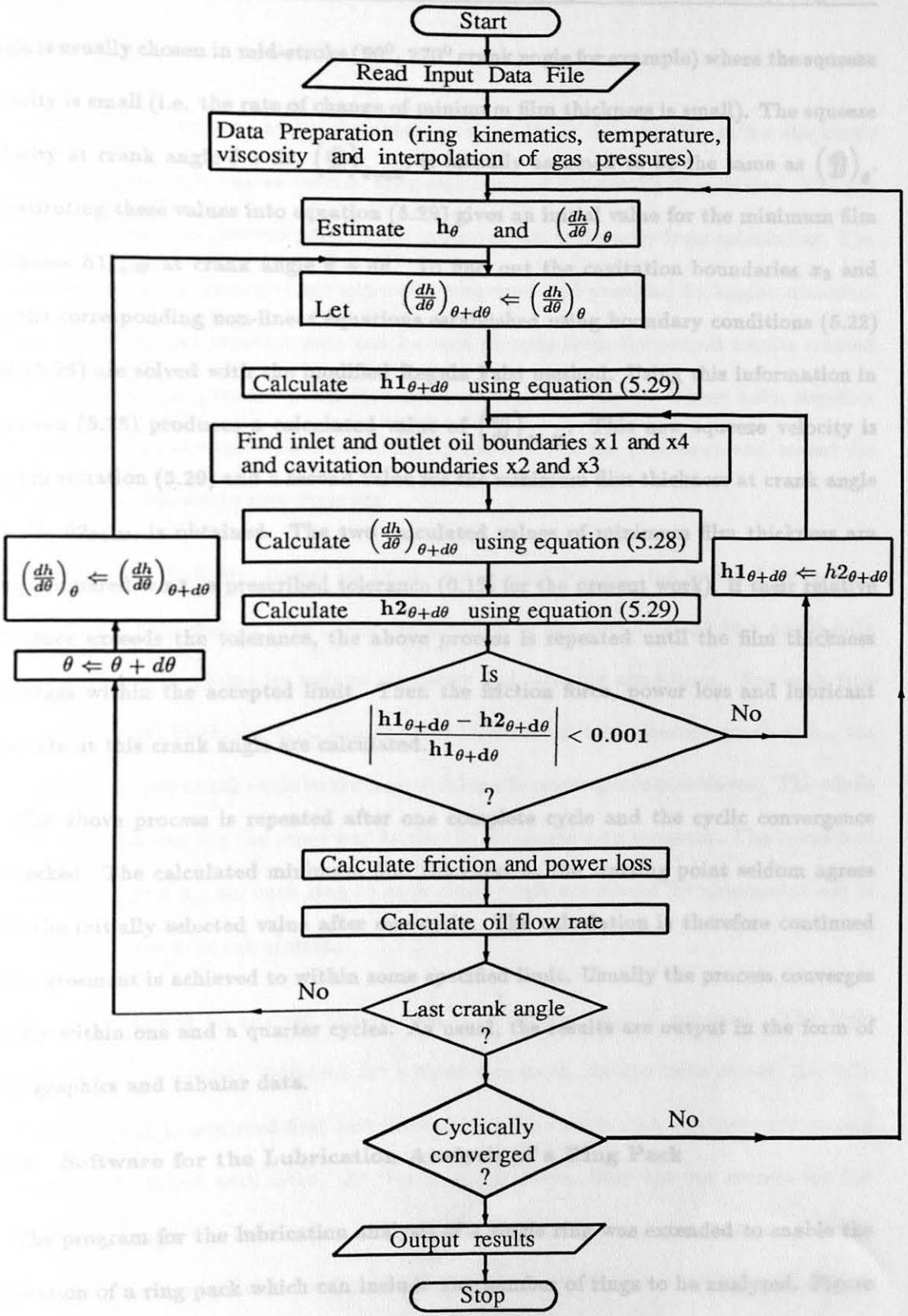

Figure 6.2. Flow Chart for the Program of a Single Ring Lubrication Analysis

angle is usually chosen in mid-stroke (90^0, 270^0 crank angle for example) where the squeeze velocity is small (i.e. the rate of change of minimum film thickness is small). The squeeze velocity at crank angle $\theta + d\theta$, $\left(\frac{dh}{d\theta}\right)_{\theta+d\theta}$, is initially assumed to be the same as $\left(\frac{dh}{d\theta}\right)_{\theta}$. Substituting these values into equation (5.29) gives an initial value for the minimum film thickness $h1_{\theta+d\theta}$ at crank angle $\theta + d\theta$. To find out the cavitation boundaries x_2 and x_3, the corresponding non-linear equations established using boundary conditions (5.22) and (5.26) are solved with the modified Regula Falsi method. Using this information in equation (5.28) produces a calculated value of $\left(\frac{dh}{d\theta}\right)_{\theta+d\theta}$. This new squeeze velocity is used in equation (5.29) and a second value for the minimum film thickness at crank angle $\theta + d\theta$, $h2_{\theta+d\theta}$, is obtained. The two calculated values of minimum film thickness are then compared w.r.t. a prescribed tolerance (0.1% for the present work). If their relative difference exceeds the tolerance, the above process is repeated until the film thickness converges within the accepted limit. Then the friction force, power loss and lubricant flow rate at this crank angle are calculated.

The above process is repeated after one complete cycle and the cyclic convergence is checked. The calculated minimum film thickness at the starting point seldom agrees with the initially selected value after one cycle. The calculation is therefore continued until agreement is achieved to within some specified limit. Usually the process converges quickly within one and a quarter cycles. As usual, the results are output in the form of both graphics and tabular data.

6.2.3 Software for the Lubrication Analysis of a Ring Pack

The program for the lubrication analysis of a single ring was extended to enable the lubrication of a ring pack which can include any number of rings to be analysed. Figure

6.3 shows the program flow chart for the new program of a ring pack lubrication analysis.

As usual, the program begins by reading in the input data which, as for the single ring program, includes engine details, temperatures and the details of each ring. The gas pressures are normally derived partly from measurement and partly from calculation. The combustion chamber pressures are generally measured and provided by engine manufacturers. The other gas pressure data can be read directly from the output results created by the inter-ring gas pressure prediction software discussed earlier. These data, together with some other calculated data (velocity, viscosity etc.), are processed and stored for later use as for the single ring program.

The program then first moves on to analyse a fully flooded ring pack. This is done by considering each ring in turn (from the top ring to the bottom ring) as a single fully flooded ring which retains its unique geometry and working conditions. For each ring the minimum film thickness h_{min} and the film thickness at zero pressure gradient h_m are calculated from one crank angle to the next until cyclic convergence is achieved. The whole process works in exactly the same way as that in the single ring program. The calculated values of h_{min} and h_m for each ring at each crank angle are stored for subsequent use in the starved lubrication calculation.

The next step is to analyse the starved case for the pack if required. The logic procedure is illustrated in Table 6.1 for a three ring pack. As the table shows, the fully flooded ring pack is analysed first and the calculated values of film thickness are correct and therefore marked with ticks. At this stage, however, they are not correct for the starved case except for the bottom ring on the downstroke, and are therefore marked with crosses. For the initial starved pass of the pack the performance of the bottom ring is considered first and the direction of computation is upward. **On the downstroke**, the

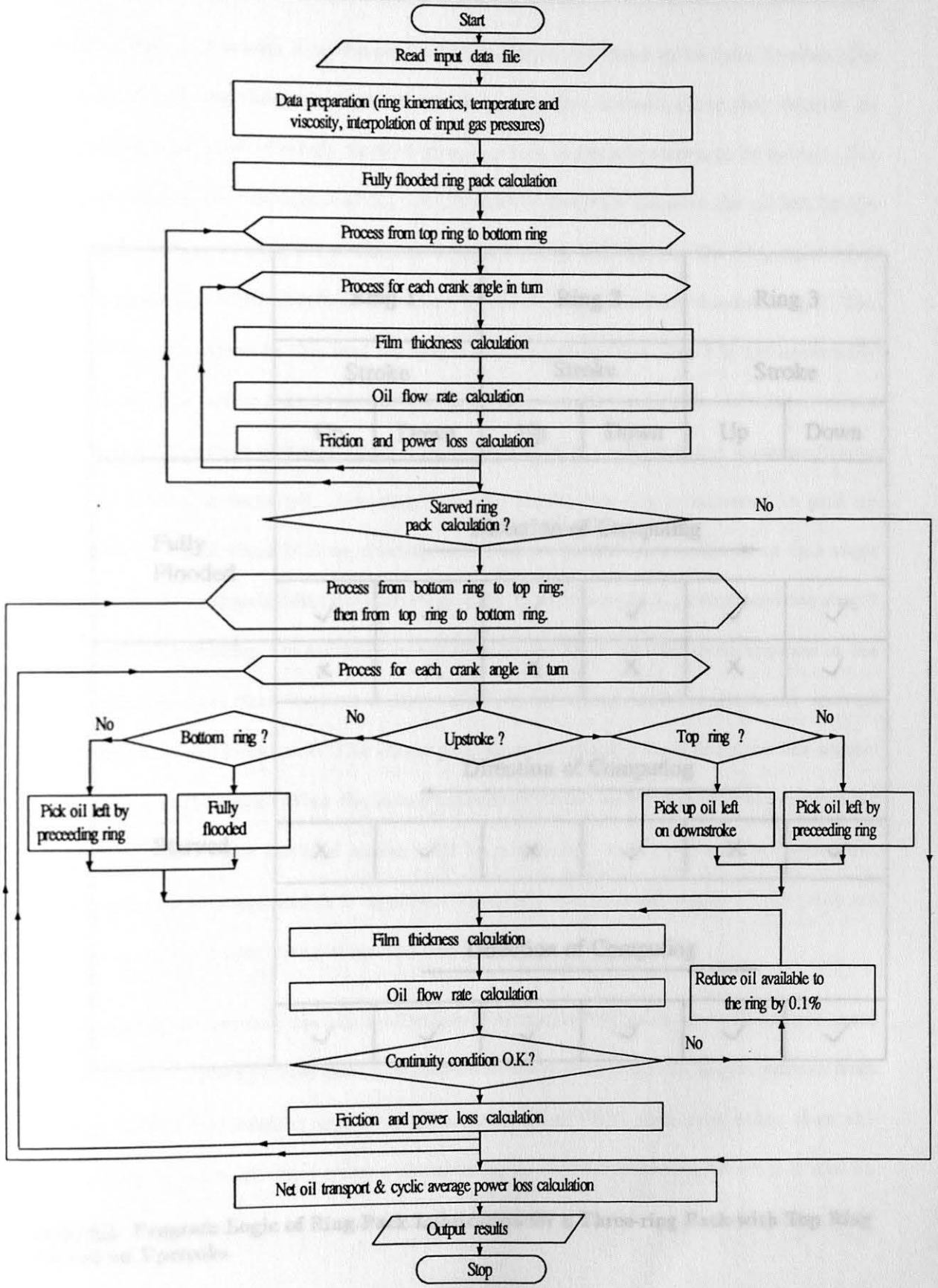

Figure 6.3. Flow Chart for the Program of a Ring Pack Lubrication Analysis

	Ring 1		Ring 2		Ring 3	
	Stroke		Stroke		Stroke	
	Up	Down	Up	Down	Up	Down
Fully Flooded	Direction of Computing →					
	✓	✓	✓	✓	✓	✓
Starved	✗	✗	✗	✗	✗	✓
	Direction of Computing ←					
	✗	✓	✗	✓	✗	✓
	Direction of Computing →					
	✓	✓	✓	✓	✓	✓

Table 6.1. Program Logic of Ring Pack Lubrication for a Three-ring Pack with Top Ring Starved on Upstroke

film thickness h_m for ring 3 is correct since the ring is assumed to be fully flooded. For ring 2 at this stroke the calculated values of h_m are also correct, since they depend on the downward passage of a fully flooded ring 3, which is already shown to be correct. For ring 1 on this stroke the values of h_m are calculated correctly because the oil left by the downward passage of ring 2 has already been correctly calculated. **On the upstroke,** ring 3 is presented with oil left on the liner by the passage of a fully flooded ring 2. The values of h_m calculated in this way for ring 3 are erroneous since ring 2 is not necessarily fully flooded and hence a cross is marked. For ring 2 on this stroke the calculated values of h_m are incorrect since they rely on a fully flooded ring 1 which is not necessarily true and thus a cross is recorded. For ring 1 at this stroke the ring is assumed to pick up the oil left by itself when it is on downstroke. Unfortunately data available at this stage are those calculated in a fully flooded ring pack. The values of h_m calculated for ring 1 using these information are unlikely to be correct and thus another cross appears in the table. It can be seen that the first analysis of the starved ring pack has produced answers which are not entirely correct. The whole procedure is repeated once again for the second starved pass of the pack. With the latest calculated values and the downward computing direction, an error-free table of results will be produced. This program logic can work for any number of rings and it is apparent that only two starved passes of the pack are required no matter how many rings the pack contains.

A problem concerning the oil availability within the ring pack at dead centres must be pointed out. During those critical times when the piston is about to go upstroke from BDC (bottom dead centre) or move downstroke from TDC, each ring other than the leading ring in the pack must move a distance equal to the separation between it and its preceding ring before it encounters the oil left on the liner by the preceding ring. The

amount of oil between the rings at dead centres is unknown since oil might accumulate in the inter-ring volumes, but it is reasonable to assume that the oil available to the ring on one stroke is that left by the same ring when it was on the previous stroke. This duration is normally short and depends mainly on the axial separation of the rings and the engine speed. The idea of the program logic is expressed clearly in the section for starved ring pack analysis in the flow chart (Figure 6.3).

After calculations for film thickness, oil flow rate, friction and power loss, the program then calculates the cyclic minimum film thickness, the net oil transport and the average power loss over one complete cycle. Two more sub-routines for the prediction of frictional power losses for the oil control ring and piston skirt are also built into the program.

6.3 Zeta Engine Piston Assembly Analysis

Each piston assembly in the Ford 1.8L H.O. Zeta engine has two compression rings and one oil control ring (see Figure 5.1(a)). The face profile of the top compression ring is produced in a symmetrical barrel shape, while the second compression ring is tapered at an angle of 1^0 across its working face so that the taper can provide an effective scraping action on the downstroke. The oil control ring is actually an assembly consisting of a crimped spacer and two narrow steel rails. The two round-faced rails are separated and expanded by the specially shaped spacer against both sides of the groove and the cylinder liner. The piston has an ovality when viewed from the top and a taper when viewed from one side through the gudgeon-pin-boss axis with the largest diameter on the thrust and non-thrust sides.

The combustion chamber pressures for the engine running at 2000, 3000, 4000, 5000, 6000, 6400 and 7000 rpm under full load, together with the cylinder bore, connecting

rod length and crank radius, can be found in Appendix B. Input data for the lubrication analysis of the piston assembly, which includes gas properties, the geometry of rings and piston, the estimated temperatures and lubricant data, are all listed in Appendix D. The crankcase pressure is assumed to be ambient. The ratio of gas specific heat is assumed to be 1.3 and the orifice discharge coefficient is taken as 0.65 (Ting & Mayer [1974] and Ruddy [1979]). Since the ring face profile plays an important role in the ring lubrication analysis, the worn ring profile, instead of that of new ring, must be used. The face profiles of the compression rings after 196 hours running have been measured with a Rank Taylor-Hobson Talysurf-4 in the Measurement Laboratory at Leeds and it has been found that they can be represented by offset parabola. The average face profiles for the compression rings have been obtained and are used in the analysis. The data on dimensions correspond to cold engine condition. No attempt is made to adjust for different amounts of thermal expansion for each component due to lack of experimental data. Indeed, the temperatures entered for a running engine in the program have been estimated on the basis of a considerable literature search. The lubricant dynamic viscosity was measured at several temperatures using a suspended level viscometer in the tribology laboratory at Leeds.

The measured combustion chamber pressure and the predicted inter-ring gas pressures for the Ford Zeta four-stroke engine at an engine speed of 3000 rpm are shown in Figure 6.4. For the combustion pressure during the power stroke (0^0 to 180^0 crank angle), the gas pressure reaches its maximum and drops rapidly at a later stage of the stroke as the piston moves downwards to BDC; then the exhaust valve is opened and the piston moves upwards into the exhaust stroke (180^0 to 360^0 crank angle); the gas pressure in the cylinder falls from the exhaust valve opening pressure to near atmospheric pressure; the intake stroke

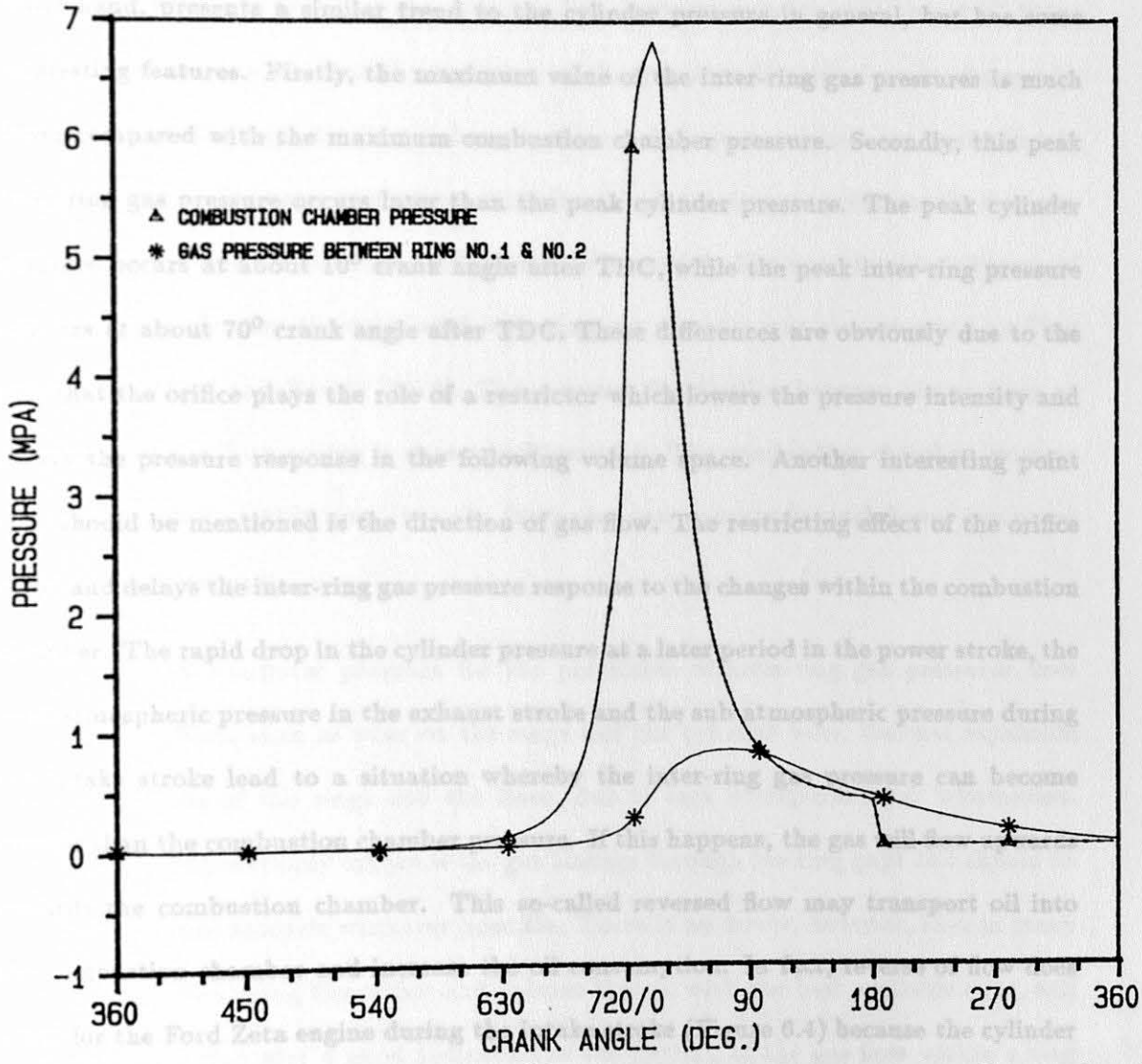

Figure 6.4. Pressure Distribution between the Compression Rings for the Ford Zeta Engine at 3000 rpm under Full Load

(360^0 to 540^0 crank angle) begins when the intake valve is opened and the exhaust valve is closed and the piston moves downwards from TDC; the piston descent creates a pressure depression which sucks in fresh air into the cylinder, the cylinder pressure during this stroke is constant and slightly below atmospheric. The inter-ring gas pressure, on the other hand, presents a similar trend to the cylinder pressure in general, but has some interesting features. Firstly, the maximum value of the inter-ring gas pressures is much lower compared with the maximum combustion chamber pressure. Secondly, this peak inter-ring gas pressure occurs later than the peak cylinder pressure. The peak cylinder pressure occurs at about 10^0 crank angle after TDC, while the peak inter-ring pressure appears at about 70^0 crank angle after TDC. These differences are obviously due to the fact that the orifice plays the role of a restrictor which lowers the pressure intensity and delays the pressure response in the following volume space. Another interesting point that should be mentioned is the direction of gas flow. The restricting effect of the orifice shifts and delays the inter-ring gas pressure response to the changes within the combustion chamber. The rapid drop in the cylinder pressure at a later period in the power stroke, the near atmospheric pressure in the exhaust stroke and the sub-atmospheric pressure during the intake stroke lead to a situation whereby the inter-ring gas pressure can become greater than the combustion chamber pressure. If this happens, the gas will flow upwards towards the combustion chamber. This so-called reversed flow may transport oil into the combustion chamber and increase the oil consumption. In fact, reverse of flow does occur for the Ford Zeta engine during the intake stroke (Figure 6.4) because the cylinder pressure drops below the atmospheric value. At the later stage of the power stroke and during the exhaust stroke, the inter-ring gas pressure surpasses the combustion chamber pressure, due to the phase lag of their pressure peaks, and also results in reverse gas flow.

It is apparent from the mass flow equation (5.12) that an increase in the parameter K results in an increase in mass flow rate. In other words, either increases in the gap area A and the gas inlet temperature or decreases of the inter-ring space volume and the engine speed will result in higher inter-ring gas pressures. Throughout the present work it has been assumed that the piston radial clearance remains constant at all times in an engine cycle, such that the variation of the gap area is equivalent to changes in the size of the ring gap. Similarly, changes of inter-ring space volumes are equivalent to variations of the ring axial separation. To reduce the inter-ring gas pressure, the ring gap size may be reduced or the ring axial separation increased. The considerable influence of the parameter K upon the calculated inter-ring gas pressure was also reported by Ting and Mayer [1974] and Ruddy [1979]. The pressure distribution between piston rings at 6000 rpm for the Zeta engine is shown in Figure 6.5. The combustion chamber pressure is similar to that at 3000 rpm, but the inter-ring gas pressure is much lower compared with that at 3000 rpm.

The present computer program for the prediction of inter-ring gas pressures does not consider effects such as wear on the rings and the cylinder bore, thermal expansion and deformation of the rings and the liner, due to lack of experimental information. These factors will certainly influence the gas leakage through the ring gaps and should be included in future analysis whenever possible. There is no doubt, however, that in many cases a calculation using the orifice and volume theory, with the best available data, will produce results that give a good indication of the pattern of the gas flow within a ring pack.

Once the combustion chamber pressure and the inter-ring gas pressure are available, the loading due to these pressures acting at the back face of piston rings can be calculated

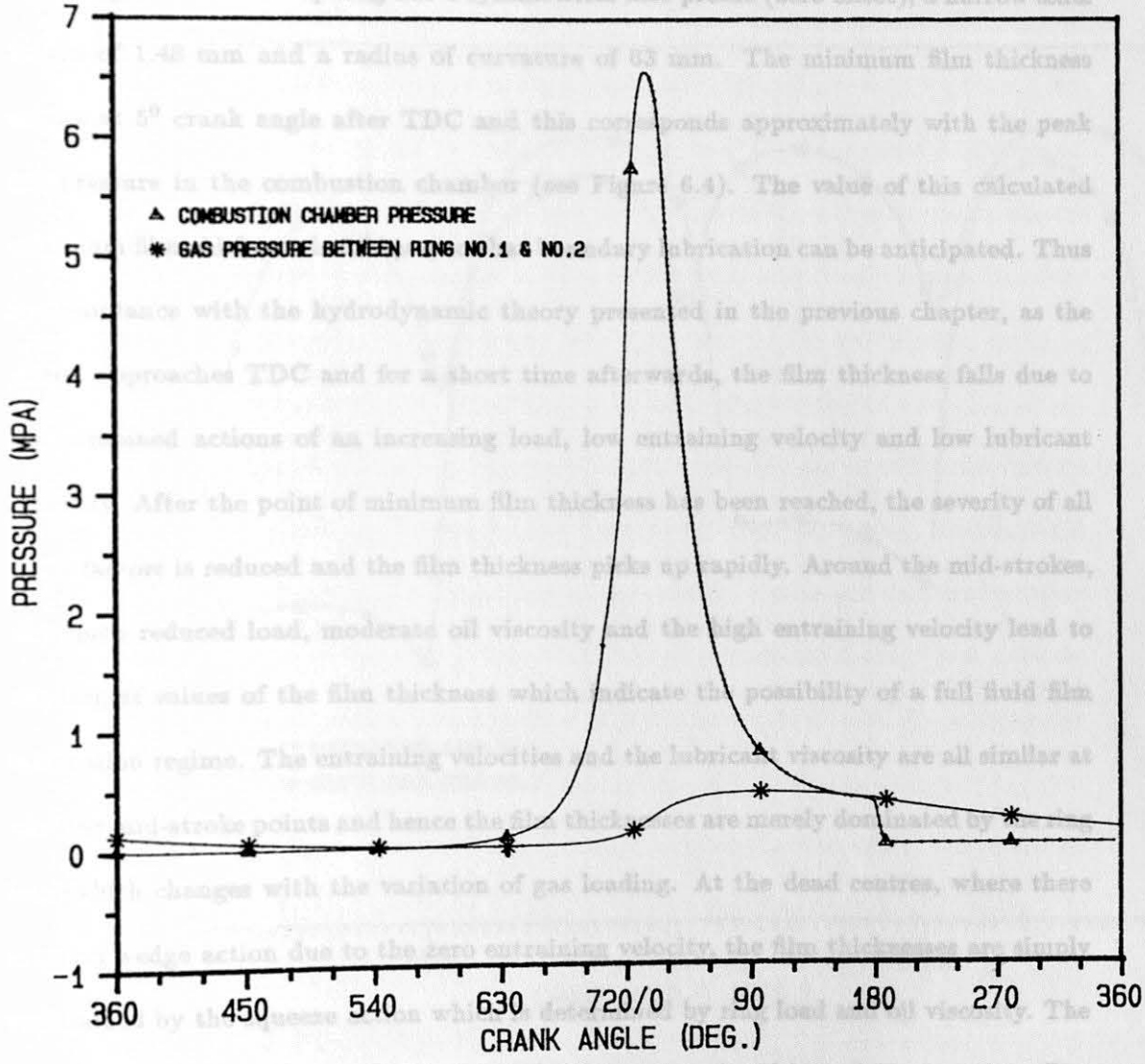

Figure 6.5. Pressure Distribution between the Compression Rings for the Ford Zeta Engine at 6000 rpm under Full Load

and the piston ring lubrication analysis can be carried out. Figure 6.6 shows the predicted cyclic variation of film thickness for the two compression rings in the Zeta engine at 3000 rpm under fully flooded conditions. It should be mentioned that the scale on the film thickness axis is logarithmic and the 0^0 crank angle represents TDC at the beginning of the firing stroke. The top ring has a symmetrical face profile (zero offset), a narrow axial height of 1.48 mm and a radius of curvature of 63 mm. The minimum film thickness occurs at 5^0 crank angle after TDC and this corresponds approximately with the peak gas pressure in the combustion chamber (see Figure 6.4). The value of this calculated minimum film thickness is 0.08 μm so that boundary lubrication can be anticipated. Thus in accordance with the hydrodynamic theory presented in the previous chapter, as the piston approaches TDC and for a short time afterwards, the film thickness falls due to the combined actions of an increasing load, low entraining velocity and low lubricant viscosity. After the point of minimum film thickness has been reached, the severity of all these factors is reduced and the film thickness picks up rapidly. Around the mid-strokes, the much reduced load, moderate oil viscosity and the high entraining velocity lead to the largest values of the film thickness which indicate the possibility of a full fluid film lubrication regime. The entraining velocities and the lubricant viscosity are all similar at the four mid-stroke points and hence the film thicknesses are merely dominated by the ring load which changes with the variation of gas loading. At the dead centres, where there is no oil wedge action due to the zero entraining velocity, the film thicknesses are simply maintained by the squeeze action which is determined by ring load and oil viscosity. The second compression ring is very thin (axial height 1.18 mm) and has a large negative offset of -0.85 and a large radius of curvature of 500 mm. This large negative offset produces enormous film thicknesses on the upstroke due to the strong wedge action and leaves a very thin film on the downstroke due to the poor entraining action. The minimum film

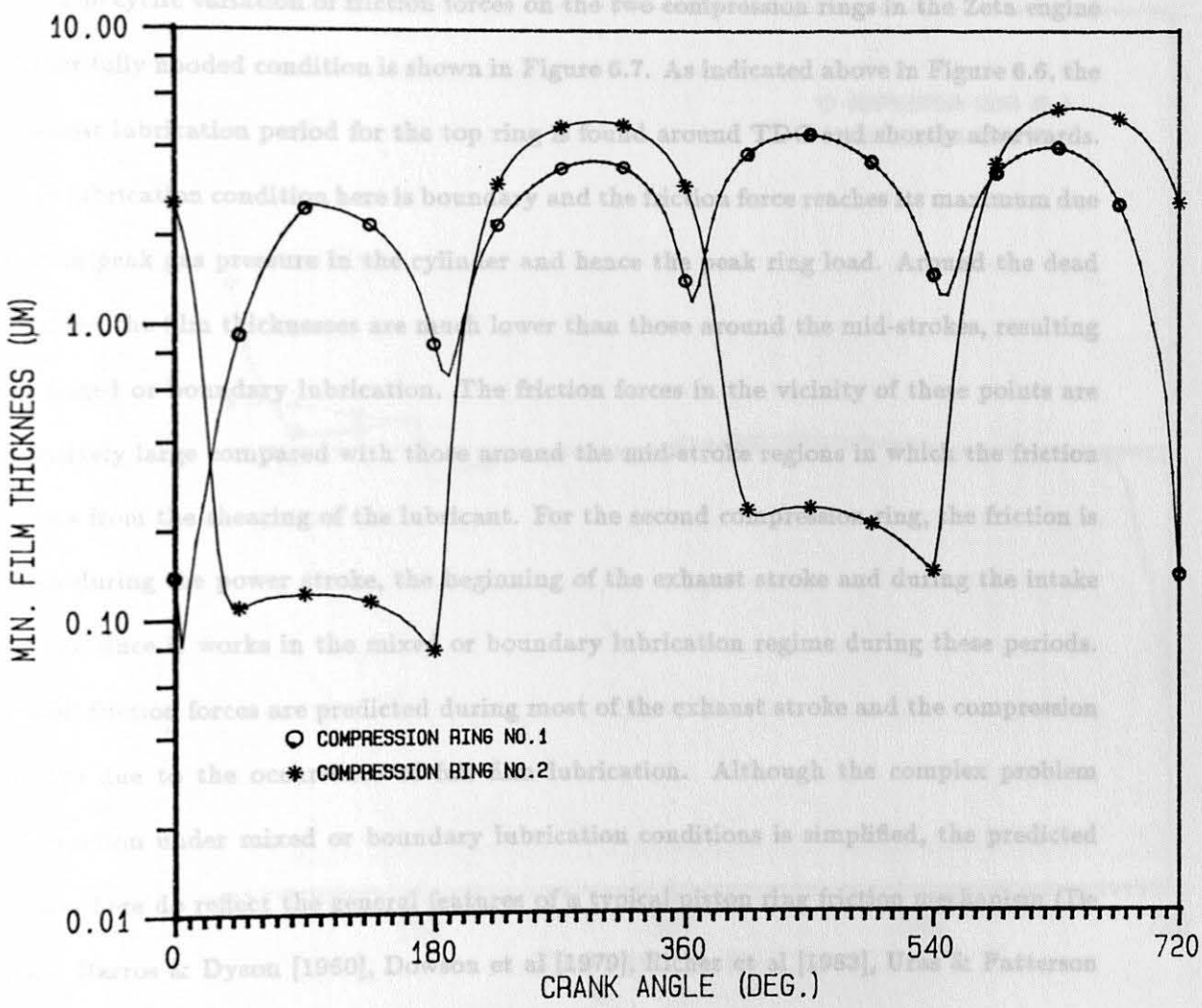

Figure 6.6. Cyclic Variation of Film Thicknesses for the Compression Rings in the Ford Zeta Engine at 3000 rpm under Fully Flooded Conditions

thickness of 0.07 μm appears at 180^0 crank angle, at the BDC point, where the protective effect from only the squeeze film action which is reduced by the narrow height and the large offset of the ring. It is almost certain that this ring enjoys hydrodynamic lubrication on the upstroke while it encounters mixed or boundary lubrication on the downstroke.

The cyclic variation of friction forces on the two compression rings in the Zeta engine under fully flooded condition is shown in Figure 6.7. As indicated above in Figure 6.6, the poorest lubrication period for the top ring is found around TDC and shortly afterwards. The lubrication condition here is boundary and the friction force reaches its maximum due to the peak gas pressure in the cylinder and hence the peak ring load. Around the dead centres, the film thicknesses are much lower than those around the mid-strokes, resulting in mixed or boundary lubrication. The friction forces in the vicinity of these points are relatively large compared with those around the mid-stroke regions in which the friction arises from the shearing of the lubricant. For the second compression ring, the friction is high during the power stroke, the beginning of the exhaust stroke and during the intake stroke since it works in the mixed or boundary lubrication regime during these periods. Small friction forces are predicted during most of the exhaust stroke and the compression stroke due to the occurrence of full film lubrication. Although the complex problem of traction under mixed or boundary lubrication conditions is simplified, the predicted traces here do reflect the general features of a typical piston ring friction mechanism (De Faro Barros & Dyson [1960], Dowson et al [1979], Richez et al [1983], Uras & Patterson [1985],[1987], Hoshi & Baba [1986], Ku & Patterson [1988] and Parker [1989]).

Figure 6.8 illustrates the instantaneous power losses for the Zeta compression rings at 3000 rpm under fully flooded conditions. As expected, power losses increase with increasing piston speed. The power losses are determined not only by the sliding speeds

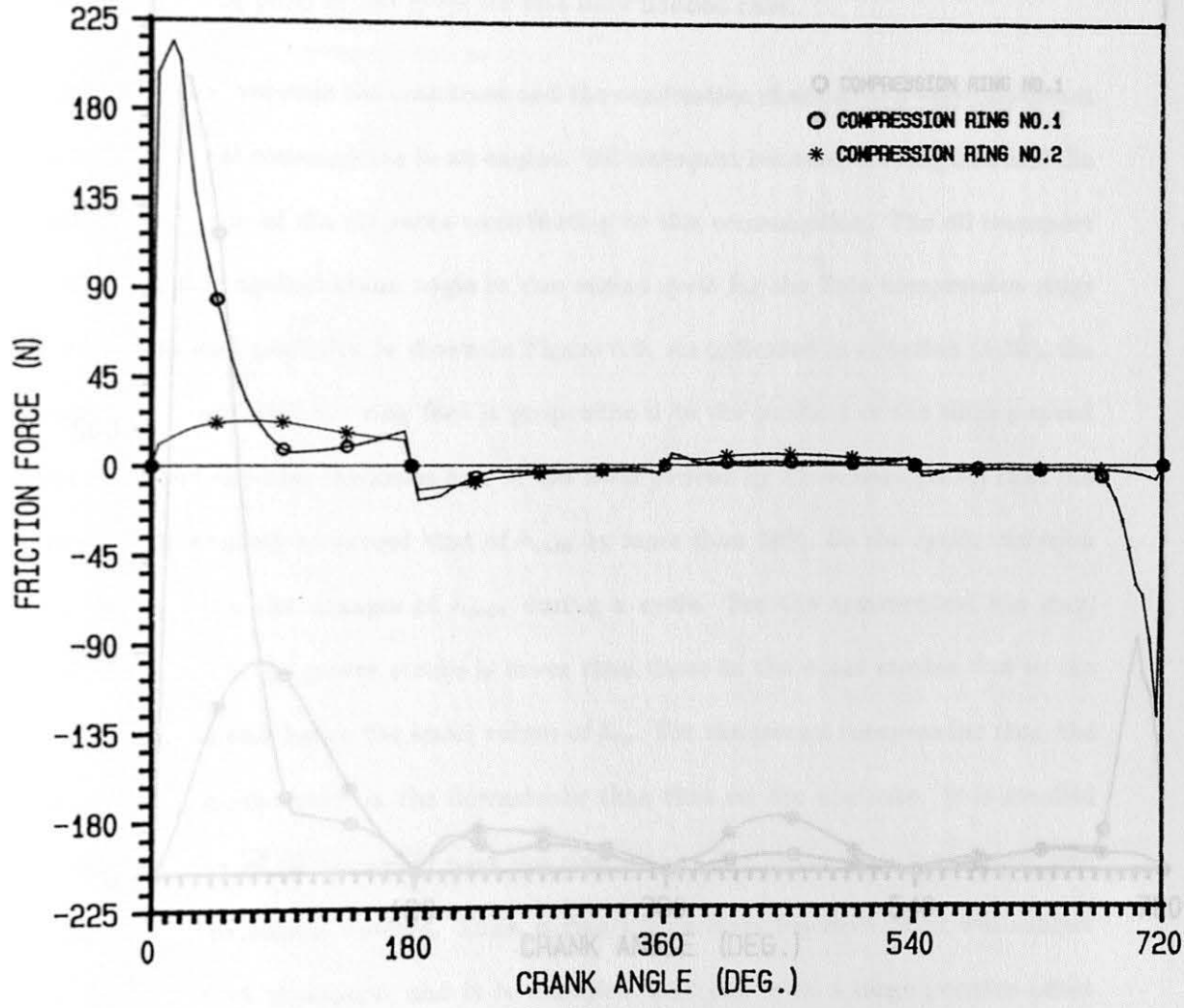

Figure 6.7. Cyclic Variation of Friction Forces on the Compression Rings in the Ford Zeta Engine at 3000 rpm under Fully Flooded Conditions

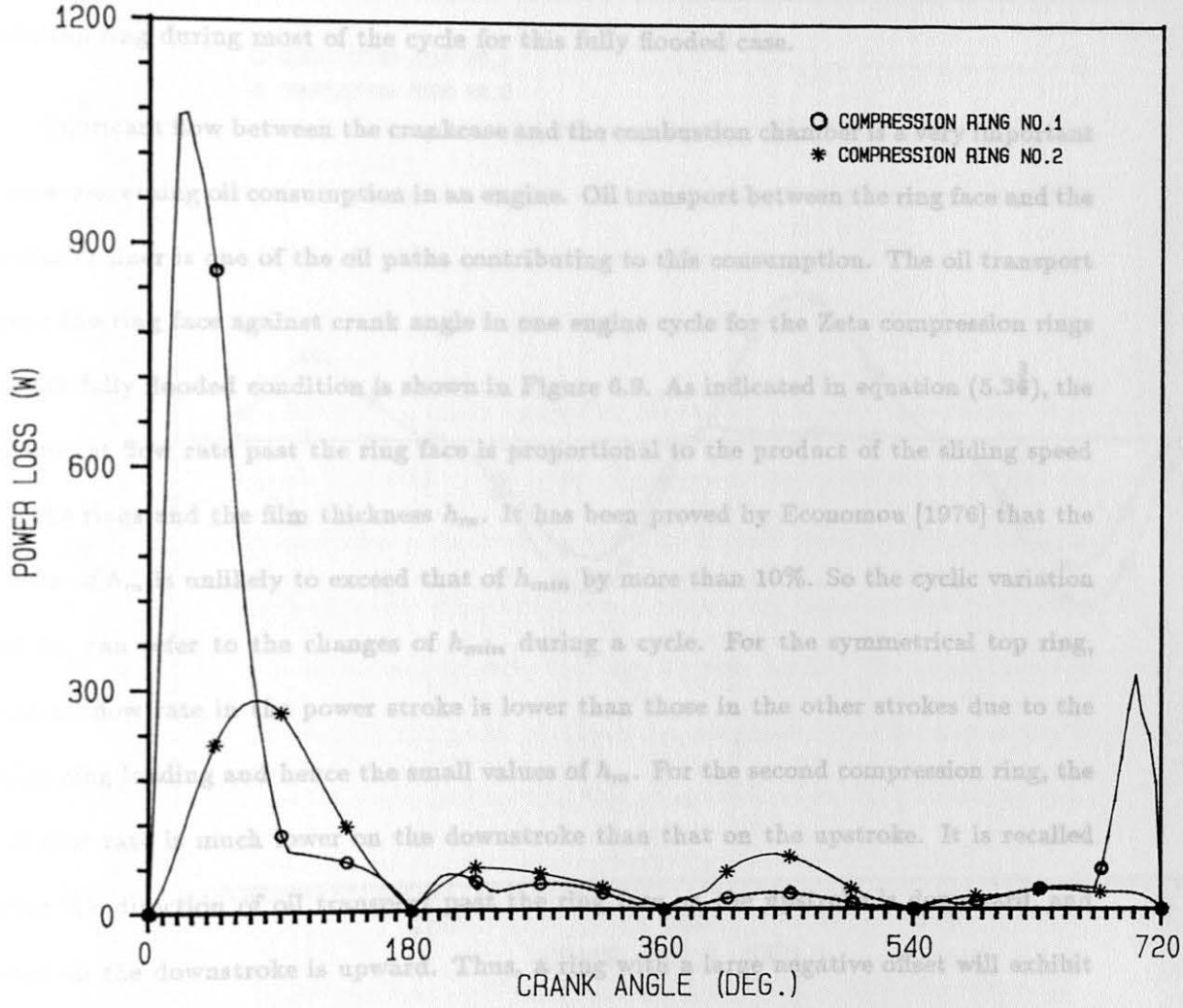

Figure 6.8. Cyclic Variation of Power Losses for the Compression Rings in the Ford Zeta Engine at 3000 rpm under Fully Flooded Conditions

of the ring but also by the friction forces acting on the ring faces. It is interesting to note that the power loss for the second compression ring is bigger than that for the top ring over most of the strokes, except for the first half of the power stroke and the latter part of the compression stroke. This means that the second ring consumes more energy than the top ring during most of the cycle for this fully flooded case.

Lubricant flow between the crankcase and the combustion chamber is a very important issue concerning oil consumption in an engine. Oil transport between the ring face and the cylinder liner is one of the oil paths contributing to this consumption. The oil transport past the ring face against crank angle in one engine cycle for the Zeta compression rings under fully flooded condition is shown in Figure 6.9. As indicated in equation (5.3$\dot{6}$), the lubricant flow rate past the ring face is proportional to the product of the sliding speed of the rings and the film thickness h_m. It has been proved by Economou [1976] that the value of h_m is unlikely to exceed that of h_{min} by more than 10%. So the cyclic variation of h_m can refer to the changes of h_{min} during a cycle. For the symmetrical top ring, the oil flow rate in the power stroke is lower than those in the other strokes due to the high ring loading and hence the small values of h_m. For the second compression ring, the oil flow rate is much lower on the downstroke than that on the upstroke. It is recalled that the direction of oil transport past the ring face on the upstroke is downward, and that on the downstroke is upward. Thus, a ring with a large negative offset will exhibit a net downward oil transport, and it is expected that one with a large positive offset exhibits a net upward oil transport. This confirms the practical evidence of the strong uni-directional oil scraping action of rings with asymmetrical profiles. In practice it may be expected that the effective offset of the ring profile will vary throughout the engine cycle. This is due to the dynamic behaviour of the ring and piston and also due to the

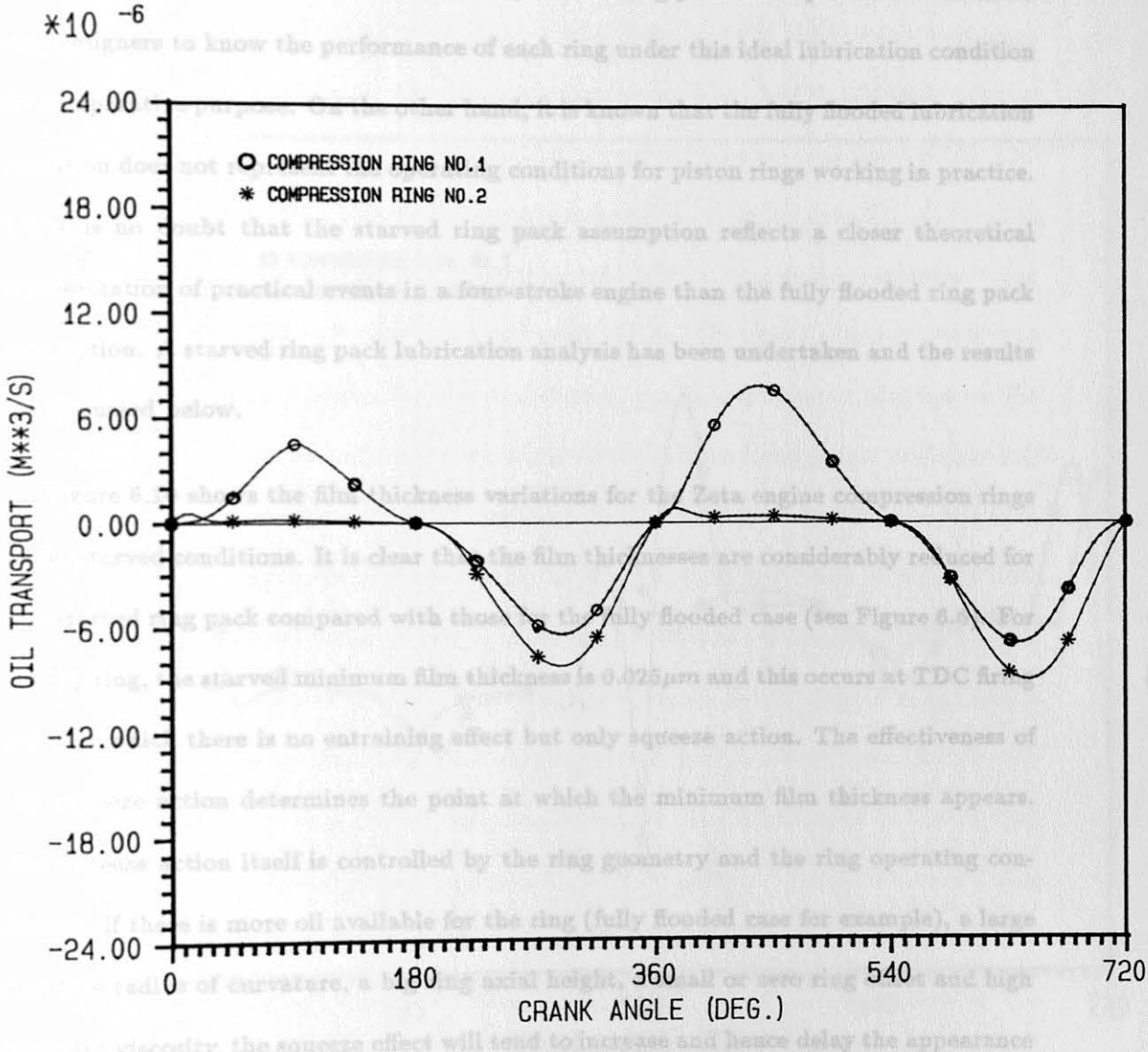

Figure 6.9. Cyclic Variation of Oil Transport Past Ring Faces for the Compression Rings in the Ford Zeta Engine at 3000 rpm under Fully Flooded Conditions

deformation of the cylinder liner.

The above discussion is based on the fully flooded ring pack assumption. It is useful for ring designers to know the performance of each ring under this ideal lubrication condition for comparative purpose. On the other hand, it is known that the fully flooded lubrication condition does not represent the operating conditions for piston rings working in practice. There is no doubt that the starved ring pack assumption reflects a closer theoretical representation of practical events in a four-stroke engine than the fully flooded ring pack assumption. A starved ring pack lubrication analysis has been undertaken and the results are discussed below.

Figure 6.10 shows the film thickness variations for the Zeta engine compression rings under starved conditions. It is clear that the film thicknesses are considerably reduced for this starved ring pack compared with those for the fully flooded case (see Figure 6.6). For the top ring, the starved minimum film thickness is $0.025\mu m$ and this occurs at TDC firing point at which there is no entraining effect but only squeeze action. The effectiveness of this squeeze action determines the point at which the minimum film thickness appears. The squeeze action itself is controlled by the ring geometry and the ring operating conditions. If there is more oil available for the ring (fully flooded case for example), a large ring face radius of curvature, a big ring axial height, a small or zero ring offset and high lubricant viscosity, the squeeze effect will tend to increase and hence delay the appearance of the minimum film thickness from the TDC firing position. Looking at the curve for the top ring film thickness variation again, two further points are worthy of note. Firstly, it can be seen that there are four peaks around TDC. This is the area over which the ring has to travel before it reaches the region of the liner previously covered by the second ring. Within this area the amount of oil available to the ring is uncertain. The assumption

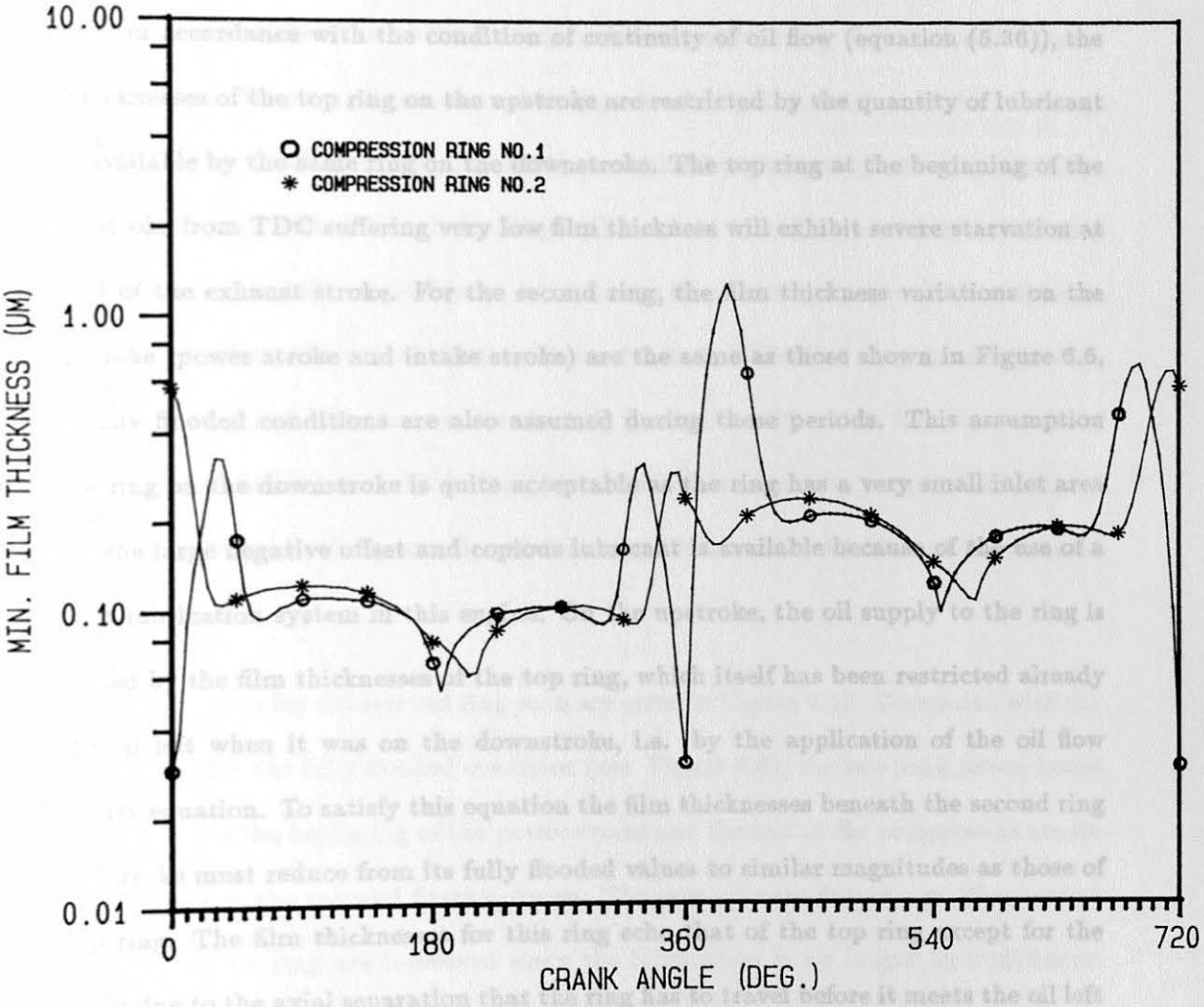

Figure 6.10. Cyclic Variation of Film Thicknesses for the Compression Rings in the Ford Zeta Engine at 3000 rpm under Starved Conditions

that the oil available to the ring on one stroke is that left by the same ring on its previous stroke seems reasonable. Secondly, the most marked change on the curve compared with the fully flooded condition is at 360^0 crank angle. Here, despite the low gas loading in this region, the film thicknesses are of the same order as those at 0^0 crank angle. This is because, in accordance with the condition of continuity of oil flow (equation (5.36)), the film thicknesses of the top ring on the upstroke are restricted by the quantity of lubricant made available by the same ring on the downstroke. The top ring at the beginning of the power stroke from TDC suffering very low film thickness will exhibit severe starvation at the end of the exhaust stroke. For the second ring, the film thickness variations on the downstroke (power stroke and intake stroke) are the same as those shown in Figure 6.6, since fully flooded conditions are also assumed during these periods. This assumption for the ring on the downstroke is quite acceptable as the ring has a very small inlet area due to the large negative offset and copious lubricant is available because of the use of a fixed-jet lubrication system in this engine. On the upstroke, the oil supply to the ring is controlled by the film thicknesses of the top ring, which itself has been restricted already by the oil left when it was on the downstroke, i.e. by the application of the oil flow continuity equation. To satisfy this equation the film thicknesses beneath the second ring on this stroke must reduce from its fully flooded values to similar magnitudes as those of the top ring. The film thicknesses for this ring echo that of the top ring except for the phase lag due to the axial separation that the ring has to travel before it meets the oil left on the liner by the top ring. The application of the principal of continuity of oil flow to the rings of the pack has been shown to have an equalizing effect on the film thicknesses beneath individual rings (Figure 6.10). This has since been confirmed experimentally by Brown and Hamilton [1977] and Moore and Hamilton [1978].

Figure 6.11 shows the friction forces in a cycle for the two compression rings in the Zeta engine under starved lubrication condition. The peak friction force for the top ring is about $140N$, compared with the value of about $210N$ under the fully flooded condition (see Figure 6.7). This is due to the so-called load relief effect since the starvation of the ring allows gas pressures to reach the exposed areas of the ring face and release part of the ring load. Because of the starved ring pack assumption, neither of the two rings can generate film thicknesses larger than the combined surface roughnesses of the rings and the liner. This means that both rings will work in mixed or boundary lubrication conditions throughout the engine cycle. Also, due to the starvation assumption and hence the load relief effect, the overall friction forces fcr each individual ring do not increase significantly compared with those under the fully flooded conditions. In fact, the results of both the film thicknesses and the friction forces for the starved ring pack are determined by the balance between the quantities of the starved lubricant available and the released load of the rings.

The power losses for the starved ring pack are given in Figure 6.12. Compared with the power losses under the fully flooded condition (see Figure 6.8), the two peak power losses for the top ring at the beginning of the power stroke and the end of the compression stroke are reduced due to the reduced friction forces. The power losses during any other period of the cycle for the ring are increased since the lubrication is no longer hydrodynamic but mixed or boundary. The same conclusion is also applicable to the second ring on the upstroke. Another interesting point is that the top ring seems to consume more energy than the second ring during most of the cycle except for the late power stroke. This is perhaps due to the larger axial ring height, the higher loadings from the increased gas pressure and the bigger elastic tension of the top ring than those of the second ring.

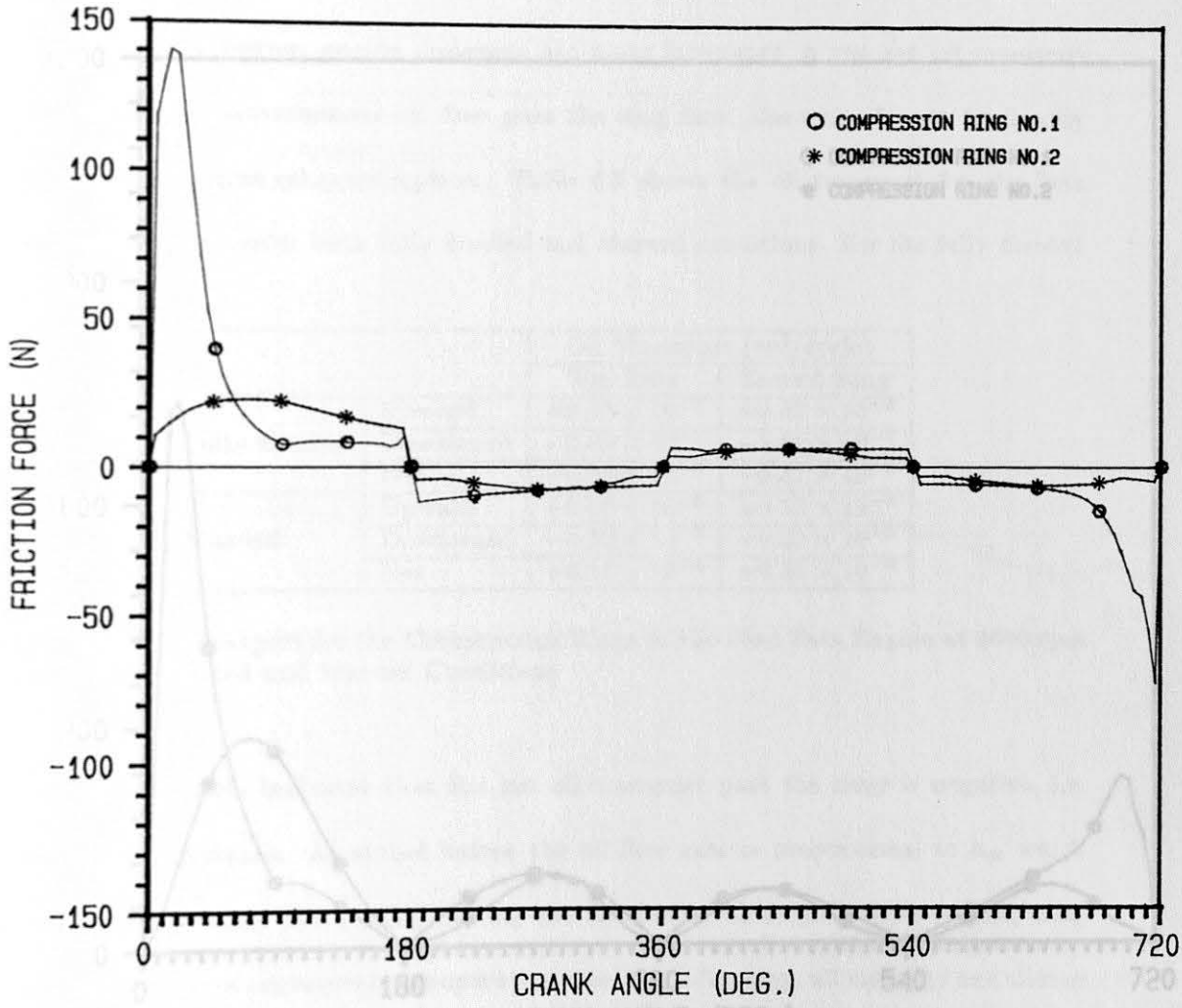

Figure 6.11. Cyclic Variation of Friction Forces on the Compression Rings in the Ford Zeta Engine at 3000 rpm under Starved Conditions

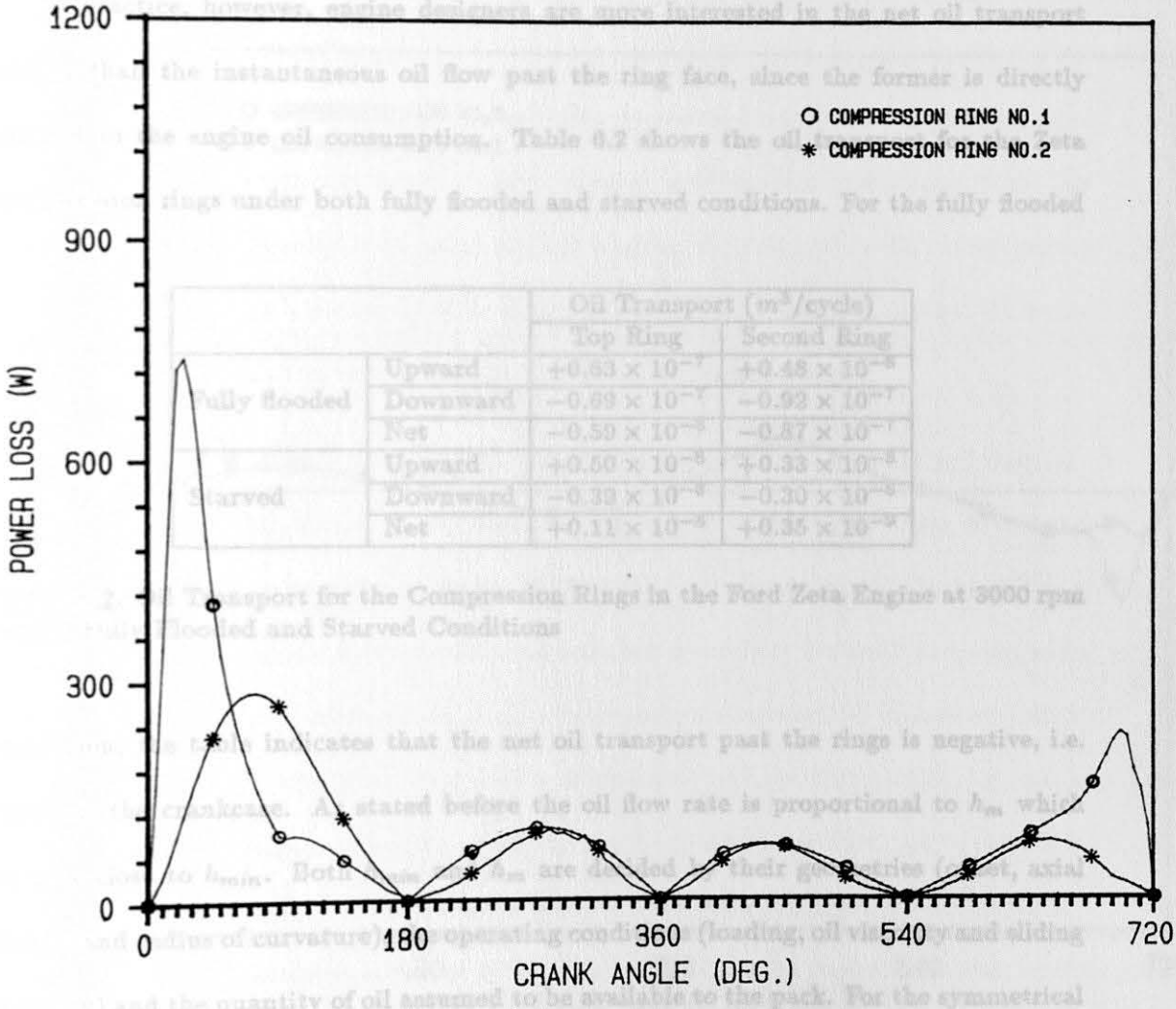

Figure 6.12. Cyclic Variation of Power Losses for the Compression Rings in the Ford Zeta Engine at 3000 rpm under Starved Conditions

The predicted cyclic variation of oil transport past the ring faces for the Zeta compression rings under the starved conditions is presented in Figure 6.13. It can be seen clearly that the oil transports are much lower than those under fully flooded conditions (see Figure 6.9).

In practice, however, engine designers are more interested in the net oil transport rather than the instantaneous oil flow past the ring face, since the former is directly related to the engine oil consumption. Table 6.2 shows the oil transport for the Zeta compression rings under both fully flooded and starved conditions. For the fully flooded

		Oil Transport (m^3/cycle)	
		Top Ring	Second Ring
Fully flooded	Upward	$+0.63 \times 10^{-7}$	$+0.48 \times 10^{-8}$
	Downward	-0.69×10^{-7}	-0.92×10^{-7}
	Net	-0.59×10^{-8}	-0.87×10^{-7}
Starved	Upward	$+0.50 \times 10^{-8}$	$+0.33 \times 10^{-8}$
	Downward	-0.39×10^{-8}	-0.30×10^{-8}
	Net	$+0.11 \times 10^{-8}$	$+0.35 \times 10^{-9}$

Table 6.2. Oil Transport for the Compression Rings in the Ford Zeta Engine at 3000 rpm under Fully Flooded and Starved Conditions

condition, the table indicates that the net oil transport past the rings is negative, i.e. towards the crankcase. As stated before the oil flow rate is proportional to h_m which is very close to h_{min}. Both h_{min} and h_m are decided by their geometries (offset, axial height and radius of curvature), the operating conditions (loading, oil viscosity and sliding velocity) and the quantity of oil assumed to be available to the pack. For the symmetrical top ring under fully flooded conditions, h_m is strongly related to ring loading. Since the loading in the power stroke (note oil transport in this stroke is upward) for the ring is much higher than those on other strokes, the values of h_m are relatively lower than those of other strokes (see Figure 6.9). So it is quite possible for the top ring under fully

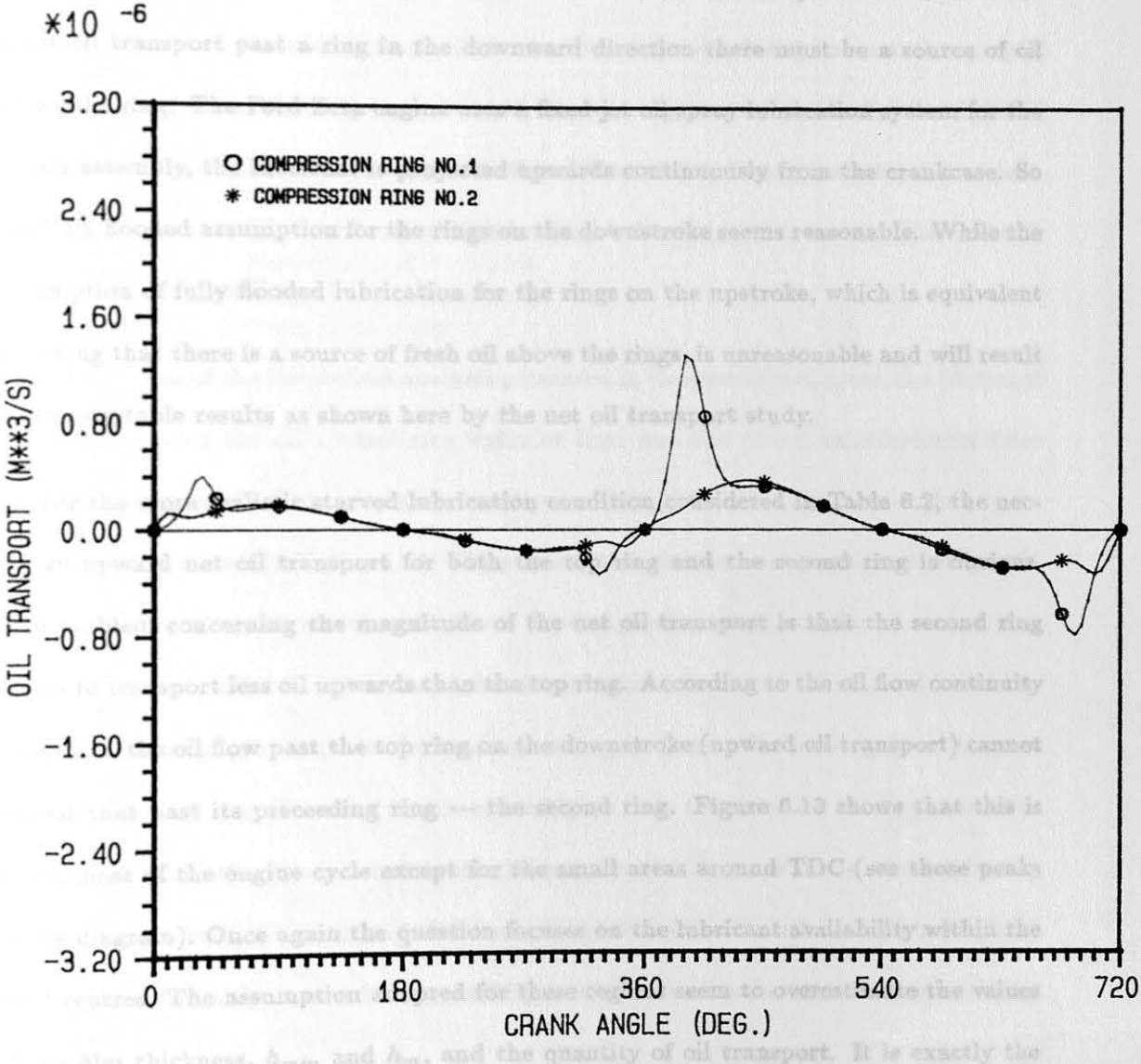

Figure 6.13. Cyclic Variation of Oil Transport Past Ring Faces for the Compression Rings in the Ford Zeta Engine at 3000 rpm under Starved Conditions

flooded assumption to have more downward oil transport than upward, i.e. negative net oil transport. For the second ring under the fully flooded assumption, h_m is dominated by the large negative ring face offset for the given working condition. The strong downward oil scraping action will no doubt present a net downward oil transport. For there to be a net oil transport past a ring in the downward direction there must be a source of oil above the ring. The Ford Zeta engine uses a fixed-jet oil spray lubrication system for the piston assembly, the lubricant is projected upwards continuously from the crankcase. So the fully flooded assumption for the rings on the downstroke seems reasonable. While the assumption of fully flooded lubrication for the rings on the upstroke, which is equivalent to saying that there is a source of fresh oil above the rings, is unreasonable and will result in unacceptable results as shown here by the net oil transport study.

For the more realistic starved lubrication condition considered in Table 6.2, the necessary upward net oil transport for both the top ring and the second ring is obvious. One problem concerning the magnitude of the net oil transport is that the second ring seems to transport less oil upwards than the top ring. According to the oil flow continuity condition, the oil flow past the top ring on the downstroke (upward oil transport) cannot exceed that past its preceeding ring — the second ring. Figure 6.13 shows that this is so for most of the engine cycle except for the small areas around TDC (see those peaks in the diagram). Once again the question focuses on the lubricant availability within the dead centres. The assumption adopted for these regions seem to overestimate the values of the film thickness, h_{min} and h_m, and the quantity of oil transport. It is exactly the unknown amount of the oil available within these zones that causes the above problem.

Oil transport is an important and complicated issue in the analyses of lubrication of a ring pack and oil consumption in an engine. Besides the influences from ring geometry

and operating conditions mentioned above, some other even more complex factors may in one way or another affect oil transport. The distortion of the piston and the liner, the oil accumulation within the pack, the gas flow through the pack and the dynamic behaviour of the ring such as ring tilting will all have some effects on oil transport and the performance of the piston rings. It is ideal for the second ring to control a proper volume of oil to enter the ring pack, so that the top ring receives just sufficient oil for it to generate an adequate film to survive in the adverse thermal and pressure environment in which it operates. Too much oil will lead to high oil consumption and too little oil will result in top ring scuffing.

On the basis of the theoretical analysis presented in the previous chapter, the frictional power losses from the oil control ring/cylinder liner and the piston skirt/cylinder liner have been calculated. This allows the total power loss picture for the Zeta engine to be determined, as shown in Figure 6.14. The power losses are the average values at a specific engine speed over one complete cycle. Since the compression rings and the oil control ring are working in the mixed or boundary lubrication regime, the friction forces and hence the power losses are proportional to the loadings acting on them. The loading from inherent elastic tension on the oil control ring is much higher than the resultant loadings from the gas pressures and the elastic tensions on the compression rings, thus the oil control ring consumes more energy than any of the the compression rings. To reduce the power losses of the piston assembly, it may be suggested that the elastic tension of the oil control ring be reduced.

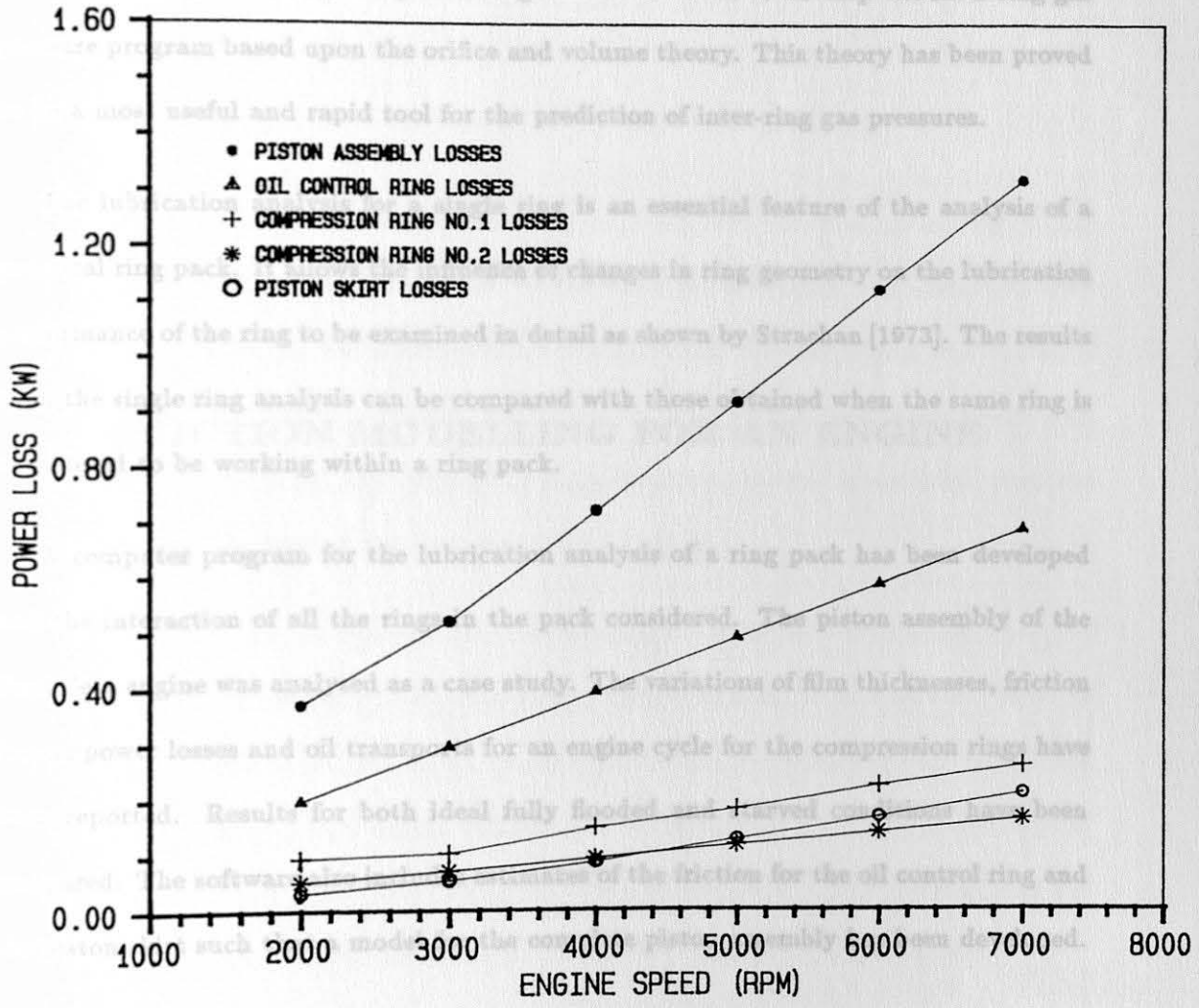

Figure 6.14. Power Losses in the Piston Assembly for the Ford Zeta Engine

6.4 Conclusions

A piston assembly friction model has been established and it is certainly a useful design aid for engineers faced with the practical problems of engine development.

The role of gas loadings on piston rings led to the need to develop the inter-ring gas pressure program based upon the orifice and volume theory. This theory has been proved to be a most useful and rapid tool for the prediction of inter-ring gas pressures.

The lubrication analysis for a single ring is an essential feature of the analysis of a practical ring pack. It allows the influence of changes in ring geometry on the lubrication performance of the ring to be examined in detail as shown by Strachan [1973]. The results from the single ring analysis can be compared with those obtained when the same ring is considered to be working within a ring pack.

A computer program for the lubrication analysis of a ring pack has been developed and the interaction of all the rings in the pack considered. The piston assembly of the Ford Zeta engine was analysed as a case study. The variations of film thicknesses, friction forces, power losses and oil transports for an engine cycle for the compression rings have been reported. Results for both ideal fully flooded and starved conditions have been compared. The software also includes estimates of the friction for the oil control ring and the piston skirt such that a model for the complete piston assembly has been developed.

The effects of piston ring dynamics, wear, thermal expansions and elastic deformation of rings, piston and cylinder liner, ring lifting and gas blow-by etc. are beyond the scope of the present work, and therefore are not included.

Part IV

FRICTION MODELLING FOR AN ENGINE

Chapter Seven

Engine Friction Model and Zeta Engine Analysis

7.1 Introduction

It is well accepted that engine friction is very important to fuel economy and significant gains in engine efficiency can be obtained by the reduction of friction. Much research work has been undertaken for the investigation of friction sources in an engine and the ways in which reductions can be achieved. So far the majority of this work has concentrated on the experimental side. Although some engine friction models are available, they are strongly empirically related and have limited application.

The extensive study of the main lubricated engine components (the bearings, the valve train and the piston assembly) described in this thesis has made it possible for a versatile engine friction model to be developed. The friction model for engines has been established in the following chapter by a simple combination of the three component models evolved earlier. The Ford 1.8L H.O. Zeta engine has been studied with the new model and the results will be compared with experimental evidence presented by other workers.

7.2 Engine Friction Model

The importance of engine friction to fuel economy has been reviewed at the beginning of this thesis. A study of friction and lubrication in the major engine components has been undertaken.

By combining all the component models established earlier into an integrated model called FLAME (Friction and Lubrication Analysis Model for Engines), the prediction of the whole engine frictional losses can be realised. FLAME is based on the component models and its validation is obviously heavily dependent on them. Fortunately, these components have been studied in depth throughout the world and the verified theories and sound engineering judgements make it possible for engineers to use FLAME with confidence. Unlike most of other engine friction models, FLAME does not use any empirically determined parameters, this makes its application unrestricted for any kind of internal combustion engine.

7.3 Zeta Engine Analysis

With all the input data available and listed in Appendices, the Ford 1.8L H.O. Zeta engine has been analysed and the results are presented below.

Figure 7.1 shows the power losses of the three main engine components versus engine speed. The total engine frictional losses are also presented with no inclusion of engine accessories. It can be seen that the power losses due to the piston assembly friction are much greater than those either from the engine bearing friction or from the valve train friction. The power losses for the bearings are lower than those for the valve train at relatively low engine speeds (2000 and 3000 rpm), but higher at high engine speeds (5000, 6000 and 7000 rpm). Although the frictional power losses from each of the three main components all increase with an increase of engine speed, the rate of increase and hence their proportions in the total engine power losses are different. At an engine speed of 3000 rpm, the bearings account for about 17% of the total engine frictional losses, the valve train about 20% and the piston assembly at some 63%. While at an engine speed of

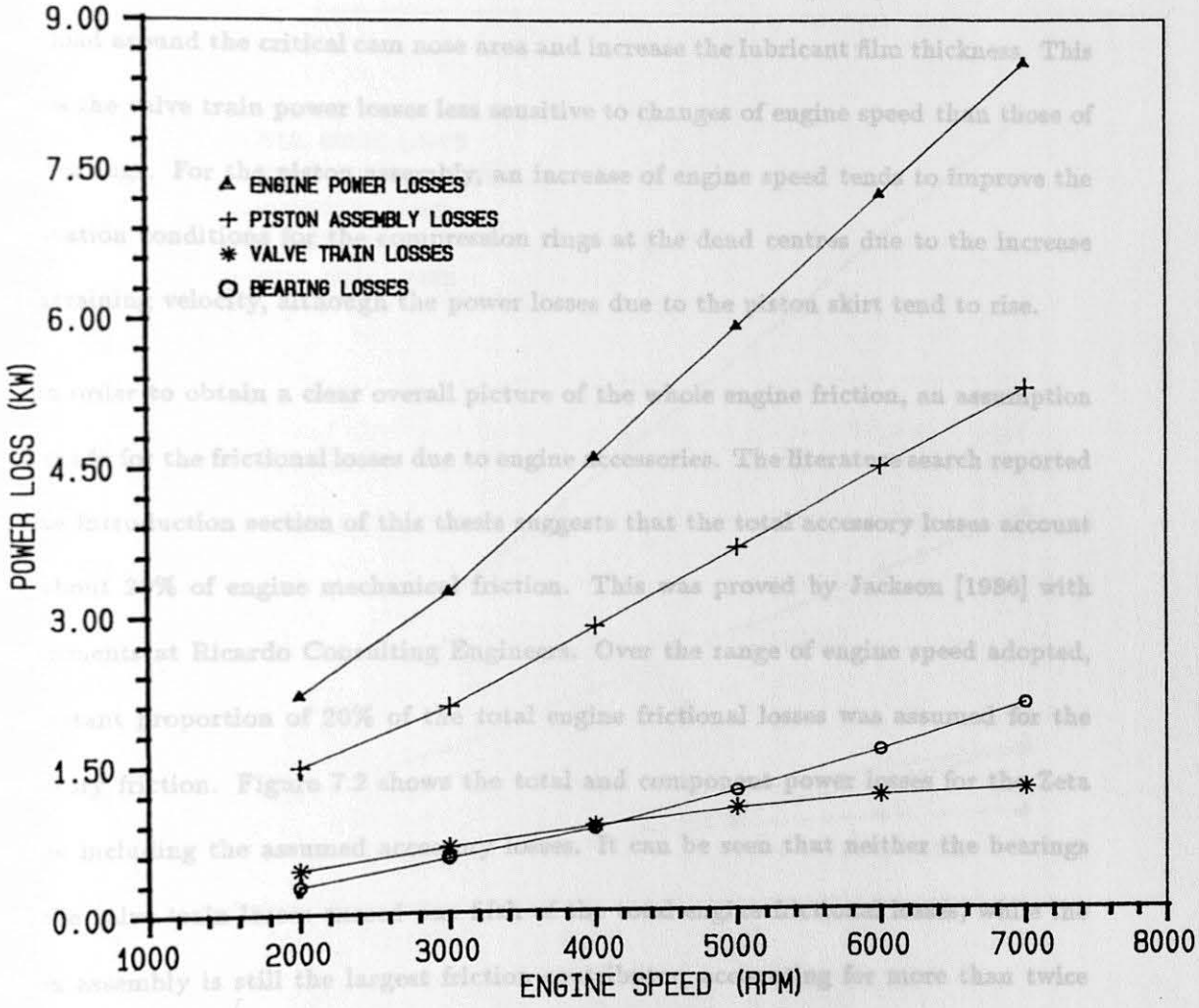

Figure 7.1. Total and Component Power Losses for the Ford Zeta Engine without Accessories

6000 rpm, these percentages become 22%, 16% and 62%, respectively. Since the bearings operate in the hydrodynamic lubrication regime, their frictional losses are directly related with the change of engine speed. The power losses from the valve train are dominated by the friction at the interfaces of cams and followers which operate almost all the time in mixed or boundary lubrication conditions. The increase of engine speed will decrease cam load around the critical cam nose area and increase the lubricant film thickness. This makes the valve train power losses less sensitive to changes of engine speed than those of the bearings. For the piston assembly, an increase of engine speed tends to improve the lubrication conditions for the compression rings at the dead centres due to the increase of entraining velocity, although the power losses due to the piston skirt tend to rise.

In order to obtain a clear overall picture of the whole engine friction, an assumption was made for the frictional losses due to engine accessories. The literature search reported in the Introduction section of this thesis suggests that the total accessory losses account for about 20% of engine mechanical friction. This was proved by Jackson [1986] with experiments at Ricardo Consulting Engineers. Over the range of engine speed adopted, a constant proportion of 20% of the total engine frictional losses was assumed for the accessory friction. Figure 7.2 shows the total and component power losses for the Zeta engine including the assumed accessory losses. It can be seen that neither the bearings nor the valve train losses exceed one fifth of the total engine frictional losses, while the piston assembly is still the largest friction contributor, accounting for more than twice the friction from any other individual component.

The distribution of these component losses for the Zeta engine, expressed in percentage of the total engine friction, is illustrated in the form of pie charts in Figures 7.3 and 7.4. The former is for the engine running at 3000 rpm while the latter is for 6000 rpm. The

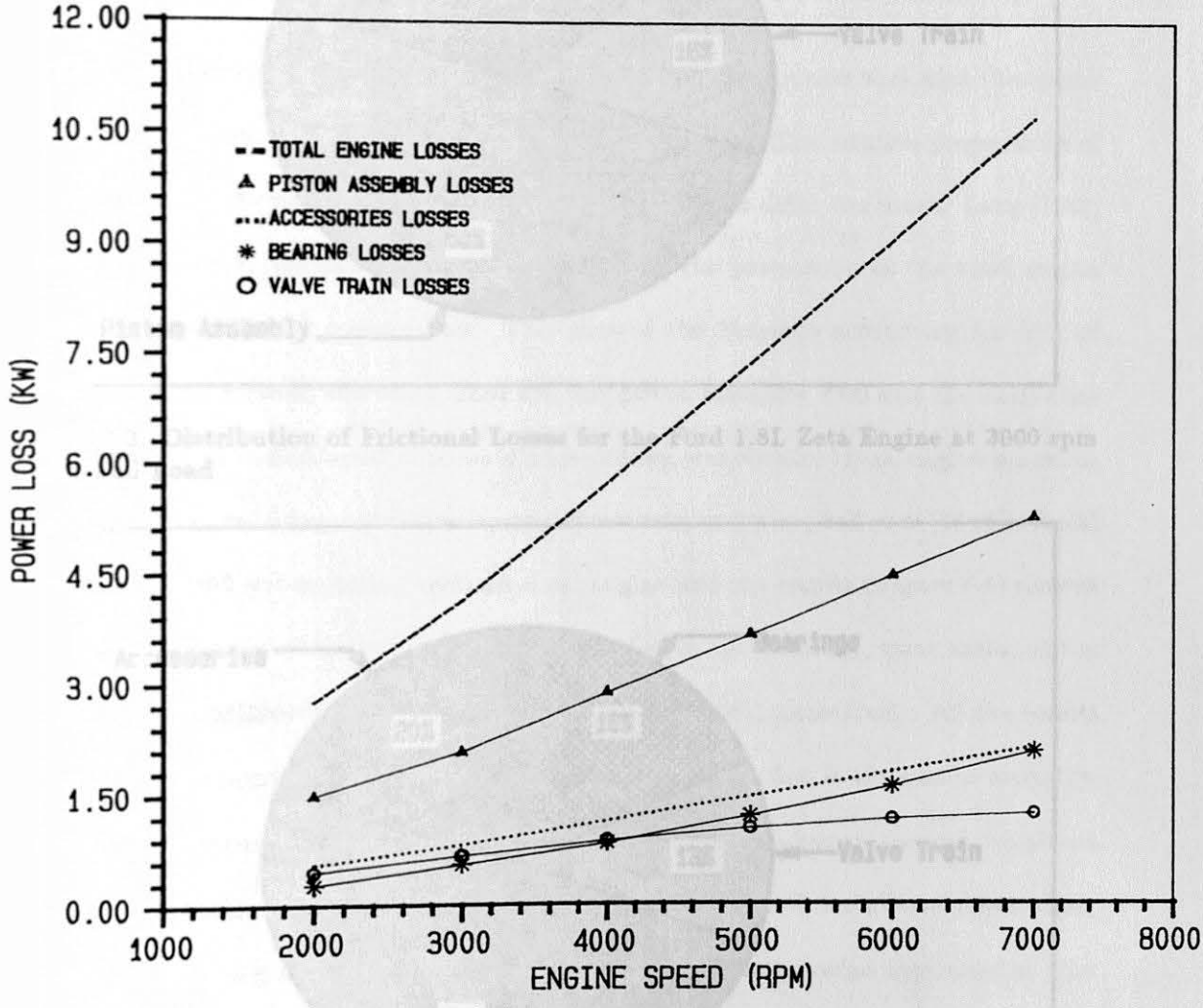

Figure 7.2. Total and Component Power Losses for the Ford Zeta Engine

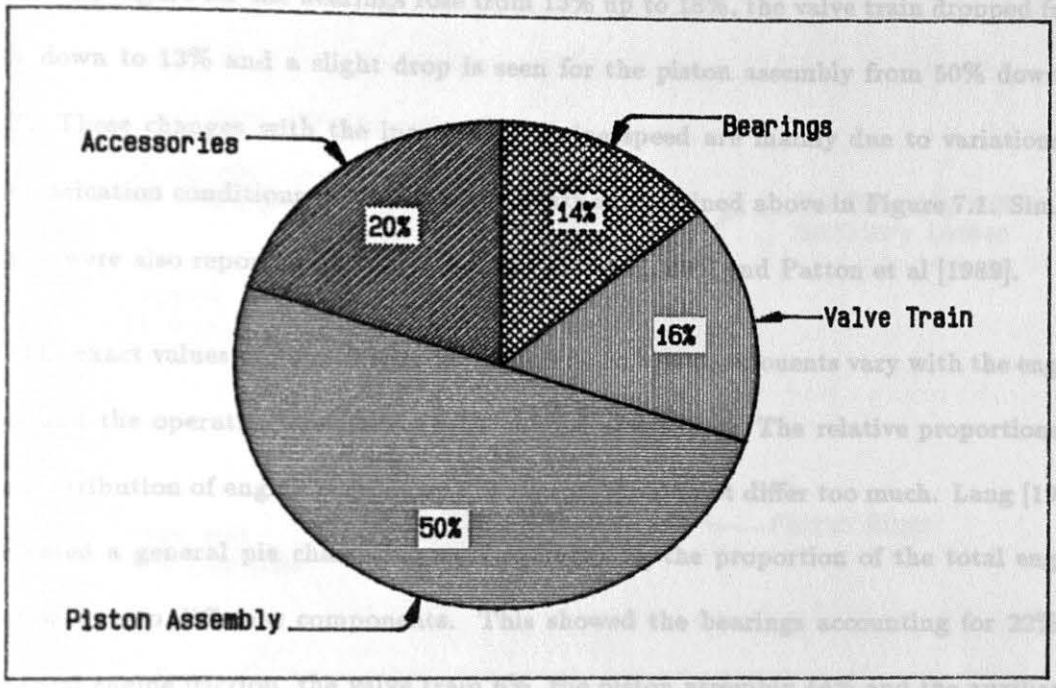

Figure 7.3. Distribution of Frictional Losses for the Ford 1.8L Zeta Engine at 3000 rpm under Full Load

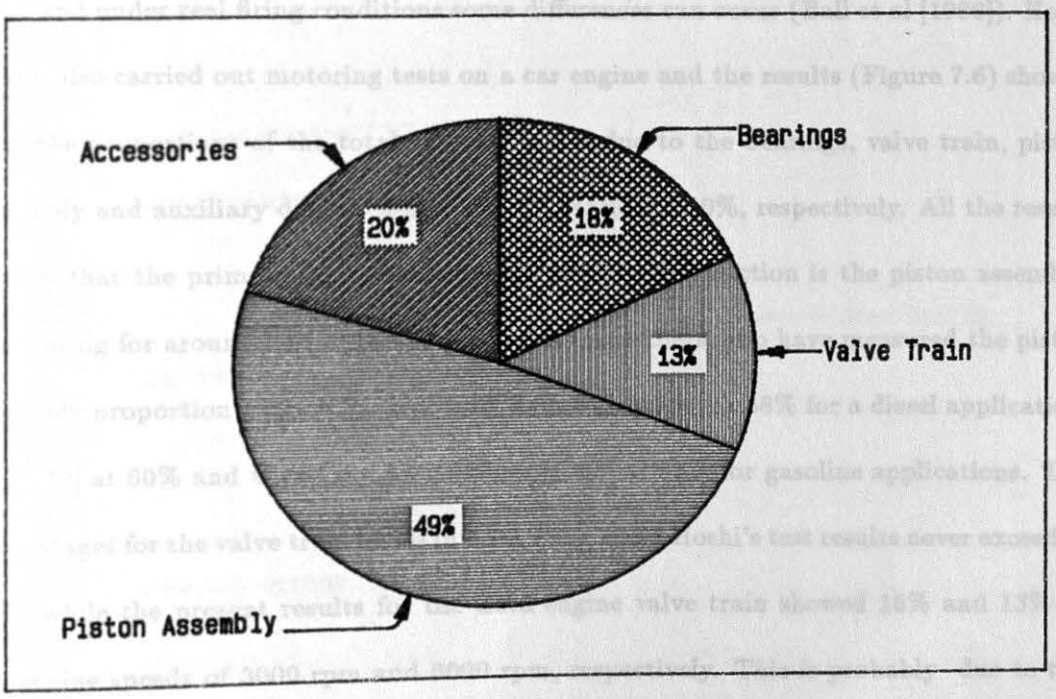

Figure 7.4. Distribution of Frictional Losses for the Ford 1.8L Zeta Engine at 6000 rpm under Full Load

percentage figure for the bearings rose from 13% up to 18%, the valve train dropped from 16% down to 13% and a slight drop is seen for the piston assembly from 50% down to 49%. These changes with the increase of engine speed are mainly due to variations in the lubrication conditions for these components as explained above in Figure 7.1. Similar trends were also reported by Cleveland and Bishop [1960] and Patton et al [1989].

The exact values of power losses for an engine and its components vary with the engine type and the operating conditions such as load and speed. The relative proportions of the contribution of engine components, however, should not differ too much. Lang [1982] presented a general pie chart (Figure 7.5) outlining the proportion of the total engine friction due to different components. This showed the bearings accounting for 22% of the total engine friction, the valve train 6%, the piston assembly 44% and the auxiliaries 28%. It should be remembered that Lang's breakdown was obtained from engine motoring tests and under real firing conditions some differences can occur (Ball et al [1986]). Hoshi [1984] also carried out motoring tests on a car engine and the results (Figure 7.6) showed that the proportions of the total engine friction due to the bearings, valve train, piston assembly and auxiliary devices were 37%, 8%, 45% and 10%, respectively. All the results proved that the primary contributor to the total engine friction is the piston assembly, accounting for around half of the total. Other researchers who have measured the piston assembly proportion include Ricardo and Hempson [1968] at 58% for a diesel application, Li [1982] at 60% and Cleveland and Bishop [1960] at 67% for gasoline applications. The percentages for the valve train losses in both Lang's and Hoshi's test results never exceeded 10%, while the present results for the Zeta engine valve train showed 16% and 13% at the engine speeds of 3000 rpm and 6000 rpm, respectively. This is probably due to the different valve train system used in these different engines. Both engines in the Lang and

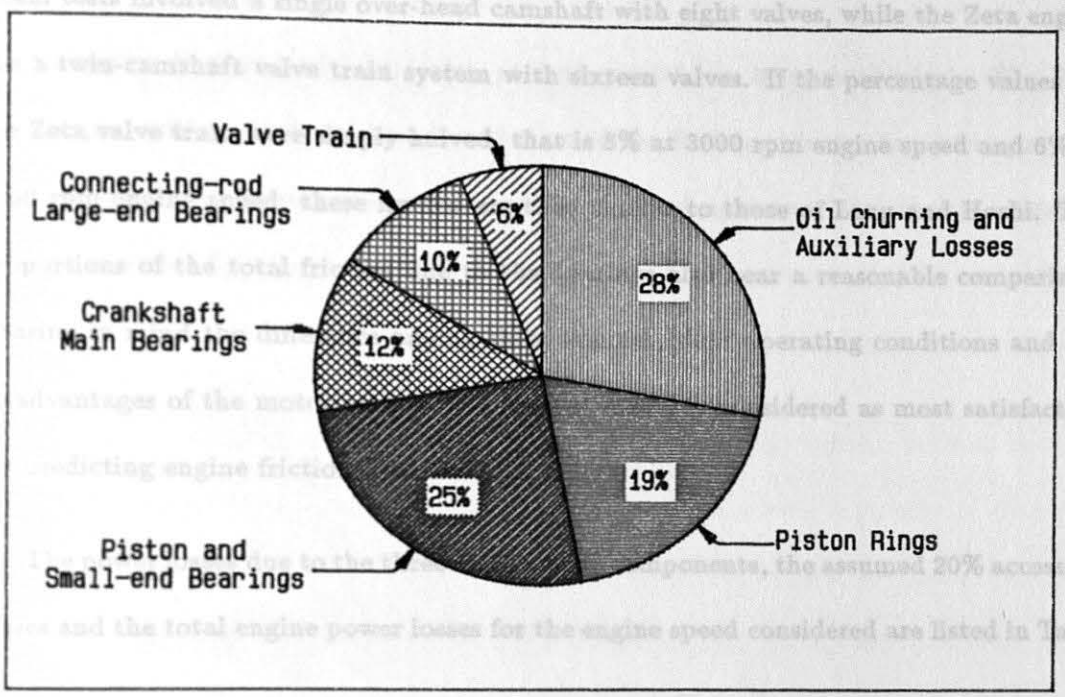

Figure 7.5. Breakdown of Mechanical Losses for a Motored Car Engine (Lang [1982])

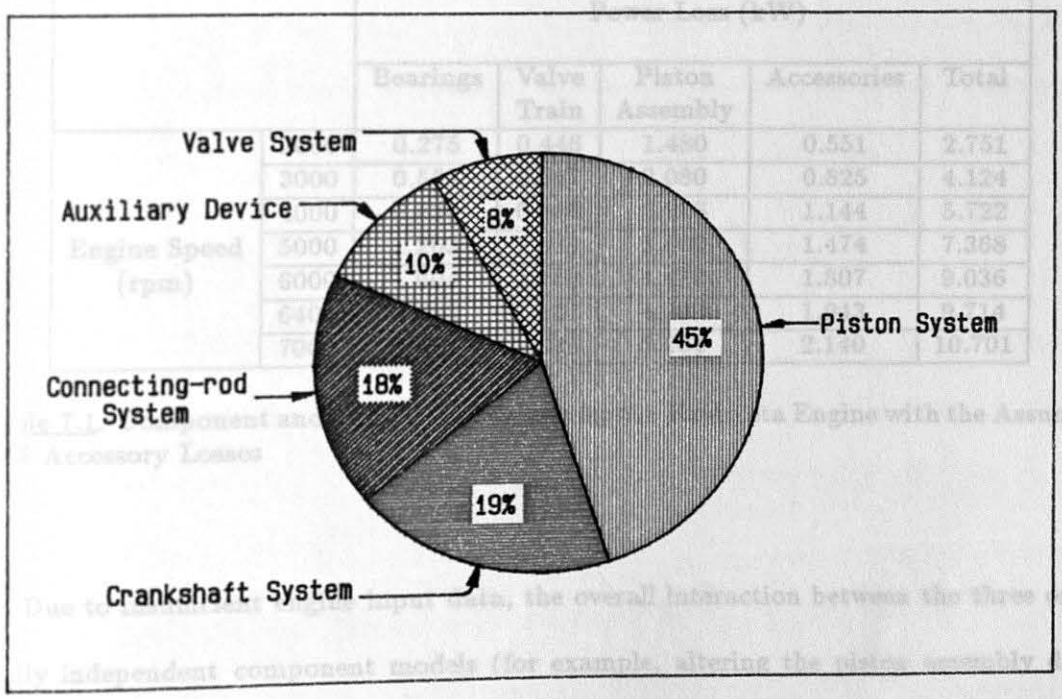

Figure 7.6. Frictional Contributions of the Components to the Total Losses for a 1.3L Automotive Engine at 5000 rpm under Full Load (Hoshi [1984])

Hoshi tests involved a single over-head camshaft with eight valves, while the Zeta engine has a twin-camshaft valve train system with sixteen valves. If the percentage values for the Zeta valve train were simply halved, that is 8% at 3000 rpm engine speed and 6% at 6000 rpm engine speed, these figures are then similar to those of Lang and Hoshi. The proportions of the total friction due to the bearings also bear a reasonable comparison. Bearing in mind the difference among these engines, their operating conditions and the disadvantages of the motoring test, the present model is considered as most satisfactory for predicting engine frictional losses.

The power losses due to the three main engine components, the assumed 20% accessory losses and the total engine power losses for the engine speed considered are listed in Table 7.1.

		Power Loss (kW)				
		Bearings	Valve Train	Piston Assembly	Accessories	Total
Engine Speed (rpm)	2000	0.275	0.446	1.480	0.551	2.751
	3000	0.552	0.667	2.080	0.825	4.124
	4000	0.836	0.866	2.876	1.144	5.722
	5000	1.203	1.031	3.660	1.474	7.368
	6000	1.604	1.153	4.472	1.807	9.036
	6400	1.785	1.187	4.800	1.943	9.714
	7000	2.074	1.223	5.264	2.140	10.701

Table 7.1. Component and Total Power Losses for the Ford Zeta Engine with the Assumed 20% Accessory Losses

Due to insufficient engine input data, the overall interaction between the three originally independent component models (for example, altering the piston assembly data could also affect the performance of engine bearings) cannot be identified.

7.4 Conclusions

An engine friction and lubrication analysis model has been established. The Ford Zeta engine was studied and the distribution of the frictional losses for the engine has been presented. The results presented here show a good agreement with the experimental findings reported by other workers.

CONCLUSIONS AND SUGGESTIONS FOR FUTURE WORK

CS.1 Conclusions

A very wide ranging study has been necessary to enable the present work to be completed. This work represents a huge research project concerning the study of all major engine components. It covers complicated engine parts, such as big-end bearings, main bearings, cams and followers, camshaft bearings, piston rings and piston skirts as well as the relatively simple components such as follower guides and valve guides. The large quantity of work has involved not only a vast literature search and computer coding, but also the assimilation of a wide range of engineering science/technical data obtained by measuring the geometry of components and reading the design drawings. Conclusions can be drawn conveniently within the sub-divisions used in this thesis.

(A) Conclusions from Engine Bearing Friction Model

(a) The Short Bearing Mobility Method has proved to be one of the most effective methods for dealing with bearing lubrication problems. It is quick and simple and provides results which compare well with full numerical solutions.

(b) To reduce the friction it is possible within limits to employ bearings of smaller diameter, smaller length with larger clearance and a lower viscosity oil. These modifications have to be undertaken carefully, as stiffness, strength, film thickness, misalignment and noise problems may appear.

(c) Rapid methods usually provide answers which may be used on a comparative basis against previous experience and allow the effect of the interrelation of the many variables to be studied. Examples include the quasi-steady load approach and the Petroff equation as presented in this study. The former in particular gives very close agreement with more accurate numerical methods.

(d) Grooving arrangements have a great effect on bearing performance. Centrally grooved bearings have a good oil supply condition but relatively small minimum film thickness and large power loss, since the load carrying lands are small. Although ungrooved bearings seem to be the best selection in theory, the delivery of oil is clearly a problem. The solution may be partially grooved bearings with oil grooves arranged according to each individual application (Jones et al [1982], Goenka [1984], Martin [1985] and Campbell et al [1986]) or oil holes.

(B) Conclusions from Engine Valve Train Friction Model

(a) Elastohydrodynamic or mixed lubrication analysis has presented a very good explanation of the performance of automobile cams and followers. This is particularly important since current design approaches are conventionally based mainly on a consideration of boundary lubrication.

(b) The results of a tribological analysis of a tapered cam acting against a non-rotating domed follower show fairly close agreement with those of the cam operating against the follower with rotation, especially for the results of frictional power loss.

(c) Although transient effects in the lubrication analysis of a cam and follower system are important, the quasi-static approach has proved to be effective and sufficient for designers to study various options at the design stage.

(d) The friction, and hence power loss, at the cam/follower interfaces contribute most of the valve train friction. The camshaft bearings losses are more modest while the contributions from the follower/guide and valve/guide friction is very small.

(e) Possible improvements in the valve train efficiency for the arrangement studied may be obtained by the employment of a larger follower radius of curvature, smaller cam base circle radius, lower viscosity oil, larger valve equivalent mass and lower valve spring rate. These suggestions have to be investigated very carefully as considerations of permitted physical space, valve bounce, efficient combustion, wear and noise control are also necessary.

(C) Conclusions from Engine Piston Assembly Friction Model

(a) The orifice and volume theory for calculating the inter-ring gas pressures provides a most useful, rapid and satisfactory method for giving an approximate indication of piston ring gas loadings.

(b) The lubrication analyses of a fully flooded single ring and a fully flooded ring pack are essential developments for the more realistic starved ring pack analysis. When the fully flooded results are compared with the starved results, they enable an assessment to be made of the effect of starvation on the performance of piston rings.

(c) The analysis of a ring pack in which the rings are analysed in isolation from one another and with ample lubricant at all times produces values of film thickness and oil transport much greater than those likely to occur in the pack. This has confirmed once again that the interaction between rings should be taken into account in studies of ring pack lubrication. This is particularly important in the calculation of oil transport within ring packs.

(d) It is suggested that the number of piston rings used should be as few as possible, on condition that the gas sealing function is not sacrificed. This is because of the restriction of lubricant supply each ring can pass on to those following it. More rings will mean more severe starvation of lubricant to the rings, higher friction and more likelihood of ring scuffing.

(e) Simple approaches have been developed for the prediction of friction for the oil control ring and the piston skirt. The friction due to the oil control ring may be reduced by decreasing the elastic tension, while the skirt friction may be reduced by reducing the surface area of the skirt and increasing the piston radial clearance. These guidelines must be judiciously considered, since the former tends to increase oil consumption, while the latter may cause large engine noise.

(D) Conclusions from the Engine Friction Model

(a) For the Ford Zeta engine, it has been confirmed that about half of the engine friction is due to the piston assembly, while the frictional losses due to the bearings and the valve train together account for roughly a similar proportion of the total friction.

(b) It is believed that this is the first time that data for a modern twin-camshaft, sixteen-valve engine has been presented. The results recorded here show a good agreement with the experimental findings reported by other researchers.

CS.2 Suggestions for Future Work

The following suggestions for future research are mainly concerned with the extension of the theory presented in the present work. However, a number of other aspects which require further understanding are also summarized.

(a) The friction models for the main engine components and for the entire engine have been established on the basis of sound and sophisticated theories. However, a great deal of experimental work still remains to be carried out, particularly for modern twin-camshaft engines. Whenever possible, experimental tests should be undertaken separately for each of the three main engine components and for the engine as a whole.

(b) Thermal effects are very important in the analysis of engines and engine components. It is felt essential for engine manufacturers to build an engine thermal analysis model to predict temperature variations around every part of an engine.

(c) For journal bearings, oil groove type (circumferential, axial or hole), groove number (single or double), groove location and groove size have important influences on bearing performance. Thus the engine bearing friction model should be extended to include partially grooved journal bearings and holes which are particularly popular in automotive engines.

(d) Crankshaft and camshaft modelling could be improved if their flexibilities were taken into account in bearing analysis. This means that these shafts should be treated as more realistically indeterminate rather than statically determinate problems, although this approach might be very complicated.

(e) The present valve train friction model includes a tapered cam and non-rotating follower system and a cam and flat faced follower system. It can be further extended to include any other type of valve train in common use in modern internal combustion engines, namely, a cam and centrally pivoted follower system, a cam and end pivoted follower system, a desmodromic system and a cam and roller follower system. The last one is particularly important since an obvious method of cutting down frictional losses within the valve train is to incorporate roller followers.

(f) It is apparent that the follower rotation for a tapered cam acting against a domed follower system should be modelled and included in the valve train friction model.

(g) Parametric studies must be undertaken for the friction and lubrication analysis, not only for a fully flooded single ring, but also for the rings within a starved ring pack.

(h) Experimental investigations are needed for the understanding of the mechanism of oil transport and accumulation within a ring pack. This will allow a more realistic assumption to be made of the amount of oil available to each ring, particularly to the leading ring at dead centres.

(i) A better understanding of piston ring performance requires the dynamic behaviour of the ring to be investigated.

(j) A full friction and lubrication analysis of an oil control ring will improve the simple approach for the ring in the present work. In addition, detailed consideration of the quantity of oil available to compression rings may be undertaken.

(k) The development of numerical solutions for the friction and lubrication for piston skirts may be worthy of consideration. Examples include a finite element method incorporated with the hydrodynamic theory and EHL analysis.

(l) Nearly all theoretical analyses for piston ring lubrication found in the literature adopted an axial symmetry assumption. It is time now to carry out a three-dimensional analysis which will take account of the thermal and elastic distortions of the piston rings and the cylinder bore.

(m) Oil consumption studies have become even more urgent these days, especially for the diesel industry. This is a direct result of the necessity to reduce the level of oil consumption in order to meet the forthcoming particulate emissions legislation.

(n) To predict the life of piston rings, the mechanism of wear of piston rings and cylinder liners in relation to design, operating conditions and materials must be investigated.

(o) If sufficient engine input data are available, parametric studies should be carried out on the engine friction model, such that the influence of engine design changes upon the total engine friction, not just on an individual component, can be predicted. For example, a change in cylinder bore would affect not only piston assembly friction but also engine bearing friction.

(p) To form a complete engine friction model, engine auxiliaries need to be tested and modelled.

BIBLIOGRAPHY

Introduction

[1] AUILER,J.A.,ZEROZEK,J.D. & BLUMBERG,P.N.,[1977] ,"Optimization in Automotive Engine Calibration for Better Fuel Economy–Methods and Application", SAE 770076

[2] BALL,W.F.,JACKSON,N.S.,PILLEY,A.D. & PORTER,B.C.,[1986] ,"The Friction of a 1.6 Litre Automotive Engine–Gasoline and Diesel", SAE 860418

[3] BARTZ,W.,[1985] ,"Potential Fuel Savings by Use of Low-friction Engine and Transmission Lubricants", Proc.Instn.Mech.Engrs. Conf. on Reduction of Friction and Wear in Combustion Engines, Paper C69/85, pp75-85

[4] DORGHAM,M.A.(Editor),[1982] ,"Ford Energy Report", Proc.Int. Association for Vehicle Design, Special Publication SP1

[5] GOENKA,P.,[1991] ,"Role of Tribology in Vehicle Design–General Motors Perspective", Proc. 17th Leeds-Lyon Symposium on Tribology: Vehicle Tribology, Elsevier, pp479-493

[6] GOTO,T.,HAMAI,K.,KAI,S. & MASUDA,T.,[1990] ,"A Friction Prediction Model for Gasoline Engines", Proc. Japan Int. Trib. Conf., Nagoya, pp143-148

[7] GROTH,K.,[1977] ,"Recent Methods for Investigating Friction Losses in Engine Running Gear", MIRA Translation No.52/83

[8] HAMAI,K.,GOTO,T.,MUSADA,T.,ARAI,T. & GOTOH,T.,[1991] ,"Present Status and Future Direction of Engine Tribology at Nissan", Proc. 17th Leeds-Lyon Symposium on Tribology: Vehicle Tribology, Elsevier, pp495-502

[9] HAMAI,K.,MUSADA,T.,GOTO,T. & KAI,S.,[1991] ,"Development of a Friction Prediction Model for High Performance Engines", Lub.Eng., Vol.47, No.7, pp567-573

[10] HENEIN,N.A.,FRAGOULIS,A. & BRYZIK,W.,[1989] ,"Instantaneous frictional Torque Components in a Diesel Engine", SAE 890214

[11] **HOSHI,M.,[1984]** ,"Reducing Friction Losses in Automobile Engines", Trib.Int., Vol.17, No.4, pp185-189

[12] **MARSHALL,J.M.,PARKER,D.D. & STANOJEVIC,M.,[1987]** ,"The Engine Bearing—Fifty Years On", Proc.Instn.Mech.Engrs. Conf. on Tribology–Friction, Lubrication and Wear–Fifty Years On, Vol.2, Paper C212/87, pp771-779

[13] **MARTIN,F.A.,[1983]** ,"Developments in Engine Bearings", Proc. 9th Leeds-Lyon Symposium on Tribology:Tribology of Reciprocating Engines, Butterworths, pp9-28

[14] **McGEEHAN,J.A.,[1978]** ,"A Literature Review of the Effects of Piston and Ring Friction and Lubricating Oil Viscosity on Fuel Economy", SAE 780673

[15] **MILLINGTON,B. & HARTLES,E.R.,[1968]** ,"Frictional Losses in Diesel Engines", SAE 680590

[16] **MONAGHAN,M.L.,[1988]** ,"Engine Friction–A Change in Emphasis", Proc. Instn. Mech.Engrs., Vol.202, No.D4, pp215-226

[17] **MONAGHAN,M.L.,[1989]** ,"Putting Friction in Its Place", Proc.Instn.Mech.Engrs. Conf. on Reduction of Friction and Wear in Combustion Engines, Paper 375/KN1, pp1-5

[18] **NEALE,M.,[1991]** ,"The Tribology of Engine Design", The 6th Annual BP-IMechE Tribology Lecture, Birmingham

[19] **PARKER,D.A.,[1990]** ,"The Tribology of Automotive Components– Development of Verified Computational Design Techniques", Proc.Instn. Mech.Engrs., Vol204, No.D1, Pt.D, J.Automobile Eng., pp1-9

[20] **PARKER,D.A. & ADAMS,D.R.,[1982]** ,"Friction Losses in the Reciprocating Internal Combustion Engine", Proc.Instn.Mech.Engrs. Conf. on Tribology: Key to the Efficient Engine, Paper C5/82, pp31-39

[21] **PARKER,D.A.,ADAMS,D.R. & BARRETT,D.J.S.,[1982]** ,"The Reduction of Friction in the Internal Combustion Engine", AE Technical Symposium, Paper No.29, pp29.1-29.9

[22] **PATTON,K.J.,NITSCHKE,R.G. & HEYWOOD,J.B.,[1989]** ,"Development and Evaluation of Friction Model for Spark Ignition Engines", SAE 890836

[23] **PINKUS,O. & WILCOCK,D.F.,[1978]** ,"The Role of Tribology in Energy Conservation", Lub.Eng., Vol.34, No.11, pp599-610

[24] **POHLMANN,J.D. & KUCK,H.A.,[1984]** ,"Analysis and Computer Simulation of Design and Combustion Parameters Influencing the Fuel Consumption of Piston Engines", SAE 840180

[25] **POHLMANN,J.D. & KUCK,H.A.,[1985]** ,"The Influence of Design Parameters on Engine Friction", Proc.Instn.Mech.Engrs.Conf. on Reduction of Friction and Wear in Combustion Engines, Paper C73/85, pp67-73

[26] **REZEKA,S.F. & HENEIN,N.A.,[1984]** ,"A New Approach to Evaluate Instantaneous Friction and Its Components in Internal Combustion Engines", SAE 840179

[27] **RUDDY,B.L. & HILDYARD,M.L.,[1991]** ,"A Review of Tribological Aspects of Piston Assembly Design", Proc. 17th Leeds-Lyon Symposium on Tribology: Vehicle Tribology, Elsevier, pp93-102

[28] **SMITH,D.J. & GRIFFITHS,D.W.,[1985]** ,"Experimental Techniques for Selecting an Engine for Fuel Economy Measurements of Lubricants", Proc.Instn.Mech. Engrs.Conf. on Reduction of Friction and Wear in Combustion Engines, Paper C66/85, pp103-110

[29] **TAYLOR,C.M.,[1991]** ,"Valve Train Lubrication Analysis", Proc. 17th Leeds-Lyon Symposium on Tribology: Vehicle Tribology, Elsevier, pp119-131

[30] **TAYLOR,C.M.,[1992]** ,"Fluid-film Lubrication in the Internal Combustion Engine–An Invited Review", J.Phys. D: Appl.Phys., Vol.25, No.1A, ppA91-A100

[31] **TING,L.L.,[1985]** ,"A Review of Present Information on Piston Ring Tribology", SAE 852355

Part I Friction Modelling for Engine Bearings

[32] **BOOKER,J.F.,[1965]** , "A Table of the Journal Bearing Integral", J.Basic Eng., Trans. ASME, Ser.D, Vol.187, pp533-535

[33] **BOOKER,J.F.,[1965]** , "Dynamically Loaded Journal Bearings: Mobility Method of Solution", J.Basic Eng., Trans. ASME, Ser.D, Vol.187, pp537-546

[34] **BOOKER,J.F.,[1971]** , "Dynamically Loaded Journal Bearings: Numerical Application of the Mobility Method", J.Lub.Tech., Trans. ASME, Ser.F, Vol.93-94, pp168-176

[35] **BOOKER,J.F., GOENKA,P.K. & Van LEEUWEN,H.J.,[1982]** , "Dynamic Analysis of Rocking Journal Bearings with Multiple Offset Segments", J.Lub.Tech., Trans. ASME, Vol.104, pp478-480

[36] **BOOKER,J.F.,[1989]** , "Basic Equations for Fluid Films with Variable Properties", J.Trib., Trans. ASME, Vol.111, No.3, pp475 -483

[37] **BUCKHOLZ,R.H.& HWANG,B.,[1986]** ,"The Accuracy of Short Bearing Theory for Newtonian Lubricants", J.Trib., Trans. ASME, Vol.108, No.1, pp73-79

[38] **CAMERON,A.,[1976]** , "Basic Lubrication Theory", John Wiley & Sons, London

[39] **CAMPBELL,J., LOVE,P.P., MARTIN,F.A.& REFIQUE,S.O.[1967- 1968]** , "Bearings for Reciprocating Machinery: A Review of the Present State of Theoretical,Experimental and Service Knowledge", Proc.Instn.Mech.Engrs., Vol.182, Pt.3A, pp51-74

[40] **CAMPBELL,B.D.,GOJON,R.,SERRE,Y.& WARRINER,J.F.[1986]** , "Developments in Engine Bearing Design Techniques", AE Technical Symposium, Paper No.11, pp11.1-11.7

[41] **CLAYTON,C.A.,[1987]** , "Improved Engine Bearing Design Analysis", Internal Report, Dept.Mech.Eng., Leeds Univ.

[42] **DUBOIS,G.B. & OCVIRK,F.W.,[1953]** , "Analytical Derivation and Experimental Evaluation of Short Bearing Approximation for Full Journal Bearings', NACA Techn. Note 1157

[43] **DUNNING,S.M.,[1980]** , "A Study of Cavitation Erosion under Conditions of Hydrodynamic Lubrication", PhD Thesis, Dept.Mech.Eng., Leeds Univ.

[44] **GOENKA,P.K.,[1984]** , "Dynamically Loaded Journal Bearings: Finite Element Method Analysis", J.Trib., Trans. ASME, Vol.106, No.1, pp429-439

[45] **JONES,G.J.,[1983]** , "Crankshaft Bearings: Oil Film History", Proc. 9th Leeds-Lyon Symposium on Tribology: Tribology of Reciprocating Engines, Butterworths, pp83-88

[46] **JONES,G.J., LEE,C.S. & MARTIN,F.A.,[1982]** , "Crankshaft Bearings: Advances in Predictive Techniques Incorporating the Effects of Oil Holes and Grooving", AE Technical Symposium, Paper No.1, pp1.1-1.8

[47] **LaBOUFF,G.A. & BOOKER,J.F.,[1985]** , "Dynamically Loaded Journal Bearings: A Finite Element Treatment for Rigid and Elastic Surfaces", J.Trib., Trans. ASME, Vol.107, No.4, pp505-515

[48] **MARTIN,F.A. & BOOKER,J.F., [1966-1967]** , "Influence of Engine Inertia Forces on Minimum Film Thickness in Con-rod Big-end Bearings", Proc.Instn. Mech.Engrs., Vol.181, Pt.1, No.30, pp749- 764

[49] **MARTIN,F.A.,[1974]** , "Design Procedures for Dynamically Loaded Bearings", CG48/74, the Glacier Metal Co.

[50] **MARTIN,F.A.,[1985]** , "Friction in Internal Combustion Engines", Proc.Instn. Mech.Engrs.Conf. on Reduction of Friction and Wear in Combustion Engines, Paper C67/85, pp1-17

[51] **MARTIN,F.A., BOOKER,J.F. & LO,P.M.,[1987]** ,"Power Loss in Connecting Rod Bearings", Proc.Instn. Mech.Engrs.Conf. on Tribology: Friction and Wear, Paper C167/87, pp701-708

[52] **MARTIN,F.A. & WARRINER,J.F.,[1990]** , Private Communication

[53] **MASPEYROT,P. & FRENE,J.,[1988]** , "Shape Defects and Misalignment Effects in Connecting-rod Bearings", Proc. 15th Leeds-Lyon Symposium on Tribology: Tribological Design of Machine Elements, Elsevier, pp317-322

[54] **REYNOLDS,O.,[1886]** , "On the Theory of Lubrication and Its Application to Mr.Beauchamp Tower's Experiments Including an Experimental Determination of Viscosity of Olive Oil", Phil. Trans.Roy.Soc., Ser.A, Vol.177, Pt.1, pp157-234

[55] **RITCHIE,G.S.,[1975]** , "The Prediction of Journal Loci in Dynamically Loaded Internal Combustion Engine Bearings", Wear, Vol.35, pp291-297

[56] **ROHDE,S.M.(Edt.),[1983]** , "Fluid Film Lubrication: A Century of Progress", Joint Lub. Conf., ASME Publication

[57] **ROSENBERG,R.C.,[1982]** , "General Friction Consideration for Engine Design", SAE 821576

[58] **ROSS,J.M.,[1971]** , "Bearing Orbit Analysis", Machine Design, Vol.43, No.25, pp140-145

[59] **SAFAR,Z.S.,[1984]** , "Energy Loss due to Misalignment of Journal Bearings", Trib.Int., Vol.17, No.2, pp107-109

[60] **SHAW,M.C. & MACKS,E.F.,[1949]** , "Analysis and Lubrication of Bearings", McGRAW-HILL Book Co. Inc., New York

[61] **SINGH,D.V., SINHASAN,R. & PAL,R.,[1989]** , "Performance Characteristics of an Ungrooved Big-end Bearing with Misalignment", Trib.Trans., Vol.32, No.2, pp234-238

[62] **SMITH,E.H.,[1983]** , "Temperature Variations in Crankshaft Bearings", Proc. 9th Leeds-Lyon Symposium on Tribology: Tribology of Reciprocating Engines, Butterworths, pp97-102

[63] **SPIKES,R.H.,[1982]** ,"Engine Bearing Design Up-to-date", Proc. Instn. Mech. Engrs. Conf. on Tribology: Key to the Efficient Engine, Paper C1/82, pp1-8

[64] **STOLARSKI,T.A.,[1990]** , "Tribology in Machine Design", Heinemann Newnes, Oxford

[65] **VICKERY,P.E.,[1975]** , "Friction Losses in Automotive Plain Bearings", SAE 750052

[66] **WHITE,M.F.,[1989]** , "Dynamic Loading and Response of Bearings in Reciprocating Machinery", Wear, Vol.130, No.1, pp81-92

Part II Friction Modelling for an Engine Valve Train

[67] **ALAMSYA,C., DILLICH,S.& PETTIT,A.,[1989]** , "Effects of Initial Surface Finish on Cam Wear", Wear, Vol.134, No.1, pp29-47

[68] **ARMSTRONG,W.B. & BUUCK,B.A.,[1981]** , "Valve Gear Energy Consumption: Effect of Design and Operation Parameters", SAE 810787

[69] **BAIR,S., GRIFFIOEN,J.A. & WINER,W.O.,[1986]** , "The Tribological Behaviour of an Automotive Cam and Flat Lifter System", J.Trib., Trans. ASME, Vol.108, No.3, pp478-487

[70] **BALL,A.D.,[1988]** , "A Tribological Study of the Design and Performance of Automotive Cams", PhD Thesis, Dept.Mech.Eng., Leeds Univ.

[71] **BALL,A.D.,[1989]** , "A Computer Program for Valve Train Analysis", Internal Report, Dept.Mech.Eng., Leeds Univ.

[72] **BALL,A.D., DOWSON,D. & TAYLOR,C.M.,[1989]** , "Cam and Follower Design", Proc. 15th Leeds-Lyon Symposium on Tribology: Tribological Design of Machine Elements, Elsevier, pp111-130

[73] **BEDEWI,M.A.A., DOWSON,D. & TAYLOR,C.M.,[1986]** , "Elastohydrodynamic Lubrication of Line Contacts Subjected to Time Dependent Loading with Particular Reference to Rolling Bearings and Cams and Followers", Proc. 12th Leeds-Lyon Symposium on Tribology: Mechanisms and Surface Distress, Butterworths, pp289-304

[74] **BELL,J.C., DAVIES,P.J. & FU,W.B.,[1986]** , "Prediction of Automotive Valve Train Wear Patterns with Simple Mathematical Models", Proc. 12th Leeds-Lyon Symposium on Tribology: Mechanisms and Surface Distress, Butterworths, pp323-333

[75] **BOVINGTON,C.H. & HUBBARD,A.,[1989]** , "Lubricant Additive Effects on Valve Train Friction and Wear", Proc.Instn.Mech.Engrs.Conf. on Reduction of Friction and Wear in Combustion Engines, Paper C375/021, pp79-84

[76] **CHEN,F.Y.,[1982]** , "Mechnianics and Design of Cam Mechanisms", Pergamon Press

[77] **CHILDS,T.H.C.,[1991]** , Private Communication

[78] **CHITTENDEN,R.J., DOWSON,D., DUNN,J.F. & TAYLOR,C.M.,[1985]** , "A Theoretical Analysis of the Isothermal Elastohydrodynamic Lubrication of Concentrated Contacts, Part I, Direction of Entrainment Coincident with the Major Axis of the Hertzian Contact Ellipse", Proc. R. Soc. London, Vol.397, Ser.A, pp245-269

[79] **CHITTENDEN,R.J., DOWSON,D., DUNN,J.F. & TAYLOR,C.M.,[1985]** , "A Theoretical Analysis of the Isothermal Elastohydrodynamic Lubrication of Concentrated Contacts, Part II, General Case, with Lubricant Entrainment along either Principal Axis of the Hertzian Contact Ellipse or at Some Intermediate Angle", Proc. R. Soc. London, Vol.397, Ser.A, pp271-294

[80] **CHITTENDEN,R.J., DOWSON,D. & TAYLOR,C.M.,[1987]** , "The Estimation of Minimum Film Thickness in the Design of Concentrated Contacts", Proc.Instn.Mech.Engrs.Conf. on Tribology–Friction, Lubrication and Wear–Fifty Years On, Vol.2, Paper C175/87, pp807-818

[81] **DOWSON,D., HARRISON,P. & TAYLOR,C.M.,[1986]** , "The Lubrication of Automotive Cams and Followers", Proc. 12th Leeds-Lyon Symposium on Tribology: Mechanisms and Surface Distress, Butterworths, pp305-322

[82] **DOWSON,D., HARRISON,P., TAYLOR,C.M. & ZHU,G.,[1990]** , "Experimental Observations of Lubricant Film State between a Cam and Bucket Follower Using Electrical Resistivity Technique", Proc. Japan Int. Trib. Conf., Nagoya, pp119-124

[83] **DOWSON,D. & HIGGINSON,G.R.,[1977]** , "Elastohydrodynamic Lubrication", Pergamon Press

[84] **DOWSON,D., TAYLOR,C.M. & XU,H.,[1991]** , "Elastohydrodynamic Lubrication of Elliptical Contacts with Spin and Rolling", Proc.Instn.Mech.Engrs., Vol.205, No.3, Pt.C, pp165-174

[85] **DOWSON,D., TAYLOR,C.M. & ZHU,G.,[1987]** , "Mixed Lubrication of a Cam and Flat Faced Follower", Proc. 13th Leeds-Lyon Symposium on Tribology: Fluid Film Lubrication–Osborne Reynolds Centenary, Elsevier, pp599-609

[86] **DOWSON,D., TAYLOR,C.M. & ZHU,G.,[1989]** , "An Experimental Study of the Tribology of a Cam and Flat Faced Follower", Proc.Instn.Mech. Engrs.Conf. on Reduction of Friction and Wear in Combustion Engines, Paper C375/025, pp97-108

[87] **DOWSON,D., TAYLOR,C.M. & ZHU,G.,[1992]** , "A Transient Elastohydrodynamic Lubrication Analysis of a Cam and Follower", J.Phys. D: Appl. Phys., Vol.25, No.1A, ppA313-A320

[88] **DYSON,A.,[1977]** , "Elastohydrodynamic Lubrication and Wear of Cams Bearing against Cylindrical Tappets", SAE 770018

[89] **DYSON,A.,[1980]** , "Kinematics and Wear Patterns of Cam and Finger Follower Automotive Valve Gear", Trib.Int., Vol.13, No.3, pp121-132

[90] **DYSON,A. & NAYLOR,H.,[1960-61]** , "Application of the Flash Temperature Concept to Cam and Tappet Wear Problems", Proc.Instn.Mech.Engrs., (A.D.), No.8, pp255-280

[91] **E.S.D.U. Item No.78035, [1978]** , "Contact Phenomenon, Stresses, Deflections and Contact Dimensions for Normally Loaded Unlubricated Elastic Components"

[92] **HAMILTON,G.M.,[1980]** , "The Hydrodynamics of a Cam Follower", Trib.Int., Vol.13, No.3, pp113-119

[93] **HAMROCK,B.J. & DOWSON,D.,[1981]** , "Ball Bearing Lubrication– the Elastohydrodynamics of Elliptical Contacts", John Wiley & Sons

[94] **HARRISON,P.,[1985]** , "A Study of the Lubrication of Automotive Cams", PhD Thesis, Dept.Mech.Eng., Leeds Univ.

[95] **HELDEN,A.K., MEER,R.J., STAADEN,J.J. & GELDEREN,E., [1985]** , "Dynamic Friction in Cam/Tappet Lubrication", SAE 850441

[96] **HERTZ,H.,[1882]** , "On the Contact of Elastic Solids", J.Reine und Angewandte Mathematik, Vol.92, pp156-171

[97] **JOHNSON,K.L.,[1970]** , "Regimes of Elastohydrodynamic Lubrication", J. Mech. Eng. Sci., Vol.12, No.1, pp9-16

[98] **LIM,C.E., EVANS,H.P. & SNIDLE,R.W.,[1983]** , "Kinematics and Lubrication Conditions at Cam Contact in a Centrally Pivoted Cam-Finger Follower", SAE 830309

[99] **McGEEHAN,J.A. & YAMAGUCHI,E.S.,[1990]** , "Effect of Additives and Engine Blow-by on Camshaft Wear Control", Proc. Japan Int. Trib. Conf., Nagoya, pp2035-2040

[100] **MULLER,R.,[1966]** , "The Effect of Lubrication on Cam and Tappet Performance", MTZ, Vol.27, Pt.2, pp58-61, MIRA Translation No.27/66

[101] **NAYLOR,H.,[1967-68]** , "Cams and Friction Drives", Proc.Instn. Mech.Engrs., Vol.182, Pt.3A, Paper 15, pp237-247

[102] **PIEPRZAK,J.M., WILLERMET,P.A. & KLASSEN,D.,[1989]** , "A Tappet Rotation Monitor Based on Light Reflectance–Development and Functional Testing", SAE 890722

[103] **REINICKE-MURMANN,J. & KREUTER,P.,[1990]** , "Analysis and Development of Camshaft Drive Systems Using a Computer Simulation Model", SAE 900448

[104] **ROGER,G., SOUTHAM,R. & REINICKE-MURMANN,J.,[1990]** , "Analysis of Potential Improvements in Engine Behaviour Due to Ceramic Valve Train Components", SAE 900452

[105] **SPEIL,W.,[1988]** , "Hydraulic Valve Lash Adjustment", Technical Seminar–INA Products in Automotive Applicationa, INA Walzlager Schaeffler KG

[106] **STARON,J.T. & WILLERMET,P.A.,[1983]** , "An Analysis of Valve Train Friction in Terms of Lubrication Principles", SAE 830165

[107] **SUN,D.C. & ROSENBERG,R.C.,[1987]** , "An Experimental Study of Automotive Cam-Lifter Interface Friction", ASLE Trans., Vol.30, No.2, pp167-176

[108] **THUMIM,A.D.,[1971]** , "Cam Design by Computer", Machine Design, Vol.43, No.21, pp81-84

[109] **VICHARD,J.P.,[1971]** , "Transient Effects in the Lubrication of Hertzian Contacts", J.Mech.Eng.Sci., Vol.13, No.3, pp173-189

[110] **VICHARD,J.P. & GODET,M.R.,[1967-68]** , "Simultaneous Measurement of Load, Friction and Film Thickness in a Cam-and-tappet System", Proc. Instn. Mech. Engrs., Vol.182, Pt.3G, Report 21, pp109-113

[111] **WEAVER,N.,[1989]** , "Tribological Considerations in Cam/follower Design", M.Sc. Automotive Eng. Project, Ford Motor Co. Ltd.

[112] **WILLERMET,P.A. & PIEPRZAK,J.,[1989]** , "Some Effects of Lubricant Composition and Tappet Rotation on Cam/Tappet Friction", J.Trib., Trans. ASME, Vol.111, No.4, pp683-691

[113] **WILLERMET,P.A., PIEPRZAK,J. & DAILEY,D.P.,[1990]** , "Tappet Rotation and Friction Reduction in a Center Pivot Rocker Arm Contact", J.Trib., Trans. ASME, Vol.112, No.4, pp655-661

[114] **WILLIAMSON,B.P., GALLIARD,I.R. & BENWELL,S.,[1989]** , "Measurement of Oil Film Thickness in the Elastohydrodynamic Contact between a Cam and Bucket Follower in a Motored Cylinder Head, Part I, Newtonian Oils", SAE 892150

[115] **ZHU,G.,[1988]** , "A Theoretical and Experimental Study of the Tribology of a Cam and Follower", PhD Thesis, Dept.Mech.Eng., Leeds Univ.

[116] **ZHU,G.,[1990],[1991]** , Private Communication

Part III Friction Modelling for an Engine Piston Assembly

[117] **ALLEN,D.G.,DUDLEY,B.,MIDDLETON,V. & PARKER,D.A.,[1976]** , "Prediction of Piston Ring/Cylinder Bore Oil Film Thickness in Two Particular Engines and Correlation with Experimental Evidence", Proc.Instn.Mech.Engrs.Conf. on Piston Ring Scuffing, Paper C73/75, pp107-123

[118] **BROWN,S.R. & HAMILTON,G.M.,[1975]** ,"Hydrodynamic Pressure under a Piston Ring", Nature, Vol.253, pp341-342

[119] **BROWN,S.R. & HAMILTON,G.M.,[1976]** ,"Pressure Measurements between the Rings and Cylinder Liner of an Engine", Proc.Instn.Mech. Engrs.Conf. on Piston Ring Scuffing, Paper C72/75, pp99-106

[120] **BROWN,S.R. & HAMILTON,G.M.,[1977]** ,"The Partially Lubricated Piston Ring", J.Mech.Eng.Sci., Vol.19, No.2, pp81-89

[121] **BROWN,S.R. & HAMILTON,G.M.,[1978]** ,"Negative Pressures under a Lubricated Piston Ring", J.Mech.Eng.Sci., Vol.20, No.1, pp49-57

[122] **DOWSON,D.,ECONOMOU,P.,RUDDY,B. & STRACHAN,P.,[1979]** , "Piston Ring Lubrication—part II, Theoretical Analysis of a Single Ring and a Complete Ring Pack", ASME Conf. on Energy Conservation through Fluid Film Lubrication Technology—Frontiers in Research & Design, ASME Publication, pp23-52

[123] **ECONOMOU,P.,[1976]** ,"A Study of the Lubrication and Dynamics of Piston Rings", PhD Thesis, Dept.Mech.Eng., Leeds Univ.

[124] **EWEIS,M.,[1935]** ,"Reibungs und Undichtigkeitsverluste an Kolbenringen", Forschungshefte des Vereins Deutscher Ingenieure, No.371

[125] **DE FARO BARROS,A. & DYSON,A.,[1960]** ,"Piston Ring Friction– Rig Measurements with Low Viscosity Oils", J.Inst.Pet., Vol.46, No.433, pp1-18

[126] **FEUGA,L. & BURY,C.,[1984]** ,"Piston and Ring Mechanical Losses", SAE 841296

[127] **FURUHAMA,S. & HIRUMA,M.,[1972]** ,"Axial Movement of Piston Rings in the Groove", ASLE Trans., Vol.15, No.4, pp278-287

[128] **FURUHAMA,S. & TAGIGUCHI,M.,[1979]** ,"Measurement of Piston Frictional Force in Actual Operating Diesel Engine", SAE 790855

[129] **GERE,J.M. & TIMOSHEKO,S.P.,[1984]** ,"Mechanics of Materials", Brooks /Cole Eng. Division, Monterey, California, USA

[130] **HAMILTON,G.M. & MOORE,S.L.,[1974]** ,"Measurement of the Oil-film Thickness between the Piston Rings and Liner of a Small Diesel Engine", Proc.Instn.Mech. Engrs., Vol.188, pp253-261

[131] **HAMILTON,G.M. & MOORE,S.L.,[1974]** ,"Comparison between Measured and Calculated Thickness of the Oil Film Lubricating Piston Ring", Proc.Instn.Mech. Engrs., Vol.188, pp262-268

[132] **HAMILTON,G.M. & MOORE,S.L.,[1976]** ,"Measurement of Piston Ring Profile during Running in", Proc.Instn.Mech.Engrs.Conf. on Piston Ring Scuffing, Paper C69/75, pp61-70

[133] **HOSHI,M. & BABA,Y.,[1986]** ,"A Study of Piston Friction Force in an Internal Combustion Engine", ASLE Trans., Vol.30, No.4, pp444-451

[134] **HWU,C.J. & WENG,C.I.,[1991]** ,"Elastohydrodynamic Lubrication of Piston Rings", Wear, Vol.151, pp289-302

[135] **KOLL,G.D. & PEEKEN,H.J.,[1982]** ,"Hydrodynamic Lubrication of Piston Skirts", J.Lub.Tech., Trans. ASME, Vol.104, No.4, pp504-509

[136] **KU,Y. & PATTERSON,D.J.,[1988]** ,"Piston and Ring Friction by the Fixed Sleeve Method", SAE 880571

[137] **KUO,T.,SELLNAU,M.,THEOBALD,M. & JONES,J.,[1989]** ,"Calculation of Flow in the Piston-Cylinder-Ring Crevices of a Homogeneous Charge Engine and Comparison with Experiment", SAE 890838

[138] **LOOK,D.C. & SAUER,H.J.,[1986]** ,"Engineering Thermodynamics", PWS Eng.

[139] **MOORE,S.L. & HAMILTON,G.M.,[1978]** ,"The Starved Lubrication of Piston Rings in a Diesel Engine", J.Mech.Eng.Sci., Vol.20, No.6, pp345-352

[140] **MOORE,S.L. & HAMILTON,G.M.,[1980]** ,"The Piston at Top Dead Centre", Proc.Instn.Mech.Engrs., Vol.194, pp373-381

[141] **NAMAZIAN,M. & HEYWOOD,J.B.,[1982]** ,"Flow in the Piston-Cylinder-Ring Crevices of a Spark Ignition Engine: Effect on Hydrocarbon Emissions, Efficiency and Power", SAE 820088

[142] **OH,K.P.,LI,C.H. & GOENKA.P.K.,[1987]** ,"Elastohydrodynamic Lubrication of Piston Skirts", J.Trib., Trans. ASME, Vol.109, No.2, pp356-362

[143] **PACHERNEGG,S.J.,[1971]** ,"The Hydraulics of Oil Scraping", SAE 710816

[144] **PARKER,D.A.,[1989]** ,"The T & N Technology Ring Pack Program— An Application Case Study", AutoTech 89 Congress, Vol.C399/24, No.4

[145] **PARKER,D.A.,ADAMS,D.R. & DONNISON,G.,[1989]** ,"The Measurement and Reduction of Piston Assembly Friction", Proc.Instn.Mech.Engrs. Conf. on Reduction of Friction and Wear in Combustion Engines, Paper C375/017, pp27-34

[146] **RICHEZ,M.,CONSTANS,B. & WINQUIST,K.,[1983]** ,"Theoretical and Experimental Study of Ring/Liner Friction", Proc. 9th Leeds-Lyon Symposium on Tribology: Tribology of Reciprocating Engines, Butterworths, pp122-131

[147] **ROHDE,S.M.,[1980]** ,"A Mixed Friction Model for Dynamically Loaded Contacts with Application to Piston Ring Lubrication", ASME Conf. on Surface Roughness Effects in Hydrodynamic and Mixed Lubrication, ASME Publication, pp19-50

[148] **RUDDY,B.L.,[1979]** ,"The Lubrication and Dynamics of Piston Rings and the Theoretical Prediction of Ring Pack Gas Flow", PhD Thesis, Dept.Mech.Eng., Leeds Univ.

[149] **RUDDY,B.L.,DOWSON,D. & ECONOMOU,P.,[1981]** ,"The Prediction of Gas Pressures within the Ring Packs of Large Bore Diesel Engines", J.Mech.Eng.Sci., Vol.23, No.6, pp295-304

[150] **RYDER,G.H.,[1980]** ,"Strength of Materials", The Macmillan Press Ltd, London and Basingstoke

[151] **SHIN,K.,YATEISHI,Y. & FURUHAMA,S.,[1985]** ,"Measurement and Characteristics of Instantaneous Piston Ring Frictional Force", Proc. Instn.Mech.Engrs. Conf. on Reduction of Friction and Wear in Combustion Engines, Paper C61/85, pp87-94

[152] **STRACHAN,P.J.,[1973]** ,"A Study of Piston Ring Lubrication", PhD Thesis, Dept.Mech.Eng., Leeds Univ.

[153] **TAKIGUCHI,M.,MACHIDA,K. & FURUHAMA,S.,[1988]** ,"Piston Friction Force of a Small High Speed Gasoline Engine", J.Trib., Trans. ASME, Vol.110, No.1, pp112-118

[154] **THRING,R.H.,[1989]** ,"Piston Skirt Friction in Internal Combustion Engines", Proc.Instn.Mech.Engrs. Conf. on Reduction of Friction and Wear in Combustion Engines, Paper C375/002, pp7-11

[155] **TING,L.L. & MAYER,J.E.,[1974]** ,"Piston Ring Lubrication and Cylinder Bore Wear Analysis, Part I—Theory", J.Lub.Tech., Trans. ASME, Vol.96, Ser.F, No.3, pp305-314

[156] **TING,L.L. & MAYER,J.E.,[1974]** ,"Piston Ring Lubrication and Cylinder Bore Wear Analysis, Part II—Theory Verification", J.Lub.Tech., Trans. ASME, Vol.96, Ser.F, No.2, pp258-266

[157] **URAS,H.M. & PATTERSON,D.J.,[1985]** ,"Oil and Ring Effects on Piston Ring Assembly Friction by the Instantaneous IMEP Method", SAE 850440

[158] **URAS,H.M. & PATTERSON,D.J.,[1987]** ,"Effect of Some Piston Variables on Piston and Ring Assembly Friction", SAE 870088

[159] **WU,G. & CHEN,Z.,[1992]** ,"The Numerical Study of Piston Ring Elastohydrodynamic Lubrication by the Multigrid Method", Trib.Trans., Vol.35, No.1, pp135-141

Part IV Friction Modelling for an Engine

[160] **CLEVELAND,A.E. & BISHOP,I.N.,[1960]** ,"Fuel Economy", SAE Journal, Vol.68, August 1960, pp26-32

[161] **JACKSON,N.S.,[1986]** ,"A New Method for the Measurement of Engine Friction and its Components Including Auxiliary Losses under Normal Running Conditions", Internal Report, Ricardo Consulting Engineers

[162] **LANG,O.R.,[1982]** ,"Reibungsverluste in Verbrennugsmotoren (Friction Losses in Combustion Engines)", Schmiertechnic Tribologie 29, pp90-92

[163] **LI,C.H.,[1982]** ,"Piston Thermal Deformation and Friction Consideration", SAE 820086

[164] **RICARDO,H. & HEMPSON,J.G.G.,[1968]** ,"The High Speed Internal Combustion Engine", Blackie, London

APPENDIX A
Technical Data for Bearings of a Ruston & Hornsby 6VEB-X Mk III Turbo-charged Diesel Engine

A.1 General Data

6	Bays
1	Cylinder per bay
1	Out of balance component per bay

Bay length (mm)	444.5
Cylinder bore (mm)	260.35
Crank radius (mm)	184.15
Connecting rod length (mm)	782.32
Piston assembly mass (kg)	82.07
Connecting rod mass (kg)	81.62
Flywheel mass (kg)	0.0
Lubricant dynamic viscosity (cP)	15.0
Engine speed (rpm)	600

A.2 Cylinder Positions and Angles

Bay	Cylinder	Distance from Front of Bay (mm)	Angle of Bore (Deg.)	Angle to TDC Firing Position (Deg.)
1	1	222.25	0.0	0.0
2	2	222.25	0.0	120.0
3	3	222.25	0.0	600.0
4	4	222.25	0.0	240.0
5	5	222.25	0.0	480.0
6	6	222.25	0.0	360.0

A.3 Crank Components

Bay	Components	Out-of-balance Moment (N.m)	Distance from Front of Bay (mm)	Angular Position (Deg.)
1	1	139.19	222.25	0.0
2	1	139.19	222.25	240.0
3	1	139.19	222.25	120.0
4	1	139.19	222.25	120.0
5	1	139.19	222.25	240.0
6	1	139.19	222.25	0.0

A.4 Bearing Dimensions

	Diameter (mm)	Length (mm)	Radial Clearance (mm)	Ungrooved Region
Big-end	203.2	57.15	0.08255	full
Main 1	203.2	57.15	0.08255	full
Main 2	203.2	57.15	0.08255	full
Main 3	203.2	57.15	0.08255	full
Main 4	203.2	57.15	0.08255	full
Main 5	203.2	57.15	0.08255	full
Main 6	203.2	57.15	0.08255	full
Main 7	203.2	57.15	0.08255	full

A.5 Cylinder Pressure

Crank Angle (Deg.)	Pressure (bar)	Crank Angle (Deg.)	Pressure (bar)	Crank Angle (Deg.)	Pressure (bar)	Crank Angle (Deg.)	Pressure (bar)
0.0	47.37	180.0	1.76	360.0	1.21	540.0	1.21
10.0	64.12	190.0	1.41	370.0	1.21	550.0	1.21
20.0	48.61	200.0	1.35	380.0	1.21	560.0	1.21
30.0	34.82	210.0	1.21	390.0	1.21	570.0	1.21
40.0	25.51	220.0	1.21	400.0	1.21	580.0	1.21
50.0	18.62	230.0	1.21	410.0	1.21	590.0	1.41
60.0	14.48	240.0	1.21	420.0	1.21	600.0	1.41
70.0	11.52	250.0	1.21	430.0	1.21	610.0	1.76
80.0	9.03	260.0	1.21	440.0	1.21	620.0	2.10
90.0	7.59	270.0	1.21	450.0	1.21	630.0	2.45
100.0	6.59	280.0	1.21	460.0	1.21	640.0	3.14
110.0	5.90	290.0	1.21	470.0	1.21	650.0	4.10
120.0	5.41	300.0	1.21	480.0	1.21	660.0	6.10
130.0	5.00	310.0	1.21	490.0	1.21	670.0	8.65
140.0	4.72	320.0	1.21	500.0	1.21	680.0	12.45
150.0	4.10	330.0	1.21	510.0	1.21	690.0	18.62
160.0	3.14	340.0	1.21	520.0	1.21	700.0	26.55
170.0	2.45	350.0	1.21	530.0	1.21	710.0	34.82

APPENDIX B
Technical Data for Ford 1.8L H.O. Zeta Engine Bearings

B.1 General Data

4	Bays
1	Cylinder per bay
3	Out of balance components per bay

Bay length (mm)	91.80
Cylinder bore (mm)	80.62
Crank radius (mm)	38.35
Connecting rod length (mm)	136.19
Piston assembly mass (kg)	0.48
Connecting rod mass (kg)	0.60
Flywheel mass (kg)	8.26

B.2 Cylinder Positions and Angles

Bay	Cylinder	Distance from Front of Bay (mm)	Angle of Bore (Deg.)	Angle to TDC Firing Position (Deg.)
1	1	45.9	0.0	0.0
2	2	45.9	0.0	540.0
3	3	45.9	0.0	180.0
4	4	45.9	0.0	360.0

B.3 Crank Components

(see next page)

Bay	Components	Out-of-balance Moment (N.m)	Distance from Front of Bay (mm)	Angular Position (Deg.)
1	1	134.10	23.19	180.0
1	2	116.40	45.90	0.0
1	3	53.20	68.62	180.0
2	1	53.20	23.19	0.0
2	2	116.40	45.90	180.0
2	3	134.10	68.62	0.0
3	1	134.10	23.19	0.0
3	2	116.40	45.90	180.0
3	3	53.20	68.62	0.0
4	1	53.20	23.19	180.0
4	2	116.40	45.90	0.0
4	3	134.10	68.62	180.0

B.4 Bearing Dimensions

	Diameter (mm)	Length (mm)	Radial Clearance (mm)	Ungrooved Region
Big-end	46.9	19.10	0.0210	no groove
Main 1	58.0	18.30(7.175)	0.0175	120/240
Main 2	58.0	18.30(7.175)	0.0175	120/240
Main 3	58.0	18.30(7.175)	0.0175	120/240
Main 4	58.0	18.30(7.175)	0.0175	120/240

B.5 Cylinder Pressure

B.5.1 Engine Speed = 2000 rpm

(see next page)

Crank Angle (Deg.)	Pressure (bar)	Crank Angle (Deg.)	Pressure (bar)	Crank Angle (Deg.)	Pressure (bar)	Crank Angle (Deg.)	Pressure (bar)
0.0	38.59	180.0	1.87	360.0	-0.01	540.0	-0.01
10.0	64.25	190.0	1.24	370.0	-0.01	550.0	-0.01
20.0	62.88	200.0	0.61	380.0	-0.01	560.0	0.02
30.0	46.69	210.0	-0.01	390.0	-0.01	570.0	0.05
40.0	32.75	220.0	-0.01	400.0	-0.01	580.0	0.11
50.0	23.46	230.0	-0.01	410.0	-0.01	590.0	0.19
60.0	17.37	240.0	-0.01	420.0	-0.01	600.0	0.30
70.0	13.33	250.0	-0.01	430.0	-0.01	610.0	0.45
80.0	10.58	260.0	-0.01	440.0	-0.01	620.0	0.66
90.0	8.68	270.0	-0.01	450.0	-0.01	630.0	0.95
100.0	7.32	280.0	-0.01	460.0	-0.01	640.0	1.37
110.0	6.35	290.0	-0.01	470.0	-0.01	650.0	1.99
120.0	5.64	300.0	-0.01	480.0	-0.01	660.0	2.91
130.0	5.01	310.0	-0.01	490.0	-0.01	670.0	4.32
140.0	4.38	320.0	-0.01	500.0	-0.01	680.0	6.53
150.0	3.75	330.0	-0.01	510.0	-0.01	690.0	9.93
160.0	3.13	340.0	-0.01	520.0	-0.01	700.0	14.73
170.0	2.50	350.0	-0.01	530.0	-0.01	710.0	19.91

B.5.2 Engine Speed = 3000 rpm

Crank Angle (Deg.)	Pressure (bar)	Crank Angle (Deg.)	Pressure (bar)	Crank Angle (Deg.)	Pressure (bar)	Crank Angle (Deg.)	Pressure (bar)
0.0	59.20	180.0	0.03	360.0	0.00	540.0	-0.01
10.0	66.62	190.0	0.03	370.0	-0.01	550.0	0.00
20.0	66.35	200.0	0.03	380.0	-0.01	560.0	0.02
30.0	43.73	210.0	0.03	390.0	-0.01	570.0	0.03
40.0	30.74	220.0	0.03	400.0	-0.01	580.0	0.10
50.0	22.02	230.0	0.03	410.0	-0.01	590.0	0.18
60.0	16.24	240.0	0.03	420.0	-0.01	600.0	0.25
70.0	12.53	250.0	0.03	430.0	-0.01	610.0	0.42
80.0	9.96	260.0	0.03	440.0	-0.01	620.0	0.61
90.0	8.15	270.0	0.03	450.0	-0.01	630.0	0.88
100.0	6.91	280.0	0.03	460.0	-0.01	640.0	1.26
110.0	5.99	290.0	0.03	470.0	-0.01	650.0	1.82
120.0	5.32	300.0	0.03	480.0	-0.01	660.0	2.69
130.0	4.84	310.0	0.03	490.0	-0.01	670.0	4.20
140.0	4.69	320.0	0.03	500.0	-0.01	680.0	6.71
150.0	4.22	330.0	0.03	510.0	-0.01	690.0	11.00
160.0	4.05	340.0	0.03	520.0	-0.01	700.0	18.27
170.0	3.94	350.0	0.03	530.0	-0.01	710.0	27.56

B.5.3 Engine Speed = 4000 rpm

(see next page)

Crank Angle (Deg.)	Pressure (bar)	Crank Angle (Deg.)	Pressure (bar)	Crank Angle (Deg.)	Pressure (bar)	Crank Angle (Deg.)	Pressure (bar)
0.0	40.39	180.0	1.97	360.0	-0.01	540.0	-0.01
10.0	67.22	190.0	1.31	370.0	-0.01	550.0	-0.01
20.0	65.78	200.0	0.65	380.0	-0.01	560.0	0.02
30.0	48.86	210.0	-0.01	390.0	-0.01	570.0	0.05
40.0	34.29	220.0	-0.01	400.0	-0.01	580.0	0.11
50.0	24.58	230.0	-0.01	410.0	-0.01	590.0	0.19
60.0	18.21	240.0	-0.01	420.0	-0.01	600.0	0.30
70.0	13.98	250.0	-0.01	430.0	-0.01	610.0	0.45
80.0	11.11	260.0	-0.01	440.0	-0.01	620.0	0.66
90.0	9.12	270.0	-0.01	450.0	-0.01	630.0	0.95
100.0	7.70	280.0	-0.01	460.0	-0.01	640.0	1.37
110.0	6.68	290.0	-0.01	470.0	-0.01	650.0	1.99
120.0	5.94	300.0	-0.01	480.0	-0.01	660.0	2.91
130.0	5.28	310.0	-0.01	490.0	-0.01	670.0	4.32
140.0	4.61	320.0	-0.01	500.0	-0.01	680.0	6.53
150.0	3.95	330.0	-0.01	510.0	-0.01	690.0	9.93
160.0	3.29	340.0	-0.01	520.0	-0.01	700.0	14.73
170.0	2.63	350.0	-0.01	530.0	-0.01	710.0	19.91

B.5.4 Engine Speed = 5000, 6000, 6400 rpm

Crank Angle (Deg.)	Pressure (bar)	Crank Angle (Deg.)	Pressure (bar)	Crank Angle (Deg.)	Pressure (bar)	Crank Angle (Deg.)	Pressure (bar)
0.0	57.28	180.0	0.04	360.0	0.04	540.0	-0.02
10.0	65.46	190.0	0.04	370.0	0.00	550.0	-0.01
20.0	60.11	200.0	0.04	380.0	-0.03	560.0	0.00
30.0	42.31	210.0	0.04	390.0	-0.02	570.0	0.04
40.0	29.76	220.0	0.04	400.0	-0.02	580.0	0.09
50.0	21.29	230.0	0.04	410.0	-0.02	590.0	0.16
60.0	15.69	240.0	0.04	420.0	-0.02	600.0	0.26
70.0	12.10	250.0	0.04	430.0	-0.02	610.0	0.40
80.0	9.61	260.0	0.04	440.0	-0.02	620.0	0.59
90.0	7.86	270.0	0.04	450.0	-0.02	630.0	0.85
100.0	6.65	280.0	0.04	460.0	-0.02	640.0	1.23
110.0	5.77	290.0	0.04	470.0	-0.02	650.0	1.77
120.0	5.12	300.0	0.04	480.0	-0.02	660.0	2.63
130.0	4.65	310.0	0.04	490.0	-0.02	670.0	4.11
140.0	4.30	320.0	0.04	500.0	-0.02	680.0	6.59
150.0	4.05	330.0	0.04	510.0	-0.02	690.0	10.81
160.0	3.89	340.0	0.04	520.0	-0.02	700.0	18.34
170.0	3.78	350.0	0.04	530.0	-0.02	710.0	27.66

B.5.5 Engine Speed = 7000 rpm (see next page)

Crank Angle (Deg.)	Pressure (bar)	Crank Angle (Deg.)	Pressure (bar)	Crank Angle (Deg.)	Pressure (bar)	Crank Angle (Deg.)	Pressure (bar)
0.0	54.46	180.0	0.04	360.0	0.01	540.0	-0.03
10.0	61.20	190.0	0.04	370.0	-0.03	550.0	-0.02
20.0	57.07	200.0	0.04	380.0	-0.03	560.0	0.00
30.0	40.15	210.0	0.04	390.0	-0.03	570.0	0.03
40.0	28.23	220.0	0.04	400.0	-0.03	580.0	0.08
50.0	20.59	230.0	0.04	410.0	-0.03	590.0	0.15
60.0	14.86	240.0	0.04	420.0	-0.03	600.0	0.26
70.0	11.69	250.0	0.04	430.0	-0.03	610.0	0.39
80.0	9.08	260.0	0.04	440.0	-0.03	620.0	0.58
90.0	7.42	270.0	0.04	450.0	-0.03	630.0	0.85
100.0	6.27	280.0	0.04	460.0	-0.03	640.0	1.22
110.0	5.43	290.0	0.04	470.0	-0.03	650.0	1.76
120.0	4.81	300.0	0.04	480.0	-0.03	660.0	2.62
130.0	4.37	310.0	0.04	490.0	-0.03	670.0	4.09
140.0	4.14	320.0	0.04	500.0	-0.03	680.0	6.56
150.0	3.89	330.0	0.04	510.0	-0.03	690.0	10.76
160.0	3.73	340.0	0.04	520.0	-0.03	700.0	17.89
170.0	3.55	350.0	0.04	530.0	-0.03	710.0	26.01

B.6 Lubricant Details

Lubricant — ESSO 5W/30
supplied at 2.9 bar and 150^0 *C*

		Dynamic Viscosity (cP)	
		Big-end bearings	Main bearings
Engine Speed (rpm)	2000	3.30	3.03
	3000	2.90	2.57
	4000	2.56	2.22
	5000	2.29	1.95
	6000	2.07	1.75
	6400	2.00	1.68
	7000	1.89	1.58

APPENDIX C
Technical Data for Ford 1.8L H.O. Zeta Engine Valve Train

C.1 General Data

Camshaft speeds (rpm)	500-3500
Operating temperature (^0C)	95
Valve timing (Deg.)	246
Angle between valve axis and cylinder axis (Deg.)	20

C.2 Cam Data

Cam width (mm)	11.0
Base circle radius (mm)	18.0
Cam taper angle (Deg.)	0.01667
Young's modulus (GN/m^2)	170.0
Poisson's ratio	0.28
Load over cam base circle (N)	64.251

Cam lift data for intake cams

Cam Angle (Deg.)	Lift (mm)	Cam Angle (Deg.)	Lift (mm)
-81.0	0.000000	0.0	9.300000
-80.0	0.000000	1.0	9.296453
-79.0	0.000000	2.0	9.285814
-78.0	0.000000	3.0	9.268088
-77.0	0.000000	4.0	9.243282
-76.0	0.000000	5.0	9.211408
-75.0	0.000000	6.0	9.172479
-74.0	0.000015	7.0	9.126513
-73.0	0.000851	8.0	9.073530
-72.0	0.002930	9.0	9.013554
-71.0	0.006672	10.0	8.946611
-70.0	0.012321	11.0	8.872732
-69.0	0.019917	12.0	8.791949
-68.0	0.029295	13.0	8.704298
-67.0	0.040101	14.0	8.609818
-66.0	0.051829	15.0	8.508552
-65.0	0.063875	16.0	8.400542

Cam Angle (Deg.)	Lift (mm)	Cam Angle (Deg.)	Lift (mm)
-64.0	0.075922	17.0	8.285839
-63.0	0.087969	18.0	8.164493
-62.0	0.100015	19.0	8.036557
-61.0	0.118955	20.0	7.902089
-60.0	0.165468	21.0	7.761152
-59.0	0.239553	22.0	7.613831
-58.0	0.341211	23.0	7.460234
-57.0	0.470441	24.0	7.300496
-56.0	0.626830	25.0	7.134778
-55.0	0.808173	26.0	6.963263
-54.0	1.010057	27.0	6.786163
-53.0	1.225866	28.0	6.603713
-52.0	1.446775	29.0	6.416173
-51.0	1.667685	30.0	6.223829
-50.0	1.888594	31.0	6.026991
-49.0	2.109503	32.0	5.825997
-48.0	2.330413	33.0	5.621207
-47.0	2.551322	34.0	5.413007
-46.0	2.772232	35.0	5.201810
-45.0	2.993142	36.0	4.988053
-44.0	3.214051	37.0	4.772197
-43.0	3.434961	38.0	4.554729
-42.0	3.655870	39.0	4.336163
-41.0	3.876780	40.0	4.117035
-40.0	4.097690	41.0	3.897836
-39.0	4.318525	42.0	3.678637
-38.0	4.538776	43.0	3.459439
-37.0	4.757887	44.0	3.240240
-36.0	4.975325	45.0	3.021041
-35.0	5.190589	46.0	2.801842
-34.0	5.403203	47.0	2.582644
-33.0	5.612720	48.0	2.363445
-32.0	5.818719	49.0	2.144246
-31.0	6.020808	50.0	1.925048
-30.0	6.218621	51.0	1.705849
-29.0	6.411822	52.0	1.486650
-28.0	6.600101	53.0	1.267451

Cam Angle (Deg.)	Lift (mm)	Cam Angle (Deg.)	Lift (mm)
-27.0	6.783175	54.0	1.053311
-26.0	6.960788	55.0	0.852981
-25.0	7.132715	56.0	0.673025
-24.0	7.298756	57.0	0.517818
-23.0	7.458737	58.0	0.389547
-22.0	7.612514	59.0	0.288623
-21.0	7.759972	60.0	0.215046
-20.0	7.901018	61.0	0.168816
-19.0	8.035587	62.0	0.149932
-18.0	8.163620	63.0	0.137886
-17.0	8.285059	64.0	0.125839
-16.0	8.399850	65.0	0.113792
-15.0	8.507941	66.0	0.101745
-14.0	8.609285	67.0	0.089699
-13.0	8.703838	68.0	0.077652
-12.0	8.791556	69.0	0.065605
-11.0	8.872401	70.0	0.053558
-10.0	8.946338	71.0	0.041812
-9.0	9.013331	72.0	0.030938
-8.0	9.073353	73.0	0.021419
-7.0	9.126377	74.0	0.013605
-6.0	9.172379	75.0	0.007672
-5.0	9.211337	76.0	0.003611
-4.0	9.243237	77.0	0.001224
-3.0	9.268063	78.0	0.000146
-2.0	9.285803	79.0	0.000019
-1.0	9.296450	80.0	0.000000

Cam lift data for exhaust cams

Cam Angle (Deg.)	Lift (mm)	Cam Angle (Deg.)	Lift (mm)
-79.0	0.000000	0.0	8.267276
-78.0	0.000000	1.0	8.264489
-77.0	0.000000	2.0	8.255671
-76.0	0.000000	3.0	8.240988
-75.0	0.000000	4.0	8.220459
-74.0	0.000000	5.0	8.194107
-73.0	0.000000	6.0	8.161964
-72.0	0.000063	7.0	8.124064
-71.0	0.001661	8.0	8.080442

Cam Angle (Deg.)	Lift (mm)	Cam Angle (Deg.)	Lift (mm)
-70.0	0.006952	9.0	8.031140
-69.0	0.016294	10.0	7.976199
-68.0	0.028000	11.0	7.915659
-67.0	0.040000	12.0	7.849563
-66.0	0.052000	13.0	7.777952
-65.0	0.064000	14.0	7.700869
-64.0	0.076000	15.0	7.618355
-63.0	0.088000	16.0	7.530451
-62.0	0.100000	17.0	7.437200
-61.0	0.115567	18.0	7.338643
-60.0	0.151624	19.0	7.234823
-59.0	0.212348	20.0	7.125780
-58.0	0.298017	21.0	7.011557
-57.0	0.408668	22.0	6.892195
-56.0	0.543872	23.0	6.767737
-55.0	0.701547	24.0	6.638223
-54.0	0.878171	25.0	6.503696
-53.0	1.070041	26.0	6.364197
-52.0	1.273545	27.0	6.219769
-51.0	1.485307	28.0	6.070452
-50.0	1.702339	29.0	5.916289
-49.0	1.922183	30.0	5.757322
-48.0	2.143060	31.0	5.593593
-47.0	2.363976	32.0	5.425148
-46.0	2.584391	33.0	5.252040
-45.0	2.803813	34.0	5.074330
-44.0	3.021761	35.0	4.892089
-43.0	3.237776	36.0	4.705406
-42.0	3.451427	37.0	4.514384
-41.0	3.662316	38.0	4.319146
-40.0	3.870088	39.0	4.119840
-39.0	4.074435	40.0	3.916650
-38.0	4.275103	41.0	3.709824
-37.0	4.471895	42.0	3.499675
-36.0	4.664646	43.0	3.286573
-35.0	4.853212	44.0	3.070936
-34.0	5.037470	45.0	2.853222

Cam Angle (Deg.)	Lift (mm)	Cam Angle (Deg.)	Lift (mm)
-33.0	5.217308	46.0	2.633922
-32.0	5.392631	47.0	2.413552
-31.0	5.563354	48.0	2.192642
-30.0	5.729400	49.0	1.971770
-29.0	5.890697	50.0	1.751957
-28.0	6.047176	51.0	1.534986
-27.0	6.198771	52.0	1.323307
-26.0	6.345414	53.0	1.119892
-25.0	6.487041	54.0	0.928099
-24.0	6.623587	55.0	0.751524
-23.0	6.754994	56.0	0.593869
-22.0	6.881203	57.0	0.458668
-21.0	7.002162	58.0	0.348017
-20.0	7.117826	59.0	0.262348
-19.0	7.228152	60.0	0.201624
-18.0	7.333106	61.0	0.165567
-17.0	7.432655	62.0	0.150000
-16.0	7.526767	63.0	0.138000
-15.0	7.615410	64.0	0.126000
-14.0	7.698551	65.0	0.114000
-13.0	7.776159	66.0	0.102000
-12.0	7.848200	67.0	0.090000
-11.0	7.914643	68.0	0.078000
-10.0	7.975456	69.0	0.066000
-9.0	8.030606	70.0	0.054000
-8.0	8.080060	71.0	0.042000
-7.0	8.123788	72.0	0.030095
-6.0	8.161758	73.0	0.019196
-5.0	8.193942	74.0	0.010427
-4.0	8.220314	75.0	0.004427
-3.0	8.240850	76.0	0.001196
-2.0	8.255531	77.0	0.000095
-1.0	8.264343	78.0	0.000000

C.3 Follower and Follower Guide Data

Radius of curvature of domed face (m)	8.0
Follower mass (kg)	0.054
Diameter of follower (mm)	28.4
Follower height (mm)	26.5
Young's modulus (GN/m^2)	204.0
Poison's ratio	0.29
Follower guide length (mm)	22.0
Radial clearance at follower/guide (mm)	0.024

C.4 Valve and Valve Guide Data

Diameter of valve stem for intake cam (mm)	6.043
Diameter of valve stem for exhaust cam (mm)	6.025
Valve guide length (mm)	36.0
Mass of valve,spring collar and clips (kg)	0.06
Radial clearance at valve/guide (mm)	0.02
Valve spring stiffness (N/m)	37634.0
Valve spring mass (kg)	0.035
Initial spring compression (mm)	5.5801

C.5 Camshaft and Camshaft Bearing Data

Cam positions and angles

Bay	Cam	Distance from Front of Bay (mm)	Angle to Max. Lift (Deg.)	Bay Length (mm)
1	1	50.4	0.0	69.9
2	2	19.5	0.0	91.8
2	3	72.3	270.0	
3	4	19.5	270.0	91.8
3	5	72.3	90.0	
4	6	19.5	90.0	91.8
4	7	72.3	180.0	
	8	19.5	180.0	

Camshaft bearing dimensions

	Diameter (mm)	Length (mm)	Radial Clearance (mm)	Ungrooved Region
Bearing No.1	25.97	20.0(9.0)	0.0225	full
Bearing No.2	25.97	17.0(7.5)	0.0225	full
Bearing No.3	25.97	17.0(7.5)	0.0225	full
Bearing No.4	25.97	17.0(7.5)	0.0225	full
Bearing No.5	25.97	17.0(7.5)	0.0225	full

C.6 Lubricant Data

Lubricant	ESSO 5W/30
Dynamic viscosity at ambient pressure and 95^{0}C (Pa.s)	0.009865
Viscosity-pressure coefficient (m^2/N)	0.22E-7

APPENDIX D
Technical Data for Ford 1.8L H.O. Zeta Engine Piston Assembly

D.1 General Data

2	Compression rings
1	Oil control ring
4	Stroke

Engine speeds (rpm)	2000-7000
Crankcase pressure (Pa)	0.0
Mean piston radial clearance (mm)	0.22785
Ratio of gas specific heats	1.3
Orifice discharge coefficient	0.65
Axial separation between compression rings (mm)	4.046
Surface roughness of cylinder liner (μm)	0.70

D.2 Piston Ring Data

	Top Ring	Second Ring	Oil Control Ring
Ring gap (mm)	0.4628	0.4628	
Radius of curvature (m)	0.063	0.500	
Ring height (mm)	1.484	1.184	0.500
Elastic tension (MPa)	0.200	0.134	1.890
Offset	0.0	-0.85	
Surface roughness (μm)	0.72	2.56	
Distance between ring groove & gudgeon-pin-boss axis (mm)	25.28	19.70	

D.3 Estimated Temperature Data (^{0}C)

Estimated Temperatures							
	Engine Speed (rpm)						
	2000	3000	4000	5000	6000	6400	7000
Mean combustion chamber	700	750	800	850	900	920	950
Top ring groove	170	195	210	220	230	235	240
Second ring groove	160	180	195	210	220	225	230
Maximum liner	165	185	195	200	210	215	220
Medium liner	150	170	180	185	195	200	205
Minimum liner	140	160	170	175	185	190	195

D.4 Lubricant Data

Lubricant	ESSO 5W/30
Dynamic viscosity at ambient pressure and 95^0C (Pa.s)	0.009865
Dynamic viscosity at ambient pressure and 135^0C (Pa.s)	0.005123